



**University of Messina**  
**Departement of Engineering**

**RWTH Aachen University**  
**ITMC**

---

**Development of Advanced Catalysts to Store Renewable Energy by  
Converting CO<sub>2</sub>**

---

**DOCTORAL THESIS**

**SINCHEM - Sustainable Industrial Chemistry**  
**Erasmus Mundus - Joint Doctoral Research program**

**Dottorato di XXX ciclo in**  
**Ingegneria e Chimica dei Materiali e delle Costruzioni**  
**Coordinator: Prof. Signorino Galvagno**  
**SSD: Chim04**

**Supervisor (HOME): Prof.ssa Siglinda PERATHONER**  
**Co-Supervisor: Dr. Eng. Salvatore ABATE**  
**Supervisor (HOST): Prof. Dr. Regina PALKOVITS**

**Chalachew Mebrahtu ASMELASH**

**October 2017**

***“Entwicklung fortschrittlicher Katalysatoren zur Speicherung erneuerbarer  
Energien durch Umsetzung von CO<sub>2</sub>”***

**Der Fakultät für Mathematik, Informatik und Naturwissenschaften der RWTH Aachen  
University vorgelegte Dissertation zur Erlangung des akademischen Grades eines Doktors  
der Naturwissenschaften**

von

***M.Sc. Chalachew Mebrahtu ASMELASH***

aus. ***SHIRE, ÄTHIOPIEN***

DEDICATION

***Dedicated  
To  
My Parents and  
My Wonderful Wife***

## EPIGRAPH

"I almost wish I hadn't gone down that rabbit-hole — and yet — and yet — it's rather curious, you know, this sort of life!" -**Alice in Wonderland**

The research presented in this Ph.D. thesis was carried out at the University of Messina, Department of Engineering, Laboratory of Catalysis for Sustainable Productions and Energy (CASPE/INSTM) and RWTH Aachen, ITMC, Chair of Heterogeneous Catalysis and Chemical Technology.



This work was co-funded through a SINCEM Grant. SINCEM is a Joint Doctorate programme selected under the Erasmus Mundus Action 1 Programme (FPA 2013-0037), the European Union's Seventh Framework Programme for the Fuel Cells and Hydrogen Joint Technology Initiative under grant agreement n° 621210 for the HELMETH project (Integrated High-Temperature Electrolysis and Methanation for Effective Power to Gas Conversion) and as part of the “Competence Center Power to Fuel” of RWTH Aachen University and project “Power to Fuel” of JARA Energy, which both are funded by the Excellence Initiative by the German federal and state governments to promote science and research at German universities.

## ACKNOWLEDGEMENT

First and foremost, praise God for his blessings and mercy for giving me health and strength in completing this work. I would like to express my earnest appreciation to my Ph.D. supervisors Prof. Siglinda Perathoner, Prof. Dr. Regina Palkovits, and Dr. Eng. Salvatore Abate, you have been tremendous mentors to me. I would especially like to thank Prof. Siglinda Perathoner for encouraging my research and allowing me to grow as a research scientist. Your advice on both the research as well as my career has been priceless. I have been very lucky to have your constant support during my Ph.D. and to share your passion for the research we have done.

I would like to thank Prof. Gabriele Centi for showing interest in my work from the beginning and for inspiring a brand new path for my research during my stay in his working group. Prof. Centi's insight has taught me so much over the years and will be a source of motivation as I continue academic research on CO<sub>2</sub> conversion to fuels and utilization.

I am thankful to Prof. Dr. Regina Palkovits and her research group at the ITMC, RWTH Aachen University. Regina has given me countless opportunities to pursue new ideas as well as her enthusiasm for teaching new ideas and immediate problem-solving abilities has always inspired me. In addition to all the members of the Palkovits's group, I would especially like to thank members of the syngas sub-group and Mr. Florian Krebs for the kind help, sharing ideas and guidance during my stay in the ITMC, RWTH Aachen.

During the time I spent working on the Ph.D. project, I realized the importance of cooperation and guidance. This project wouldn't be finished without the assistance of other people. Thus, under the completion of this study, I would like to thank all the past and present members of the Prof. Gabriele Centi and Prof. Siglinda Perathoner research group for making the Ph.D. a very enjoyable experience. I would especially like to thank Dr. Eng. Salvatore Abate for not only always taking the time to teach me something new, and for all the reactor dance playlists but also for being a great friend. I have really enjoyed both working and hanging out with everyone in the laboratory of Catalysis for Sustainable Productions and Energy (University of Messina) and would like to

thank Chen, Francesco, Giorgia, Gianfranco, Claudio, Chiara, Paola, Rosalba, Katia, Serena, Leo, Bhanu, and Atif.

In addition to all the wonderful people with whom I was lucky enough to work, I would also like to thank all my friends, specifically those around Messina and Aachen: Shiming Chen, Roberto Di Chio, Francesco Tavella, Andrés Felipe Sierra Salazar, Paolo Delia, Xinde Wang, Christian Landini, Matilde Solmi, Marco Zanette, and Hoang Phuoc.

I thank the SINCEM program, the committee, all the Professors and Ph.D. students for their constant support and encouragement. A special thanks go to Prof. Stefania Albonetti (SINCEM coordinator) for her help and guidance on all the academic and administrative matters. I would also thank to the SINCEM local coordinators Dr. Francesca Pollicino, Dr. Angela Garozzo and Anna Maria Casella (University of Messina) and Dr. Stefanie Mersmann (ITMC, RWTH Aachen University) for their help provided to carry out my Ph.D. thesis based on the cotutelle between University of Messina (Italy) and RWTH Aachen University (Germany).

Finally, I would like to express my sincere gratitude to the support and encouragement I got from my beloved wife Etabezahu Bahiru and my Mom. Their constant love, encouragement, and support have made me believe in myself and there are no words to describe the love and appreciation I feel for them. I thank you very much from the bottom of my heart. May God give you his rewards for your sacrifices!

**Chalachew Mebrahtu ASMELASH**



## LIST OF ABBREVIATIONS

AAS - Atomic Absorption Spectroscopy  
BET - Brunauer-Emmet-Teller  
BS - Basic Sites  
CCS - Carbon Capture and Storage  
CNG - Compressed Natural Gas  
CNTs - Carbon Nano Tubes  
CSP - Concentrated Solar Power  
DFT - Density Functional Theory  
DI- Deionized  
DSC - Differential Scanning Calorimeter  
EDX - Energy Dispersive X-ray  
EU - European Union  
FC - Fuel Cell  
FID - Flame Ionization Detector  
GC - Gas Chromatography  
GHSV - Gas Hourly Space Velocity  
HT - High Temperature  
HTs - Hydrotalcites  
ICP - OES - Inductively Coupled Plasma-Optical Emission Spectroscopy  
LT- Low Temperature  
NS - Nanosheet  
P2G - Power to Gas  
PEM - Proton Exchange Membrane  
SEM - Scanning Electron Microscopy  
SNG - Synthetic Natural Gas  
SOEC - Solid oxide electrolysis cell  
SR - Sabatier Reaction  
SSA - Specific Surface Area  
STEM - Scanning Transmission Electron Microscopy  
TCD - Thermal Conductivity Detector

TEM - Transmission Electron Microscopy  
TGA - Thermogravimetric Analysis  
TOF- Turnover Frequency  
TPD - Temperature Programmed Desorption  
TPR - Temperature Programmed Reduction  
TPV - Total Pore Volume  
XPS - X-ray Photoelectron Spectroscopy  
XRD - X-ray Diffraction  
XRF - X-ray Fluorescence

## ABSTRACT (English)

Reduction of greenhouse gases such as CO<sub>2</sub> requires enhancing the way how we store and use carbon sources. As the same time, the need of replacing non-renewable energy sources with renewables such as the wind and solar is growing. Therefore, due to the intermittent nature of renewable energy sources, a combined way to solve both issues is in demand. Among the possible solutions solar fuels production mainly methane by the Power to Gas (P2G) process (from renewable H<sub>2</sub> and CO<sub>2</sub>) enables to solve both long-term as well as large-scale energy storage and transportation problems. Solar or renewable fuels are mainly synthetic hydrocarbons that derive from hydrogen (from water electrolysis using surplus renewable electricity) and the CO<sub>2</sub> (from industries and captured). Possible examples of the fuels which can be produced using this process include methanol, methane, and liquid hydrocarbons. Compared amongst, those, methane is the most promising solution. Methane can be prepared with a single reaction (Sabatier reaction), has higher energy density and can be easily distributed using the existing natural gas network.

The methanation of CO<sub>2</sub> is an exothermic reaction favored at lower temperatures, but due to kinetic limitations, a catalyst needs to be utilized. For a catalyst to be of use in the industry it needs to meet certain cost, activity, selectivity, stability, recovery, reuse, and handling requirements. Nickel-based catalysts are the most commonly studied for CO<sub>2</sub> methanation because of their high activity and low price. However, conventional Ni catalysts supported on alumina are easily deactivated as a result of sintering of Ni particles and coke deposition during the exothermic methanation reaction. Hence, Ni-based catalysts with improved properties are still in need for this reaction at the industrial level.

This Ph.D. work, therefore, presents the synthesis and application of advanced Ni-based catalysts with better catalytic activity and stability than the conventional Ni/Al<sub>2</sub>O<sub>3</sub> catalyst. In order to achieve the principal goal of the study, four types of catalysts were prepared using different methods. In the laboratory of catalysis for sustainable energy and productions (University of Messina) mixed oxide supported Ni-based catalysts and Ni catalysts with unique structure were prepared and their catalytic activities were investigated towards low-temperature CO<sub>2</sub> methanation. As part of the project, during the mobility to RWTH Aachen, hydrotalcite derived

Ni-Fe catalysts were synthesized in order to study the effect Fe as second metal and support basicity in the low-temperature CO<sub>2</sub> methanation reaction.

For the studies on the effect of mixed oxide supports, ternary and quaternary mixed oxide supports were prepared by an impregnation-precipitation method using commercial  $\gamma$ -Al<sub>2</sub>O<sub>3</sub> powder as a host. The percentage of loading ZrO<sub>2</sub>, TiO<sub>2</sub> and CeO<sub>2</sub> promoters from their respective salt precursors were varied from 5 - 15%. As-prepared samples were characterized by BET, XRD, H<sub>2</sub>-TPR, CO-chemisorption, and CO-TPD analyses. The CO<sub>2</sub> methanation performance was evaluated at 5 bar pressure, temperature range of 300-400°C and different Gas Hourly Space Velocities (GHSVs) by using a high throughput reactor. Experimental results showed that enhanced catalytic activity depends on both textural improvements (for the ternary mixed oxide supported Ni-based catalysts) and reducibility and metal dispersion (for the quaternary mixed oxide supported Ni-based catalysts). The comparison between both groups of catalysts revealed that addition of CeO<sub>2</sub> to the ternary mixed oxide further improves the catalytic performance.

In order to study the effect of Fe as second metal in hydrotalcite derived catalysts, (Mg, Al)<sub>x</sub>O<sub>y</sub> supported Ni-Fe bimetallic catalysts were prepared using Ni-Mg-Fe-Al hydrotalcite-like precursors by co-precipitation at pH=10±0.5. The catalytic performance of Ni-Fe/MgAlO<sub>x</sub> catalysts was investigated in the synthetic natural gas production from CO<sub>2</sub> at 335°C, atmospheric pressure, and gas hourly space velocity of 12020 h<sup>-1</sup>. The catalysts were characterized by XRD, ICP-OES, BET specific surface area, TGA-DSC, STEM, H<sub>2</sub>-TPR, and irreversible acid adsorption. XRD analysis of the co-precipitated sample after drying confirmed the hydrotalcite-like structure of the precursors. STEM-EDS investigations proved that Ni-Fe alloys were obtained after the reduction pretreatment at 600°C. Among the investigated catalysts in the CO<sub>2</sub> methanation reaction, Ni-Fe catalyst with a relatively lower content of Fe (Fe/Ni=0.1) showed better activity with a rate of 6.96 mmol CO<sub>2</sub> conversion/mol<sub>metal</sub>/s, 99.3% of CH<sub>4</sub> selectivity and excellent stability for 24 h at 335°C.

Moving to the investigation on the effect of support basicity on the catalytic performance of hydrotalcite derived Ni-Fe, catalysts with various amount of MgO were prepared using the same procedure developed in the chapter described above. As-prepared materials were characterized by

XRD, H<sub>2</sub>-TPR, CO<sub>2</sub>-TPD, XRF and SEM and STEM techniques. Reduction at 900°C led to the formation of metallic Ni-Fe alloyed particles supported on a spinel type (Mg, Al)O<sub>x</sub> matrix. Catalytic measurements under differential conditions at 300°C revealed a reproducible CO<sub>2</sub> conversion into CH<sub>4</sub>. Higher CO<sub>2</sub> methanation activity was recorded over the Ni<sub>0.2</sub>Fe<sub>0.02</sub>Mg<sub>0.55</sub>Al<sub>0.23</sub> with 0.251 mol CO<sub>2</sub> conv./mol<sub>Ni+Fe</sub>/s CO<sub>2</sub> conversion rate and 97% CH<sub>4</sub> selectivity at 300°C. Catalytic CO<sub>2</sub> methanation of this catalyst was found much better than the other catalysts with relatively higher active metal loadings. The Mg<sub>0.75</sub>Al<sub>0.25</sub> (the Lewis base support) was inactive towards the CO<sub>2</sub> methanation reaction under similar pretreatments and reaction conditions. The better activity of Ni<sub>0.2</sub>Fe<sub>0.02</sub>Mg<sub>0.55</sub>Al<sub>0.23</sub> catalyst can be due to the optimal amount of basic sites, better metal dispersion and smaller average particle size obtained after reduction of the mixed oxide.

Finally, the effect of catalyst morphology was studied by preparing nanosheet-like catalysts via a two-step hydrothermal method and characterized by several physicochemical analyses methods. Catalytic behavior in CO<sub>2</sub> methanation was investigated in the 300-350°C temperature range and 5 bar pressure using a Microactivity Efficient equipment (Micromeritics) with two fixed bed continuous reactors. The catalytic performance was also compared with a commercial methanation catalyst. A higher activity at 300°C (about 860 mol<sub>CH<sub>4</sub></sub> mol<sub>Ni</sub><sup>-1</sup> h<sup>-1</sup>) and 99% of selectivity to CH<sub>4</sub> with stable performance for more than 50 h were observed for the nanosheet-like sample promoted by iron. With respect to a commercial methanation catalysts, the Fe-promoted nanosheet-like samples show an activity almost similar (slightly improved) with a lower rate of deactivation at 300°C. The improved properties of as-prepared catalysts comprehend to the synergy between NS structure and Fe promotion.

**Keywords:** Power to Gas, solar/renewable fuels, CO<sub>2</sub> methanation, nickel-based catalyst, mixed oxide supports, textural improvement, reducibility, hydrotalcite, Fe promotion, support basicity, nanosheet, hydrothermal synthesis, and stability.

## ABSTRACT (Italian)

La necessità di ridurre l'emissione di gas serra, in particolare CO<sub>2</sub>, richiede uno sviluppo nell'utilizzo e accumulo di fonti di carbone. Allo stesso tempo, si fa sempre più marcata la necessità di sostituire le fonti energetiche derivanti dai combustibili fossili, con quelle rinnovabili come eolico e solare. A causa della natura intermittente delle fonti energetiche rinnovabili, è richiesto un sforzo per risolvere entrambi i problemi, ottimizzando i processi di produzione e stoccaggio dell'energia. Tra le possibili soluzioni, la produzione di combustibili derivanti da fonti rinnovabili come il sole, principalmente metano, tramite il processo Power to Gas (P2G) (da rinnovabili H<sub>2</sub> e CO<sub>2</sub>) consente di risolvere sia i problemi di stoccaggio che di trasporto di energia su larga scala. I combustibili rinnovabili ottenuti tramite tale tecnologia, sono principalmente idrocarburi sintetici che derivano dalla reazione tra l'idrogeno (proveniente dall'elettrolisi ad acqua che utilizza l'eccesso di elettricità rinnovabile prodotta) e CO<sub>2</sub> (catturata e proveniente da altri processi). I combustibili che possono essere prodotti dal questo processo includono metanolo, metano e idrocarburi liquidi. Tra i vari prodotti, Il metano offre potenzialità maggiori per i seguenti motivi: può essere prodotto con una sola reazione (reazione Sabatier), ha una densità energetica elevata e può essere facilmente distribuito utilizzando la rete di gas naturale esistente.

La metanazione della CO<sub>2</sub> è una reazione esotermica favorita a basse temperature, ma a causa delle limitazioni cinetiche, è necessario utilizzare un catalizzatore al fine di raggiungere le performance richieste. Un buon catalizzatore industriale, deve soddisfare determinati requisiti come: costo, attività, selettività, stabilità, riutilizzo e gestione. I catalizzatori a base di nichel sono quelli più studiati per la metanazione di CO<sub>2</sub> a causa della loro elevata attività e basso costo. Tuttavia, i catalizzatori convenzionali a base di Ni supportati su allumina sono facilmente disattivati a seguito del “*sintering*” delle particelle metalliche e deposizione di “*coke*” durante la reazione di metanazione. Pertanto, uno studio su catalizzatori a base di Ni al fine di migliorarne la resa e la stabilità, è richiesto per uno sviluppo del processo a livello industriale.

Questo lavoro di tesi riporta, la sintesi e l'applicazione di catalizzatori avanzati a base di Ni con performace migliori, in termini di attività catalitica e stabilità, rispetto ad un catalizzatore commerciale Ni/Al<sub>2</sub>O<sub>3</sub>. A tal fine, sono stati preparati quattro tipi di catalizzatori con procedure

differenti. Nel laboratorio di catalisi per la produzione di energia sostenibile (Università di Messina) sono stati preparati catalizzatori a base di ossidi misti e catalizzatori con struttura unica (*nanosheet- NS*) e la loro attività catalitica è stata studiata nella reazione di metanazione a temperature relativamente basse (<350°C). Durante la mobilità a RWTH Aachen, sono stati sintetizzati catalizzatori a base di Ni con diversi contenuti di Fe al fine di studiare l'effetto del Fe come promotore per la reazione di metanazione.

I supporti di ossido misto ternario e quaternario sono stati preparati mediante un metodo di impregnazione-precipitazione usando  $\gamma$ -Al<sub>2</sub>O<sub>3</sub> commerciale come elemento principale, a cui sono stati aggiunti altri ossidi, in particolare ZrO<sub>2</sub>, TiO<sub>2</sub> e CeO<sub>2</sub> variando la percentuale in peso, in un range 5-15%. I campioni preparati sono stati caratterizzati tramite analisi BET, XRD, H<sub>2</sub>-TPR, CO-chemisorbimento e CO-TPD. La reazione di metanazione è stata effettuata a 5 bar di pressione, range di temperatura di 300-400°C, a diverse velocità di spaziali (GHSVs) usando un multireattore “*throughput reactor technology*” ad alto rendimento. I risultati sperimentali hanno mostrato che l'aumento dell'attività catalitica dipende dall' aumento di area superficiale, per i catalizzatori supportati su ossidi ternari. Il confronto tra i due gruppi di catalizzatori ha rivelato che l'aggiunta di CeO<sub>2</sub> all'ossido misto ternario (sistemi quaternari) migliora ulteriormente la performance catalitica. Tale comportamento è stato attribuito ad una migliore riducibilità e dispersione metallica del Ni nei sistemi quaternari.

Al fine di studiare l'effetto di Fe come promotore nei catalizzatori aventi struttura di idrotalcite, sono stati preparati idrotalciti contenenti precursori di Ni-Mg-Fe-Al mediante la tecnica di co-precipitazione a pH = 10 ± 0,5. La reazione catalitica è stata studiata alla temperatura di 335°C, pressione atmosferica e velocità spaziale di 12020 h<sup>-1</sup>. I materiali sintetizzati sono stati caratterizzati tramite tecniche XRD, ICP-OES, BET, TGA-DSC, STEM, H<sub>2</sub>-TPR e assorbimento di acido irreversibile. L'analisi XRD del campione co-precipitato dopo l'essiccazione ha confermato la struttura di idrotalcite. Le indagini STEM-EDS hanno dimostrato che le leghe Ni-Fe sono state ottenute dopo il pretrattamento di riduzione a 600°C. Tra i catalizzatori studiati, il catalizzatore Ni-Fe con un contenuto relativamente inferiore di Fe (Fe/Ni = 0,1) ha mostrato una migliore attività con una conversione di 6,96 mmol di CO<sub>2</sub> convertita/mole di metallo, 99,3% di selettività a CH<sub>4</sub> ed eccellente stabilità per 24 h a T=335°C.

L'effetto dei siti basici del supporto sull'attività catalitica è stato studiato su catalizzatori a struttura di idrotalcite, preparati secondo la procedura descritta prima, ma variando la quantità di MgO. I materiali preparati sono stati caratterizzati tramite tecniche XRD, H<sub>2</sub>-TPR, CO<sub>2</sub>-TPD, XRF e SEM e STEM. La riduzione ad elevata temperatura 900°C, ha condotto alla formazione di particelle di lega metallica Ni-Fe supportate su una matrice di tipo spinello (Mg, Al)O<sub>x</sub>. Il catalizzatore Ni<sub>0.2</sub>Fe<sub>0.02</sub>Mg<sub>0.55</sub>Al<sub>0.23</sub> si è mostrato essere il più attivo, nella metanazione di CO<sub>2</sub>, con una conversione di 0,251 moli di CO<sub>2</sub> convertiti/mol<sub>Ni+Fe</sub>/s e una selettività a CH<sub>4</sub> del 97% a T=300°C. Il catalizzatore Mg<sub>0.75</sub>Al<sub>0.25</sub> (supporto basico di Lewis) si è rivelato inattivo nelle stesse condizioni di reazione. L'attività del catalizzatore Ni<sub>0.2</sub>Fe<sub>0.02</sub>Mg<sub>0.55</sub>Al<sub>0.23</sub> è stata relazionata alla quantità ottimale di siti basici, a una migliore dispersione metallica e alla dimensione media delle particelle.

Infine, l'effetto della morfologia del catalizzatore è stato studiato preparando catalizzatori con struttura a "nanosheet" (NS) utilizzando un metodo idrotermale in due fasi. I catalizzatori preparati sono stati caratterizzati tramite diversi metodi di analisi fisico-chimica. L'attività catalitica nella metanazione di CO<sub>2</sub> è stata studiata nell'intervallo di temperatura 300-350°C e, pressione di 5 bar usando un reattore PID (Micromeritics) costituito da due reattori a letto fisso. L'attività catalitica è stata anche confrontata con un catalizzatore di metanazione commerciale. Si è osservata un'elevata attività a 300°C (circa 860 mol CH<sub>4</sub> molNi<sup>-1</sup> h<sup>-1</sup>) e 99% di selettività con comportamento stabile per più di 50 ore per il campione di con struttura NS dopato con Fe. Rispetto ad un catalizzatore di metanazione commerciale, tali catalizzatori dopati con Fe mostrano un'attività a 300°C più di tre volte superiore e con una velocità di disattivazione di 40 volte inferiore nelle prime ore del testing. La migliore attività dei catalizzatori con morfologia NS è stato attribuito ad un effetto sinergico tra la struttura NS e il Fe.

**Parole chiave:** "Power to gas", Combustibili solari o rinnovabili, metanazione della CO<sub>2</sub>, catalizzatori a base di nichel, supporti di ossido misto, proprietà strutturali, idrotalcite, promotore del Fe, basicità del supporto, "nanosheet", sintesi idrotermale, e stabilità.



## ABSTRACT (German)

Die Reduzierung von Treibhausgasen wie CO<sub>2</sub> benötigt eine Weiterentwicklung der Art und Weise wie Kohlenstoffquellen gelagert und genutzt werden. Gleichzeitig wächst die Notwendigkeit nicht erneuerbare Energien durch erneuerbare Energien wie Wind und Solar zu ersetzen. Auf Grund der zeitlich schwankenden Verfügbarkeit erneuerbarer Energien ist eine Kombination gefragt, die beide Probleme löst. Unter den möglichen Lösungen Solartreibstoffe Produktion vor allem Methan durch die Power-to-Gas Technologie löst sowohl die Problematik der Langzeitspeicherung, als auch der Speicherung im industriellen Maßstab und dessen Transport. Sogenannte Solar- oder erneuerbare Brennstoffe sind im Wesentlichen synthetische Kohlenwasserstoffe auf der Basis von Wasserstoff und Kohlenstoffdioxid. Wasserstoff wird hierbei durch Wasserelektrolyse mit überschüssigem Strom aus erneuerbaren Energien erzeugt, wohingegen CO<sub>2</sub> entweder aus der Industrie oder durch CO<sub>2</sub>-Abscheidung erhalten wird. Beispiele für Brennstoffe, die durch den Power-to-X Prozess hergestellt werden können, sind unter anderem Methanol, Methan und flüssige Kohlenwasserstoffe. Im Vergleich ist Methan das vielversprechendste Produkt. Es kann durch eine einzelne Reaktion (Sabatier Reaktion) hergestellt werden, besitzt eine hohe Energiedichte und kann direkt über das bereits existierende Erdgasnetzwerk verteilt werden.

Die Methanisierung von CO<sub>2</sub> ist eine exotherme Reaktion, die bevorzugt bei niedrigen Temperaturen abläuft. Aufgrund von kinetischen Limitierungen werden geeignete Katalysatoren eingesetzt. Ein Katalysator in der industriellen Anwendung muss bestimmte Kriterien, wie Kosten, Aktivität, Selektivität, Stabilität, Rückgewinnung, Wiederverwendbarkeit und Handhabbarkeit erfüllen. Nickel basierte Materialien sind bislang die am meisten Untersuchten Katalysatoren für CO<sub>2</sub> Methanisierung wegen ihrer hohen Aktivität und niedrigem Preis. Allerdings deaktivieren konventionelle auf Aluminiumoxid geträgerte Nickel-Katalysatoren leicht durch Sintern der Nickelpartikel und Kohlenstoffbildung während der Reaktion. Folglich sind Nickel basierte Katalysatoren mit verbesserten Eigenschaften notwendig für diese Reaktion im industriellen Maßstab.

Diese Doktorarbeit zeigt die Synthese und Anwendung von weiterentwickelten Nickelbasierten Katalysatoren mit verbesserter katalytischen Aktivität und Stabilität im Vergleich zu

konventionellen Ni/Al<sub>2</sub>O<sub>3</sub> Katalysatoren. Um dieses Ziel zu erreichen wurden vier Katalysatorarten durch verschiedene Methoden hergestellt. Im Labor für Katalyse für nachhaltige Energie und Produktion (Universität Messina) wurden nickelbasierte Katalysatoren geträgert auf Mischoxiden und Nickelkatalysatoren mit einzigartiger Struktur synthetisiert und deren katalytische Aktivität in der Niedrigtemperatur CO<sub>2</sub> Methanisierung untersucht. Während des Aufenthaltes an der RWTH Aachen wurden hydrotalcit-basierte Ni-Fe Katalysatoren hergestellt um den Effekt von Eisen als Zweitmetall und die Basizität des Trägermaterials zu untersuchen.

In der Studie über den Einfluss von Mischoxidträgermaterialien wurden ternäre und quaternäre Mischoxide durch eine Imprägnierungs-Fällungsmethode mit kommerziellem  $\gamma$ -Al<sub>2</sub>O<sub>3</sub> Pulver als Basis hergestellt. Die prozentuale Beladung mit ZrO<sub>2</sub>, TiO<sub>2</sub> und CeO<sub>2</sub> Promotoren wurde ausgehend von deren jeweiligen Salz-Präkursoren im Bereich von 5 – 15% variiert. Die Materialien wurden durch BET, XRD, H<sub>2</sub>-TPD, CO-Chemisorption und CO-TPD Analyse charakterisiert, sowie deren Verhalten in der CO<sub>2</sub> Methanisierung bei 5 bar Druck, einem Temperaturbereich von 300-400 °C und verschiedenen Raumgeschwindigkeiten (GHSV) in einem Hochdurchsatzreaktor bewertet. Die experimentellen Ergebnisse zeigen, dass eine verbesserte katalytische Aktivität sowohl durch strukturelle Verbesserung (im Falle der ternären Ni/Mischoxidkatalysatoren), als auch besserer Reduzierbarkeit und Metalldispersion (bei quaternären Ni/Mischoxidkatalysatoren) erzielt wird. Der Vergleich beider Gruppen an Katalysatoren zeigt, dass der Zusatz von CeO<sub>2</sub> zu ternären Mischoxiden die katalytische Leistung weiter steigert.

Für die Untersuchung des Einflusses von Eisen als zweites Metall wurden bimetallische Ni-Fe Katalysatoren aus hydrotalcitartigen Ni-Mg-Fe-Al Vorstufen durch Co-Fällung bei pH = 10 ± 0,5 hergestellt. Die katalytische Aktivität der Ni-Fe/MgAlO<sub>x</sub> Katalysatoren wurde in der synthetischen Erdgas (SNG) Produktion aus CO<sub>2</sub> bei 335 °C, atmosphärischem Druck und einer Raumgeschwindigkeit (GHSV) von 12020 h<sup>-1</sup> ermittelt. Die Katalysatoren wurden durch XRD, ICP-OES, BET spezifische Oberfläche, TGA-DSC, STEM, H<sub>2</sub>-TPR und irreversibler Säureadsorption charakterisiert. XRD Analyse der getrockneten co-gefällten Vorstufen bestätigte deren hydrotalciteartige Struktur. STEM-EDS Untersuchungen zeigten, dass Ni-Fe Legierungen erhalten wurden nach der Reduktion bei 600°C. Unter den untersuchten Katalysatoren in der CO<sub>2</sub>

Methanisierungsreaktion zeigten Ni-Fe Katalysatoren mit niedrigem Eisenanteil ( $\text{Fe/Ni} = 0,1$ ) die beste Aktivität mit einer Rate von  $6,96 \text{ mmol CO}_2/\text{mol}_{\text{Metall}}/\text{s}$ , 99,3% Methanselektivität und exzellenter Stabilität über einen Zeitraum von 24 Stunden bei  $335^\circ\text{C}$ .

Im Folgenden wurde der Einfluss der Basizität des Trägermaterials auf die katalytische Aktivität der hydrotalcit basierten Ni-Fe Katalysatoren untersucht. Die Materialien besitzen in diesem Fall einen unterschiedlichen Anteil an MgO und wurden nach gleichem Schema wie im vorherigen Kapitel hergestellt. Die Katalysatoren wurden durch XRD,  $\text{H}_2$ -TPD,  $\text{CO}_2$ -TPD, XRF und SEM/STEM charakterisiert. Die Reduktion bei  $900^\circ\text{C}$  führte zur Bildung von metallisch legierten Ni-Fe Partikeln auf einer spinellartigen  $(\text{Mg}, \text{Al})\text{O}_x$  Matrix. Katalytische Messungen unter differentiellen Bedingungen bei  $300^\circ\text{C}$  zeigten eine reproduzierbare  $\text{CO}_2$  Umsetzung zu Methan. Der höchste Umsatz wurde für die Zusammensetzung  $\text{Ni}_{0,2}\text{Fe}_{0,02}\text{Mg}_{0,55}\text{Al}_{0,23}$  mit  $0,251 \text{ mol}_{\text{CO}_2} \text{ conv.}/\text{mol}_{\text{Ni+Fe}}/\text{s}$  und einer  $\text{CH}_4$  Selektivität von 97% beobachtet. Die katalytische  $\text{CO}_2$  Methanisierung war bei diesem Katalysator deutlich besser als bei höheren aktiven Metallbeladungen. Das Lewis-basische Trägermaterial  $\text{Mg}_{0,75}\text{Al}_{0,25}$  allein war unter gleichen Testbedingungen inaktiv. Die verbesserte Aktivität des  $\text{Ni}_{0,2}\text{Fe}_{0,02}\text{Mg}_{0,55}\text{Al}_{0,23}$  Katalysators kann auf eine ausgewogene Menge an Basenzentren, besserer Metalldispersion und kleinerer mittlerer Partikelgröße nach der Reduktion der Mischoxide zurückgeführt werden.

Letztendlich wurde der Einfluss der Morphologie betrachtet durch Synthese von nanoplättchenartige Katalysatoren. Sie wurden durch eine zweistufige hydrothermal Methode hergestellt und durch verschiedenen physio-chemischen Analysemethoden charakterisiert. Dessen katalytisches Verhalten in der  $\text{CO}_2$  Methanisierung wurde bei  $300\text{-}350^\circ\text{C}$  und 5 bar Druck in einer Microactivity Efficient Anlage (Micromeritics) in zwei kontinuierlichen Festbettreaktoren untersucht. Die nanoplättchenartigen Katalysatoren mit Eisen als Promotor zeigten die höchste Aktivität bei  $300^\circ\text{C}$  von  $860 \text{ mol}_{\text{CH}_4} \text{ mol}_{\text{Ni}}^{-1} \text{ h}^{-1}$  und 99% Methanselektivität und einer Stabilität von über 50 Stunden. Verglichen mit kommerziellen Katalysatoren unter den gleichen Bedingungen diese Materialien eine nahezu ähnliche (leicht verbesserte) Aktivität und untere Deaktivierungsrate. Die verbesserten Eigenschaften entstehen durch Synergie zwischen der nanoplättchenartigen Struktur und Eisen als Promotor.

**Schlagwörter:** Power-to-Gas, Solar/erneuerbare Brennstoffe, CO<sub>2</sub> Methanisierung, Nickel-basierte Katalysatoren, Mischoxid-Trägermaterial, strukturelle Verbesserung, Reduzierbarkeit, Hydrotalcit, Fe-Promotor, Basizität des Trägermaterials, Nanoplättchen, hydrothermal Synthese und Stabilität.

## TABLE OF CONTENTS

DEDICATION.....	iii
EPIGRAPH.....	iv
ACKNOWLEDGEMENT.....	vii
LIST OF ABBREVIATIONS.....	ix
ABSTRACT.....	xi
TABLE OF CONTENTS.....	xxi
LIST OF FIGURES.....	xxv
LIST OF TABLES.....	xxxix

### CHAPTER

### PAGE N<sup>o</sup>

<b>1. General Introduction .....</b>	<b>1</b>
1.1. World energy outlook.....	1
1.2. CO <sub>2</sub> emissions and climate change .....	2
1.3. CO <sub>2</sub> utilization as feedstock .....	3
1.3.1. General aspects of CO <sub>2</sub> separation and usage.....	3
1.3.2. CO <sub>2</sub> for energy storage and transportation: the P2G concept .....	5
1.4. The CO <sub>2</sub> methanation: Sabatier reaction .....	7
1.4.1. Thermodynamics of CO <sub>2</sub> methanation.....	8
1.4.2. Kinetics and mechanism of CO <sub>2</sub> methanation .....	9
1.4.3. Catalysts for CO <sub>2</sub> methanation.....	10
1.4.3.1. Supported Ni-based catalysts.....	11
1.5. Thesis aim and scope.....	13
1.6. References .....	15
<b>2. Ternary and quaternary mixed oxides supported Ni catalysts for CO<sub>2</sub> methanation: a comparison with Ni/<math>\gamma</math>-Al<sub>2</sub>O<sub>3</sub> conventional catalyst .....</b>	<b>22</b>
2.1. Introduction .....	22
2.2. Scope of the chapter .....	23
2.3. Experimental .....	24

2.3.1. Synthesis of mixed oxide supported Ni-based catalysts .....	24
2.3.2. Characterization of as-prepared catalysts .....	25
2.2.3. Catalytic CO <sub>2</sub> methanation .....	25
2.3. Results and discussion.....	27
2.3.1. Ternary mixed oxides supported Ni-based catalysts .....	27
2.3.1.1. Characterization results .....	27
2.3.1.2. Catalytic activity in CO <sub>2</sub> methanation of the ternary mixed oxides supported Ni-based catalysts.....	33
2.3.2. Quaternary mixed oxides supported Ni-based catalysts .....	35
2.3.2.1. Characterization results .....	35
2.3.2.2. Comparison of ternary and quaternary mixed oxides supported Ni-based catalysts: the effect of CeO <sub>2</sub> .....	40
2.3.3. Structure and activity relationships.....	42
2.4. Conclusion.....	44
2.5. References .....	45
ANNEX <sup>2</sup> .....	47
<b>3. Synthesis, characterization and activity pattern of hydrotalcite derived Ni-Fe catalysts for CO<sub>2</sub> methanation .....</b>	<b>49</b>
3.1. Introduction .....	49
3.2. Scope of the chapter .....	51
3.3. Experimental .....	51
3.3.1. Synthesis of catalysts .....	51
3.3.2. Characterization of as-prepared catalysts .....	51
3.3.3. Catalytic CO <sub>2</sub> methanation test.....	53
3.4. Results and Discussion.....	54
3.4.1. Characterization results.....	54
3.4.2. Catalytic activity tests towards CO <sub>2</sub> methanation.....	67
3.4.2.1. Factors affecting the catalytic performance of Ni-Fe catalysts .....	67
3.4.2.1.1. Effect of Fe to Ni ratio .....	68
3.4.2.1.2. Particle size effect .....	71
3.4.2.1.3. Effect of basic sites.....	72

3.4.2.2. Effect of reduction temperature .....	73
3.4.2.3. Stability test .....	75
3.5. Characterization of the spent catalysts .....	76
3.6. Conclusion.....	80
3.7. References .....	82
ANNEX <sup>3</sup> .....	85
<b>4. Effect of support basicity on hydrotalcite derived Ni-Fe catalysts towards low-temperature CO<sub>2</sub> methanation .....</b>	<b>87</b>
4.1. Introduction .....	87
4.2. Scope of the chapter .....	88
4.3. Experimental .....	88
4.3.1. Catalysts preparation.....	88
4.3.2. Characterization of as-prepared catalysts .....	89
4.3.3. Catalytic performance .....	90
4.4. Results and Discussion.....	91
4.4.1. Characterization results.....	91
4.4.2. Activity, selectivity, and stability of the hydrotalcite derived catalysts towards CO <sub>2</sub> methanation.....	101
4.5. Conclusion.....	106
4.6. References .....	107
ANNEX <sup>4</sup> .....	109
<b>5. Fe - promoted Ni/<math>\gamma</math>-Al<sub>2</sub>O<sub>3</sub> nanosheets as highly active and stable catalyst for CO<sub>2</sub> methanation .....</b>	<b>111</b>
5.1. Introduction .....	111
5.2. Scope of the chapter .....	112
5.3. Experimental .....	113
5.3.1. Synthesis of materials .....	113
5.3.2. Catalyst characterizations .....	114
5.3.3. Catalytic activity tests .....	116
5.4. Results and Discussion.....	117
5.4.1. Characterization results.....	117

5.4.2. Catalytic activity tests .....	128
5.4.2.1. Factors affecting the catalytic activity .....	133
5.4.2.1.1. Effect of catalyst structure and Fe promotion .....	133
5.4.2.1.2. Effect of CO <sub>2</sub> adsorption sites .....	134
5.5. Characterization of spent catalysts .....	136
5.6. Conclusion.....	138
5.7. References .....	139
ANNEX <sup>5</sup> .....	141
<b>6. General conclusion and outlooks .....</b>	<b>143</b>
<b>Curriculum vitae .....</b>	<b>147</b>



## LIST OF FIGURES

<b>Figure 1.1</b> Estimated renewable energy share of global energy production by the end of 2016 (adapted from [5]).	1
<b>Figure 1.2</b> Amount of CO <sub>2</sub> emitted per year (adapted from [8]).	2
<b>Figure 1.3</b> Schematic overview of possible routes of the CO <sub>2</sub> conversion to incorporate renewable energy in the chemical and energy chains (adapted from [14]).	5
<b>Figure 1.4</b> Power-to-gas pathway through both low-temperature (LT) and high-temperature (HT) electrolysis devices (adapted from [18]).	7
<b>Figure 1.5</b> Equilibrium conversion as well as H <sub>2</sub> and CH <sub>4</sub> content for CO <sub>2</sub> methanation ((H <sub>2</sub> /CO <sub>2</sub> ) <sub>in</sub> = 4, no inert gases) (adapted from [21]).	8
<b>Figure 1.6</b> Possible mechanisms of CO <sub>2</sub> methanation.	9
<b>Figure 2.1</b> High-throughput reactor (Amtech high-throughput technology SPIDER 16) used for the catalytic CO <sub>2</sub> methanation.	26
<b>Figure 2.2</b> XRD of (a) 20%Ni on the different supports; (b) $\gamma$ -Al <sub>2</sub> O <sub>3</sub> and $\gamma$ -Al <sub>2</sub> O <sub>3</sub> -ZrO <sub>2</sub> -TiO <sub>2</sub> mixed-oxide supports.	28
<b>Figure 2.3</b> H <sub>2</sub> -TPR profiles: (a) 20%Ni/ $\gamma$ -Al <sub>2</sub> O <sub>3</sub> , (b) 20%Ni/C5, (c) 20%Ni/C10 and (d) 20%Ni/C15.	30
<b>Figure 2.4</b> CO-TPD profiles of (a) 20%Ni/ $\gamma$ -Al <sub>2</sub> O <sub>3</sub> , (b) 20%Ni/C5, (c) 20%Ni/C10 and (d) 20%Ni/C15.	31
<b>Figure 2.5</b> Catalytic performance of different Ni samples for CO <sub>2</sub> methanation. Reaction conditions: gas mixture with CO <sub>2</sub> :H <sub>2</sub> = 1:4, P = 5 bar, and: (a) GHSV=2000 h <sup>-1</sup> , (b) GHSV= 3000 h <sup>-1</sup> and (c) GHSV= 4000 h <sup>-1</sup> .	34
<b>Figure 2.6</b> XRD of (a) 20%Ni on the different supports; (b) $\gamma$ -Al <sub>2</sub> O <sub>3</sub> and $\gamma$ -Al <sub>2</sub> O <sub>3</sub> -ZrO <sub>2</sub> -TiO <sub>2</sub> -CeO <sub>2</sub> mixed-oxide support.	36
<b>Figure 2.7</b> H <sub>2</sub> -TPR profiles: (a) 20%Ni/ $\gamma$ -Al <sub>2</sub> O <sub>3</sub> , (b) 20%Ni/C5-5%CeO <sub>2</sub> , (c) 20%Ni/C10-10%CeO <sub>2</sub> and (d) 20%Ni/C15-15%CeO <sub>2</sub> .	38
<b>Figure 2.8</b> H <sub>2</sub> -TPR profiles of (a) C15-15%CeO <sub>2</sub> mixed oxide support and (b) 20%Ni/C15-15%CeO <sub>2</sub> catalyst.	40

<b>Figure 2.9</b> Catalytic performance in CO <sub>2</sub> methanation of the Ni samples supported on the ternary and quaternary system. Reaction conditions: gas mixture with CO <sub>2</sub> :H <sub>2</sub> = 1:4, P = 5 bar, and (a) GHSV = 2000 h <sup>-1</sup> , (b) GHSV = 3000 h <sup>-1</sup> and (c) GHSV = 4000 h <sup>-1</sup> . .....	41
<b>Figure 2.10</b> Structure and catalytic performance relationships: (A) Activity vs BET specific surface area of the ternary-mixed oxide supported catalysts, (B) Activity vs metal dispersion of Ni/Al and catalysts supported on the mixed oxides. Reaction conditions: 350°C, 5 bar and 4000 h <sup>-1</sup> . .....	42
<b>Figure 3.1</b> (a) assembled and validated set-up and (b) on-line gas chromatograph used for the CO <sub>2</sub> methanation tests.....	54
<b>Figure 3.2</b> XRD patterns of the dried HT precursors: (a) Ni/(Mg, Al)O <sub>x</sub> , (b) Ni-Fe/(Mg, Al)O <sub>x</sub> (Fe/Ni=0.1), (c) Ni-Fe/(Mg, Al)O <sub>x</sub> (Fe/Ni=0.5), (d) Ni-Fe/(Mg, Al)O <sub>x</sub> (Fe/Ni=1), (e) Ni-Fe/(Mg, Al)O <sub>x</sub> (Fe/Ni=1.5) and (f) Fe/(Mg, Al)O <sub>x</sub> . .....	56
<b>Figure 3.3</b> XRD patterns of the catalysts after calcination at 450°C: (a) Ni/(Mg, Al)O <sub>x</sub> , (b) Ni-Fe/(Mg, Al)O <sub>x</sub> (Fe/Ni=0.1), (c) Ni-Fe/(Mg, Al)O <sub>x</sub> (Fe/Ni=0.5), (d) Ni-Fe/(Mg, Al)O <sub>x</sub> (Fe/Ni=1), (e) Ni-Fe/(Mg, Al)O <sub>x</sub> (Fe/Ni=1.5) and (f) Fe/(Mg, Al)O <sub>x</sub> . Crystalline phases: MgO periclase (●) JCPDS 00-043-1022 NaNO <sub>3</sub> (□) JCPDS 00-036-1474, and spinel (▲).....	58
<b>Figure 3.4</b> H <sub>2</sub> -TPR profiles of the catalysts after calcination at 450°C: (a) Ni/(Mg, Al)O <sub>x</sub> , (b) Ni-Fe/(Mg, Al)O <sub>x</sub> (Fe/Ni = 0.1), (c) Ni-Fe/(Mg, Al)O <sub>x</sub> (Fe/Ni = 0.5), (d) Ni-Fe/(Mg, Al)O <sub>x</sub> (Fe/Ni = 1), (e) Ni-Fe/(Mg, Al)O <sub>x</sub> (Fe/Ni = 1.5) and (f) Fe/(Mg, Al)O <sub>x</sub> .....	60
<b>Figure 3.5</b> STEM images of reduced HTs derived bimetallic catalysts: (a) Ni-Fe/(Mg, Al)O <sub>x</sub> (Fe/Ni=0.1), (b) Ni-Fe/(Mg, Al)O <sub>x</sub> (Fe/Ni=0.5), (c) Ni-Fe/(Mg, Al)O <sub>x</sub> (Fe/Ni=1) and (d) Ni-Fe/(Mg, Al)O <sub>x</sub> (Fe/Ni=1). .....	63
<b>Figure 3.6</b> Ni <sub>2p3/2</sub> XPS spectra: (a) Ni-Fe/(Mg, Al)O <sub>x</sub> (Fe/Ni = 0.1) and (b) Ni-Fe/(Mg, Al)O <sub>x</sub> (Fe/Ni = 0.5). .....	66
<b>Figure 3.7</b> Fe <sub>2p3/2</sub> XPS spectrum for Ni-Fe/(Mg, Al)O <sub>x</sub> (Fe/Ni=0.5) catalyst. ....	67
<b>Figure 3.8</b> Effect of Fe/Ni ratio on the CO <sub>2</sub> methanation reaction (Reaction conditions: gas mixture with CO <sub>2</sub> :H <sub>2</sub> = 1:4, P = 1 atm, T = 335°C, and GHSV = 12020 h <sup>-1</sup> ): (a) Ni/(Mg, Al)O <sub>x</sub> , (b) Ni-Fe/(Mg, Al)O <sub>x</sub> (Fe/Ni = 0.1), (c) Ni-Fe/(Mg, Al)O <sub>x</sub> (Fe/Ni = 0.5), (d) Ni-Fe/(Mg, Al)O <sub>x</sub> (Fe/Ni = 1), (e) Ni-Fe/(Mg, Al)O <sub>x</sub> (Fe/Ni = 1.5) and (f) Fe/(Mg, Al)O <sub>x</sub> . .....	68

<b>Figure 3.9</b> Synergistic effect of Fe-Ni alloys compared to sole metals on CO <sub>2</sub> methanation rate. .....	69
<b>Figure 3.10</b> Effect of Fe content on CH <sub>4</sub> (○) and CO (Δ) selectivity in comparison to sole metals. Reaction conditions: gas mixture with CO <sub>2</sub> :H <sub>2</sub> = 1:4, P = 1 atm, T = 335°C, and GHSV = 12020 h <sup>-1</sup> . .....	70
<b>Figure 3.11</b> Influence of metal particle size on activity (a) and product selectivity (b) in CO <sub>2</sub> methanation. Reaction conditions: gas mixture with CO <sub>2</sub> :H <sub>2</sub> = 1:4, P = 1 atm, T = 335°C, and GHSV = 12020 h <sup>-1</sup> . .....	72
<b>Figure 3.12</b> CO <sub>2</sub> conversion rate vs. total basic sites of the HTs derived catalysts. Reaction conditions: gas mixture with CO <sub>2</sub> :H <sub>2</sub> = 1:4, P = 1 atm, T = 335°C, and GHSV = 12020 h <sup>-1</sup> . .....	73
<b>Figure 3.13</b> Effect of reduction treatment on the CO <sub>2</sub> methanation reaction (Reaction conditions: gas mixture with CO <sub>2</sub> :H <sub>2</sub> = 1:4, P = 1 atm, T = 335°C, and GHSV = 12020 h <sup>-1</sup> ): (a) Ni- Fe/(Mg, Al)O <sub>x</sub> (Fe/Ni=0.1) at 600°C, (b) Ni-Fe/(Mg, Al)O <sub>x</sub> (Fe/Ni=0.1) at 500°C, (c) Ni-Fe/(Mg, Al)O <sub>x</sub> (Fe/Ni=0.5) at 600°C, (d) Ni-Fe/(Mg, Al)O <sub>x</sub> (Fe/Ni=0.5) at 500°C. .....	74
<b>Figure 3.14</b> Effect of reduction pretreatment on CH <sub>4</sub> (□) and CO (■) selectivity: (a) Ni-Fe/(Mg, Al)O <sub>x</sub> (Fe/Ni=0.1) at 600°C, (b) Ni-Fe/(Mg, Al)O <sub>x</sub> (Fe/Ni=0.1) at 500°C, (c) Ni- Fe/(Mg, Al)O <sub>x</sub> (Fe/Ni=0.5) at 600°C, (d) Ni-Fe/(Mg, Al)O <sub>x</sub> (Fe/Ni=0.5) at 500°C. 75	75
<b>Figure 3.15</b> Stability of catalyst activity and CH <sub>4</sub> selectivity with the reaction time over Ni- Fe/(Mg, Al)O <sub>x</sub> (Fe/Ni=0.1) catalyst. Reaction conditions: gas mixture with CO <sub>2</sub> :H <sub>2</sub> = 1:4, P = 1 atm, T = 335°C, and GHSV = 12020 h <sup>-1</sup> . .....	76
<b>Figure 3.16</b> XRD pattern of the catalysts after the CO <sub>2</sub> methanation (a) Ni-Fe/(Mg, Al)O <sub>x</sub> (Fe/Ni = 0.1) and (b) Ni-Fe/(Mg, Al)O <sub>x</sub> (Fe/Ni = 0.5): formation of Ni-Fe alloys (□). .....	77
<b>Figure 3.17</b> Dependence of d(200) spacing for Fe-Ni alloys as a function of the Fe/(Ni + Fe) molar ratio for catalysts after CO <sub>2</sub> methanation: (a) Ni-Fe/(Mg, Al)O <sub>x</sub> (Fe/Ni = 0.1) and (b) Ni-Fe/(Mg, Al)O <sub>x</sub> (Fe/Ni = 0.5). The dashed line describes theoretical behavior using Vegard's law with fcc Ni metal (JCPDS 01-070-1849) and fcc γ-Fe (JCPDS 01-089- 4185) as references (■). .....	78
<b>Figure 3.18</b> TG analysis of spent catalyst Ni-Fe/(Mg, Al)O <sub>x</sub> (Fe/Ni=0.1) HTs.....	79
<b>Figure 3.19</b> Raman spectrum of Ni-Fe/(Mg, Al)O <sub>x</sub> (Fe/Ni=0.1) HTs spent catalyst.....	80

<b>Figure 4.1</b> XRD diffraction patterns of dried samples: (a) $\text{Mg}_{0.75}\text{Al}_{0.25}$ (b) $\text{Ni}_{0.12}\text{Fe}_{0.012}\text{Mg}_{0.63}\text{Al}_{0.238}$ (c) $\text{Ni}_{0.2}\text{Fe}_{0.02}\text{Mg}_{0.55}\text{Al}_{0.23}$ (d) $\text{Ni}_{0.4}\text{Fe}_{0.04}\text{Mg}_{0.35}\text{Al}_{0.21}$ (e) $\text{Ni}_{0.6}\text{Fe}_{0.06}\text{Mg}_{0.15}\text{Al}_{0.19}$ and (f) $\text{Ni}_{0.75}\text{Fe}_{0.075}\text{Al}_{0.175}$ .....	91
<b>Figure 4.2</b> XRD diffraction patterns of calcined samples: (a) $\text{Mg}_{0.75}\text{Al}_{0.25}$ (b) $\text{Ni}_{0.12}\text{Fe}_{0.012}\text{Mg}_{0.63}\text{Al}_{0.238}$ (c) $\text{Ni}_{0.2}\text{Fe}_{0.02}\text{Mg}_{0.55}\text{Al}_{0.23}$ (d) $\text{Ni}_{0.4}\text{Fe}_{0.04}\text{Mg}_{0.35}\text{Al}_{0.21}$ (e) $\text{Ni}_{0.6}\text{Fe}_{0.06}\text{Mg}_{0.15}\text{Al}_{0.19}$ and (f) $\text{Ni}_{0.75}\text{Fe}_{0.075}\text{Al}_{0.175}$ .....	92
<b>Figure 4.3</b> XRD diffraction patterns of reduced samples: (b) $\text{Ni}_{0.12}\text{Fe}_{0.012}\text{Mg}_{0.63}\text{Al}_{0.238}$ (c) $\text{Ni}_{0.2}\text{Fe}_{0.02}\text{Mg}_{0.55}\text{Al}_{0.23}$ (d) $\text{Ni}_{0.4}\text{Fe}_{0.04}\text{Mg}_{0.35}\text{Al}_{0.21}$ (e) $\text{Ni}_{0.6}\text{Fe}_{0.06}\text{Mg}_{0.15}\text{Al}_{0.19}$ and (f) $\text{Ni}_{0.75}\text{Fe}_{0.075}\text{Al}_{0.175}$ .....	93
<b>Figure 4.4</b> $\text{H}_2$ -TPR profiles of calcined samples: (a) $\text{Mg}_{0.75}\text{Al}_{0.25}$ (b) $\text{Ni}_{0.12}\text{Fe}_{0.012}\text{Mg}_{0.63}\text{Al}_{0.238}$ (c) $\text{Ni}_{0.2}\text{Fe}_{0.02}\text{Mg}_{0.55}\text{Al}_{0.23}$ (d) $\text{Ni}_{0.4}\text{Fe}_{0.04}\text{Mg}_{0.35}\text{Al}_{0.21}$ (e) $\text{Ni}_{0.6}\text{Fe}_{0.06}\text{Mg}_{0.15}\text{Al}_{0.19}$ and (f) $\text{Ni}_{0.75}\text{Fe}_{0.075}\text{Al}_{0.175}$ .....	95
<b>Figure 4.5</b> $\text{CO}_2$ -TPD profiles of calcined catalysts: (a) $\text{Mg}_{0.75}\text{Al}_{0.25}$ (b) $\text{Ni}_{0.12}\text{Fe}_{0.012}\text{Mg}_{0.63}\text{Al}_{0.238}$ (c) $\text{Ni}_{0.2}\text{Fe}_{0.02}\text{Mg}_{0.55}\text{Al}_{0.23}$ (d) $\text{Ni}_{0.4}\text{Fe}_{0.04}\text{Mg}_{0.35}\text{Al}_{0.21}$ (e) $\text{Ni}_{0.6}\text{Fe}_{0.06}\text{Mg}_{0.15}\text{Al}_{0.19}$ and (f) $\text{Ni}_{0.75}\text{Fe}_{0.075}\text{Al}_{0.175}$ .....	96
<b>Figure 4.6</b> SEM images of dried samples: (a) $\text{Mg}_{0.75}\text{Al}_{0.25}$ (b) $\text{Ni}_{0.12}\text{Fe}_{0.012}\text{Mg}_{0.63}\text{Al}_{0.238}$ (c) $\text{Ni}_{0.2}\text{Fe}_{0.02}\text{Mg}_{0.55}\text{Al}_{0.23}$ (d) $\text{Ni}_{0.4}\text{Fe}_{0.04}\text{Mg}_{0.35}\text{Al}_{0.21}$ (e) $\text{Ni}_{0.6}\text{Fe}_{0.06}\text{Mg}_{0.15}\text{Al}_{0.19}$ and (f) $\text{Ni}_{0.75}\text{Fe}_{0.075}\text{Al}_{0.175}$ .....	98
<b>Figure 4.7</b> Dark field STEM images and the corresponding histograms of nickel particle size distribution for the reduced catalysts: (b) $\text{Ni}_{0.12}\text{Fe}_{0.012}\text{Mg}_{0.63}\text{Al}_{0.238}$ (c) $\text{Ni}_{0.2}\text{Fe}_{0.02}\text{Mg}_{0.55}\text{Al}_{0.23}$ (d) $\text{Ni}_{0.4}\text{Fe}_{0.04}\text{Mg}_{0.35}\text{Al}_{0.21}$ (e) $\text{Ni}_{0.6}\text{Fe}_{0.06}\text{Mg}_{0.15}\text{Al}_{0.19}$ and (f) $\text{Ni}_{0.75}\text{Fe}_{0.075}\text{Al}_{0.175}$ .....	100
<b>Figure 4.8</b> Rate of $\text{CO}_2$ conversion of all prepared catalysts under differential reaction conditions: gas mixture with $\text{CO}_2:\text{H}_2 = 1:4$ , $P = 1$ atm, $T = 300^\circ\text{C}$ , and $\text{GHSV} = 217430 \text{ h}^{-1}$ : (a) $\text{Mg}_{0.75}\text{Al}_{0.25}$ (b) $\text{Ni}_{0.12}\text{Fe}_{0.012}\text{Mg}_{0.63}\text{Al}_{0.238}$ (c) $\text{Ni}_{0.2}\text{Fe}_{0.02}\text{Mg}_{0.55}\text{Al}_{0.23}$ (d) $\text{Ni}_{0.4}\text{Fe}_{0.04}\text{Mg}_{0.35}\text{Al}_{0.21}$ (e) $\text{Ni}_{0.6}\text{Fe}_{0.06}\text{Mg}_{0.15}\text{Al}_{0.19}$ and (f) $\text{Ni}_{0.75}\text{Fe}_{0.075}\text{Al}_{0.175}$ .....	102
<b>Figure 4.9</b> Selectivity towards $\text{CH}_4$ and $\text{CO}$ of all prepared catalysts under differential reaction conditions: gas mixture with $\text{CO}_2:\text{H}_2 = 1:4$ , $P = 1$ atm, $T = 300^\circ\text{C}$ , and $\text{GHSV} = 217430 \text{ h}^{-1}$ : (a) $\text{Mg}_{0.75}\text{Al}_{0.25}$ (b) $\text{Ni}_{0.12}\text{Fe}_{0.012}\text{Mg}_{0.63}\text{Al}_{0.238}$ (c) $\text{Ni}_{0.2}\text{Fe}_{0.02}\text{Mg}_{0.55}\text{Al}_{0.23}$ (d) $\text{Ni}_{0.4}\text{Fe}_{0.04}\text{Mg}_{0.35}\text{Al}_{0.21}$ (e) $\text{Ni}_{0.6}\text{Fe}_{0.06}\text{Mg}_{0.15}\text{Al}_{0.19}$ and (f) $\text{Ni}_{0.75}\text{Fe}_{0.075}\text{Al}_{0.175}$ .....	103

<b>Figure 4.10</b> Stability of Ni <sub>0.2</sub> Fe <sub>0.02</sub> Mg <sub>0.55</sub> Al <sub>0.23</sub> catalyst under differential reaction conditions: gas mixture with CO <sub>2</sub> :H <sub>2</sub> = 1:4, P = 1 atm, T = 300°C, and GHSV = 217430 h <sup>-1</sup> ). .....	104
<b>Figure 4.11</b> (A) Comparison of % Mg vs catalytic activity (differential reaction conditions: gas mixture with CO <sub>2</sub> :H <sub>2</sub> = 1:4, P = 1 atm, T = 300°C, and GHSV = 217430 h <sup>-1</sup> ): (a) Mg <sub>0.75</sub> Al <sub>0.25</sub> (b) Ni <sub>0.12</sub> Fe <sub>0.012</sub> Mg <sub>0.63</sub> Al <sub>0.238</sub> (c) Ni <sub>0.2</sub> Fe <sub>0.02</sub> Mg <sub>0.55</sub> Al <sub>0.23</sub> (d) Ni <sub>0.4</sub> Fe <sub>0.04</sub> Mg <sub>0.35</sub> Al <sub>0.21</sub> (e) Ni <sub>0.6</sub> Fe <sub>0.06</sub> Mg <sub>0.15</sub> Al <sub>0.19</sub> and (f) Ni <sub>0.75</sub> Fe <sub>0.075</sub> Al <sub>0.175</sub> . (B) Rate of CO <sub>2</sub> conversion vs total amount of basic sites: (c) Ni <sub>0.2</sub> Fe <sub>0.02</sub> Mg <sub>0.55</sub> Al <sub>0.23</sub> (d) Ni <sub>0.4</sub> Fe <sub>0.04</sub> Mg <sub>0.35</sub> Al <sub>0.21</sub> (e) Ni <sub>0.6</sub> Fe <sub>0.06</sub> Mg <sub>0.15</sub> Al <sub>0.19</sub> and (f) Ni <sub>0.75</sub> Fe <sub>0.075</sub> Al <sub>0.175</sub> .....	105
<b>Figure 5.1</b> Microactivity Efficient equipment (Micromeritics) used for the catalytic CO <sub>2</sub> methanation tests. ....	116
<b>Figure 5.2</b> XRD pattern of Ni(OH) <sub>2</sub> nanoparticles obtained from the first-step hydrothermal reaction.....	118
<b>Figure 5.3</b> Ni2p <sub>3/2</sub> and O1s XPS spectra of Ni(OH) <sub>2</sub> nanoparticles obtained from the first-step hydrothermal reaction. ....	118
<b>Figure 5.4</b> XRD patterns of samples calcined at 500°C: (a) 25%Ni-Al <sub>2</sub> O <sub>3</sub> -NS and (b) 25%Ni-2.5%Fe-Al <sub>2</sub> O <sub>3</sub> -NS.....	119
<b>Figure 5.5</b> A) XRD patterns of samples reduced at 600°C: (a) 25%Ni-Al <sub>2</sub> O <sub>3</sub> -NS and (b) 25%Ni-2.5%Fe-Al <sub>2</sub> O <sub>3</sub> -NS. B) 47-56° region in the XRD patterns: (a) 25%Ni-Al <sub>2</sub> O <sub>3</sub> -NS and (b) 25%Ni-2.5%Fe-Al <sub>2</sub> O <sub>3</sub> -NS.....	120
<b>Figure 5.6</b> d-spacing value for Fe-Ni alloy formation as a function of the Fe/(Ni + Fe) molar ratio of 25%Ni-2.5%Fe-Al <sub>2</sub> O <sub>3</sub> -NS catalyst reduced at 600°C or after long-term (>50 h) catalytic tests, with respect to the linear relation described using Vegard's law between <i>fcc</i> Ni metal (JCPDS 01-070-1849) and <i>fcc</i> γ-Fe (JCPDS 01-089-4185).....	120
<b>Figure 5.7</b> H <sub>2</sub> -TPR profiles. I - top Figure: 25%Ni-Al <sub>2</sub> O <sub>3</sub> -NS (a) calcined, (b) reduced. II - bottom Figure: 25%Ni-2.5%Fe-Al <sub>2</sub> O <sub>3</sub> -NS (a) calcined, (b) reduced.....	121
<b>Figure 5.8</b> SEM-EDX images of calcined (a) 25%Ni-Al <sub>2</sub> O <sub>3</sub> -NS, (b) 25%Ni-2.5%Fe-Al <sub>2</sub> O <sub>3</sub> -NS and (c) 25%Ni-2.5%Fe-Al <sub>2</sub> O <sub>3</sub> -B samples. ....	123
<b>Figure 5.9</b> TEM images of reduced and spent catalysts: 25%Ni-Al <sub>2</sub> O <sub>3</sub> -NS (a) reduced at 600°C (b) spent and 25%Ni-2.5%Fe-Al <sub>2</sub> O <sub>3</sub> -NS (c) reduced at 600°C (d) spent. ....	125
<b>Figure 5.10</b> XPS spectra of 25%Ni-Al <sub>2</sub> O <sub>3</sub> -NS and 25%Ni-2.5%Fe-Al <sub>2</sub> O <sub>3</sub> -NS catalysts: (a) reduced at 600°C, (b) after long-term catalytic tests. ....	126

<b>Figure 5.11</b> CO <sub>2</sub> TPD profiles of selected calcined catalysts.....	127
<b>Figure 5.12</b> Catalytic CO <sub>2</sub> methanation at (I) 300°C and (II) 350°C (gas mixture with CO <sub>2</sub> :H <sub>2</sub> = 1:4, P = 5 bar, and GHSV = 10000 h <sup>-1</sup> ): (A) integral rate in CO <sub>2</sub> depletion (mol CO <sub>2</sub> per mol Ni and time in s) and (B) CO <sub>2</sub> conversion (%): (a) 25%Ni-Al <sub>2</sub> O <sub>3</sub> -NS, (b) 25%Ni-2.5%Fe-Al <sub>2</sub> O <sub>3</sub> -B, (c) 25%Ni-2.5%Fe-Al <sub>2</sub> O <sub>3</sub> -NS and (d) equilibrium. ....	129
<b>Figure 5.13</b> Stability test in CO <sub>2</sub> methanation for 50 h of time on stream (Reaction conditions: gas mixture with CO <sub>2</sub> :H <sub>2</sub> = 1:4, T = 300°C, P = 5 bar, and GHSV = 10000 h <sup>-1</sup> ): (a) 25%Ni-2.5%Fe-Al <sub>2</sub> O <sub>3</sub> -NS and (b) commercial catalyst (ca. 76 wt% Ni on Al <sub>2</sub> O <sub>3</sub> ) and (c) equilibrium. ....	130
<b>Figure 5.14</b> Arrhenius plots for CO <sub>2</sub> hydrogenation on different catalysts. Reaction conditions: gas mixture with CO <sub>2</sub> :H <sub>2</sub> = 1:4, T = 300°C-350°C, P = 5 bar, and GHSV = 10000 h <sup>-1</sup> . ....	132
<b>Figure 5.15</b> Relationship between TOF and amount of basic sites (BS) (Reaction conditions: gas mixture with CO <sub>2</sub> :H <sub>2</sub> = 1:4, T = 300°C, P = 5 bar, and GHSV = 10,000 h <sup>-1</sup> ).....	135
<b>Figure 5.16</b> A) XRD patterns of spent catalysts: (a) 25%Ni-Al <sub>2</sub> O <sub>3</sub> -NS and (b) 25%Ni-2.5%Fe-Al <sub>2</sub> O <sub>3</sub> -NS. B) 47-56° regional XRD patterns: (a) 25%Ni-Al <sub>2</sub> O <sub>3</sub> -NS and (b) 25%Ni-2.5%Fe-Al <sub>2</sub> O <sub>3</sub> -NS. ....	136
<b>Figure 5.17</b> TGA profiles (in air) of catalysts after reaction: (a) 25%Ni-2.5%Fe-Al <sub>2</sub> O <sub>3</sub> -NS, (b) 25%Ni-Al <sub>2</sub> O <sub>3</sub> -NS and (c) 25%Ni-2.5%Fe-Al <sub>2</sub> O <sub>3</sub> -B (B stands for bulk-type).....	137

## LIST OF TABLES

<b>Table 1.1</b> Examples of common synthesis methods used to develop carbon dioxide methanation catalysts in recent years. ....	12
<b>Table 2.1</b> Designation of the as-synthesized catalysts. ....	24
<b>Table 2.2</b> Physicochemical properties of the as-synthesized catalysts. ....	27
<b>Table 2.3</b> Real vs. theoretical support composition obtained by XRD. ....	29
<b>Table 2.4</b> Quantitative H <sub>2</sub> -TPR data for the as-synthesized catalysts. ....	31
<b>Table 2.5</b> Quantitative CO-TPD data for the as-synthesized catalysts. ....	32
<b>Table 2.6</b> Physicochemical properties of the quaternary oxide supported catalysts. ....	35
<b>Table 2.7</b> Quaternary supports: real estimated by XRD vs. theoretical support composition. ....	37
<b>Table 2.8</b> CO chemisorption results for reduced Ni-based catalysts. ....	37
<b>Table 2.9</b> Quantitative H <sub>2</sub> -TPR data for the as-synthesized catalysts. Consumed hydrogen refers to a gram of catalyst. ....	39
<b>Table 2.10</b> Long-term tests at 300°C and GHSV of 4000 h <sup>-1</sup> for the best catalysts investigated, Ni/C5 and Ni/C15-15%CeO <sub>2</sub> . ....	43
<b>Table 3.1</b> Physicochemical properties of calcined HTs: BET surface area, total pore volume, and elemental compositions. ....	55
<b>Table 3.2</b> Summary of XRD analyses of the dried precursors. ....	57
<b>Table 3.3</b> Quantitative H <sub>2</sub> -TPR analyses for the calcined catalysts. ....	61
<b>Table 3.4</b> Basic site measurements of the calcined catalysts. ....	62
<b>Table 3.5</b> Summary of STEM-EDS analyses results of representative samples. ....	64
<b>Table 3.6</b> STEM images and EDS elemental mapping of reduced catalysts evidence Fe-Ni alloys, both elements are located at the same particles seen in STEM images. ....	64
<b>Table 4.1</b> Physicochemical properties of calcined samples. ....	94
<b>Table 4.2</b> Distribution of the basic sites at different desorption temperatures. ....	97
<b>Table 4.3</b> The average Ni particle size estimated based on STEM images of the reduced samples. ....	101
<b>Table 5.1</b> Physicochemical properties and metal content of samples. ....	117
<b>Table 5.2</b> Quantitative H <sub>2</sub> -TPR analysis and CO-chemisorption measurements for the calcined catalysts. ....	122

<b>Table 5.3</b> Summary of average particle diameter (nm) and metal dispersion from TEM analyses. .....	125
<b>Table 5.4</b> Integrated peak areas and temperature maximum of basic sites (BS). .....	128
<b>Table 5.5</b> Integral rate of reaction and rate of deactivation at 300°C of 25%Ni-2.5%Fe-Al <sub>2</sub> O <sub>3</sub> -NS with respect to a commercial catalyst (ca. 76 wt-% Ni on Al <sub>2</sub> O <sub>3</sub> ). .....	131
<b>Table 5.6</b> TOF values of most active catalysts at temperatures ranging from 300°C-350°C.....	131
<b>Table 5.7</b> Activation energy ( $E_a$ ) for the most active catalysts at temperatures ranging from 300°C-350°C.....	132



# CHAPTER 1

# 1. General Introduction

## 1.1. World energy outlook

The economic development of countries is directly related to the energy consumption. The energy sources can be either renewable or nonrenewable. But currently, nonrenewable energy (natural gas, coal, oil) is considered as the main energy source in the world. Almost, 35% of world's primary source of energy is from natural gas. The fossil fuels share is also about 80% of overall energy production [1]. As the same time, due to the increase in world population and industrialization, the energy usage, such as, coal, natural gas, and petroleum are increasing daily, which results in an immense increase in the emission of GHG (Green House Gases) to the atmosphere [2, 3]. Therefore, from a low-carbon economy future and sustainable energy production standpoint, the production of fossil fuels should decrease and replace by renewable energy sources [4].

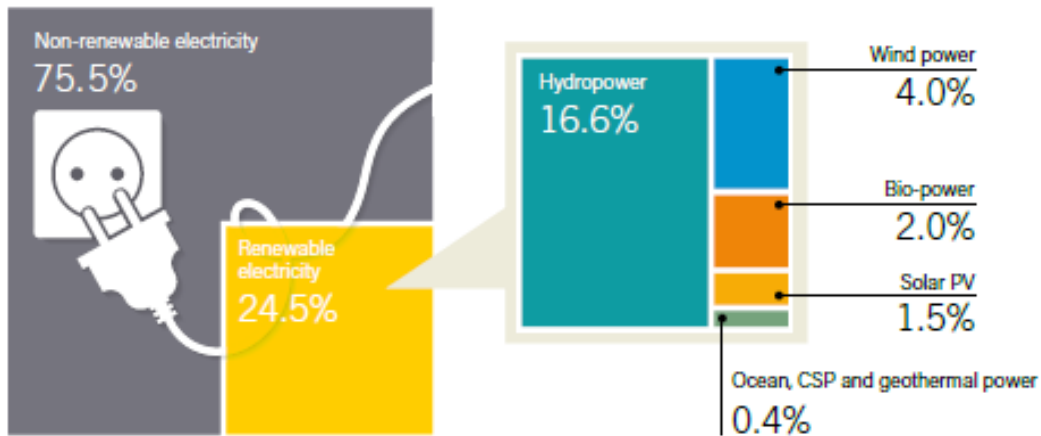


**Figure 1.1** Estimated renewable energy share of global energy production by the end of 2016 (adapted from [5]).

However, according to a data by the end of 2016, renewable energy source contributes only about 24.5% of the total energy consumption (**Figure 1.1**) [5]. Renewable energy is an energy that comes from resources which are naturally replenished, these energy sources include, sunlight, wind, rain, tides, biomass, waves, and geothermal heat. Amongst, wind, solar, and biomass are three emerging renewable sources of energy during the present decade.

## 1.2. CO<sub>2</sub> emissions and climate change

The use of fossil fuels as a primary source of energy (Global annual energy consumption ca. 500 EJ in 2014) leads to an emission of a massive amount of CO<sub>2</sub> (one of the GHGs) to the atmosphere. Recently, CO<sub>2</sub> as a greenhouse gas has led to a record increase in the atmosphere which considered to be the main cause of climate change [6]. In this regard, an agreement recently achieved at the 2015 United Nations Climate Change Conference (COP21) that aims to limit the increase in the global average temperature to less than 2°C above pre-industrial levels. Thus, in order to reach this objective, the decrease of CO<sub>2</sub> emissions is compulsory [7].

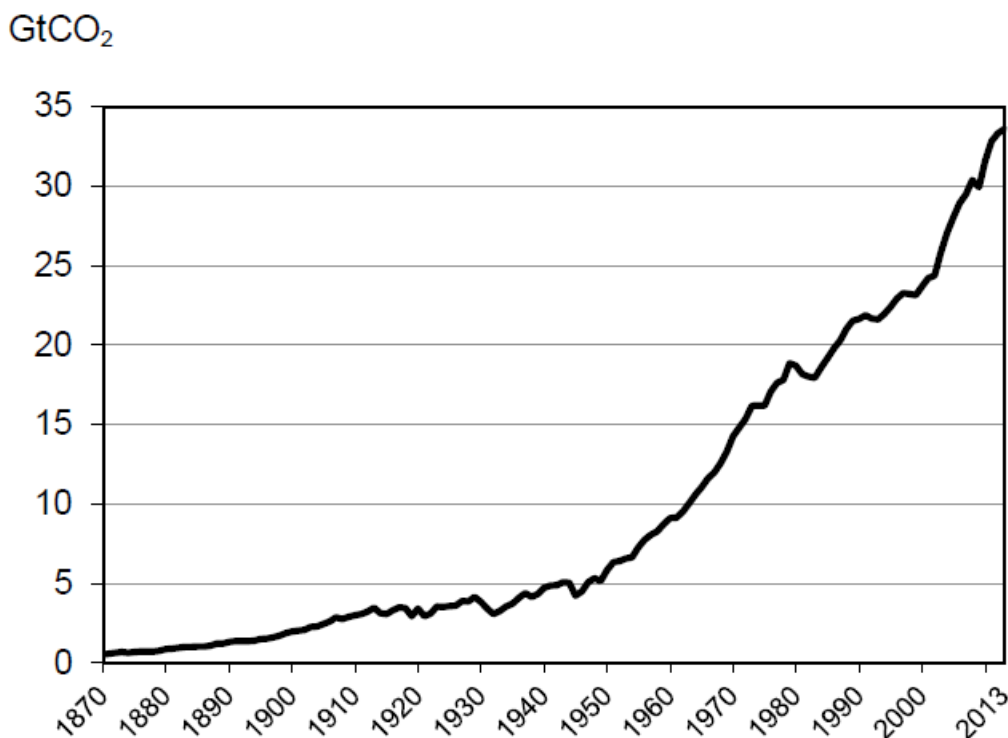


**Figure 1.2** Amount of CO<sub>2</sub> emitted per year (adapted from [8]).

Though significant efforts are emerging to decrease fossil fuel consumption and reduce CO<sub>2</sub> emissions, emissions are likely to rise continuously for at least the next decade as the trends from the previous decades shown in **Figure 1.2** [8]. From the time when the industrial revolution, annual CO<sub>2</sub> emissions from the combustion of fuel have intensely increased from near zero to over 32 GtCO<sub>2</sub> in 2014 [8]. Hence, a smooth way of changing our energy vectors to renewables and low carbon economy is still required. In order to achieve this, using CO<sub>2</sub> as a feedstock is a substantial route to decrease the amount of CO<sub>2</sub> currently releasing to the atmosphere.

### 1.3. CO<sub>2</sub> utilization as feedstock

The total increase in energy demands together with the ever-growing concerns about the future of the environment has led to a boost in the usage of “cleaner” energy solutions. Moreover, those solutions are forced into the market and established due to the strict regulations and goals set by many countries and organizations. Particularly, in EU many agreements have been signed, like the EU 20-20-20 strategy. Which, refers to 20% reduction in emissions, 20% energy from renewables and 20% increase in efficiency [9].

Based on the reasons explained above, recently, development of many alternative energy sources to replace fossil fuels has increased. Those, mainly focus on the development of cleaner energy sources. Like wind turbines and solar panels. The problem with those renewable energy sources is intermittent nature of the energy produced. This results in the need for long-term and large-scale energy storage solutions. But, the storage of renewable energy in such a large scale with the use of batteries and capacitors is not yet economically and practically feasible. Thus, recycling of CO<sub>2</sub> as feedstock for the production of fuels and fine chemicals leads to an overall CO<sub>2</sub> neutral circular economy and successful renewable energy storage. Therefore, captured or industrial CO<sub>2</sub> can be used as a raw material for the synthesis of different products like methane, methanol, ethanol, formic acid and dimethyl carbonate [10].

#### 1.3.1. General aspects of CO<sub>2</sub> separation and usage

One of the main sources of CO<sub>2</sub> can be the flue gas from different industries and combustion plants. Presently, different methods of CO<sub>2</sub> separation from flue gas are applied in both industrial processes and post-combustion capture systems. These methods include absorption, adsorption, membranes, cryogenic separation and chemical reactions [11]. The separated CO<sub>2</sub> can be used both in general industrial applications and as a chemical feedstock for the production of chemicals. Among the general industrial applications: CO<sub>2</sub> can be used in food production to carbonate beer, soft drink, wine and as a preservative in order to limit food oxidation. It can also be used for fire suppression and water treatment plants for re-mineralization of desalted and highly soft water [12].

In addition to the general applications, CO<sub>2</sub> has a huge potential to use as a chemical feedstock with a number of industrial opportunities. Since CO<sub>2</sub> is mostly produced from the combustion of fuels, converting CO<sub>2</sub> to synthetic fuels can simplify the recycling of a substantial amount of carbon, thus allowing processes to approach a closed cycle with carbon neutrality. But, the conversion CO<sub>2</sub> to fuels requires a constant supply of energy. Therefore, such processes need to combine with renewable energy sources to either electrochemically reduce CO<sub>2</sub> or to produce renewable hydrogen in order to the renewable H<sub>2</sub> as a reactant for the thermochemical conversion of CO<sub>2</sub> to solar fuels.

The development of renewable energy projects is increasing in number which results in the production of excess electrical energy that cannot be sent to the electrical grid due to either the longer distance from the existing electrical grid or excess productions at the time when the demand is less. This excess renewable electricity can be therefore used to produce hydrogen via the water electrolysis (Eq. 1.1) process which is considered as a renewable electricity storage route [13]. If such practices are applied and enable to produce renewable H<sub>2</sub>, this excess hydrogen can be used as a reactant to convert CO<sub>2</sub> into solar fuels.



**Figure 1.3** summarizes the possible routes of the CO<sub>2</sub> conversion combined with renewable energy in the sustainable energy and production. The renewable energy is used either directly (in the solar thermal production of syngas) or indirectly, according to two main possibilities: (i) production of renewable H<sub>2</sub> or (ii) generation of electrons, or electrons/protons (by photo-oxidation of water), used in the electrochemical paths. Among the possible routes, the application of solar fuels generated from CO<sub>2</sub> as storage and transportation methods for excess renewable electricity offers a solution to properly use the inconsistent potential of renewable energy while reducing CO<sub>2</sub> emissions [14].

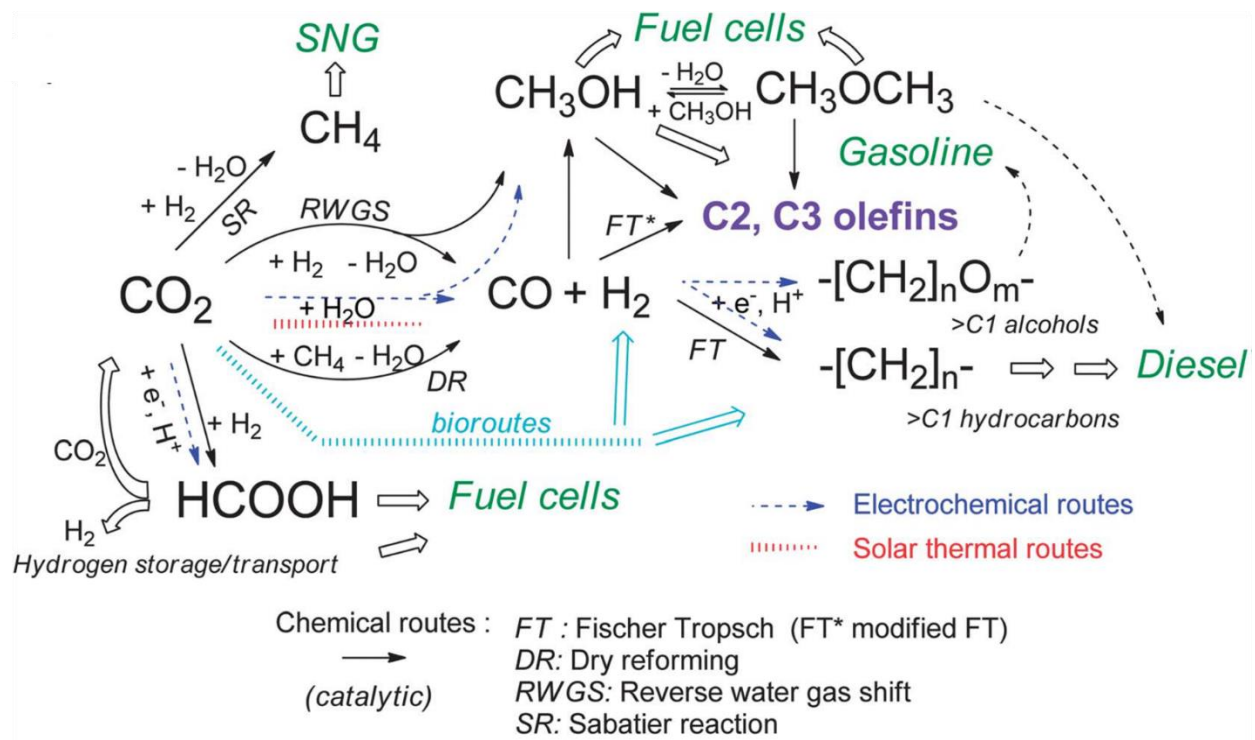


**Figure 1.3** Schematic overview of possible routes of the CO<sub>2</sub> conversion to incorporate renewable energy in the chemical and energy chains (adapted from [14]).

Owing to the large worldwide demand for natural gas and uneven global geographical distribution of its supply, SNG from CO<sub>2</sub> provides a good opportunity for the development and advancement of joint renewable energy storage and CO<sub>2</sub> utilization projects. This can be achieved by the CO<sub>2</sub> methanation reaction starting from the production of the H<sub>2</sub> from water electrolysis. Moreover, the CO<sub>2</sub> methanation reaction also offers the advantage of being well established in terms of technology. It is also thermodynamically favorable reaction at lower temperatures and pressures, given a suitable catalyst which makes the process more practical and energy efficient.

### 1.3.2. CO<sub>2</sub> for energy storage and transportation: the P2G concept

Production of CO<sub>2</sub> derived molecules such as methane enables to store and transport renewable energy almost without loss. One of the emerging processes for CO<sub>2</sub> conversion into solar fuels is the Synthetic Natural Gas (SNG) production using the Power to Gas (P2G) concept will likely play a significant role in the challenge of long-term and large capacity renewable energy storage [15].

The P2G is a three-step process which involves: the generation of renewable electricity, renewable H<sub>2</sub> production by water electrolysis using excess the renewable electricity (from wind turbines during the night when the energy demand is lower, for example), and using the renewable H<sub>2</sub> for the thermochemical conversion of CO<sub>2</sub> to methane (CH<sub>4</sub>) via Sabatier reaction. The produced CH<sub>4</sub> can be introduced into the available natural gas infrastructure or storage services, or it can be readily used in all other well-established natural gas facilities [16, 17].

In a typical P2G plant (**Fig. 1.4**), renewable electricity is fed to electrolyzers to reduce H<sub>2</sub>O and/or CO<sub>2</sub>. In this way, renewable electricity can be effectively stored in large amounts in a chemical fuel (H<sub>2</sub> or a syngas). This process can be achieved by either low or high-temperature electrolysis process. During the low-temperature electrolysis (e.g., Polymer Electrolyte Membrane (PEM) and alkaline electrolyzers) H<sub>2</sub> only is produced. The renewable H<sub>2</sub> can be used for Fuel Cell-vehicles. Regarding the production of synthetic natural gas, with water (at a lower temperature) or steam (at higher temperature) electrolysis, CO<sub>2</sub> is introduced and mixed with H<sub>2</sub> before methanation reaction. On the other hand, using the high temperature-electrolysis based on Solid oxide Electrolysis Cells (SOEC), co-electrolysis of carbon dioxide and steam is also possible. Carbon dioxide, when co-introduced with steam to the reactor, acts indeed as a reactant for the electrochemical processes and/or is converted internally via shift reactions to produce more steam. Therefore, syngas methanation can be performed for the production of SNG and finally feed into natural gas distribution lines [18]. Hence, researches are undergoing for the optimization of this process in a pilot and semi-pilot scales.

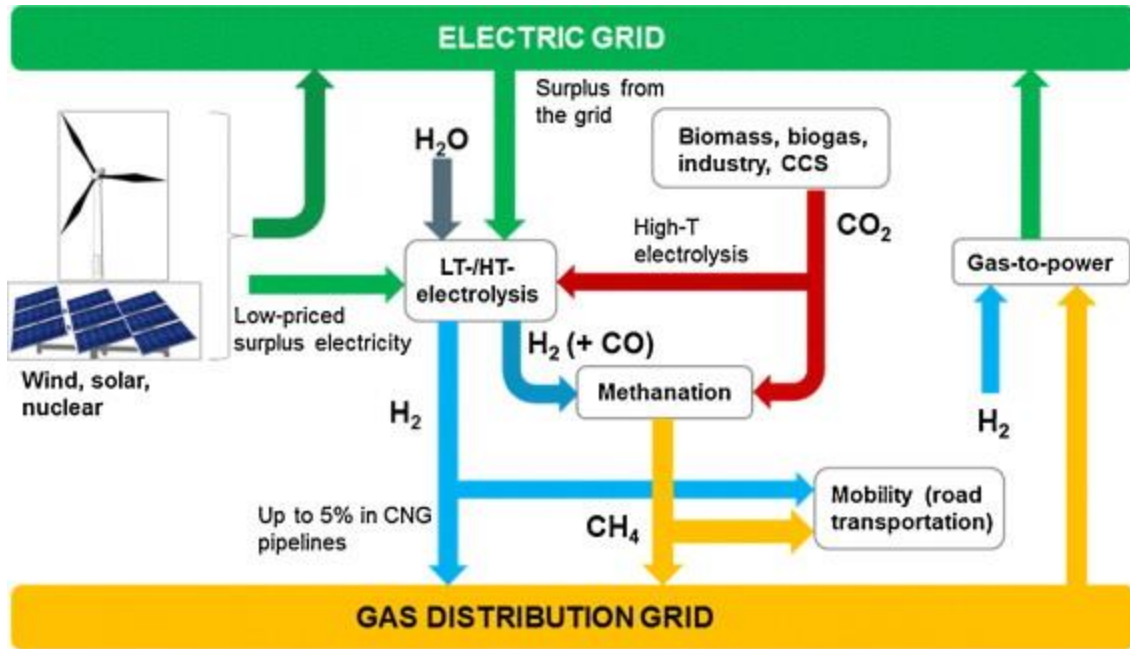
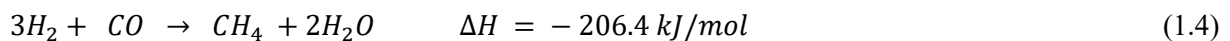
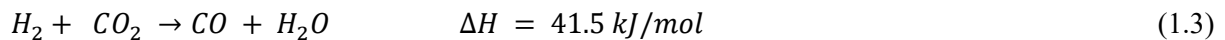
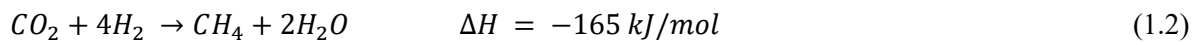


**Figure 1.4** Power-to-gas pathway through both low-temperature (LT) and high-temperature (HT) electrolysis devices (adapted from [18]).

#### 1.4. The CO<sub>2</sub> methanation: Sabatier reaction

The CO<sub>2</sub> methanation (Sabatier reaction) is known as an exothermic reaction where H<sub>2</sub> and CO<sub>2</sub> react to form CH<sub>4</sub> and H<sub>2</sub>O and follows the reaction process shown in [equation \(1.2\)](#). The most recognized mechanism of the CO<sub>2</sub> methanation reaction is the one involves CO formation and then hydrogenation of CO to produce methane. It is a combination of a reversed endothermic water-gas-shift-reaction and an exothermic CO methanation, both which can be seen in [equation \(1.3\)](#) and [\(1.4\)](#) respectively.





The overall reaction (Eq. 1.2) is favored at a lower temperature, but due to kinetic limitations (lower CH<sub>4</sub> production and selectivity), a catalyst needs to be utilized [19]. The implementation of this reaction, therefore, requires a careful heat management to maintain the reaction at relatively low temperature for a favorable equilibrium composition but at enough temperature to overcome activation energy barrier.

#### 1.4.1. Thermodynamics of CO<sub>2</sub> methanation

The CO<sub>2</sub> methanation reaction is thermodynamically favorable ( $\Delta G_{298\text{ K}} = -130.8\text{ kJ/mol}$ ); however, the reduction of the fully oxidized carbon to CH<sub>4</sub> is an eight-electron process with substantial kinetic confines, which therefore needs a catalyst to achieve adequate rates and selectivity towards CH<sub>4</sub> [20]. Moreover, the highly exothermic nature of CO<sub>2</sub> methanation reaction, high reaction temperatures also contributes to the overall lower performance CO<sub>2</sub> conversion to methane. Therefore, as shown in Fig. 1.5, a temperature below 225°C (1 bar) or 300°C (20 bar) is required to reach a CO<sub>2</sub> conversion of at least 98%. Additionally, the positive effect of pressure is apparent as shown in Fig. 1.5. Accordingly, relatively higher pressure should be used in order to obtain higher CO<sub>2</sub> conversion and selectivity to CH<sub>4</sub> [21].

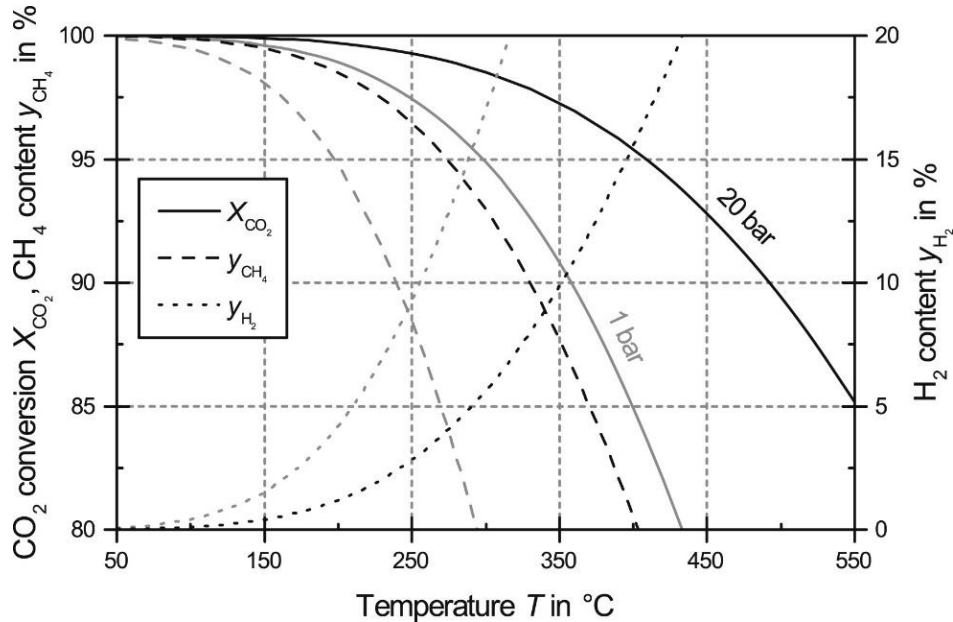


**Figure 1.5** Equilibrium conversion as well as H<sub>2</sub> and CH<sub>4</sub> content for CO<sub>2</sub> methanation ((H<sub>2</sub>/CO<sub>2</sub>)<sub>in</sub> = 4, no inert gases) (adapted from [21]).

The  $\text{H}_2$ :  $\text{CO}_2$  ratio also significantly affects the final product of the reaction. Low ratios tend to provide larger amounts of high molecular mass products while at higher ratios, more methane is produced. Therefore, in order to avoid higher carbon deposition on the catalyst surface and preserve high selectivity towards  $\text{CH}_4$ , the  $\text{H}_2$ :  $\text{CO}_2$  ratio should not be lower than 4:1. Additionally, the presence of water, originating in either the reverse water gas shift reaction or added steam, seems to inhibit carbon formation not only during the  $\text{CO}_2$  methanation but also during the  $\text{CO}$  methanation [22]. But, the presence of excess  $\text{H}_2\text{O}$  in the catalytic bed also facilitates the oxidation of reduced metal particles which in turn results in faster deactivation of the catalyst.

#### 1.4.2. Kinetics and mechanism of $\text{CO}_2$ methanation

Kinetics and mechanism of  $\text{CO}_2$  methanation over Ni catalysts have been investigated by many researchers [23-27]. For the methanation of  $\text{CO}_2$ , nickel catalysts are active at temperatures above  $150^\circ\text{C}$ , but the exact reaction mechanism is still subject to debate. The key question is whether the reaction occurs (i) by the dissociative adsorption of  $\text{CO}_2$  to form  $\text{CO}$  on the surface of the catalyst which, in turn, is hydrogenated to  $\text{CH}_4$  by the same mechanism involved in  $\text{CO}$  methanation [23-27], or (ii) by the direct hydrogenation of  $\text{CO}_2$  to  $\text{CH}_4$  without  $\text{CO}$  formation as intermediate [28].

**Figure 1.6** summarizes the two possible routes.

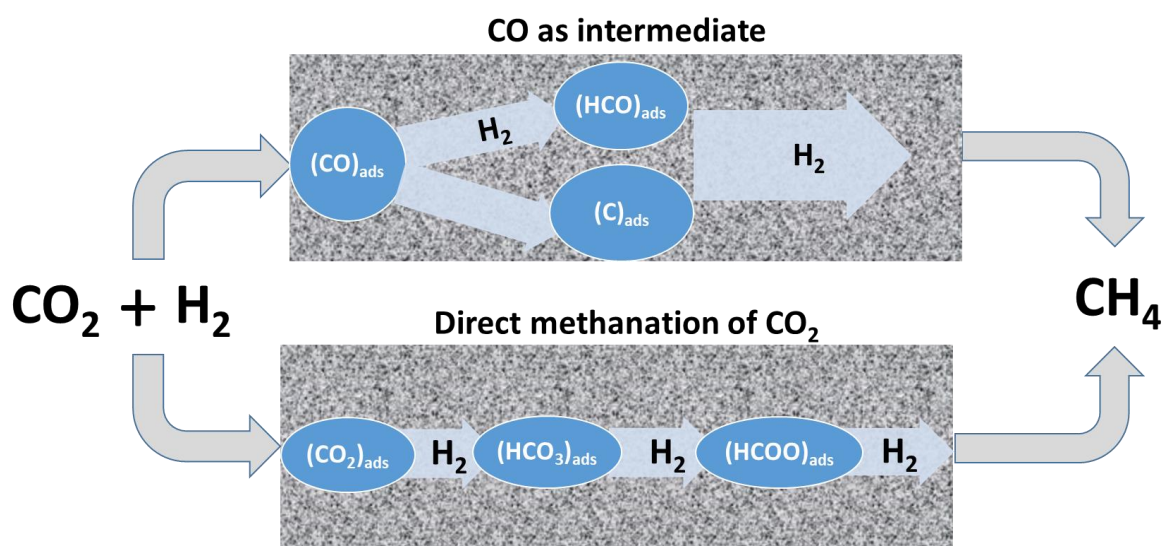


**Figure 1.6** Possible mechanisms of  $\text{CO}_2$  methanation.

In case of direct CO<sub>2</sub> methanation, the presence of formate species as the main reaction intermediates is suggested. Regarding the pathway where CO<sub>2</sub> reacts to be transformed into CO, it is generally agreed that the Sabatier process proceeds through the reverse water gas shift reaction forming CO<sub>ad</sub> and H<sub>2</sub>O. The adsorbed CO is subsequently hydrogenated through a series of reactions to methane. Alternatively, CO can be formed due to the dissociative adsorption of CO<sub>2</sub> on the catalyst. Besides CO, deposited surface carbon is another important byproduct. CO<sub>2</sub> methanation reaction can be inhibited by the surface carbon accumulated on the active site of the catalyst. Though lots of investigations are made on the mechanism and kinetics of CO<sub>2</sub> methanation, there is still a debate on the types of intermediates and rate-determining step during the reaction.

#### 1.4.3. Catalysts for CO<sub>2</sub> methanation

The methanation reaction is limited by thermodynamics (being a reversible exothermic reaction). So, it is necessary to design catalysts of suitable activity to reach conversions close to equilibrium at moderate reaction temperatures (<350°C) and high space-velocities. In fact, due to equilibrium, in once-through reactors, it is not possible to meet SNG specifications at higher temperatures. In addition, stability is often the main issue, especially for catalysts active at the lower temperatures. Therefore, it is still open the challenge to develop highly active and stable catalysts for operations at temperatures lower than 350°C.

Both supported noble and non-noble metals are known to be used as catalysts for CO<sub>2</sub> methanation. Graf et al. [29] arranged the activity of the metals as follows: Ru > Fe > Ni > Co > Rh > Pd > Pt. In addition to the high activity, the noble metal ruthenium (Ru) has further positive characteristics such as high CH<sub>4</sub> selectivity at low temperatures, and high resistance to oxidizing atmospheres [30-32]. Among the noble metals investigated for CO<sub>2</sub> methanation Rh [33-45] and Ru [46-57] supported in different oxides are commonly used. The other noble metals like Pd [58-61] and Pt [62, 63] are also used, but the least appropriate materials for the CO<sub>2</sub> methanation.

Despite the fact supported noble metal catalysts such as Ru so far demonstrates a high performance towards CO<sub>2</sub> methanation the main drawback is their high price that limits industrial application. Therefore, supported Ni-based catalysts were the catalysts of interest in this thesis as the industrial application of such materials is feasible economically.

#### 1.4.3.1. Supported Ni-based catalysts

Nickel supported on different metal oxides (mainly on  $\gamma$ -Al<sub>2</sub>O<sub>3</sub>) is the most common metal used for the CO<sub>2</sub> methanation. It has high activity, high CH<sub>4</sub> selectivity, and a low price [64]. The main disadvantage of Ni is its high tendency to oxidize in oxidizing atmospheres like the other non-noble metals Fe or Co and sintering at reaction temperatures [65-66]. Different supports have been investigated for Ni catalysts since, as is well known, the catalytic performance strongly depends on the nature and properties of the support. The most common supports investigated includes  $\gamma$ -Al<sub>2</sub>O<sub>3</sub>, zeolites, SiO<sub>2</sub>, TiO<sub>2</sub>, CeO<sub>2</sub>, and ZrO<sub>2</sub>. Other materials were also investigated as nickel supports, such as hydrotalcite and carbon nanotubes (CNTs).

Among the supported Ni catalysts, the Ni supported on  $\gamma$ -Al<sub>2</sub>O<sub>3</sub> shows a high catalytic activity, although it suffers from severe carbon deposition or poor stability due to the high reaction temperature used [67, 68]. Therefore, the aim throughout the years was to develop  $\gamma$ -Al<sub>2</sub>O<sub>3</sub> supported Ni-based catalysts able to show both high activity and resistance to carbonaceous deposits during the methanation reaction. Different characterization techniques also used in order to study the improved catalytic properties of Ni/ $\gamma$ -Al<sub>2</sub>O<sub>3</sub> catalysts [69-76]. Other supports like SiO<sub>2</sub> [77-81], TiO<sub>2</sub> [82], CeO<sub>2</sub> [83-85], ZrO<sub>2</sub> [83-85], hydrotalcite [86, 87], zeolites [88] and CNTs [89] are also investigated towards CO<sub>2</sub> methanation.

Different synthesis methods are used to prepare supported Ni-based catalysts for the CO<sub>2</sub> methanation reaction. **Table 1.1** summarizes some of the synthesis methods used in recent papers for the preparation of Ni-based catalysts with better activity and stability.

**Table 1.1** Examples of common synthesis methods used to develop carbon dioxide methanation catalysts in recent years.

Catalyst	Synthesis method	Reaction Temp. (°C)/ <b>P (bar)</b>	CO <sub>2</sub> Conversion (%)	CH <sub>4</sub> Selectivity (%)	Ref.
25 wt % Ni/Al <sub>2</sub> O <sub>3</sub>	I-CP	325/ <b>15</b>	67.3	87	90
12 wt % Ni/γ-Al <sub>2</sub> O <sub>3</sub>	IWI	210/ <b>20</b>	80	99.5	91
15 wt % Ni-TiO <sub>2</sub>	DP	218/ <b>10</b>	50	99	92
Ni <sub>0.8</sub> Mg <sub>0.2</sub> O@SiO <sub>2</sub>	CP	250/ <b>10</b>	78	99	93
20 wt % Ni/Al <sub>2</sub> O <sub>3</sub>	HT	234/ <b>10</b>	50	-	81
0.8% wt % Ru/TiO <sub>2</sub>	BS	180/ <b>10</b>	100	100	94

I-CP: Impregnation-Co-precipitation, IWI: Incipient Wet Impregnation, DP: Deposition Precipitation, CP: Co-precipitation, HT: Hydrothermal, BS: Barrel-sputtering.

Although Ni-based catalysts synthesized using different methods are preferred in catalytic methanation reaction, there still exist some problems, such as carbon deposition, sintering, Ni(CO)<sub>4</sub> formation, and sulfur poisoning during CO<sub>2</sub> methanation for SNG production [95, 96]. Therefore, the stability of methanation catalyst is of great importance besides the activity and selectivity. It is well known that the deactivation of supported metal catalysts by carbon or coke formation is a serious problem in methanation process [97]. The typical causes are: (1) polluting the active metal surface, (2) blocking the voids and pores of catalysts, (3) physical disintegration of the catalyst support [98]. Moreover, oxidation of reduced metal particles during the reaction also contributes a significant role for the deactivation of supported Ni-based catalysts for CO<sub>2</sub> methanation [99-101].

Therefore, based on the problems explained above, developing Ni-based methanation catalysts with high activity at low temperature, good redox properties and better stability at reaction temperature are still required for industrial applications.

## 1.5. Thesis aim and scope

The principal goal of this thesis is to develop advanced Ni-based catalysts with better activity and stability than conventional Ni/Al<sub>2</sub>O<sub>3</sub> catalyst at lower reaction temperatures (below 350°C).

*Chapter 2* is focused on the improvement of the  $\gamma$ -Al<sub>2</sub>O<sub>3</sub> support by applying different promoters: 1) ternary ( $\gamma$ -Al<sub>2</sub>O<sub>3</sub>-TiO<sub>2</sub>-ZrO<sub>2</sub>) mixed oxides with different ratio of the promoters were synthesized and used as supports for Ni. 2) quaternary ( $\gamma$ -Al<sub>2</sub>O<sub>3</sub>-TiO<sub>2</sub>-ZrO<sub>2</sub>-CeO<sub>2</sub>) mixed oxides i.e. CeO<sub>2</sub> was added to the ternary mixed oxides and its promotional effect was studied. 3) 20% Ni supported in all the mixed oxide supports were prepared and catalytic performance towards CO<sub>2</sub> methanation reaction was studied at different reaction temperatures and GHSVs. The structure and activity relationships were also studied.

*Chapter 3* deals with the synthesis, characterization and activity pattern of hydrotalcite derived Ni-Fe catalysts. Based on the results in *Chapter 2*, it was noted that synthesis of Ni-based catalysts with higher active metal loading is not feasible. Hence, hydrotalcite derived catalysts were selected for the study in *Chapter 3*, as different authors claim that HTs derived catalysts are a promising type of catalysts for CO<sub>2</sub> methanation. Therefore, the combined advantages of hydrotalcite-like precursors and the synergistic effect of Ni-Fe alloys were investigated. The synthesis of Ni-Fe based catalysts from hydrotalcite-like precursor results in a support that offers stabilizing properties by an oxide, spinel-like matrix with a tunable amount of Lewis basic sites for CO<sub>2</sub> activation.

In *Chapter 3*, the effect of different factors on the catalytic CO<sub>2</sub> methanation was investigated. But, no direct correlation was observed on how the amount of basic sites enhance the catalytic performance of the HTs derived catalysts. Therefore, *Chapter 4* deals with 1) tailoring the basic sites of hydrotalcite based Ni-Fe catalysts in order to study the effect of support basicity (Fe to Ni ratio was used based on the value optimized in *Chapter 3*). 2) activity towards CO<sub>2</sub> methanation was studied and effect of the basic sites was investigated under differential reaction conditions.

*Chapter 5* focused on the application of novel nanostructured materials with improved properties in CO<sub>2</sub> methanation prepared via a two-step hydrothermal synthesis in the presence of Fe as a promoter. This chapter mainly discusses how the microstructure (shape and geometry of both the active metal and support) of catalysts can enhance the performance. The two-step hydrothermal preparation method leads to the formation of nanosheets-like catalysts, due to a partial dissolution of the metal hydroxides formed during the first-step of hydrothermal reaction. The catalytic performance and stability of the nanosheet like catalysts were tested and compared with commercial methanation catalyst at 300°C.

## 1.6. References

- [1] N.F. Nasir, W.R.W. Daud, S.K. Kamarudin, Z. Yaakob, *Renew Sustainable Energy Rev*, 22 (2013) 631-639.
- [2] J.G. Rebordinos, J. Kampwerth, D.W. Agar, *Energy*, 133 (2017) 327-337.
- [3] M. Ahmed, A.M. Khan, S. Bibi, M. Zakaria, *Renewable and Sustainable Energy Reviews*, 75 (2017) 86-97.
- [4] M. Beller, G. Centi, L. Sun, *ChemSusChem*, (9) 2016, 1-9.
- [5] *Renewables 2017, Global status report*, Paris: REN 21 Secretariat.
- [6] IPCC. *Climate Change 2014: mitigation of climate change*. C. Edenhofery, R. Pichs-Madruga, Y. Sokona, E. Farahani, S. Kadner, K. Seyboth (Eds.), *et al.*, *Contributing Group III to the fifth assessment report of the intergovernmental panel on climate change*, Cambridge University Press, Cambridge and New York NY (2014).
- [7] IPCC. R.K. Pachauri, L.A. Meyer (Eds.), *Climate change 2014: Synthesis Report. The contribution of Working Groups I, II and III to the Fifth Assessment Report of the Intergovernmental Panel on climate change [Core Writing Team]* Geneva (2014).
- [8] International Energy Agency (IEA), *Key CO<sub>2</sub> emissions trends*, Excerpt from CO<sub>2</sub> emissions from fuel combustion (2016 edition).
- [9] COM (2014) 15 final, *Communication From The Commission To The European Parliament, The Council, The European Economic and Social Committee and The Committee Of The Regions, A policy framework for climate and energy in the period from 2020 to 2030*, European Commission, Brussels, (2014) 1-18.
- [10] G. Centi, S. Perathoner, *Catal. Today*, 148 (2009) 191-205.
- [11] IPCC 2005, *Capture of CO<sub>2</sub>*, in B. Metz, O. Davidson, H.C. de Connick, M. Loos, L.A. Meyer, (Ed.) *IPCC Special Report on Carbon dioxide capture and storage*. Prepared by working group III of the intergovernmental panel on climate change, Cambridge, United Kingdom and New York, NY, USA, (2005) 107-171.
- [12] A.J. Hunt, E.H.K. Sin, R. Marriott, J.H. Clark, *Chemsuschem*, 3 (2010) 306-322.
- [13] J. Turner, G. Sverdrup, M.K. Mann, P.-C. Maness, B. Kroposki, M. Ghirardi, R.J. Evans, D. Blake, *International Journal of Energy Research*, 32 (5) (2008) 379-407.
- [14] G. Centi, E.A. Quadrelli, S. Perathoner, *Energy & Environmental Science*, 6 (2013) 1711-1731.



- [15] R. Schlögl, *Chemical Energy Storage*, De Gruyter Pub. Berlin 2012.
- [16] M. Götz, J. Lefebvre, F. Mörs, A. McDaniel Koch, F. Graf, S. Bajohr, R. Reimert, T. Kolb, *Renewable Energy*, 85 (2016) 1371-1390.
- [17] F. D. Meylan, V. Moreau, S. Erkman, *Energy Policy*, 94 (2016) 366-376.
- [18] E. Giglio, A. Lanzini, M. Santarelli, P. Leone, *Journal of Energy Storage*, 1 (2015) 22-37.
- [19] K. P. Brooks, J. Hu, H. Zhu, J. K. Robert, *Chemical Engineering Science*, 62 (4) (2007) 1161-1170.
- [20] J. N. Park, E. W. McFarland, *J. Catal.*, 266 (2009) 92-97.
- [21] M. Gotz, J. Lefebvre, F. Mors, A. M. Koch, F. Graf, S. Bajohr, R. Reimert, T. Kolb, *Renew Energ.*, 85 (2016) 1371-1390.
- [22] J.J. Gao, Y.L. Wang, Y. Ping, D.C. Hu, G.W. Xu, F.N. Gu, F.B. Su, *RSC Advances*, 2 (2012) 2358-2368.
- [23] S.I. Fujita, M. Nakamura, T. Doi, N. Takezawa, *Appl. Catal. A: Gen.* 104 (1) (1993) 87-100.
- [24] S. Fujita, H. Terunuma, M. Nakamura, N. Takezawa. *Ind. Eng. Chem. Res.*, 30 (6) (1991) 1146-1151.
- [25] J. L. Falconer, A. E. Zağli, *Journal of Catalysis*, 62 (2) (1980) 280-285.
- [26] P. A. Aldana, F. Ocampo, K. Kolb, B. Louis, F. Thibault-Starkyz, M. Daturi, P. Bazin, S. Thomas, A. C. Roger, *Catal. Today*, 215 (2013) 201-207.
- [27] R. A. Hubble, J. Y. Lim, J. S. Dennis, *Faraday Discuss.* 192 (2016) 529-544.
- [28] J. Y. Lim, J. McGregor, A. J. Sederman, J. S. Dennis, *Chemical Engineering Science*, 141 (2016) 28-45.
- [29] F. Graf, M. Gotz, M. Henel, T. Schaaf, R. Tichler, Bonn 2014.
- [30] G. A. Mills, F. W. Steffgen, *Catalytic methanation. Cat. Rev., Sci. Eng.*, 8 (1) (1974) 159-210.
- [31] J. Hu, K. P. Brooks, J. D. Holladay, D. T. Howe, T. M. Simon, *Catal. Today*, 125 (2007) 103-110.
- [32] P. Brooks, J. Hu, H. Zhu, R. J. Kee, *Chem. Eng. Sci.*, 62 (4) (2007) 1161-1170.
- [33] M. Jacquemin, A. Beuls, P. Ruiz, *Catal. Today*, 157 (2010) 462-466.

- [34] A. Beuls, C. Swalus, M. Jacquemin, G. Heyen, A. Karelovic, P. Ruiz, *Appl. Catal. B Environ.* 113-114 (2012) 2-10.
- [35] A. Karelovic, P. Ruiz, *Appl. Catal. B Environ.*, 113-114 (2012) 237-249.
- [36] R. Wijayapalaa, F. Yu, C.U. Pittman, T.T. Mlsna, *Appl. Catal. A Gen.*, 480 (2014) 93-99.
- [37] C. Swalus, M. Jacquemin, C. Poleunis, P. Bertrand, P. Ruiz, *Appl. Catal. B Environ.*, 125 (2012) 41-50.
- [38] A. Karelovic, P. Ruiz, *J. Catal.*, 301 (2013) 141-153.
- [39] F. Solymosi, A. Erdöhelyi, T. Bánsági, *J. Catal.*, 68 (1981) 371-382.
- [40] Z.L. Zhang, A. Kladi, X.E. Verykios, *J. Catal.*, 148 (1994) 737-747.
- [41] F. Solymosi, I. Tombácz, J. Koszta, *J. Catal.*, 95 (1985) 578-586.
- [42] A.T. Bell, *J. Mol. Catal. A*, 100 (1995) 1-11.
- [43] K.J. Williams, A.B. Boffa, M. Salmeron, A.T. Bell, G.A. Somorjai, *Catal. Lett.*, 9 (1991) 415-426.
- [44] A. Trovarelli, C. Deleitenburg, G. Dolcetti, J.L. Lorca, *J. Catal.*, 151 (1995) 111-124.
- [45] C. Deleitenburg, A. Trovarelli, *J. Catal.*, 156 (1995) 171-174.
- [46] M. Kusmierz, *Catal. Today*, 137 (2008) 429-432.
- [47] G.A. Mills, F.W. Steffgen, *Catalytic Methanation. Catal. Rev.* 8 (1974) 159-210.
- [48] G.D. Weatherbee, C.H. Bartholomew, *J. Catal.*, 87 (1984) 352-362.
- [49] S. Sugawa, K. Sayama, K. Okabe, H. Arakawa, *Energy Convers. Manag.*, 36 (1995) 665-668.
- [50] S. Scirè, C. Crisafulli, R. Maggiore, S. Minicò, S. Galvagno, *Catal. Lett.*, 51 (1998) 41-45.
- [51] D. Li, N. Ichikuni, S. Shimazu, T. Uematsu, *Appl. Catal. A Gen.*, 172 (1998) 351-358.
- [52] D. Li, N. Ichikuni, S. Shimazu, T. Uematsu, *Appl. Catal. A Gen.*, 180 (1999) 227-235.
- [53] S. Toemen, W.A.W.A. Bakar, R. Ali, *J. CO<sub>2</sub> Util.*, 13 (2016) 38-49.
- [54] G. Garbarino, D. Bellotti, P. Riani, L. Magistri, G. Busca *Int. J. Hydrogen Energy*, 40 (2015) 9171-9182.

- [55] G. Garbarino, D. Bellotti, E. Finocchio, L. Magistri, G. Busca, *Catal. Today*, 277 (2016) 21-28.
- [56] Z. Kowalczyk, K. Stołeczki, W. Raróg-Pilecka, E. Miskiewicz, E. Wilczkowska, Z. Karpinski, *Appl. Catal. A Gen.*, 342 (2008) 35-39.
- [57] T. Li, S. Wang, D. Gao, S. Wang, *J. Fuel Chem. Technol.*, 42 (2014) 1440-1446.
- [58] P. Albers, J. Pietsch, S.F. Parker, *J. Mol. Catal. A Chem.*, 173 (2001) 275-286.
- [59] Y. Chen, K. Tomishige, K. Yokoyama, K. Fujimoto, *Appl. Catal. A Gen.*, 165 (1997) 335-347.
- [60] J. Martins, N. Batail, S. Silva, S. Rafik-Clement, A. Karelovic, D.P. Debecker, A. Chaumonnot, D. Uzio, *Catal. Commun.*, 58 (2015) 11-15.
- [61] R. Delmelle, R.B. Duarte, T. Franken, D. Burnat, L. Holzer, A. Borgschulte, *Int. J. Hydrogen Energy*, 41 (2015) 20185-20191.
- [62] M. A. Vannice, C.C.T. Wu, *Journal of Catalysis*, 82 (1) (1983) 213-222.
- [63] K.-P. Yu, W.-Y. Yu, M.-C. Kuo, Y.-C. Liou and S.-H. Chien, *Appl. Catal. B*, 84 (2008) 112-118.
- [64] J. Gao, Q. Liu, F. Gu, B. Liu, Z. Zhong, F. Su, *RSC Adv.*, 5 (2015) 22759-22776.
- [65] M. Gotz, J. Lefebvre, F. Mors, A. M. Koch, F. Graf, S. Bajohr, R. Reimert, T. Kolb, *Renew. Energy*, 85 (2016) 1371-1390.
- [66] P. J. Lunde, F. L. Kester, *Ind. Eng. Chem. Proc. Des. Dev.*, 13 (1) (1974) 27-33.
- [67] H. Muroyama, Y. Tsuda, T. Asakoshi, H. Masitah, T. Okanishi, T. Matsui, K. Eguchi, *J. Catal.*, 343 (2016) 178-184.
- [68] H. Takano, Y. Kirihata, K. Izumiya, N. Kumagai, H. Habazaki, K. Hashimoto, *App. Surf. Sci.*, 358 (2016) 653-663.
- [69] A.E. Aksoylu, A.N. Akin, Z.I. Önsan, D.L. Trimm, *Appl. Catal. A Gen.*, 145 (1996) 185-193.
- [70] S. Rahmani, M. Rezaei, F. Meshkania, *J. Ind. Eng. Chem.*, 20 (2014) 1346-1352.
- [71] G. Garbarino, P. Riani, L. Magistri, G. Busca, *Int. J. Hydrogen Energy*, 39 (2014) 11557-11565.
- [72] B. Mutz, H.W.P. Carvalho, S. Mangold, W. Kleist, J.D. Grunwaldt, *J. Catal.*, 327 (2015) 48-53.

- [73] B.M. Weckhuysen, *Phys. Chem. Chem. Phys.*, 5 (2003) 4351-4360.
- [74] H. Topsøe, *J. Catal.*, 216 (2003) 155-164.
- [75] J.D. Grunwaldt, B.S. Clausen, *Top. Catal.*, 18 (2002) 37-43.
- [76] M.A. Banares, *Catal. Today*, 100 (2005) 71-77.
- [77] X. Zhang, W.-j. Sun and W. Chu, *J. Fuel Chem. Technol.*, 41 (2013) 96-101.
- [78] X. L. Yan, Y. Liu, B. R. Zhao, Z. Wang, Y. Wang, C. J. Liu, *Int. J. Hydrogen Energy*, 38 (2013) 2283-2291.
- [79] M. A. A. Aziz, A. A. Jalil, S. Triwahyono, M. W. A. Saad, *Chem. Eng. J.*, 260 (2015) 757-764.
- [80] M. A. A. Aziz, A. A. Jalil, S. Triwahyono, S. M. Sidik, *Appl. Catal. A*, 486 (2014) 115-122.
- [81] M. A. A. Aziz, A. A. Jalil, S. Triwahyono, R. R. Mukti, Y. H. Taufiq-Yap, M. R. Sazegar, *Appl. Catal. B*, 147 (2014) 359-368.
- [82] V. M. Shinde, G. Madras, *AIChE J.*, 60 (2014) 1027-1035.
- [83] G. Zhou, H. Liu, K. Cui, A. Jia, G. Hu, Z. Jiao, Y. Liu, X. Zhang, *Appl. Surf. Sci.*, 383 (2016) 248-252.
- [84] M.V. Konishcheva, D.I. Potemkin, S.D. Badmaev, P.V. Snytnikov, E.A. Paukshtis, V.A. Sobyenin, V.N. Parmon, *Top. Catal.*, 59 (2016) 1424-1430.
- [85] B. Nematollahi, M. Rezaei, E. Nemati Lay, *J. Rare Earth*, 33 (2015) 619-628.
- [86] S. Abate, K. Barbera, E. G. Deorsola, S. Bensaid, S. Perathoner, R. Pirone, G. Centi, *Ind. Eng. Chem. Res.*, 55 (2016) 8299-8308.
- [87] L. He, Q. Lin, Y. Liu, Y. Huang, *J. Energy Chem.*, 23 (2014) 587-592.
- [88] I. Graca, L.V. González, M.C. Bacariza, A. Fernandes, C. Henriques, J.M. Lopes, M. F. Ribeiro, *Appl. Catal. B Environ.*, 147 (2014) 101-110.
- [89] Y. Feng, W. Yang, S. Chen, W. Chu, *Integr. Ferroelectr.*, 151 (2014) 116-125.
- [90] J. Zhang, Y. Bai, Q. Zhang, X. Wang, T. Zhang, Y. Tan, Y. Han, *Fuel*, 132 (2014) 211-218.
- [91] J. Y. Lim,; J. McGregor,; A. J. Sederman,; J. S. Dennis, *Chem. Eng. Sci.*, 141 (2016) 28-45.
- [92] J. Liu, C. Li, F. Wang, S. He, H. Chen, Y. Zhao, M. Wei, D. G. Evans and X. Duan, *Catal. Sci. Technol.*, 3 (2013) 2627-2633.

- [93] Y. R. Li, G. X. Lu and J. T. Ma, *RSC Adv.*, 4 (2014) 17420-17428.
- [94] T. Abe, M. Tanizawa, K. Watanabe and A. Taguchi, *Energy Environ. Sci.*, 2 (2009) 315-321.
- [95] J. Sehested, *Catal. Today*, 111 (2006) 103-110.
- [96] H. H. Gierlich, M. Fremery, A. Skov, J. R. Rostrup-Nielsen, Deactivation Phenomena of a Ni-based Catalyst for High-Temperature Methanation, in *Studies in Surface Science and Catalysis*, ed. B. Delmon and G. F. Froment, Elsevier, (1980) 459-469.
- [97] X. Bai, S. Wang, T. Sun and S. Wang, *Catal. Lett.*, (2014) 1-10.
- [98] C. H. Bartholomew, *Catal. Rev.: Sci. Eng.*, 24 (1982) 67-112.
- [99] B. Mutz, M. Belimov, W. Wang, P. Sprenger, M.-A. Serrer, D. Wang, P. Pfeifer, W. Kleist, J.-D. Grunwaldt, *ACS Catal.*, 7 (2017) 6802-6814.
- [100] G. Du, S. Lim, Y. Yang, C. Wang, L. Pfefferle, G.L. Haller, *Journal of Catalysis*, 249 (2007) 370-379.
- [101] F. Ocampo, B. Louis, L. Kiwi-Minsker, A.-C. Roger, *Applied Catalysis A: General*, 392 (2011) 36-44.

# **CHAPTER 2**

## 2. Ternary and quaternary mixed oxides supported Ni catalysts for CO<sub>2</sub> methanation: a comparison with Ni/ $\gamma$ -Al<sub>2</sub>O<sub>3</sub> conventional catalyst

### 2.1. Introduction

Nickel-based catalysts are the most commonly studied for CO<sub>2</sub> methanation because of their high activity and cheaper price from an industrial perspective [1]. However, conventional Ni-based catalysts supported on  $\gamma$ -Al<sub>2</sub>O<sub>3</sub> are easily deactivated as a result of sintering of Ni particles and coke deposition during the exothermic methanation reaction. In order to increase their catalytic activities, Ni/Al<sub>2</sub>O<sub>3</sub> catalysts usually need to have a high Ni content, which may cause faster deactivation of the catalyst during long-term operation [2]. Therefore, a catalyst with lower Ni loading and higher activity is required. In this chapter, we focus our attention on the improvement of the  $\gamma$ -Al<sub>2</sub>O<sub>3</sub> support.

The type of support used for heterogeneous catalysts is an important factor to consider in solving such problems. Because “metal-support effects” i.e. an interaction between the support and active metal governs the activity of supported catalysts. The support determines in the reducibility, dispersion as well as the stability of the active metal [3]. Improvements to the support can affect in three aspects: (i) enhance the dispersion of the active metal, (ii) inhibit/decrease the formation of spinels which are considered as inactive phases and (iii) tailor the reducibility of the oxide precursors through improving metal-support interaction [4]. The main problem of  $\gamma$ -Al<sub>2</sub>O<sub>3</sub> support during methanation reaction is the sintering in the presence of water (a product of methanation reaction) at high temperature.

For the improvement of the Ni/ $\gamma$ -Al<sub>2</sub>O<sub>3</sub> catalysts, it is frequently reported in the literature by  $\gamma$ -Al<sub>2</sub>O<sub>3</sub> modification with the addition of alkali metals, rare earth oxides, and other basic oxides. So far, different modifiers such as; ZrO<sub>2</sub>, SiO<sub>2</sub>, MgO, La<sub>2</sub>O<sub>3</sub>, CeO<sub>2</sub>, and TiO<sub>2</sub> have been added to the conventional Ni/ $\gamma$ -Al<sub>2</sub>O<sub>3</sub> CO<sub>2</sub> methanation catalyst. Promoters can be mainly classified into two types: (1) electron promoter to change the electron mobility of catalyst. (2) Structure promoter to improve the dispersion and thermal stability of catalyst by changing the chemical component,

crystal texture, pore structure, dispersion state, and mechanical strength of the catalyst. Some oxide promoters can serve both functions [5].

The  $\gamma$ -Al<sub>2</sub>O<sub>3</sub>-ZrO<sub>2</sub> [4], CeO<sub>2</sub>-ZrO<sub>2</sub> [6-8], ZrO<sub>2</sub>-Al<sub>2</sub>O<sub>3</sub> [9] and SiO<sub>2</sub>-Al<sub>2</sub>O<sub>3</sub> [10] mixed oxide supported Ni-based catalysts were reported to be active for methanation of CO<sub>2</sub> and CO with better conversion because of their excellent properties. The main advantage of using mixed oxide supports is to get inherent favorable properties of all the individual metal oxide supports. The addition of CeO<sub>2</sub> can improve the reducibility of the methanation catalyst by altering the interaction between Ni and Al<sub>2</sub>O<sub>3</sub> [11, 12]. TiO<sub>x</sub> species and ZrO<sub>2</sub> were found to effectively restrict the formation of NiAl<sub>2</sub>O<sub>4</sub> spinel phase and weaken the Ni-Al<sub>2</sub>O<sub>3</sub> interaction, leading to a higher exposure of Ni species and thus enhancing the CO/CO<sub>2</sub> adsorption capacity. In addition, electron transfer from TiO<sub>x</sub> could increase the electron cloud density of Ni which facilitates the dissociation of CO [13]. Therefore, the addition of metal oxide promoters to the conventional  $\gamma$ -Al<sub>2</sub>O<sub>3</sub> support can help on the synthesis of Ni-based catalysts with highest reducibility and chemisorption capacity due to a better dispersion of the nickel species on the mixed metal oxide supports.

## 2.2. Scope of the chapter

The main objective of this chapter is to study the behavior of various mixed oxides containing or not CeO<sub>2</sub> as promoter towards CO<sub>2</sub> methanation. In order to obtain a reliable comparison between mixed oxide supported Ni-based catalysts, ternary and quaternary mixed oxide supported catalysts were tested by using a high throughput reactor at a low gas hourly space velocity, in the range 2000 - 4000 h<sup>-1</sup>, 5 bar of pressure and a stoichiometric mixture of H<sub>2</sub>/CO<sub>2</sub> = 4 without any diluent. Specifically, the addition of ZrO<sub>2</sub>-TiO<sub>2</sub> and ZrO<sub>2</sub>-TiO<sub>2</sub>-CeO<sub>2</sub> to Ni/ $\gamma$ -Al<sub>2</sub>O<sub>3</sub> catalysts was investigated. The physicochemical properties and reducibility of these materials were also analyzed by X-ray diffraction (XRD), Brunauer-Emmet-Teller (BET) surface area analysis, and H<sub>2</sub>-TPR. The catalytic data and characterization results obtained, allow to derive relationships between the catalytic activity and characteristics of the as-prepared mixed oxide supported catalysts, and analyze better the role of CeO<sub>2</sub>.



## 2.3. Experimental

### 2.3.1. Synthesis of mixed oxide supported Ni-based catalysts

Two groups of mixed oxides supported Ni-based catalysts, containing or not CeO<sub>2</sub>, were prepared using a method described in Ref. [4] except increasing the number of loaded metal oxide promoters. Typically, commercial  $\gamma$ -Al<sub>2</sub>O<sub>3</sub> (Sasol-Puralox SCCa-20/200) was impregnated with aqueous solutions of Zirconyl nitrate, Titanium (IV) isopropoxide and Cerium (III) nitrate hexahydrate salts of different ratios to get the desired percentages of mixed oxide supports. After 2 h under continuous stirring, an aqueous solution of 25 wt-% ammonium hydroxide was added slowly till pH reaches a value of 10 when precipitation-deposition occurs. The pH was then maintained nearly constant at about 10, up to complete the precipitation-deposition process. The precipitate was filtered, washed with deionized water repeatedly and dried overnight in an oven at 120°C, then it was calcined at 550°C for 4 h with a temperature ramp of 20°C/minute. 3 g of each calcined mixed oxide support was then impregnated (with incipient wet impregnation method) with an aqueous solution of Ni(NO<sub>3</sub>)<sub>2</sub>.6H<sub>2</sub>O to obtain a final loading of 20 wt.-% Ni on the mixed oxide supports. The samples were then dried in an oven at 120°C for 16 h, and calcined at 450°C for 5 h with a temperature ramp of 20°C/minute. For comparison, 3 g of commercial  $\gamma$ -Al<sub>2</sub>O<sub>3</sub> was impregnated with 20%Ni and treated as the other synthesized supports. **Table 2.1** summarizes the adopted nomenclature for the prepared samples.

**Table 2.1** Designation of the as-synthesized catalysts.

Notation	Catalysts
Ni/ $\gamma$ -Al <sub>2</sub> O <sub>3</sub>	20%Ni/100% $\gamma$ -Al <sub>2</sub> O <sub>3</sub>
Ni/C5	20%Ni/90% $\gamma$ -Al <sub>2</sub> O <sub>3</sub> -5%ZrO <sub>2</sub> -5%TiO <sub>2</sub>
Ni/C10	20%Ni/80% $\gamma$ -Al <sub>2</sub> O <sub>3</sub> -10%ZrO <sub>2</sub> -10%TiO <sub>2</sub>
Ni/C15	20%Ni/70% $\gamma$ -Al <sub>2</sub> O <sub>3</sub> -15%ZrO <sub>2</sub> -15%TiO <sub>2</sub>
Ni/C5-5%CeO <sub>2</sub>	20%Ni/85% $\gamma$ -Al <sub>2</sub> O <sub>3</sub> -5%ZrO <sub>2</sub> -5%TiO <sub>2</sub> -5%CeO <sub>2</sub>
Ni/C10-10%CeO <sub>2</sub>	20%Ni/70% $\gamma$ -Al <sub>2</sub> O <sub>3</sub> -10%ZrO <sub>2</sub> -10%TiO <sub>2</sub> -10%CeO <sub>2</sub>
Ni/C15-15%CeO <sub>2</sub>	20%Ni/55% $\gamma$ -Al <sub>2</sub> O <sub>3</sub> -15%ZrO <sub>2</sub> -15%TiO <sub>2</sub> -15%CeO <sub>2</sub>

### 2.3.2. Characterization of as-prepared catalysts

Specific surface areas were obtained from N<sub>2</sub> adsorption-desorption isotherms by the BET method. The samples were outgassed under vacuum at 100°C for 5 h. Isotherms were obtained at the temperature of liquid nitrogen using Micrometrics ASAP 2010.

Atomic absorption spectroscopy (AAS), Perkin-Elmer Analyst 200 instrument was used to analyze the content of Ni metal in each catalyst. Samples for analysis were prepared by dissolving 10 mg of the calcined catalyst in hydrofluoric acid.

Structure and crystalline nature of the catalysts were studied using a Bruker D2-Phaser diffractometer operating with Cu K $\alpha$  radiation at 30 kV and 10 mA. Measurements were performed in the 2 $\theta$  range of 10-90°. The average crystallite size of the samples was also calculated by the Scherrer equation.

Reducibility of the calcined catalysts was studied by H<sub>2</sub> temperature-programmed reduction using a Micromeritics 2920 system equipped with a TCD detector. About 100 mg of calcined sample was first pretreated using He (50 mL/min) for 1 hr at 120°C. Then, the H<sub>2</sub>-TPR profile was recorded under the flow of 5% H<sub>2</sub> in Ar up to 950°C with the ramp of 10°C/min.

Metal dispersion and metallic surface area were determined by CO chemisorption using the same instrument used for H<sub>2</sub>-TPR analyses. 50 mg of catalyst was reduced in-situ at 500°C for 1 h using 50 mL/min of 5% H<sub>2</sub> in Ar prior to the CO chemisorption analysis. Then the CO chemisorption was performed at 35°C by using 30 mL/min of 10% CO in He until saturation. The CO temperature programmed desorption (CO-TPD) analyses were made after the CO-chemisorption analysis, with an increasing temperature from 35 to 900°C with a ramp of 5°C/min under He flow.

### 2.2.3. Catalytic CO<sub>2</sub> methanation

The catalytic methanation of CO<sub>2</sub> was made using a high throughput reactor (Amtech high-throughput technology SPIDER 16) having sixteen fixed-bed continuous-flow reactors operating in parallel. **Figure 2.1** summarizes the testing unit used for the catalytic CO<sub>2</sub> methanation reaction.

The catalytic bed volume is 4 mL. CO<sub>2</sub> methanation reaction was studied at 5 bar pressure and in a temperature range of 300-400°C. Other reaction parameters applied were the following: i) gas hourly space velocities of 2000, 3000 and 4000 h<sup>-1</sup>; ii) 50 mg of catalyst mixed with SiC as inert material. The catalyst was reduced in situ at 500°C using 50 mL/min of H<sub>2</sub> for 1 h before to feed a mixture of CO<sub>2</sub>/H<sub>2</sub> gases (ratio 1:4) without diluent. Products were analyzed with on-line micro-GC equipped with a TCD detector.

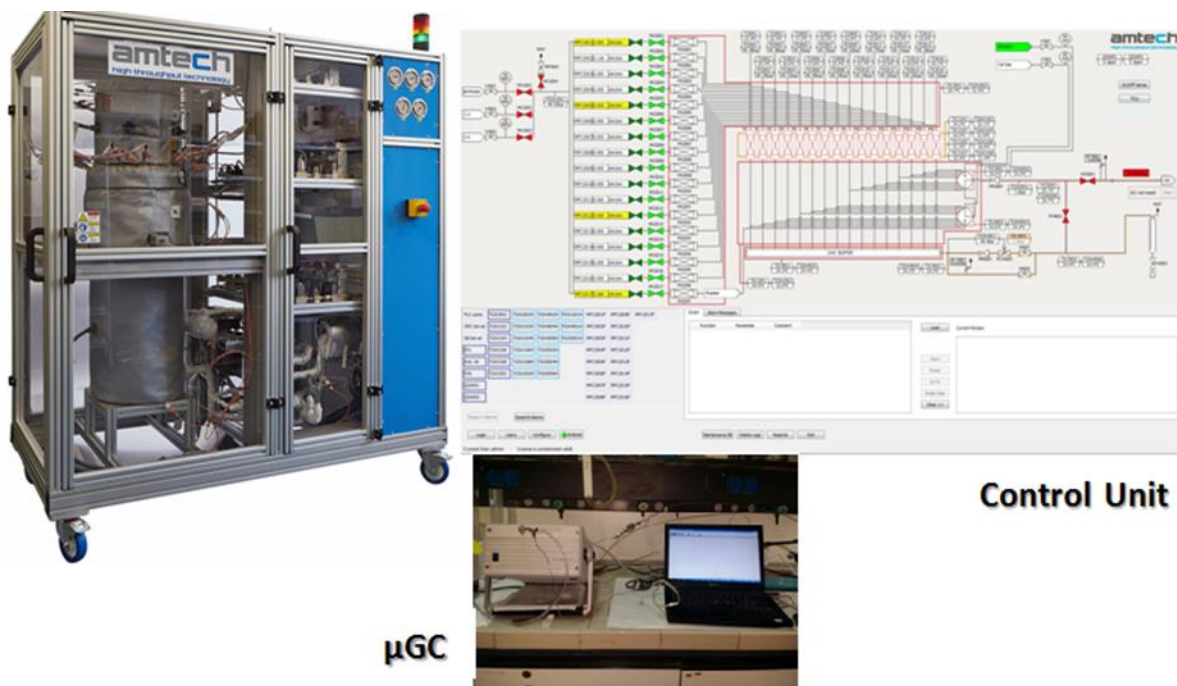


**Figure 2.1** High-throughput reactor (Amtech high-throughput technology SPIDER 16) used for the catalytic CO<sub>2</sub> methanation.

The carbon dioxide conversion ( $X_{CO_2}$ ) was calculated using [equation \(2.1\)](#) where  $F_{CO_2}$  is the CO<sub>2</sub> flow rate of CO<sub>2</sub>.

$$X_{CO_2} = \frac{F_{CO_2,in} - F_{CO_2,out}}{F_{CO_2,in}} \quad (2.1)$$

## 2.3. Results and discussion

### 2.3.1. Ternary mixed oxides supported Ni-based catalysts

#### 2.3.1.1. Characterization results

The chemical compositions (Ni wt-%) of all the calcined catalysts were determined by AAS and the results are summarized in **Table 2.2**. The wt-% of Ni in all catalysts are close to the nominal value used during the synthesis. The obtained BET surface area values of the  $\gamma$ -Al<sub>2</sub>O<sub>3</sub> support and Ni/mixed oxide supported catalysts are also reported in **Table 2.2**. The BET surface areas of mixed oxide supported catalysts were found to be decreased except for the Ni/C5 catalyst. This might be caused due to pore blockage. The pore blockages due to the localization of the promoters in the pores of the  $\gamma$ -Al<sub>2</sub>O<sub>3</sub> support, or resulting from the incorporation of Ni on the pores of both in the  $\gamma$ -Al<sub>2</sub>O<sub>3</sub> and mixed oxide supports [14]. Metallic surface area and dispersion were estimated from CO-chemisorption measurements and the results are summarized in **Table 2.2**. The catalysts with the larger BET surface area show the higher dispersion and Ni surface area.

**Table 2.2** Physicochemical properties of the as-synthesized catalysts.

Catalyst	Ni (wt. %) <sup>a</sup>	BET Surface area (m <sup>2</sup> /g) <sup>b</sup>	Crystalline size of NiO (nm) <sup>c</sup>	Nickel dispersion (%) <sup>d</sup>	Nickel surface area (m <sup>2</sup> /g- Ni) <sup>d</sup>
$\gamma$ -Al <sub>2</sub> O <sub>3</sub>	-	186	-	-	-
Ni/ $\gamma$ -Al <sub>2</sub> O <sub>3</sub>	18.05	149	13	2.00	15.74
Ni/C5	16.24	176	9	2.55	17.00
Ni/C10	18.75	164	11	2.10	13.97
Ni/C15	17.60	137	12	2.11	14.10

<sup>a</sup> Determined by AAS analysis.

<sup>b</sup> Calculated by the BET equation.

<sup>c</sup> Calculated from Ni (220) at 2 theta = 62.98° diffraction peak broadening in **Fig. 2.2 a**.

<sup>d</sup> Calculated by assuming CO/Ni<sub>atom</sub> = 1.

**Figure 2.2** present the diffraction patterns of calcined (a) 20% Ni supported on the different mixed oxides (see **Table 2.1** for acronyms) and (b) the corresponding alumina,  $\text{Al}_2\text{O}_3$ - $\text{ZrO}_2$ - $\text{TiO}_2$  mixed oxide supports. A significant difference in XRD patterns (**Figure 2.2 b**) of the  $\gamma$ - $\text{Al}_2\text{O}_3$  support and the mixed oxides can be observed. The mixed oxide supports show a new diffraction peak at  $2\theta = 27^\circ$  and its intensity increases with the amount of  $\text{TiO}_2$  loaded onto the  $\gamma$ - $\text{Al}_2\text{O}_3$ , indicating the successful incorporation of the promoter [15].

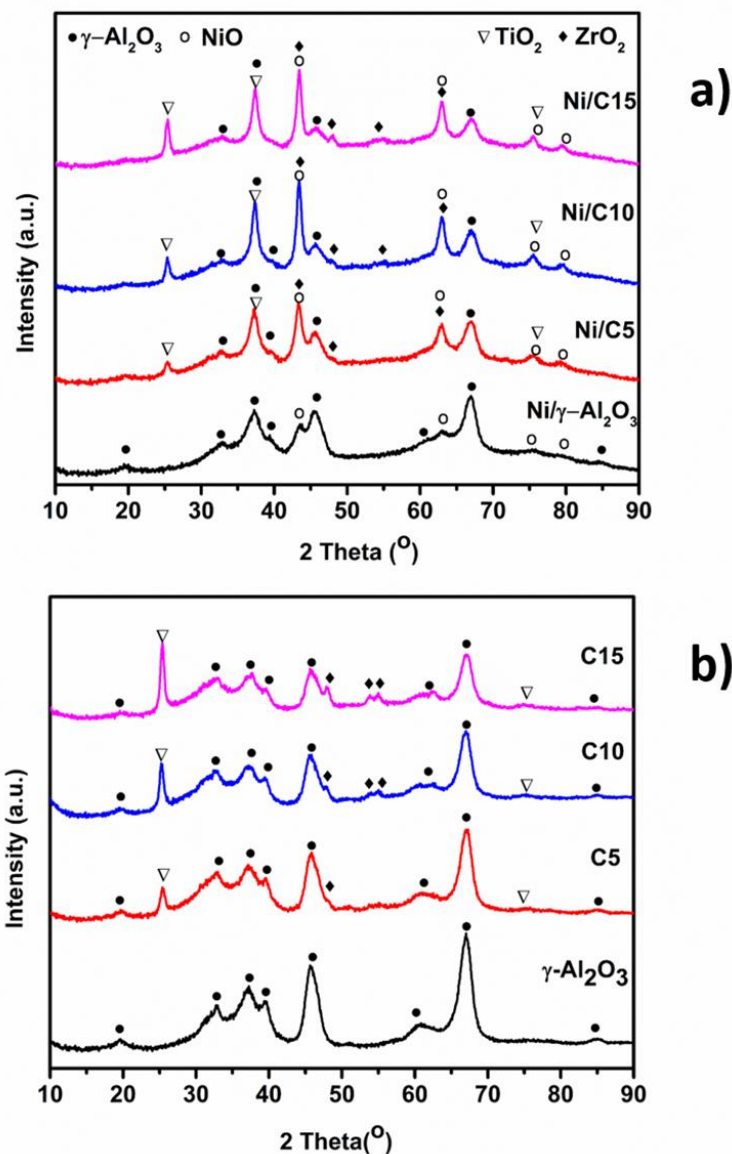


**Figure 2.2** XRD of (a) 20%Ni on the different supports; (b)  $\gamma$ - $\text{Al}_2\text{O}_3$  and  $\gamma$ - $\text{Al}_2\text{O}_3$  - $\text{ZrO}_2$ - $\text{TiO}_2$  mixed-oxide supports.

After calcination at 450°C (**Figure 2.2 a**) the mixed oxide supported catalysts exhibited reflections at  $2\theta$  of 37.24°, 43.30°, 62.92°, 75.48° and 79.50° which may be attributed to the (111), (200), (220), (311) and (222) planes of NiO, respectively [15]. The XRD patterns show the characteristic diffraction lines of ZrO<sub>2</sub>, TiO<sub>2</sub> and Al<sub>2</sub>O<sub>3</sub> phases. A semi-quantitative analysis was made by the software "diffrac.suite eva". The estimated percentage of each oxide present in the sample is close to the theoretical value used during the preparation (**Table 2.3**). It can be noted, that the amount of ZrO<sub>2</sub> deposited is always higher than that of TiO<sub>2</sub>. The average crystal sizes were also estimated using the Scherrer's equation and results are summarized in **Table 2.2**. The crystal size values of the mixed oxide supported catalysts ranges from 9-13 nm.

**Table 2.3** Real vs. theoretical support composition obtained by XRD.

Oxide	XRD composition (% wt)/Theoretical value		
	C5	C10	C15
$\gamma$ -Al <sub>2</sub> O <sub>3</sub>	92/90	85/80	74/70
TiO <sub>2</sub>	4/5	8/10	11/15
ZrO <sub>2</sub>	4/5	12/10	19/15

H<sub>2</sub>-TPR measurements were carried out in order to examine the metal-support interaction and the reducibility of the catalysts. **Fig. 2.3** shows the H<sub>2</sub>-TPR profiles obtained for the calcined catalysts. All profiles exhibit one wide asymmetric peak arising from the reduction of nickel oxide species to metallic nickel (Ni<sup>0</sup>) at temperatures between 411 and 671°C accompanied by shoulders. The H<sub>2</sub>-TPR profiles were deconvoluted and three elementary peak temperatures were identified with  $R^2$  value of 0.99. The reducible NiO species could be classified into three types:  $\alpha$ -type (surface amorphous NiO or bulk NiO),  $\beta$ -type (weakly interacted with Al<sub>2</sub>O<sub>3</sub> or called Ni-rich phase) and  $\gamma$ -type (strongly interacted with Al<sub>2</sub>O<sub>3</sub> or called Al-rich phase) [16].

The peak positions and their integrated area contributions derived from the deconvolution results are summarized in **Table 2.4**.

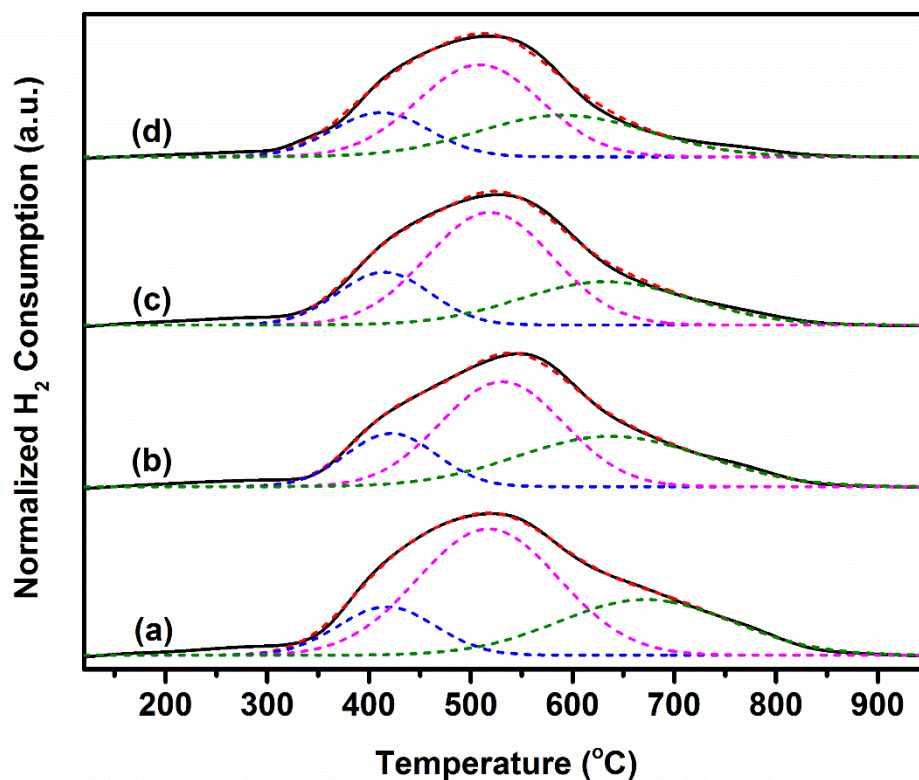


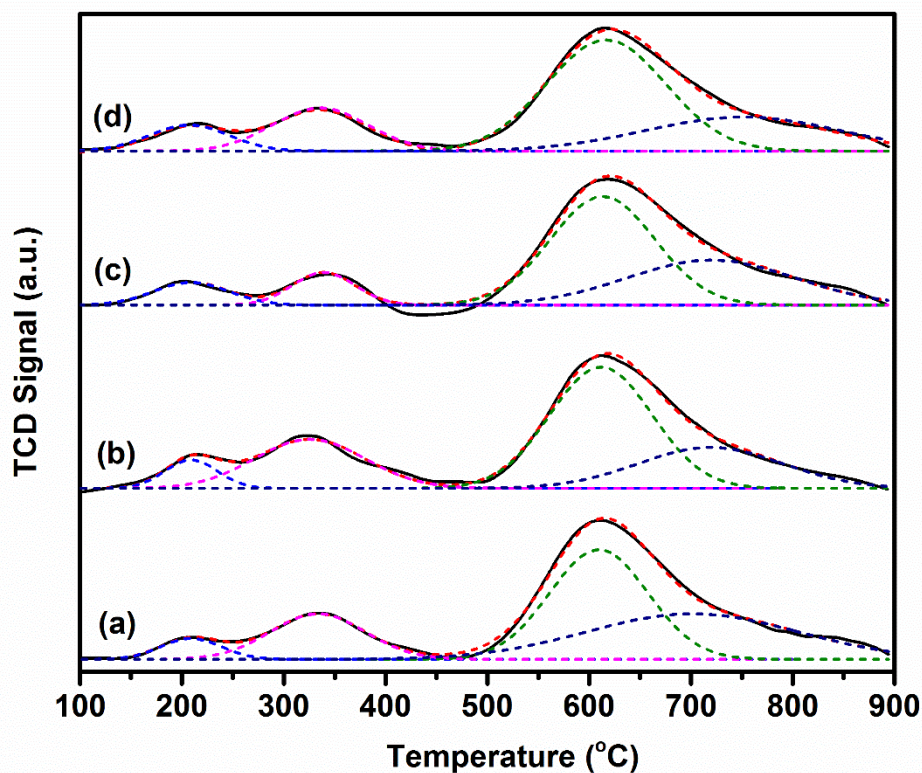
**Figure 2.3** H<sub>2</sub>-TPR profiles: (a) 20%Ni/ $\gamma$ -Al<sub>2</sub>O<sub>3</sub>, (b) 20%Ni/C5, (c) 20%Ni/C10 and (d) 20%Ni/C15.

The  $\beta$ -type of Ni species (weakly interacted with Al<sub>2</sub>O<sub>3</sub> or called Ni-rich phase) may be assumed as the active element for the methanation reaction in the low reaction temperature range (< 350-400°C). The ternary system supported Ni-based catalysts show the  $\beta$ -type peak at approximately the same temperature and similar to that of 20%Ni/ $\gamma$ -Al<sub>2</sub>O<sub>3</sub> catalyst (**Table 2.4**). However, the total amount of H<sub>2</sub> consumed during the H<sub>2</sub>-TPR analyses is higher, indicating thus a better reducibility of NiO on these samples, likely due to the weaker metal support interactions [16, 17].

**Table 2.4** Quantitative H<sub>2</sub>-TPR data for the as-synthesized catalysts.

Catalyst	Fraction of total area (%)			Peak temperature (°C)			Total H <sub>2</sub> Consumed (H <sub>2</sub> /g <sub>cat</sub> )
	$\alpha$ -type	$\beta$ -type	$\gamma$ -type	$\alpha$ -type	$\beta$ -type	$\gamma$ -type	
Ni/ $\gamma$ -Al <sub>2</sub> O <sub>3</sub>	15	56	29	417	517	671	3.7
N/C5	18	48	34	421	530	637	4.6
Ni/C10	19	53	28	415	518	632	4.7
Ni/C15	19	50	31	411	508	590	4.9

The rate-determining step in CO<sub>2</sub> methanation is likely the hydrogenation of CO, further insights on these samples could be obtained by CO-TPD measurements (**Fig. 2.4**). In addition, CO-TPD could thus provide indications on the adsorption of CO species and their strength, and on the effect induced by the type of support. To quantify these species, the CO-TPD profiles were deconvoluted in four peaks, whose amounts are summarized in **Table 2.5**.

**Figure 2.4** CO-TPD profiles of (a) 20%Ni/ $\gamma$ -Al<sub>2</sub>O<sub>3</sub>, (b) 20%Ni/C5, (c) 20%Ni/C10 and (d) 20%Ni/C15.



The low-temperature peaks (100-450°C) are indicated as  $\alpha$  sites (peaks 1 and 2) and are attributed to the molecularly adsorbed CO, while the high-temperature peaks (500-800°C) are indicated as  $\beta$  sites (peaks 3 and 4) derived from the dissociative adsorption of CO followed by associative desorption [18, 19]. No CO desorption peak was observed at lower temperatures ( $\leq 75^\circ\text{C}$ ) which are responsible for the formation  $\text{Ni}(\text{CO})_4$  species and in turn results for faster deactivation of the catalysts [18]. The two peaks in the  $\alpha$  region can be assigned to desorption from a single site chemisorption (peak 1) and from a two-site chemisorption (peak 2) [20, 21]. Depending on the catalyst support and synthesis method used, the single site or two sites chemisorption may be dominant. In the mixed oxide supported catalysts, the two-site chemisorption is predominant.

**Table 2.5** Quantitative CO-TPD data for the as-synthesized catalysts.

Catalyst	Peak temperature ( $^\circ\text{C}$ )				Total CO desorbed (mmol/g of catalyst)
	Peak 1	Peak 2	Peak 3	Peak 4	
Ni/ $\gamma$ - $\text{Al}_2\text{O}_3$	209	333	609	698	3.8
N/C5	208	325	611	718	4.3
Ni/C10	209	339	612	719	3.6
Ni/C15	209	336	617	750	4.1

The  $\beta$  region of CO desorption (temperature range of 500-800°C) is related to CO desorption from a multicomponent system. In addition to the presence of  $\beta$  sites (i.e. from stepped Ni surfaces) which give dissociative adsorption of CO (component at around 580°C), further, associative desorption ( $\text{CO}_2$  formation) is present at higher temperatures (650°C), deriving from the interaction of CO with some unreduced NiO. This can be due to the low-temperature reduction pre-treatment (500°C) of the catalysts. Due to the higher activity of a defective and stepped nickel surface in CO dissociation tests, the CO adsorption sites obtained are typical for a perturbed nickel surface in the vicinity of the mixed oxide support, mainly (100) and (111) [22]. **Table 2.5** shows that the amount of desorbed CO is higher over Ni/C5 catalyst. The trend is in agreement with the change of the exposed nickel surface area and higher BET surface area.

### 2.3.1.2. Catalytic activity in CO<sub>2</sub> methanation of the ternary mixed oxides supported Ni-based catalysts

The carbon dioxide conversion measured during catalytic methanation experiments is plotted in **Figure 2.5**, for the ternary mixed oxide supported catalysts as a function of reaction temperature. For comparison, the 20%Ni/ $\gamma$ -Al<sub>2</sub>O<sub>3</sub> catalyst was also tested under the same experimental conditions. The effect of ZrO<sub>2</sub>-TiO<sub>2</sub> oxides as promoters on the catalytic activities of a  $\gamma$ -Al<sub>2</sub>O<sub>3</sub> supported Ni-based catalyst has been investigated at different reaction temperatures and under specified conditions (H<sub>2</sub>/CO<sub>2</sub> = 4, GHSV<sub>s</sub> = 2000 h<sup>-1</sup>, 3000 h<sup>-1</sup>, 4000 h<sup>-1</sup> and 5 bar). Low gas hourly space velocities and undiluted feed mixture were chosen in order to study the catalytic activity under more severe conditions. The catalytic activities of Ni catalysts supported on the mixed oxide are higher than that of the reference 20%Ni/ $\gamma$ -Al<sub>2</sub>O<sub>3</sub> catalyst. The activity decreases on increase of GHSV, especially far from the thermodynamic equilibrium, but the CO selectivity remains quite constant. A very low amount of CO formations was always detected, even at high temperature, meaning that the catalysts showed high selectivity to methane (> 98-99%) irrespective of contact time.

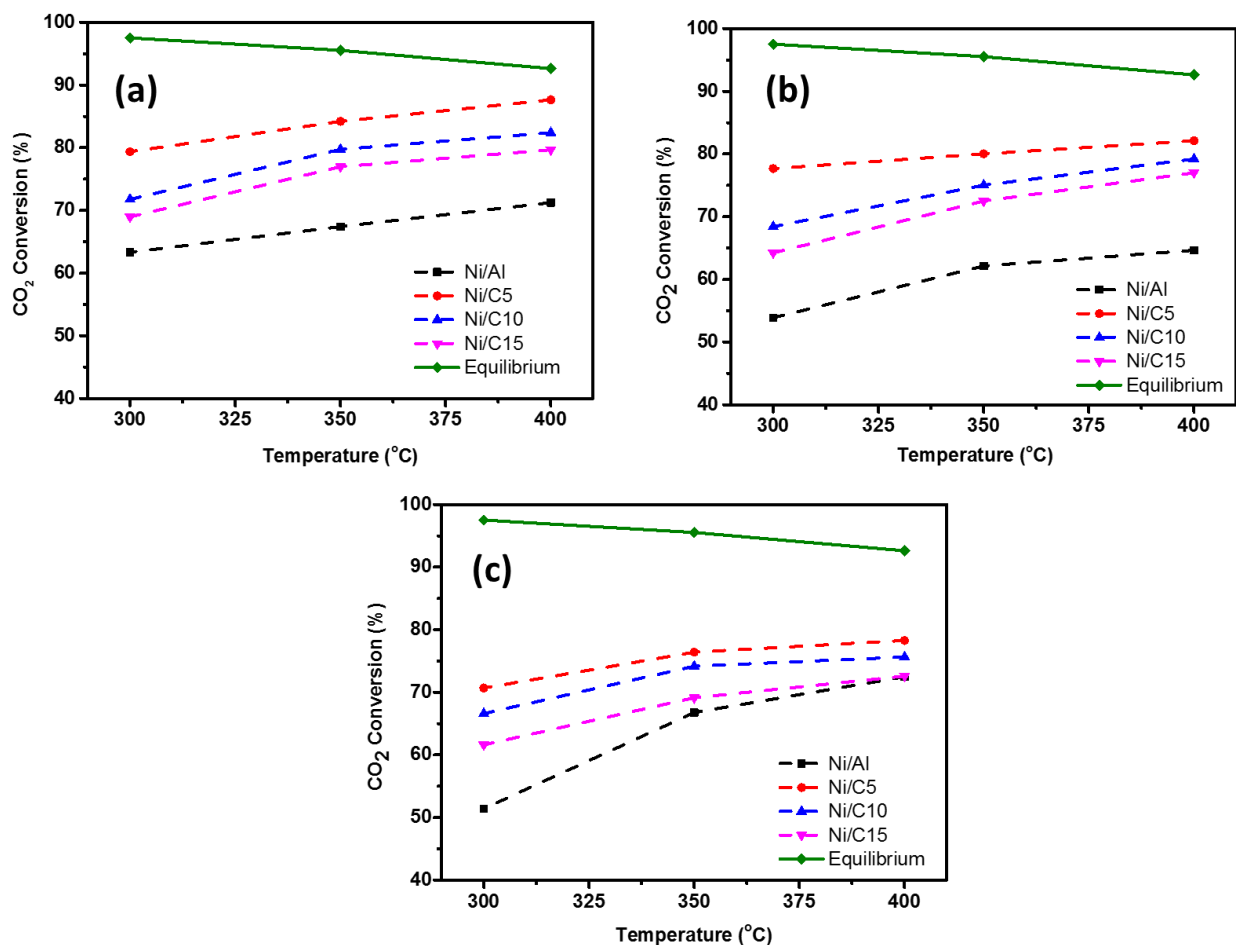


**Figure 2.5** Catalytic performance of different Ni samples for CO<sub>2</sub> methanation. Reaction conditions: gas mixture with CO<sub>2</sub>:H<sub>2</sub> = 1:4, P = 5 bar, and: (a) GHSV=2000 h<sup>-1</sup>, (b) GHSV= 3000 h<sup>-1</sup> and (c) GHSV= 4000 h<sup>-1</sup>.

Higher CO<sub>2</sub> conversion activity was recorded by using the catalyst with the highest H<sub>2</sub> consumption (in H<sub>2</sub>-TPR experiments), metallic dispersion and BET surface area. Comparison between the ternary mixed oxides supported Ni-based catalysts, the Ni/C5 catalyst shows the best performance over the whole investigated temperature range and GHSV, with the CO<sub>2</sub> conversion % value ranging from about 71 % at 300°C to about 78 % at 400°C with the highest GHSV used (4000 h<sup>-1</sup>). The higher CO<sub>2</sub> conversion activity is shown by the catalyst containing 5%ZrO<sub>2</sub>-5%TiO<sub>2</sub> as promoters, while higher ZrO<sub>2</sub>-TiO<sub>2</sub> amounts lead to less active catalysts. The addition of 5% wt of TiO<sub>2</sub> and ZrO<sub>2</sub> increases the BET surface area, while the reducibility properties, in

terms of H<sub>2</sub> consumption and β-type fraction, are very similar for all ternary systems (see [Table 2.4](#)).

### 2.3.2. Quaternary mixed oxides supported Ni-based catalysts

#### 2.3.2.1. Characterization results

Physicochemical properties of the quaternary mixed oxide supported Ni-based catalysts are summarized in [Table 2.6](#). From the BET measurements, the surface area of all mixed oxide supported catalysts is higher respect to the only  $\gamma$ -Al<sub>2</sub>O<sub>3</sub> support, moreover, the slight decrease of surface area with increasing the percentage of promoters was observed. The Ni loading ([Table 2.6](#)) was also analyzed using AAS and results are found to be close to the nominal values used during the synthesis.

**Table 2.6** Physicochemical properties of the quaternary oxide supported catalysts.

Catalyst	Ni (wt.-%) <sup>a</sup>	Surface area (m <sup>2</sup> /g) <sup>b</sup>	Crystalline size of NiO (nm) <sup>c</sup>
Ni/ $\gamma$ -Al <sub>2</sub> O <sub>3</sub>	15.42	149	15
Ni/C5-5%CeO <sub>2</sub>	16.55	166	12
Ni/C10-10%CeO <sub>2</sub>	17.20	165	16
Ni/C15-15%CeO <sub>2</sub>	16.45	151	17

<sup>a</sup> Determined by AAS analysis.

<sup>b</sup> Calculated by the BET equation.

<sup>c</sup> Calculated from Ni (220) at 2 theta = 62.98° diffraction peak broadening in [Figure 2.6 a](#).

A significant difference in XRD patterns ([Figure 2.6](#)) of the  $\gamma$ -Al<sub>2</sub>O<sub>3</sub> support and the quaternary oxide supports was observed. For the quaternary oxide supports a new diffraction peak was observed at 2 theta = 29° and its intensity increases with the increment of the ratio of the promoters onto the  $\gamma$ -Al<sub>2</sub>O<sub>3</sub> which assure the successful loading of them.

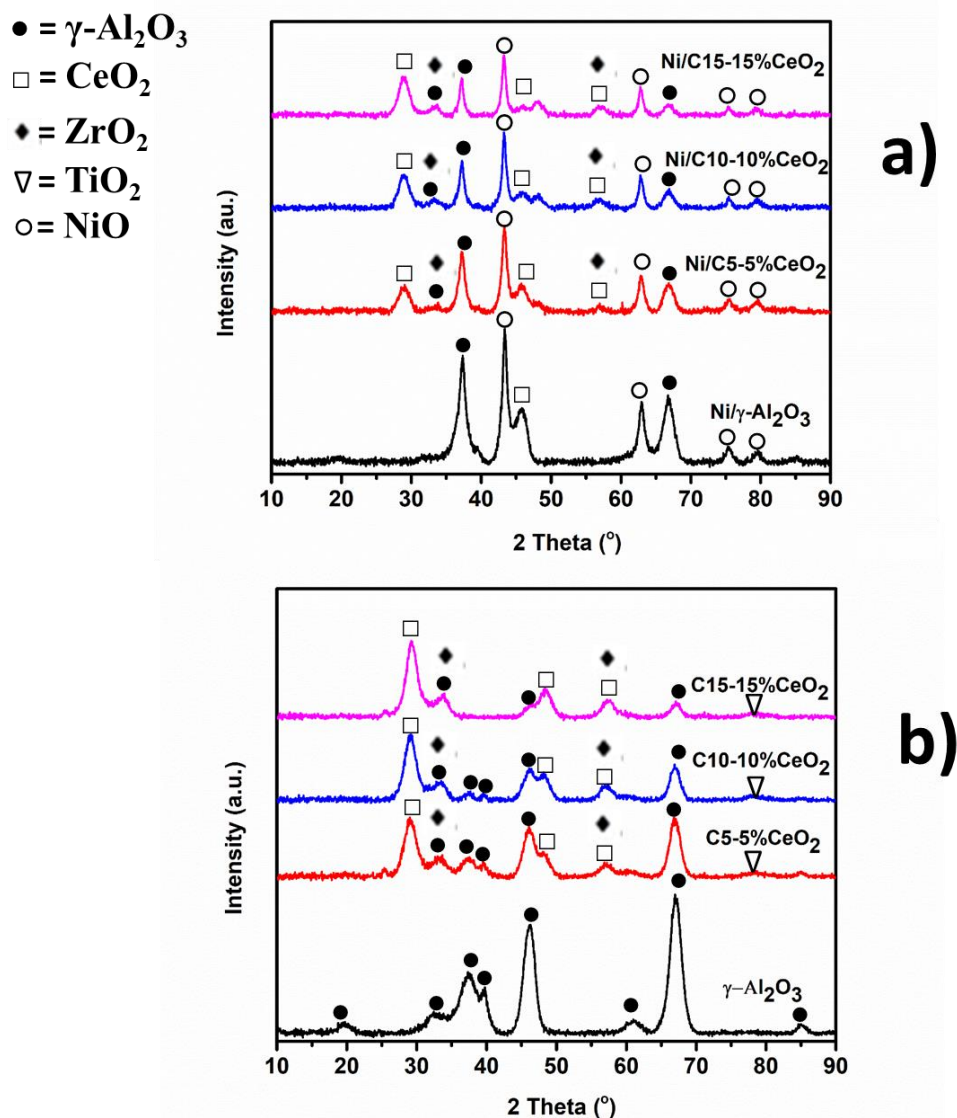


**Figure 2.6** XRD of (a) 20%Ni on the different supports; (b)  $\gamma$ -Al<sub>2</sub>O<sub>3</sub> and  $\gamma$ -Al<sub>2</sub>O<sub>3</sub>-ZrO<sub>2</sub>-TiO<sub>2</sub>-CeO<sub>2</sub> mixed-oxide support.

The Ni-based catalysts exhibited small reflections at  $2\theta$  of  $37.38^\circ$ ,  $43.28^\circ$ ,  $62.98^\circ$ ,  $75.38^\circ$  and  $79.40^\circ$  which were attributed to the (111), (200), (220), (311) and (222) planes of NiO [14], respectively. Furthermore, slight broader diffraction peaks of NiO for the Ni-based catalysts supported on the quaternary oxide were observed, suggesting the better dispersion of nickel supported in the mixed oxides, which is also confirmed by the CO chemisorption results (see **Table 2.8**). The Crystalline size of NiO was calculated by Scherrer equation from the diffraction peak Ni (220), at  $2\theta = 62.98^\circ$ , the results are reported in **Table 2.6**.

Although no clear characteristic diffraction peaks of ZrO<sub>2</sub> and TiO<sub>2</sub> phases were detected, most of them are included in the peaks attributed to the  $\gamma$ -Al<sub>2</sub>O<sub>3</sub> and/or CeO<sub>2</sub>. A semi-qualitative analysis was performed by using the software *diffpac.suite eva*, the resulting percentage of each oxide present in the sample, is close to the theoretical value used during the preparation (**Table 2.7**). Moreover, it can be noted that the amount of TiO<sub>2</sub> and ZrO<sub>2</sub> deposited is always less respect to the CeO<sub>2</sub>.

**Table 2.7** Quaternary supports: real estimated by XRD vs. theoretical support composition.

Oxide	XRD composition (% wt)/ <b>Theoretical value</b>		
	C5-5%CeO <sub>2</sub>	C10-10%CeO <sub>2</sub>	C15-15%CeO <sub>2</sub>
Al <sub>2</sub> O <sub>3</sub>	85.0/ <b>85</b>	75.0/ <b>70</b>	60.0/ <b>55</b>
TiO <sub>2</sub>	3.5/ <b>5</b>	7.5/ <b>10</b>	9.0/ <b>15</b>
CeO <sub>2</sub>	5.7/ <b>5</b>	8.8/ <b>10</b>	17.0/ <b>15</b>
ZrO <sub>2</sub>	5.8/ <b>5</b>	8.7/ <b>10</b>	14.0/ <b>15</b>

Carbon monoxide chemisorption measurements were also conducted in order to study the metallic surface area of Ni and the nickel dispersion. As a result, the nickel surface area in the reduced catalysts decreased in the order of Ni/C5-5%CeO<sub>2</sub> > Ni/C15-15%CeO<sub>2</sub> > Ni/C10-10%CeO<sub>2</sub> > Ni/ $\gamma$ -Al<sub>2</sub>O<sub>3</sub>. CO chemisorption results of all the catalysts are summarized in **Table 2.8**. Among the catalysts investigated, Ni/C5-5%CeO<sub>2</sub> has the highest metallic surface area this might be due to the highest BET surface area of the Ni/C5-5%CeO<sub>2</sub> catalyst. While the Ni dispersion slightly increases with increasing the percentage of mixed oxides.

**Table 2.8** CO chemisorption results for reduced Ni-based catalysts.

Catalyst	Nickel dispersion (%) <sup>a</sup>	Nickel surface area (m <sup>2</sup> /g-Ni) <sup>a</sup>
Ni/ $\gamma$ -Al <sub>2</sub> O <sub>3</sub>	2.33	16
Ni/C5-5%CeO <sub>2</sub>	2.67	18
Ni/C10-10%CeO <sub>2</sub>	3.17	15
Ni/C15-15%CeO <sub>2</sub>	3.38	16

<sup>a</sup> Calculated by assuming CO/Ni<sub>atom</sub> = 1

The H<sub>2</sub>-TPR profiles of the quaternary mixed oxides supported catalysts were also obtained using similar conditions explained above and deconvoluted into three Gaussian peaks ( $\alpha$ ,  $\beta$ , and  $\gamma$  peaks). These peaks were centered at 376-415°C, 460-528°C and 595-684°C, for  $\alpha$ -type,  $\beta$ -type, and  $\gamma$ -type NiO, respectively. According to the H<sub>2</sub>-TPR profiles (**Figure 2.7**) for all the catalysts,  $\beta$ -peak and  $\gamma$ -peak temperatures shift to lower temperature for the quaternary mixed oxide supported Ni-based catalysts, suggesting a weaker interaction between NiO and the mixed oxide support.

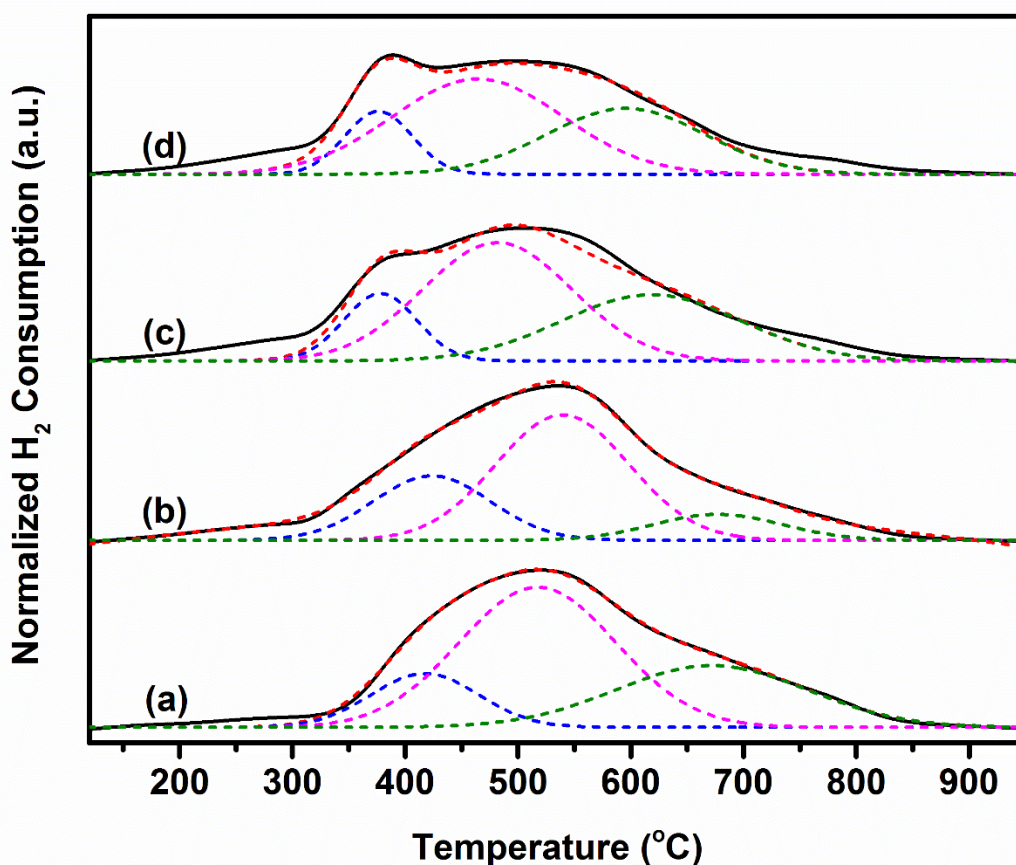


**Figure 2.7** H<sub>2</sub>-TPR profiles: (a) 20%Ni/ $\gamma$ -Al<sub>2</sub>O<sub>3</sub>, (b) 20%Ni/C5-5%CeO<sub>2</sub>, (c) 20%Ni/C10-10%CeO<sub>2</sub> and (d) 20%Ni/C15-15%CeO<sub>2</sub>.

Quantitative results of the H<sub>2</sub>-TPR profiles (**Table 2.9**) showed that all the mixed oxide supported catalysts possessed a higher fraction of  $\beta$ -type NiO. As for loading metal oxide content increases, the fraction of  $\beta$ -type NiO varies from 46% to 54%. According to the literature [17], the reduction of  $\alpha$  and  $\beta$ -type NiO would benefit the formation of Ni species which are active at low

temperatures. Therefore, increasing the fraction of  $\beta$ -type NiO which is the active species for the methanation reaction would result in an increase the conversion of  $\text{CO}_2$  at lower temperatures. Moreover, the amount of  $\text{H}_2$  consumed increases on the mixed oxides support, confirming a higher reducibility of NiO supported on these mixed oxides, due to the weaker metal support interaction.

**Table 2.9** Quantitative  $\text{H}_2$ -TPR data for the as-synthesized catalysts. Consumed hydrogen refers to a gram of catalyst.

Catalyst	Fraction of total area (%)			Peak temperature ( $^{\circ}\text{C}$ )			$\text{H}_2$ consumed ( $\text{mmol/g}_{\text{cat}}$ )
	$\alpha$ -type	$\beta$ -type	$\gamma$ -type	$\alpha$ -type	$\beta$ -type	$\gamma$ -type	
Ni/ $\gamma$ - $\text{Al}_2\text{O}_3$	22	46	32	415	516	684	3.7
Ni/C5-5% $\text{CeO}_2$	27	51	22	410	528	648	5.0
Ni/C10-10% $\text{CeO}_2$	9	52	39	376	483	618	5.4
Ni/C15-15% $\text{CeO}_2$	12	54	34	379	460	595	5.5

The  $\text{H}_2$ -TPR TPR profiles for the most active catalyst (Ni/C15-15% $\text{CeO}_2$ ) was compared with its mixed oxide support. As shown in **Figure 2.8**, a reduction peak with a very low intensity (400-600 $^{\circ}\text{C}$ ) was observed for the quaternary mixed oxide support (15% of all the promoters). Therefore, the contribution of support to the overall reduction process is almost negligible in comparison with the intense peak obtained during reduction of the Ni/C15-15% $\text{CeO}_2$  catalyst.



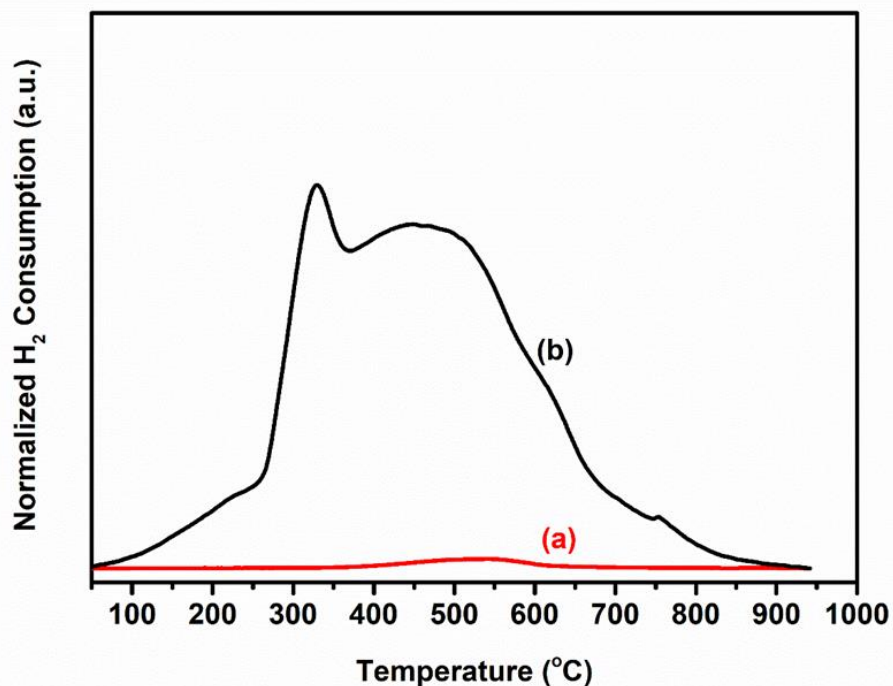


**Figure 2.8** H<sub>2</sub>-TPR profiles of (a) C15-15%CeO<sub>2</sub> mixed oxide support and (b) 20%Ni/C15-15%CeO<sub>2</sub> catalyst.

### 2.3.2.2. Comparison of ternary and quaternary mixed oxides supported Ni-based catalysts: the effect of CeO<sub>2</sub>

A high-throughput reactor was used in order to allow a direct and more reliable comparison between ternary and quaternary mixed oxide supported catalysts and analyze more precisely the effect of CeO<sub>2</sub>. A relationship between the structural/reducibility improvements of the mixed oxide supported catalysts with catalytic activity was also investigated. The quaternary mixed oxide supported Ni-based catalysts tested in the present work show an excellent activity for CO<sub>2</sub> methanation, better than that of the ternary mixed oxide supported catalysts (**Figure 2.9**). Among the quaternary mixed oxide supported Ni-based catalysts, the 20%Ni/C15-15%CeO<sub>2</sub>, which is composed of 55% $\gamma$ -Al<sub>2</sub>O<sub>3</sub>-15%ZrO<sub>2</sub>-15%TiO<sub>2</sub>-15%CeO<sub>2</sub>, shows the CO<sub>2</sub> conversion of 82% at 350°C, 5 bar, and 4000 h<sup>-1</sup>. Differently from what observed for ternary mixed oxide supported catalysts, showing better properties for about 5% promoters loading, an amount of about 15% of

promoters was found as necessary for the quaternary mixed oxides for an improved catalytic performance.

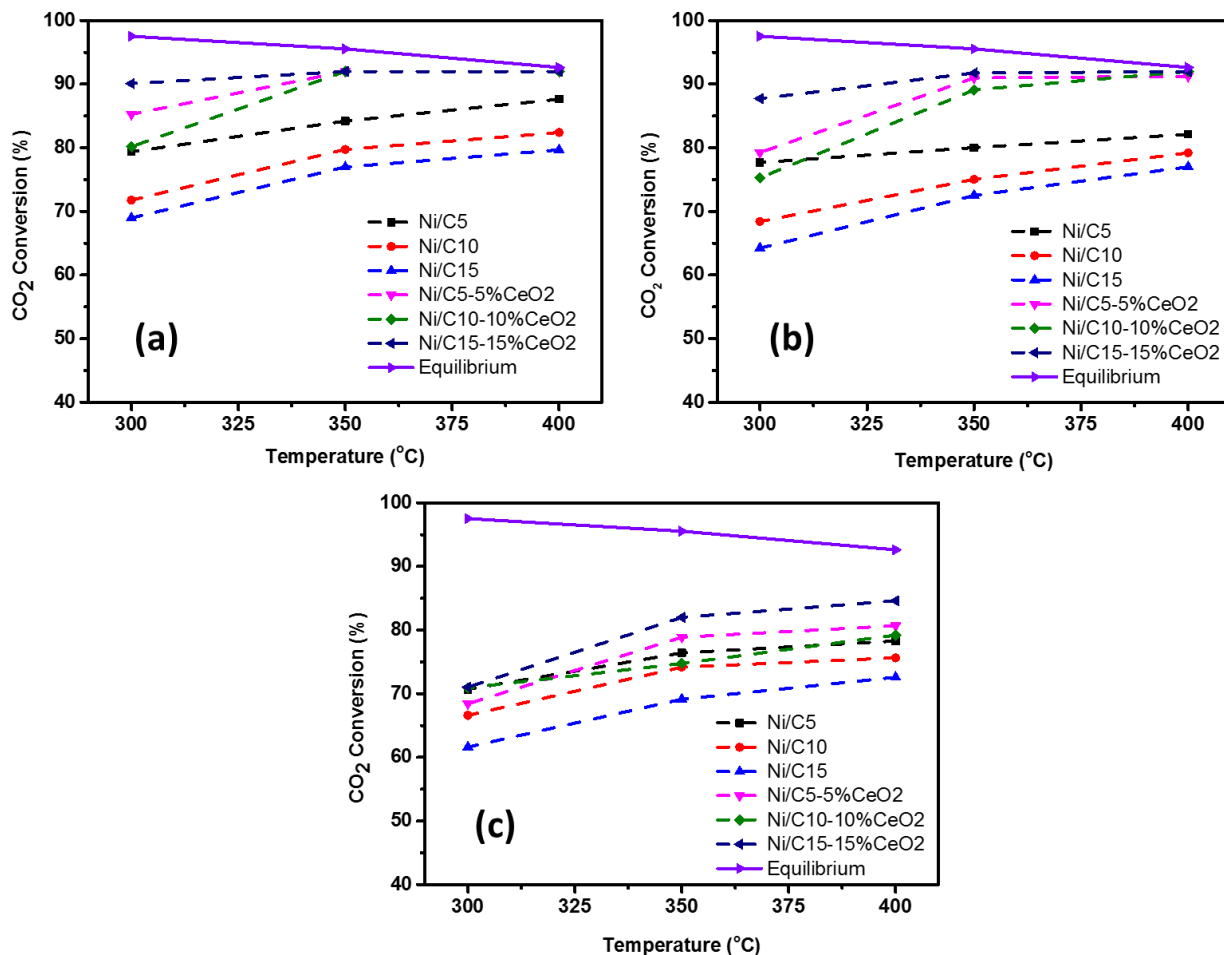


**Figure 2.9** Catalytic performance in CO<sub>2</sub> methanation of the Ni samples supported on the ternary and quaternary system. Reaction conditions: gas mixture with CO<sub>2</sub>:H<sub>2</sub> = 1:4, P = 5 bar, and (a) GHSV = 2000 h<sup>-1</sup>, (b) GHSV = 3000 h<sup>-1</sup> and (c) GHSV = 4000 h<sup>-1</sup>.

Based on the H<sub>2</sub>-TPR characterization of the quaternary mixed oxide supported catalysts, the weaker interaction between the metal and the support promotes an easier reducibility of the active metal (Ni) particularly at a lower temperature with respect to the ternary systems. It was observed that, the  $\beta$ -type peak was shifted to lower temperature (T = 460°C) with respect to that in ternary systems (T=508°C), indicating also that Ni could be reduced better at the in situ reduction temperature used (500°C underflow of pure H<sub>2</sub>) without sintering effects due to higher activation

temperatures. Ceria addition may further promote reducibility and improve CO<sub>2</sub> adsorption and dissociation on the surface of the catalyst [23, 24].

It is worth mentioning that, the results obtained for the ternary and quaternary mixed oxides as a support for Ni-based catalysts revealed that the quaternary mixed oxides show the superior catalytic activity. The better catalytic CO<sub>2</sub> conversion performance is not related to changes in the textural properties (as observed in ternary mixed oxide supported catalysts, **Fig. 2.10 (A)**), but rather to the improved reducibility, metallic dispersion, and CO adsorption property. This could be evidenced, for example, in comparing Ni/C15-15%CeO<sub>2</sub> and Ni/C5 catalysts.

### 2.3.3. Structure and activity relationships

According to the surface area improvement on the Ni/C5 catalyst, the order of reactivity in CO<sub>2</sub> methanation was found to be consistent only with the data on the BET surface area, i.e. higher surface area leads to a higher CO<sub>2</sub> conversion. **Figure 2.10 (A)** shows the correlation between BET specific surface area and catalytic activity of the Ni-based catalysts supported on ternary mixed oxides.

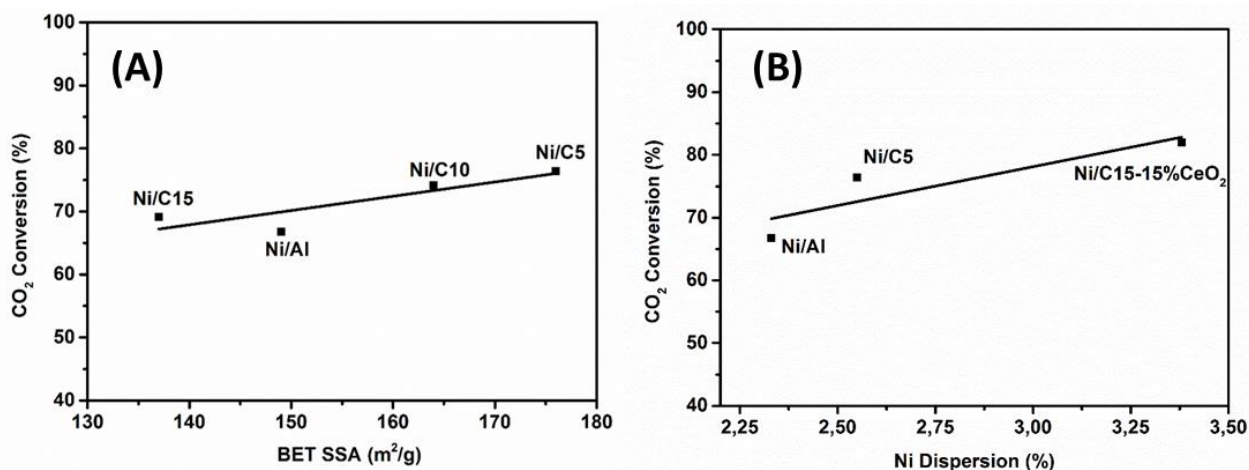


**Figure 2.10** Structure and catalytic performance relationships: **(A)** Activity vs BET specific surface area of the ternary-mixed oxide supported catalysts, **(B)** Activity vs metal dispersion of Ni/Al and catalysts supported on the mixed oxides. Reaction conditions: 350°C, 5 bar and 4000 h<sup>-1</sup>.

The catalytic activity of the Ni/ $\gamma$ -Al<sub>2</sub>O<sub>3</sub> conventional catalyst compared with the most active ternary (Ni/C5) and quaternary (Ni/C15-15%CeO<sub>2</sub>) mixed oxide supported Ni-based catalysts and reported in **Figure 2.10 (B)**. It was observed that, upon increasing the metallic dispersion and catalyst reducibility, the CO<sub>2</sub> conversion to methane increases, especially at lower temperatures (300 and 350°C). Therefore, the role of CeO<sub>2</sub> as a promoter is to increase MSA and thus the Ni dispersion, favoring the presence of  $\beta$ -type NiO species likely due to a specific interaction with the mixed oxide support. The other promoters (TiO<sub>2</sub>, ZrO<sub>2</sub>), have mainly a textural effect (an increase of the BET surface area), which also induces the dispersion of NiO and its reducibility. For example, BET of Ni/C5 is about 15% higher than that of Ni/  $\gamma$ -Al<sub>2</sub>O<sub>3</sub>, and Ni dispersion and specific surface are about 20% and 7.5% higher, respectively.

The best catalysts Ni/C5 and Ni/C15-15%CeO<sub>2</sub> were selected for longer time stability tests. The long-term tests were made for 30 h at 300°C, GHSV of 4000 h<sup>-1</sup> and 5 bar pressure. **Table 2.10** shows the CO<sub>2</sub> conversion every 6 h for both catalysts. It can be noted that the presence of CeO<sub>2</sub> not only improves the activity towards CO<sub>2</sub> methanation but also the stability. The deactivation rate (calculated from the data in **Table 2.10**) passes from 0.42 % CO<sub>2</sub> conversion decrease per hour for the Ni/C5 to 0.08 % CO<sub>2</sub> conversion decrease per hour for the Ni/C15-15%CeO<sub>2</sub>.

**Table 2.10** Long-term tests at 300°C and GHSV of 4000 h<sup>-1</sup> for the best catalysts investigated, Ni/C5 and Ni/C15-15%CeO<sub>2</sub>.

Time (h)	CO <sub>2</sub> conversion (%)	
	Ni/C5	Ni/C15-15%CeO <sub>2</sub>
6	70	71
12	68	70
18	67	70
24	64	69
30	60	69

## 2.4. Conclusion

Two groups of Ni-based catalysts supported on mixed oxides were prepared, characterized and applied for CO<sub>2</sub> methanation. The conventional  $\gamma$ -Al<sub>2</sub>O<sub>3</sub> support was modified using three promoters (CeO<sub>2</sub>, ZrO<sub>2</sub>, and TiO<sub>2</sub>). The structure and activity of newly synthesized catalysts were compared with the Ni-based catalyst supported only in  $\gamma$ -Al<sub>2</sub>O<sub>3</sub>. Different characterization techniques were used to study the physicochemical properties of as-prepared catalysts. The catalytic performance of mixed oxide supported Ni-based catalysts were found to be superior to the Ni/ $\gamma$ -Al<sub>2</sub>O<sub>3</sub> catalyst prepared using the same method. For the ternary mixed oxide supported Ni-based catalysts, improved structural properties were responsible for the better activity. Among the ternary mixed oxide supported catalysts, the Ni/C5 catalyst showed higher CO<sub>2</sub> conversion and selectivity, which might be due to the higher BET area, while the other properties are quite similar for all the ternary mixed oxide supported catalysts.

For the Ni-based catalysts supported on quaternary mixed oxides, both characterizations and activity tests results demonstrate unequivocally that CeO<sub>2</sub> inherently improves the Ni-based catalysts towards CO<sub>2</sub> methanation. When compared to the conventional Ni/ $\gamma$ -Al<sub>2</sub>O<sub>3</sub> catalyst and the ternary mixed oxides supported Ni-based catalysts, the Ni/C15-15%CeO<sub>2</sub> catalyst show higher activity i.e. 90% of CO<sub>2</sub> conversion to CH<sub>4</sub> in the reaction conditions (350°C, GHSV of 4000 h<sup>-1</sup> and 5 bar) used. Therefore, the role of CeO<sub>2</sub> as a promoter is to increase Ni dispersion and the increase the fraction of  $\beta$ -type NiO species which are reduced at lower temperatures compared to the Ni-based catalysts supported on the ternary mixed oxides. Other promoters (TiO<sub>2</sub>, ZrO<sub>2</sub>) have mainly a textural effect, i.e. to increase the BET surface area. Furthermore, the CeO<sub>2</sub> in the amount of 15 wt%, promotes also the stability decreasing the deactivation rate of about one order of magnitude with respect to the best ternary mixed oxide supported (Ni/C5) catalyst.

The study under this chapter thus showed that the use  $\gamma$ -Al<sub>2</sub>O<sub>3</sub> support promoted with different oxides at optimal composition allows enhancing the activity of catalysts towards CO<sub>2</sub> methanation. Therefore, this type of catalysts appears to be more active and stable for long-term tests, thus being likely applicable in moderate reaction conditions for effective CO<sub>2</sub> methanation under the P2G process.

## 2.5. References

- [1] X. Duan, G. Qian, X. Zhou, Z. Sui, D. Chen, W. Yuan, *Appl Catal B Environ.*, 101 (2011) 189-196.
- [2] S. Hwang, J. Lee, U.G. Hong, J.C. Jung, D.J. Koh, H. Lim, C. Byun, I. K. Song, *J Ind Eng Chem*, 18 (2012) 243-248.
- [3] J. Zhang, Z. Xin, X. Meng, M. Tao, *Fuel*, 109 (2013) 693-701.
- [4] M. Cai, J. Wen, W. Chu, X. Cheng, Z. Li, *Journal of Natural Gas Chemistry*, 20 (2011) 318-324.
- [5] J. Gao, Q. Liu, F. Gu, B. Liu, Z. Zhong, F. Su, *RSC Adv.*, 5 (2015) 22759-22776.
- [6] P.A. Ussa Aldana, F. Ocampo, K. Kolb, B. Louis, F. Thibault-Starzyk, M. Daturi, P. Bazin, S. Thomas, A.C. Roger, *Catalysis Today*, 215 (2013) 201-207.
- [7] F. Ocampo, B. Louis, L. Kiwi-Minsker, A.C. Roger, *Applied Catalysis A: general*, 392 (2011) 36-44.
- [8] Q. Pan, J. Peng, T. Sun, D. Gao, She. Wang, Shu. Wang, *Fuel Processing Technology*, 123 (2014) 166-171.
- [9] Z. Han, D. Yunyun, F. Weiping, L. Yixin, *Chinese Journal of Catalysis*, 34 (2013) 330-335.
- [10] V.M. Shinde, G. Madras, *AIChE J.*, 60 (2014) 1027-1035.
- [11] S. Tada, T. Shimizu, H. Kameyama, T. Haneda, R. Kikuchi, *International Journal of hydrogen energy*, 37 (2012) 5527-5531.
- [12] H. Liu, X. Zou, X. Wang, X. Lu, W. Ding, *Journal of Natural Gas Chemistry*, 21 (2012) 703-707.
- [13] Y. Zeng, H. Ma, H. Zhang, W. Ying, D. Fang, *Fuel*, 137 (2014) 155-163.
- [14] J. Ashok, M.L. Ang, S. Kawi, *Catalysis Today*, 281, Part 2 (2017) 304-311.
- [15] F. Ocampo, B. Louis, A.-C. Roger, *Applied Catalysis A: General*, 369 (2009) 90-96.
- [16] A. Zhao, W. Ying, H. Zhang, M. Hongfang, D. Fang, *Journal of Natural Gas Chemistry*, 21 (2012) 170-177.
- [17] J. Zhang, H. Xu, X. Jin, Q. Ge, W. Li, *Applied Catalysis A: General*, 290 (2005) 87-96.

- [18] S. Abate, K. Barbera, E. Giglio, F. Deorsola, S. Bensaid, S. Perathoner, R. Pirone, G. Centi, *Industrial & Engineering Chemistry Research*, 55 (2016) 8299-8308.
- [19] Y.H. Hu, E. Ruckenstein, *Journal of Catalysis*, 163 (1996) 306-311.
- [20] A. Taylor, D. Hayward, *Surface science*, 346 (1996) 222-236.
- [21] T.D. Gould, A.M. Lubers, B.T. Neltner, J.V. Carrier, A.W. Weimer, J.L. Falconer, J.W. Medlin, *Journal of Catalysis*, 303 (2013) 9-15.
- [22] J. Zieliński, *Journal of molecular catalysis*, 79 (1993) 187-198.
- [23] S. Park, J.M. Vohs, R.J. Gorte, *Nature*, 404 (2000) 265-267.
- [24] J.M. Rynkowski, T. Paryjczak, A. Lewicki, M.I. Szyrkowska, T.P. Maniecki, W.K. Józwiak, *Reaction Kinetics and Catalysis Letters*, 71 (2000) 55-64.

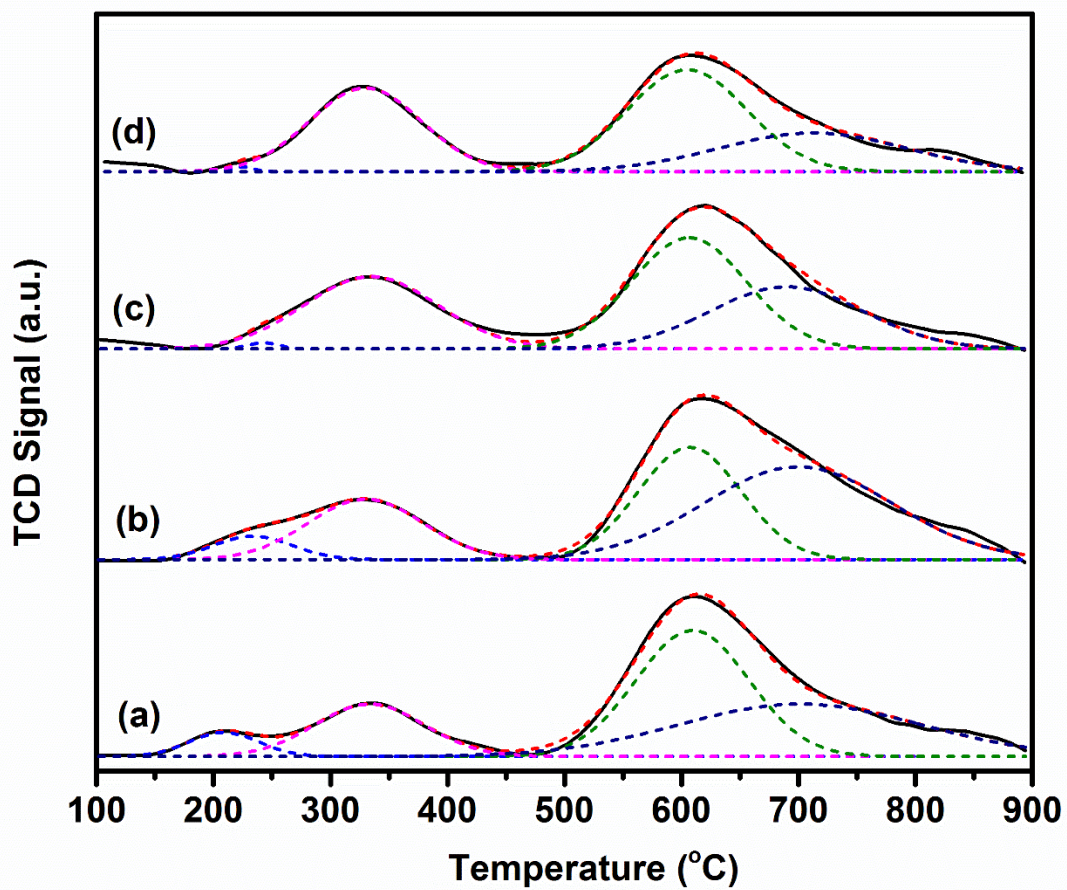


**Figure 1.** CO-TPD profiles of (a) 20%Ni/ $\gamma$ -Al<sub>2</sub>O<sub>3</sub>, (b) 20%Ni/C5-5%CeO<sub>2</sub>, (c) 20%Ni/C10-10%CeO<sub>2</sub> and (d) 20%Ni/C15-15%CeO<sub>2</sub>.



# CHAPTER 3

### 3. Synthesis, characterization and activity pattern of hydrotalcite derived Ni-Fe catalysts for CO<sub>2</sub> methanation

#### 3.1. Introduction

The formation of nickel aluminate spinel is among the origins that reduce the efficiency of Ni-based catalysts [1]. Therefore, alternative solutions are necessary to overcome the problems of conventional Ni/Al<sub>2</sub>O<sub>3</sub> catalysts for CO<sub>2</sub> methanation.

Among the possible solutions, alloying of nickel with other metals can improve the catalytic performance in terms of activity and stability [2]. One suitable modifier is iron because Fe can interact with Ni by the formation of Ni-Fe alloys and Fe species hold distinct redox properties potentially improving reducibility [3]. Ni-Fe bimetallic catalysts supported by different metal oxide materials synthesized by impregnation have been widely studied and improved the catalytic performance of conventional Ni/ $\gamma$ -Al<sub>2</sub>O<sub>3</sub> catalysts for both CO and CO<sub>2</sub> methanation. Among the investigations, Andersson et al. (2006) presented DFT calculations and synthesis/testing of Ni-Fe bimetallic catalysts supported on MgAl<sub>2</sub>O<sub>4</sub> spinel towards CO methanation [4, 5]. Hwang et al. studied mesoporous nickel (35 wt%)-metal (M = Fe, Zr, Ni, Y, and Mg) (5 wt%)-alumina xerogel catalysts in CO<sub>2</sub> methanation varying the second metal. The yield of CH<sub>4</sub> decreased in the order 35Ni5Fe > 35Ni5Zr > 35Ni5Ni > 35Ni5Y > 35Ni5Mg. The most active and selective mesoporous catalyst was 35Ni5Fe; this catalyst possesses a weak metal support interaction that is closely related to the CO dissociation energy [6]. Additional investigations on Ni-Fe bimetallic catalysts such as doping of a third active metal were also performed to synthesize Ni-Fe-Ru-Al<sub>2</sub>O<sub>3</sub> xerogel using a single step sol-gel method. Both CO<sub>2</sub> conversion and CH<sub>4</sub> yield showed volcano-shaped trends with respect to the ruthenium content. This indicates that an optimal ruthenium content was required for the maximum production of methane from carbon dioxide and hydrogen [7]. In addition, Kang et al. (2011) also synthesized Ni<sub>x</sub>-Fe<sub>1-x</sub>/Al<sub>2</sub>O<sub>3</sub> and evaluated the effect of the Fe content on co-methanation of CO and CO<sub>2</sub> [8]. Recently, Pandey and Deo (2014, 2016) also analyzed the effect of supports for Ni-Fe bimetallic catalysts. The relative enhancement in yield for the most active catalyst for each series was support dependent, and the maximum rise was achieved when Al<sub>2</sub>O<sub>3</sub> used as support. It appeared that the enhancement in yield was due to the

formation of a suitable Ni-Fe alloy and the maximum increase for Al<sub>2</sub>O<sub>3</sub> supported catalysts was due to the ability of the support to adsorb CO<sub>2</sub> [9, 10].

However, synthesis of Ni-Fe bimetallic catalysts using impregnation is hampered by a considerable inhomogeneity in the composition of the supported metal nanoparticles. Alloy particles of different structures, such as nickel-rich face-centered cubic (fcc) alloy, iron-rich body-centered cubic (bcc) alloy, or a tetragonal FeNi phase form. In addition, particle sizes are usually large (>20 nm) [11]. Since the catalytic performance of bimetallic particles is greatly influenced by the structure, surface composition, and particle size, the preparation of uniform and well-dispersed alloy particles with an optimum composition is of great importance for catalyst development.

In view of the above-mentioned challenges, it is indispensable to improve the design of tailored highly active and selective bimetallic catalysts for CO<sub>2</sub> methanation. Recently, hydrotalcite-like catalysts containing transition metals as active component found considerable attention as precursors of various catalysts. They offer access to well dispersed and homogeneous metallic particles after a reduction treatment with hydrogen [12-14]. Furthermore, this synthesis strategy provides materials with interesting properties after calcination covering high BET surface area, tailored acid/base properties, homogeneous mixtures of oxides with very small crystal size and thermal stability. Upon reduction, these materials form small and thermally stable metal crystallites and possess a “Memory effect”, which allows the reconstruction, under mild conditions, of the original hydrotalcite structure when contacting the product of the thermal treatment with aqueous solutions containing various anions [15-17].

In this chapter, hydrotalcite derived Ni-Fe bimetallic catalysts for CO<sub>2</sub> methanation with relatively low active metal content are studied. The catalysts reported in this chapter comprehend Ni-Fe alloy nanoparticles supported on MgAlO<sub>x</sub> obtained by calcination and reduction of Ni-Mg-Fe-Al hydrotalcite precursors.

### 3.2. Scope of the chapter

The main objective of the work under this chapter is to combine the advantages of hydrotalcite-like precursors and the synergistic effect of Fe-Ni alloys. The synthesis of hydrotalcite-like precursors results in a support that offers stabilizing properties by an oxide, spinel-like matrix with a tunable amount of Lewis basic sites for CO<sub>2</sub> activation. There exist a lot of hydrotalcite-like materials with different metals, but not yet for Fe-Ni-(Mg, Al)O<sub>x</sub> and in particular applied in methanation. Iron affects the basicity of the support as well as the methanation activity, therefore the optimal amount of iron is determinant in order to obtain a highly active and selective catalyst. Therefore, this chapter explains the synthesis, characterization, effect of Fe: Ni ratio and the basic support towards CO<sub>2</sub> methanation.

### 3.3. Experimental

#### 3.3.1. Synthesis of catalysts

Ni-Mg-Fe-Al HTs were prepared by co-precipitation of the respective metal nitrates [11]. An aqueous solution of Ni(NO<sub>3</sub>)<sub>2</sub>·6H<sub>2</sub>O, Mg(NO<sub>3</sub>)<sub>2</sub>·6H<sub>2</sub>O, Fe(NO<sub>3</sub>)<sub>3</sub>·9H<sub>2</sub>O and Al(NO<sub>3</sub>)<sub>3</sub>·9H<sub>2</sub>O was added slowly to an aqueous solution of Na<sub>2</sub>CO<sub>3</sub> (1 M) under stirring at RT and constant pH 10±0.5. pH of the solution was adjusted with an aqueous solution of NaOH (2 M). The resulting suspension was aged at RT for 24 h. The precipitate was filtered, washed several times with deionized water, and dried at 100°C for 16 h. The dried precursor was ground into a fine powder and then calcined at 450°C for 6 h in a static air atmosphere. Ni-Mg-Al, different Fe/Ni ratios (i.e. 0.1, 0.5, 1 and 1.5) and Fe-Mg-Al catalysts were prepared in order to study the effect Fe/Ni composition on CO<sub>2</sub> methanation. The Ni metal content was kept constant (i.e. 12 wt.-%) and the Fe content varied from 1.2 wt.-% - 18 wt.-% depending on the desired Fe to Ni ratio.

#### 3.3.2. Characterization of as-prepared catalysts

Specific surface area (Multipoint BET) and total pore volume of the calcined catalysts were determined by N<sub>2</sub> physisorption at -195.79°C using Quadrasorb SI Automated Surface Area and

Pore Size Analyzer from Quantachrome Instruments after degassing the sample at 200°C for 20 h at a residual pressure of 0.352 mbar.

XRD measurements were performed for both the dried hydrotalcite precursors and calcined catalysts using a D5000 Siemens XRD diffractometer with a Cu K $\alpha$  X-ray tube ( $\lambda = 1.54056 \text{ \AA}$ ). The tube voltage and current were 45 kV and 40 mA, respectively. Diffraction patterns were collected in the 3-90° 2 $\theta$  range.

The chemical composition of the calcined catalysts was analyzed by inductively coupled plasma-optical emission spectroscopy (ICP-OES; Spectro Analytical Instruments). Prior to the analysis of metals (Ni, Mg, Fe, Al), 30 mg of each sample was dissolved in an acidic solution composed of 8 mL of HF, 2 mL of H<sub>2</sub>SO<sub>4</sub> and 40 mL of DI water.

Thermogravimetric and differential scanning calorimetry (TGA-DSC) analyses of the dried hydrotalcite-like precursors were conducted in order to study the thermal decomposition properties in air using a Netzsch STA 409 apparatus. Samples were heated from 30 to 900°C with a heating rate of 5°C/min in air.

Temperature programmed reduction (H<sub>2</sub>-TPR) properties of the calcined catalysts were investigated using ChemBET Pulsar TPR/TPD/TPO (Quantachrome Instruments). Prior to the measurement, about 130 mg of sample was pretreated at 200°C for 1 h in He gas stream. The H<sub>2</sub>-TPR profile was then recorded from room temperature to 1000°C with a heating ramp of 10°C/min under a flow of 5% H<sub>2</sub> in Ar with a flow rate of 100 mL/min.

Basic sites of the calcined catalysts were determined using irreversible adsorption of organic acids. Acrylic acid (pK<sub>a</sub> = 4.3) and phenol (pK<sub>a</sub> = 9.9) were used as probe molecules to determine the content of total basic sites and strong basic sites, respectively [18, 19]. The weak basic sites were then quantified by subtracting the concentration of strong basic sites from the content of total basic sites. The initial and final concentrations of the acids i.e. before and after adsorption experiment were measured spectrophotometrically (StellarNet Inc.) at wavelength 245 nm and 242 nm for acrylic acid and phenol, respectively.

STEM images and EDS analyses of selected catalysts after reduction were performed using TEM (JEOL JEM-2200FS) equipped with a slow scan CCD camera Gatan for high resolution (HR) TEM, a scanning transmission electron mode (STEM) and an energy dispersive X-ray (EDX) spectrometer.

Chemical states of selected Ni-Fe (Mg, Al) $O_x$  catalysts (reduced at 600°C) were determined by X-ray photoelectron spectroscopy. The XPS signals were collected using a PHI VersaProbe II. Ni2p<sub>3/2</sub> and Fe2p<sub>3/2</sub> binding energies were recorded using AlK $\alpha$  (1486.6 eV) as the excitation source and a pass energy of 23.5 eV. The X-ray setting was 100 $\mu$ 100W20kV\_HP. A Shirley background was applied and all the XPS peaks were fitted with asymmetric function by using the Multipeak software. The binding energies obtained in the XPS analysis were calibrated using C1s as a reference with binding energy equal to 284.8 eV.

### 3.3.3. Catalytic CO<sub>2</sub> methanation test

Methanation of CO<sub>2</sub> was carried out in continuous flow fixed-bed reactor setup (**Figure 3.1**) equipped with quartz tubular reactor (ID 8 mm and porous glass frit). Each catalyst (about 370 mg) was reduced in situ with a stream of pure H<sub>2</sub> (50 mL/min) at 500°C for 1 h or at 600°C for 2 h. The reaction mixture (CO<sub>2</sub> and H<sub>2</sub>) was then continuously fed into the reactor with N<sub>2</sub> as an internal standard to account for volume contraction. The feed composition was fixed at CO<sub>2</sub>: H<sub>2</sub>: N<sub>2</sub> = 70:18:12 (Vol %) with H<sub>2</sub>: the CO<sub>2</sub> ratio of 4:1. The total feed was maintained with respect to the catalytic bed height (0.6 cm) and gas hourly space velocity of 12020 h<sup>-1</sup>. The catalytic reaction was then performed at 335°C. Formed water was trapped while leftover reaction products were analyzed using on-line gas chromatograph Bruker (Scion 456) integrated with *compassCDS* networked software and equipped with three channels: front TCD for H<sub>2</sub>, middle TCD for permanent gases (CO, CO<sub>2</sub>, CH<sub>4</sub>, and N<sub>2</sub>) and rear FID for hydrocarbons.

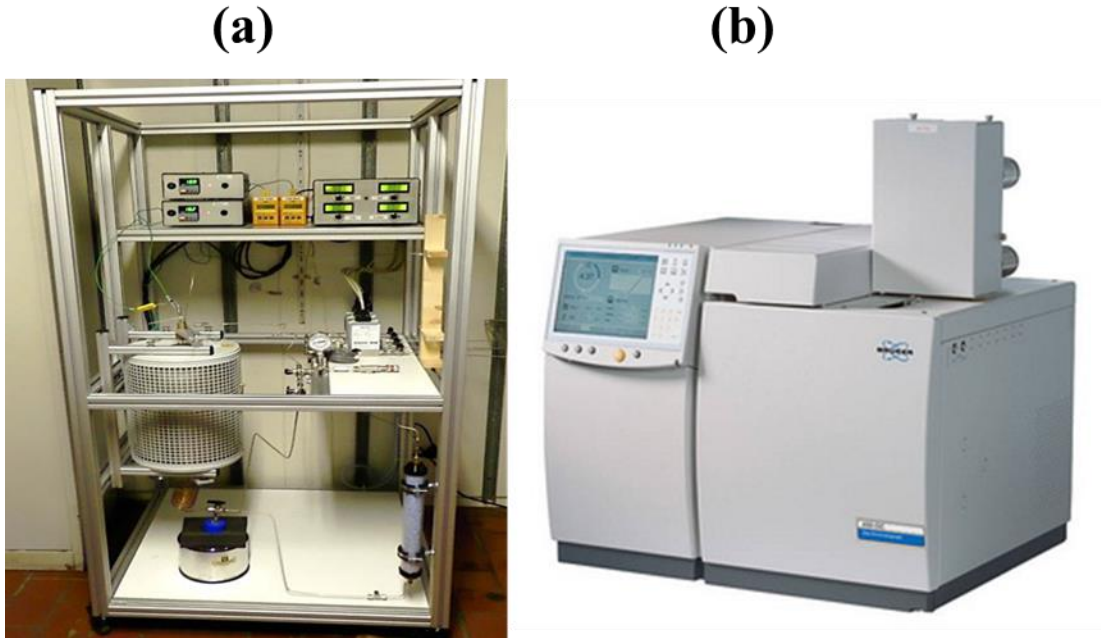


**Figure 3.1** (a) assembled and validated set-up and (b) on-line gas chromatograph used for the CO<sub>2</sub> methanation tests.

The rate of carbon dioxide conversion was calculated according to [equation 3.1](#), by use of the molar flow rate of CO<sub>2</sub> ( $F$ ), the conversion of CO<sub>2</sub> ( $X_{CO_2}$ ) and the total molar amount of iron and nickel ( $n_{Fe+Ni}$ ).

$$r_{CO_2} = \frac{F \cdot X_{CO_2}}{n_{Fe+Ni}} \quad (3.1)$$

### 3.4. Results and Discussion

#### 3.4.1. Characterization results

Detailed physicochemical properties of Ni-Fe/(Mg, Al)O<sub>x</sub> catalysts are summarized in [Table 3.1](#). Ni, Fe, Mg, and Al contents in the Ni-Fe/(Mg, Al)O<sub>x</sub> catalysts determined by ICP-OES analyses were in good agreement with the real values, indicating to the formation of only hydrotalcite-like materials with the desired Fe to Ni ratio. BET specific surface area and total pore volume calculated from the N<sub>2</sub> adsorption branch are summarized in [Table 3.1](#). The obtained BET specific surface area ranges from 22-195 m<sup>2</sup>/g, an immense difference was observed for the as-prepared

material set. This might be caused by the Fe loading, i.e. the substitution of  $\text{Al}^{3+}$  by  $\text{Fe}^{3+}$  cation in the brucite-like layers results in a decrease of BET surface area and total pore volume, pointing to a certain extent of pore blockage. The obtained results indicate that physical properties Ni-Fe/(Mg, Al) $\text{O}_x$  catalysts were strongly affected by the amount of Fe introduced.

**Table 3.1** Physicochemical properties of calcined HTs: BET surface area, total pore volume, and elemental compositions.

Catalyst	Surface area <sup>a</sup> ( $\text{m}^2/\text{g}$ )	TP Volume <sup>b</sup> ( $\text{mL}/\text{g}$ )	Atomic percentage <sup>c</sup> (%)			
			Measured composition/ <b>Nominal value</b>			
			Ni	Mg	Al	Fe
Ni/(Mg, Al) $\text{O}_x$	195	0.32	11.5/ <b>12</b>	66.9/ <b>63</b>	21.5/ <b>25</b>	0.0/ <b>0.0</b>
Ni-Fe/(Mg, Al) $\text{O}_x$ (Fe/Ni=0.1)	136	0.25	12.2/ <b>12</b>	67.3/ <b>63</b>	19.4/ <b>23.8</b>	1.1/ <b>1.2</b>
Ni-Fe/(Mg, Al) $\text{O}_x$ (Fe/Ni=0.5)	104	0.30	14.1/ <b>12</b>	66.5/ <b>63</b>	12.8/ <b>19</b>	6.5/ <b>6</b>
Ni-Fe/(Mg, Al) $\text{O}_x$ (Fe/Ni=1)	42	0.16	13.6/ <b>12</b>	63.7/ <b>63</b>	11.1/ <b>13</b>	11.5/ <b>12</b>
Ni-Fe/(Mg, Al) $\text{O}_x$ (Fe/Ni=1.5)	23	0.15	13.2/ <b>12</b>	61.3/ <b>63</b>	9.2/ <b>9</b>	16.3/ <b>18</b>
Fe/(Mg, Al) $\text{O}_x$	22	0.10	0.0/ <b>0.0</b>	76.2/ <b>75</b>	14.0/ <b>13</b>	9.7/ <b>12</b>

<sup>a, b</sup> Calculated by the Multipoint-BET equation from  $\text{N}_2$  adsorption branch.

<sup>c</sup> Measured by ICP-OES analysis.

**Figure 3.2** presents the diffraction patterns of the dried samples. The patterns obtained for the materials before calcination show the reflections typical for hydrotalcite. All samples showed reflections at  $2\theta = 11.2^\circ, 22.8^\circ, 34.9^\circ$  which correspond to  $d(003)$ ,  $d(006)$  and  $d(009)$  basal planes in HTs. The nonbasal planes  $d(015)$ ,  $d(018)$ ,  $d(110)$  and  $d(113)$  cause reflexes at  $2\theta = 38.9^\circ, 46.4^\circ, 34.9^\circ, 60.4^\circ, 61.5^\circ$ , respectively. Irrespective of Fe content, no additional phases were observed, pointing to successful incorporation of iron cations into the brucite/like layers. The intensity of reflections arising from hydrotalcite structure was decreasing with increasing iron content, pointing to decrease in crystallinity of hydrotalcite/like materials with increasing Fe loading.



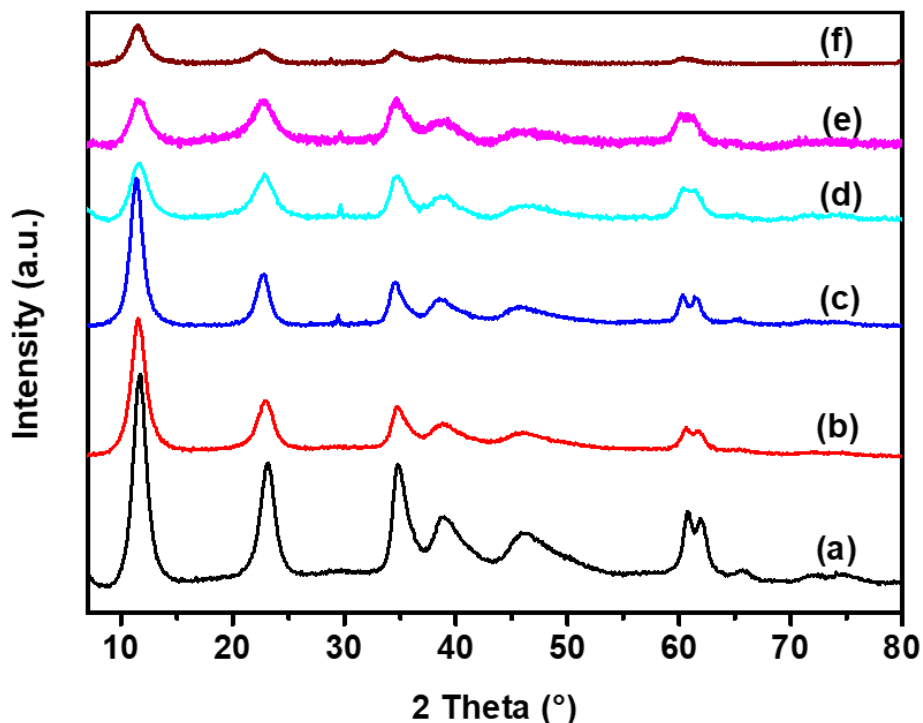


**Figure 3.2** XRD patterns of the dried HT precursors: (a) Ni/(Mg, Al)O<sub>x</sub>, (b) Ni-Fe/(Mg, Al)O<sub>x</sub> (Fe/Ni=0.1), (c) Ni-Fe/(Mg, Al)O<sub>x</sub> (Fe/Ni=0.5), (d) Ni-Fe/(Mg, Al)O<sub>x</sub> (Fe/Ni=1), (e) Ni-Fe/(Mg, Al)O<sub>x</sub> (Fe/Ni=1.5) and (f) Fe/(Mg, Al)O<sub>x</sub>.

The *d*-spacing values for all dried precursors were close to the nominal values of pure hydrotalcites (**Table 3.2**), indicating no structural changes with the incorporation of Ni and Fe [15]. The values for *d*(003) were found to be between 0.7742-0.7908 nm, which is well in line with 0.784 nm for the Mg<sub>3</sub>Al-CO<sub>3</sub> hydrotalcite. Comparing *d*(110) values for the precursors with relatively low Fe content, the *d*(110) value was 0.1529 nm which is slightly smaller than 0.1540 nm for the Mg<sub>3</sub>Al-CO<sub>3</sub> hydrotalcite. This might be due to the substitution of Ni<sup>2+</sup> for a part of Mg<sup>2+</sup> sites in the hydrotalcite structure, considering the ionic radius of Ni<sup>2+</sup> being smaller than that of Mg<sup>2+</sup> (0.069 nm for Ni<sup>2+</sup> and 0.072 nm for Mg<sup>2+</sup> in octahedral coordination) [20].

**Table 3.2** Summary of XRD analyses of the dried precursors.

Catalyst	<i>d</i> spacing <sup>a</sup> (nm)				Lattice parameters <sup>b</sup> (nm)	
	<i>d</i> <sub>(003)</sub>	<i>d</i> <sub>(006)</sub>	<i>d</i> <sub>(009)</sub>	<i>d</i> <sub>(110)</sub>	<i>a</i>	<i>c</i>
Ni/(Mg, Al)O <sub>x</sub>	0.7880	0.3901	0.2595	0.1531	0.3062	2.3465
Ni-Fe/(Mg, Al)O <sub>x</sub> (Fe/Ni=0.1)	0.7742	0.3901	0.2567	0.1529	0.3057	2.3245
Ni-Fe/(Mg, Al)O <sub>x</sub> (Fe/Ni=0.5)	0.7908	0.3914	0.2596	0.1535	0.3069	2.3525
Ni-Fe/(Mg, Al)O <sub>x</sub> (Fe/Ni=1)	0.7894	0.3921	0.2606	0.1543	0.3087	2.3553
Ni-Fe/(Mg, Al)O <sub>x</sub> (Fe/Ni=1.5)	0.7866	0.3917	0.2633	0.1545	0.3090	2.3600
Fe/(Mg, Al)O <sub>x</sub>	0.7810	0.3928	0.2601	0.1541	0.3082	2.3467

<sup>a</sup> Calculated according to Bragg's law.

<sup>b</sup> Calculated using the formulas;  $a = 2 d_{(110)}$  and  $c = d_{(003)} + 2 d_{(006)} + 3d_{(009)}$  [21].

The XRD pattern of calcined catalysts, shown in **Figure 3.3**, exhibited two main reflections at  $2\theta = 45^\circ$  and  $63^\circ$ , which may be assigned to the periclase-like structure of Mg(Ni, Al)O mixed oxides. The reflexes of the hydrotalcite-like precursor turned into a pattern similar to MgO periclase and MgAl<sub>2</sub>O<sub>4</sub> spinel. Li et al. [11] observed the same transformation into periclase and spinel phases. The complex mixture of elements was also facilitated to the formation of different periclases (e.g. MgO, Mg (Ni, Al)O) and spinels (e.g. MgAl<sub>2</sub>O<sub>4</sub>, MgFeAlO<sub>4</sub>, NiFe<sub>2</sub>O<sub>4</sub>, and Fe<sub>3</sub>O<sub>4</sub>). A distinct assignment from XRD data is quite difficult due to very similar diffraction patterns of these compounds.

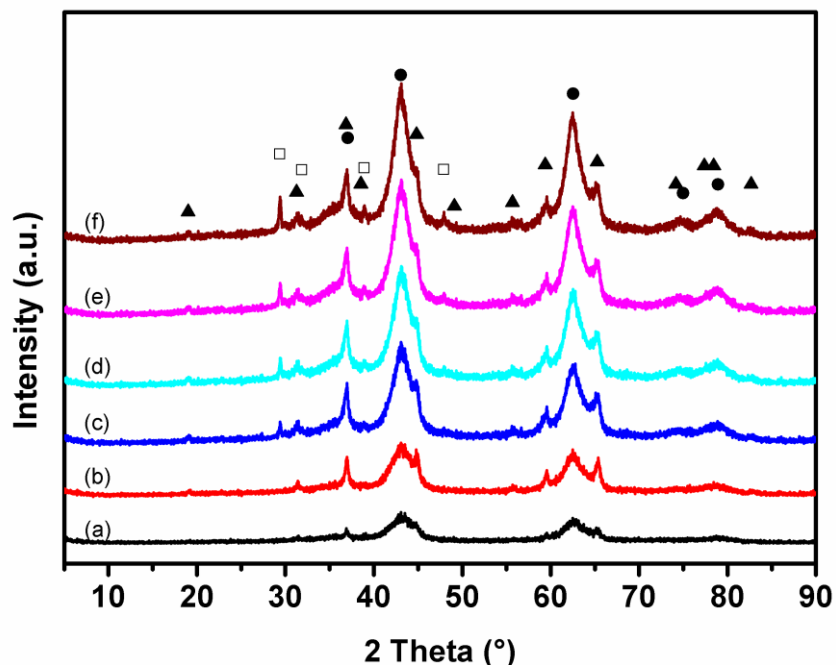


**Figure 3.3** XRD patterns of the catalysts after calcination at 450°C: (a) Ni/(Mg, Al)O<sub>x</sub>, (b) Ni-Fe/(Mg, Al)O<sub>x</sub> (Fe/Ni=0.1), (c) Ni-Fe/(Mg, Al)O<sub>x</sub> (Fe/Ni=0.5), (d) Ni-Fe/(Mg, Al)O<sub>x</sub> (Fe/Ni=1), (e) Ni-Fe/(Mg, Al)O<sub>x</sub> (Fe/Ni=1.5) and (f) Fe/(Mg, Al)O<sub>x</sub>. Crystalline phases: MgO periclase (●) JCPDS 00-043-1022 NaNO<sub>3</sub> (□) JCPDS 00-036-1474, and spinel (▲).

H<sub>2</sub>-TPR profiles of the calcined catalysts are presented in **Figure 3.4**. In general, all catalysts showed asymmetric reduction peak at high temperature arising from the reduction of strongly interacted nickel oxide. For all the nickel and iron-containing samples, the reduction peak temperatures ranged from 475 to 981°C, suggesting various types of interaction between Ni-Fe species and the Mg(Al)O<sub>x</sub> support. According to literature, pure NiO phase is reduced at temperatures 220-420°C [22-25]. Thus, it can be stated that the reduction peaks centered from 475-544°C were associated with the reduction of bulk NiO and/or Fe<sub>2</sub>O<sub>3</sub> particles weakly interacting with the support. This strong interaction among Ni/(Mg, Al)O<sub>x</sub> ions in the catalyst matrix hindering the reduction of NiO species in catalysts at a lower temperature. This difficulty of Ni reduction enhances the resistance to catalyst sintering and consequently facilitates retaining a high dispersion

and finite size of Ni<sup>0</sup>. Moreover, complete reduction of NiO species at lower temperature results in the formation of less stable Ni phases under reaction conditions [26, 27].

TPR profile of Fe/(Mg, Al)O<sub>x</sub> indicates an incomplete reduction of iron in the hydrotalcite-like structure [28] with two reduction peaks at 507°C and 952°C which is characteristic of the reduction of Fe<sup>3+</sup> to Fe<sup>2+</sup> and Fe<sup>2+</sup> to α-Fe, respectively [29]. In addition, it was observed that the higher temperature reduction peaks for catalysts with Fe/Ni ratios of 0.5-1.5 (relatively higher Fe content) shifted to lower temperatures and emphasized complete reduction till 1000°C. The lower temperature peaks of Ni-Fe/(Mg, Al)O<sub>x</sub> (Fe/Ni=0.5 to 1.5) occurred at higher temperature (i.e. 490-544°C) compared to Ni/(Mg, Al)O<sub>x</sub> and Ni-Fe/(Mg, Al)O<sub>x</sub> (Fe/Ni=0.1) catalysts i.e. 475°C, indicating the presence of stronger interactions among the different components as the content of Fe increases.

In the high-temperature reduction region of Ni-Fe/(Mg, Al)O<sub>x</sub> (Fe/Ni=1), a small peak at 660°C was observed and its intensity increased with increasing the Fe/Ni ratio to 1.5. According to literature, this peak could be assigned to the reduction of NiFe<sub>2</sub>O<sub>4</sub> spinel (formation of NiFe<sub>2</sub>O<sub>4</sub> was confirmed by XRD analysis). The reduction peak at 754°C and 798°C for Ni-Fe/(Mg, Al)O<sub>x</sub> with Fe/Ni=1 and 1.5 ratios, respectively, were caused by co-reduction of surface Fe<sup>2+</sup> and bulk Fe<sup>3+</sup> to Fe<sup>0</sup> as well as Ni<sup>2+</sup> to Ni<sup>0</sup> [30].

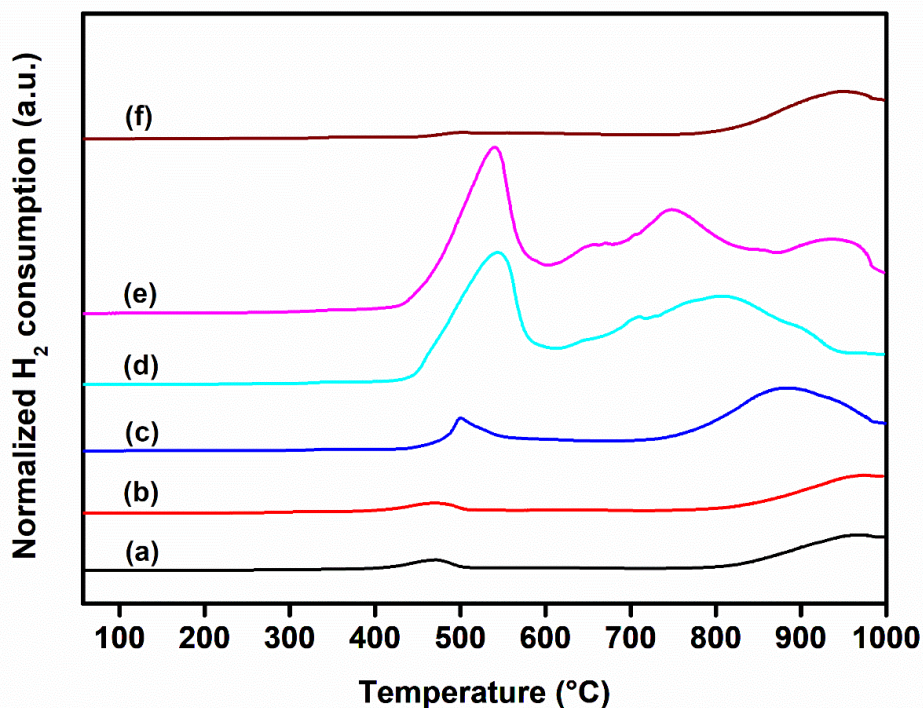


**Figure 3.4** H<sub>2</sub>-TPR profiles of the catalysts after calcination at 450°C: (a) Ni/(Mg, Al)O<sub>x</sub>, (b) Ni-Fe/(Mg, Al)O<sub>x</sub> (Fe/Ni = 0.1), (c) Ni-Fe/(Mg, Al)O<sub>x</sub> (Fe/Ni = 0.5), (d) Ni-Fe/(Mg, Al)O<sub>x</sub> (Fe/Ni = 1), (e) Ni-Fe/(Mg, Al)O<sub>x</sub> (Fe/Ni = 1.5) and (f) Fe/(Mg, Al)O<sub>x</sub>.

The H<sub>2</sub> consumption in the whole temperature range was found to be increased (**Table 3.3**) for all bimetallic catalysts compared to Ni/(Mg, Al)O<sub>x</sub> and Fe/(Mg, Al)O<sub>x</sub>; this can be due the co-reduction of Fe species with Ni due to the formation of Ni-Fe alloy nanoparticles and facilitated reduction of Ni by the addition of Fe. This phenomenon was in agreement with previous literature reports which stated that the addition of iron weakened the interaction between nickel and the support, changed the microchemical environment of nickel and iron species on the surface of the catalyst, and thus increased the amount of reduced species [5].

**Table 3.3** Quantitative H<sub>2</sub>-TPR analyses for the calcined catalysts.

Catalyst	Total Amount of H <sub>2</sub> consumed <sup>a</sup> (mmol/g <sub>cat</sub> )	Peak Temperature (°C)			
		I	II	III	IV
Ni/(Mg, Al)O <sub>x</sub>	2.2	475	971	-	-
Ni-Fe/(Mg, Al)O <sub>x</sub> (Fe/Ni = 0.1)	2.4	475	981	-	-
Ni-Fe/(Mg, Al)O <sub>x</sub> (Fe/Ni = 0.5)	14.0	490	874	-	-
Ni-Fe/(Mg, Al)O <sub>x</sub> (Fe/Ni = 1.0)	13.6	535	705	798	910
Ni-Fe/(Mg, Al)O <sub>x</sub> (Fe/Ni = 1.5)	16.0	544	650	754	943
Fe/(Mg, Al)O <sub>x</sub>	3.3	507	952	-	-

<sup>a</sup> Calculated from the H<sub>2</sub>-TPR profiles over the whole temperature range.

As total basicity of calcined hydrotalcite-derived materials is influenced by the composition of brucite-like layers, irreversible acid adsorption method was used to quantitatively determine the amount of total and strong basic sites of the calcined samples. All catalysts prepared in this study possessed a total concentration of basic sites in the range of 3.00-6.28 mmol/g. Furthermore, it is known that the basicity of synthetic hydrotalcites depends on the Mg/Al ratio [31, 32]. The content of iron (Fe<sup>3+</sup>) and nickel (Ni<sup>2+</sup>) has to be also considered as well in order to study the effect of all the cations on the total amount of basic sites [15]. **Table 3.4** summarizes the effect of cations ratio on the contribution to the different basic sites. Higher concentrations of total basic sites were obtained with (Ni+Mg)/(Fe+Al) ratios close to 3 (i.e. 2.93 and 3.22). A further increase in the M<sup>2+</sup>/M<sup>3+</sup> ratio resulted in decreasing the amount of basic sites. A similar trend was observed in other studies based on the Mg/Al ratio for prepared hydrotalcites. Sahu et al. [32] and Xie et al. [31] determined the total concentration of basic sites by benzoic acid titration using Hammett indicators, and the material with Mg/Al ration of 3 exhibited a higher amount of basic sites.

**Table 3.4** Basic site measurements of the calcined catalysts.

Catalyst	(Ni+Mg)/ (Fe+Al) Ratio <sup>a</sup>	Total basic sites <sup>b</sup> (mmol/g)	Strong basic sites <sup>c</sup> (mmol/g)	Weak basic sites <sup>d</sup> (mmol/g)
Ni/(Mg, Al)O <sub>x</sub>	3.66	3.00	0.66	2.37
Ni-Fe/(Mg, Al)O <sub>x</sub> (Fe/Ni=0.1)	3.89	3.71	0.73	2.89
Ni-Fe/(Mg, Al)O <sub>x</sub> (Fe/Ni=0.5)	4.00	3.70	0.70	3.00
Ni-Fe/(Mg, Al)O <sub>x</sub> (Fe/Ni=1)	3.42	4.85	0.30	4.56
Ni-Fe/(Mg, Al)O <sub>x</sub> (Fe/Ni=1.5)	2.93	5.22	0.38	4.84
Fe/(Mg, Al)O <sub>x</sub>	3.22	6.28	0.46	5.82

<sup>a</sup> Measured by ICP-OES.

<sup>b</sup> Irreversible adsorption of acrylic acid as a probe molecule.

<sup>c</sup> Irreversible adsorption of phenol as a probe molecule.

<sup>d</sup> Weak basic sites = Total basic sites – Strong basic site

Scanning Transmission electron microscopy was used to study the morphology and dispersion of selected reduced catalysts. STEM images of the reduced catalysts (at 600°C for 2 h) with different Fe/Ni ratios are displayed in **Figure 3.5**. The average particle size was estimated using *Image J* and found to increase as the Fe content increased. Well-dispersed small-sized nanoparticles were obtained from the HTs derived catalyst with a Fe/Ni=0.1 ratio. EDS analysis on a number of particles also approved the presence of Ni and Fe metals within a single particle which is an evidence for the formation of Ni-Fe alloys. **Table 3.5** summarizes the details of average particle size, the range of Fe/Ni ratio was determined using the EDS analysis and dispersion.

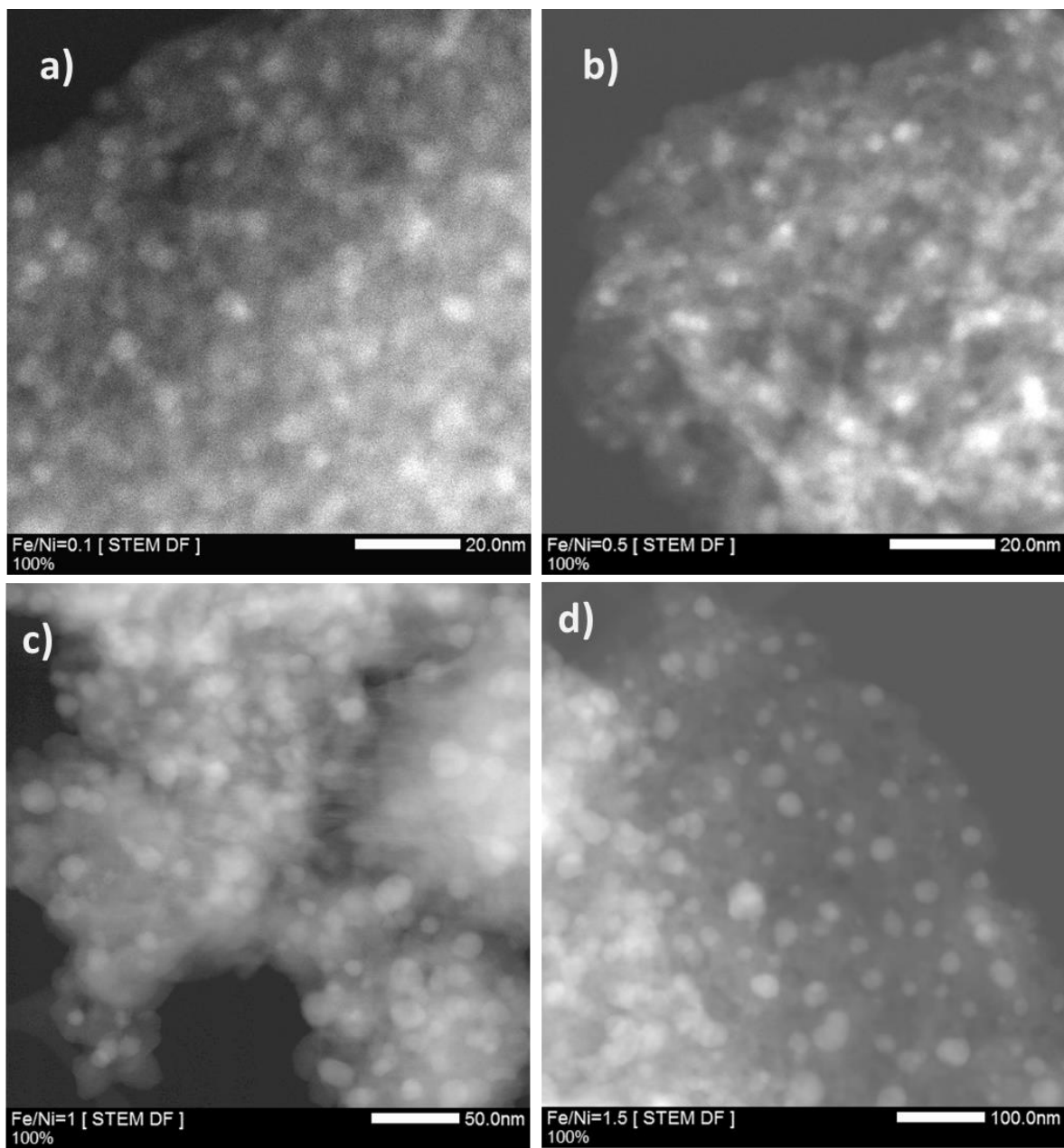


**Figure 3.5** STEM images of reduced HTs derived bimetallic catalysts: (a) Ni-Fe/(Mg, Al)O<sub>x</sub> (Fe/Ni=0.1), (b) Ni-Fe/(Mg, Al)O<sub>x</sub> (Fe/Ni=0.5), (c) Ni-Fe/(Mg, Al)O<sub>x</sub> (Fe/Ni=1) and (d) Ni-Fe/(Mg, Al)O<sub>x</sub> (Fe/Ni=1.5).



**Table 3.5** Summary of STEM-EDS analyses results of representative samples.

Catalyst	Metal content		Particle size (nm) <sup>a</sup>	Fe/Ni ratio range <sup>b</sup>	% Dispersion <sup>c</sup>
	(mmol/g)				
	Ni	Fe			
Ni-Fe/(Mg, Al)O <sub>x</sub> (Fe/Ni=0.1)	2.04	0.215	5.2	0.053-0.14	19.14
Ni-Fe/(Mg, Al)O <sub>x</sub> (Fe/Ni=0.5)	2.04	1.07	6.3	0.12-0.36	16.80
Ni-Fe/(Mg, Al)O <sub>x</sub> (Fe/Ni=1)	2.04	2.15	14.4	0.45-1.2	7.65
Ni-Fe/(Mg, Al)O <sub>x</sub> (Fe/Ni=1.5)	2.04	3.22	26.3	0.83-1.9	4.28

<sup>a</sup> Estimated using *Image J*.

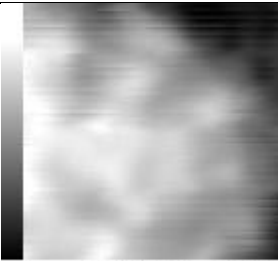
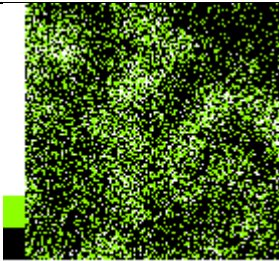
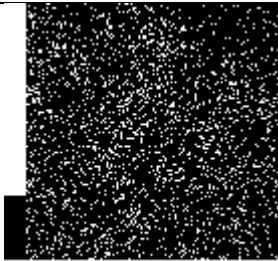
<sup>b</sup> EDS analysis on a number of particles.

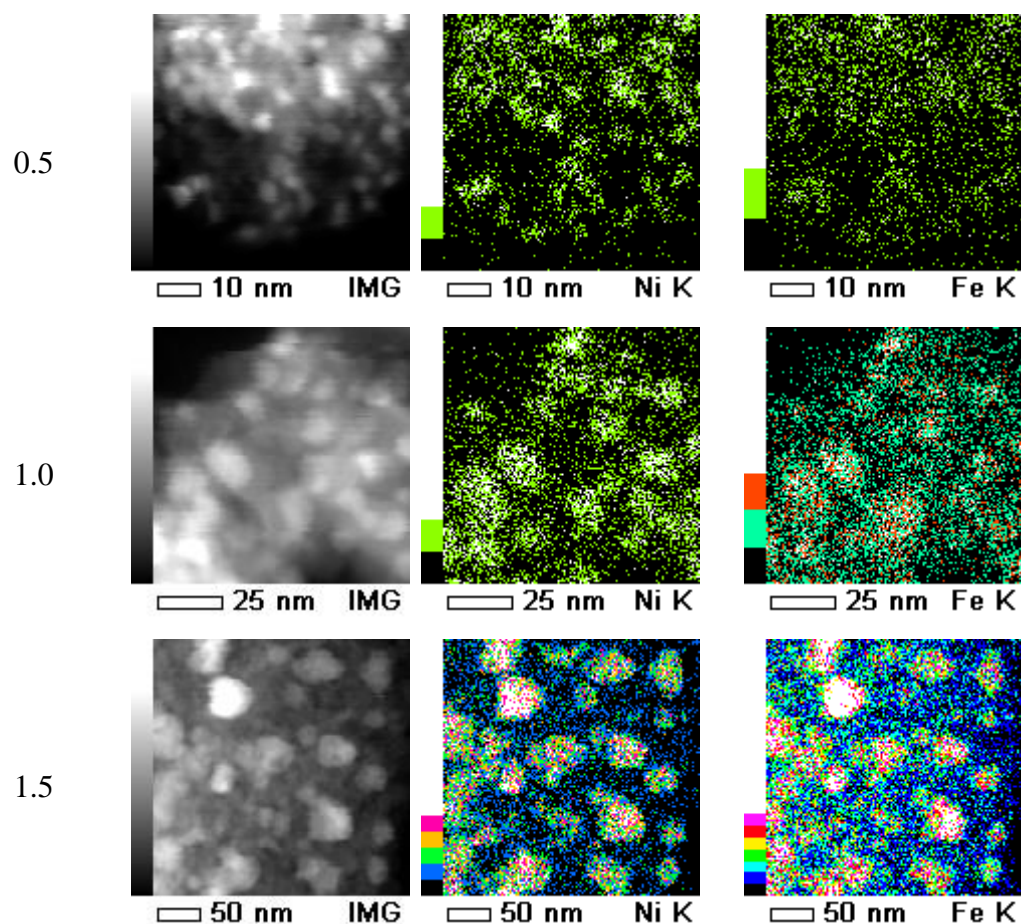
<sup>c</sup> Determined using the equation % Dispersion =  $A_{\text{Ni-Fe}}/\text{Average particle size (nm)} \times 100$ .

$A_{\text{Ni-Fe}} = A_{\text{Ni}}[\text{Ni}/(\text{Ni}+\text{Fe})] + A_{\text{Fe}}[\text{Fe}/(\text{Ni}+\text{Fe})]$ ,  $A_{\text{Ni}} = 0.971$  nm and  $A_{\text{Fe}} = 1.225$  nm [11].

The EDS analysis performed in various zones of the reduced catalysts together with STEM revealed a uniform material composition (**Table 3.6**). Rough compositions of the alloys were estimated from the EDS analysis (area and spot) on various particles and suggested a certain range of the Fe/Ni ratio. The variation between estimated values and real ones can be interpreted by the formation of particles with higher Fe/Ni ratios than those of the bulk composition that is derived from the reduction of NiFe<sub>2</sub>O<sub>4</sub> spinel on these samples [11].

**Table 3.6** STEM images and EDS elemental mapping of reduced catalysts evidence Fe-Ni alloys, both elements are located at the same particles seen in STEM images.

Fe/Ni ratio	STEM Image	EDS Mapping (Ni)	EDS Mapping (Fe)
0.1			



XPS was also used to study the chemical state and surface compositions of selected reduced catalysts. The Ni<sub>2p3/2</sub> signals for Ni-Fe/(Mg, Al)O<sub>x</sub> (Fe/Ni=0.1) and Ni-Fe/(Mg, Al)O<sub>x</sub> (Fe/Ni=0.5) catalysts appears at 855.85 eV and 855.7 eV with satellite peaks at 862.15 eV and 861.90 eV, respectively (Figure 3.6). The main peaks obtained were deconvoluted and mathematically treated to identify the chemical species of nickel present in the surface of the reduced catalysts. Accordingly, the smaller peak at around 852 eV was ascribed to the presence of Ni metal. The peaks at about 854.95-856 eV can be assigned to the NiO, Ni(OH)<sub>2</sub> and/or NiFe<sub>2</sub>O<sub>3</sub> spinel species on the surface [33, 34]. Surface compositions for the Fe/Ni ratios were calculated from the wide scan XPS and results were found to be 0.08 and 0.43 for the Ni-Fe/(Mg, Al)O<sub>x</sub> (Fe/Ni=0.1) and Ni-Fe/(Mg, Al)O<sub>x</sub> (Fe/Ni=0.5) catalysts, respectively.

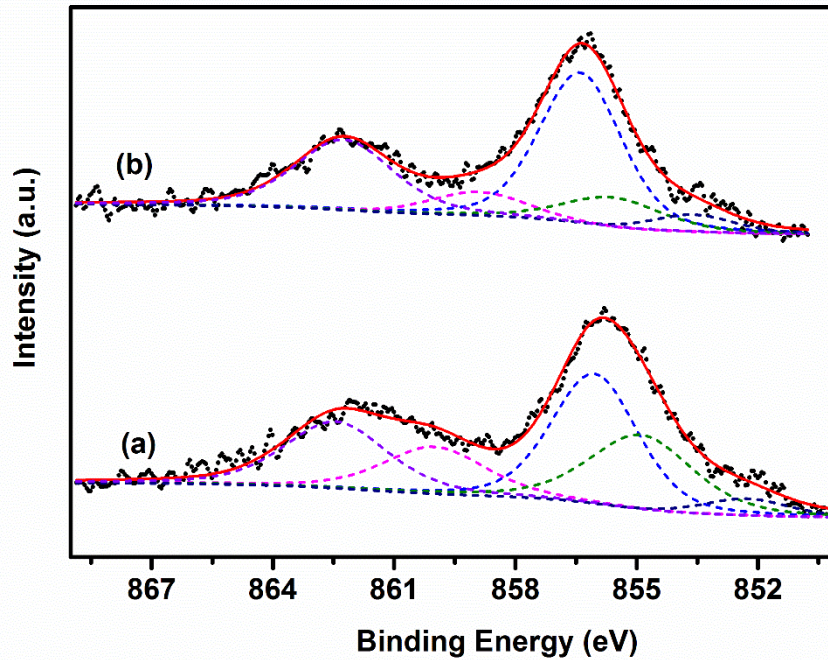


**Figure 3.6** Ni<sub>2p<sub>3/2</sub></sub> XPS spectra: (a) Ni-Fe/(Mg, Al)O<sub>x</sub> (Fe/Ni = 0.1) and (b) Ni-Fe/(Mg, Al)O<sub>x</sub> (Fe/Ni = 0.5).

Furthermore, for Ni-Fe/(Mg, Al)O<sub>x</sub> (Fe/Ni=0.1) catalyst the signals arise from Fe<sub>2p<sub>3/2</sub></sub> was very noisy and difficult to detect this might be due to the lower concentration of Fe on the surface. But for Ni-Fe/(Mg, Al)O<sub>x</sub> (Fe/Ni=0.5) catalyst, the Fe<sub>2p<sub>3/2</sub></sub> signal was detected and successfully traced as shown in **Figure 3.7**. The signals with binding energy equal to 711.5 eV and 724.6 eV are attributed to the oxidized state (Fe<sub>2</sub>O<sub>3</sub>) species of Fe.

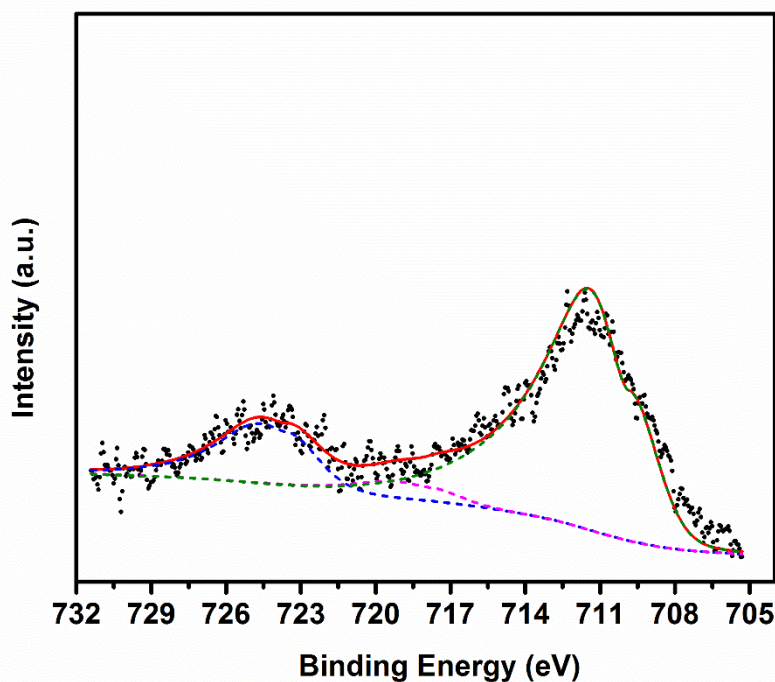


**Figure 3.7** Fe<sub>2p3/2</sub> XPS spectrum for Ni-Fe/(Mg, Al)O<sub>x</sub> (Fe/Ni=0.5) catalyst.

### 3.4.2. Catalytic activity tests towards CO<sub>2</sub> methanation

#### 3.4.2.1. Factors affecting the catalytic performance of Ni-Fe catalysts

Generally, the activity of hydrotalcite derived catalysts prepared herein can be affected by three major factors:

- i) Fe/Ni ratio since DFT based calculations proposes synergistic effects for alloys due to a closer match to the dissociation energy of CO which is considered as the rate-determining step in the CO<sub>2</sub> methanation.
- ii) Size of the active metal nanoparticles after reduction which affects the preferred reaction mechanism, therefore resulting in different product selectivity.
- iii) Amount of basic sites plays a crucial role in the stability of the main intermediate on the surface of the catalyst and the activation of CO<sub>2</sub>.

### 3.4.2.1.1. Effect of Fe to Ni ratio

Previous reports on bimetallic catalysts confirmed that the activity in methanation of carbon oxides can be influenced by the ratio of the metals used during the preparation. Accordingly, the addition of a little amount of iron to nickel in the range  $< 50$  wt.-% was found to improve significantly the catalytic activity compared to the monometallic catalysts [4, 8, 10, 35, 36]. The synergistic effect of Fe-Ni alloys can be explained as shown by Anderson et al. by a Brønsted-Evans-Polanyi (BEP) relation. Alloys (e.g. FeNi<sub>3</sub> and FeNi) exhibit a dissociation energy which is closer to the optimal dissociation energy of CO resulting in higher activity since CO splitting is considered as the rate-determining step [4, 37]. Taking a look at the first seven hours on stream (Figure 3.8) the same trend can be seen for bimetallic hydrotalcite-derived catalysts. Especially in steady state catalysts with little iron content (Fe/Ni  $\leq 1.0$ ) showed better activity than the pure monometallic catalysts.

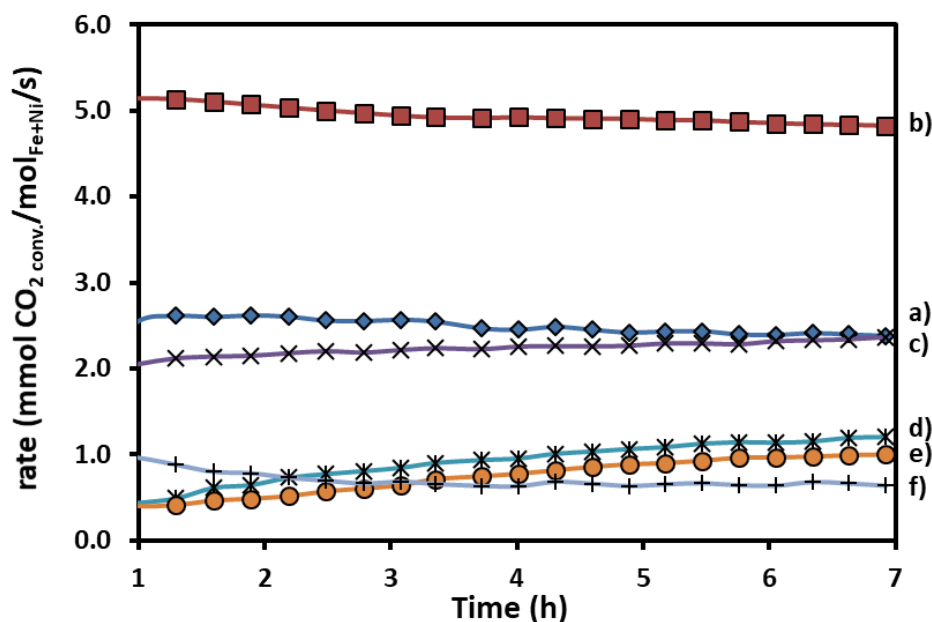


**Figure 3.8** Effect of Fe/Ni ratio on the CO<sub>2</sub> methanation reaction (Reaction conditions: gas mixture with CO<sub>2</sub>:H<sub>2</sub> = 1:4, P = 1 atm, T = 335°C, and GHSV = 12020 h<sup>-1</sup>): (a) Ni/(Mg, Al)O<sub>x</sub>, (b) Ni-Fe/(Mg, Al)O<sub>x</sub> (Fe/Ni = 0.1), (c) Ni-Fe/(Mg, Al)O<sub>x</sub> (Fe/Ni = 0.5), (d) Ni-Fe/(Mg, Al)O<sub>x</sub> (Fe/Ni = 1), (e) Ni-Fe/(Mg, Al)O<sub>x</sub> (Fe/Ni = 1.5) and (f) Fe/(Mg, Al)O<sub>x</sub>.

Based on the arguments by Andersson et al. [4] that the conversion rate is higher at the optimal CO dissociation energy our results differ from that prediction in some aspects. The overall trend

is still the same but higher rates for lower iron content than the optimal value which indicate an influence of additional factors. These factors comprehend to particle size, etc. and will be discussed later in this chapter. Other authors also described the best ratio being Fe/Ni=0.33 impregnated on alumina [5, 38]. However, we could ensure the use of even less iron (Fe/Ni=0.1) for the hydrotalcite derived system improved the activity significantly (Figure 3.8). Recently, Wang et al. [39] reported quite similar results for pure nickel-aluminum based hydrotalcite catalysts. They showed that the addition of less iron (Fe/Ni=0.025 and Fe/Ni=0.05) increased the activity at most due to enhanced adsorption of H<sub>2</sub> compared to a monometallic nickel-aluminum hydrotalcite. Furthermore, they demonstrated that the activity can be increased by adding magnesium to a nickel-aluminum based hydrotalcite resulting in an enhanced CO<sub>2</sub> adsorption and improved dispersion of the active metal. However, they did not address the combination of both beneficial effects at the same time.

Figure 3.9 shows the correlation between the deviation of optimal CO dissociation energy  $\Delta E_{\text{diss, optimal}}$  for the rate-determining step and the catalyst activity as a function of iron content shows the general trend but also significant deviations.

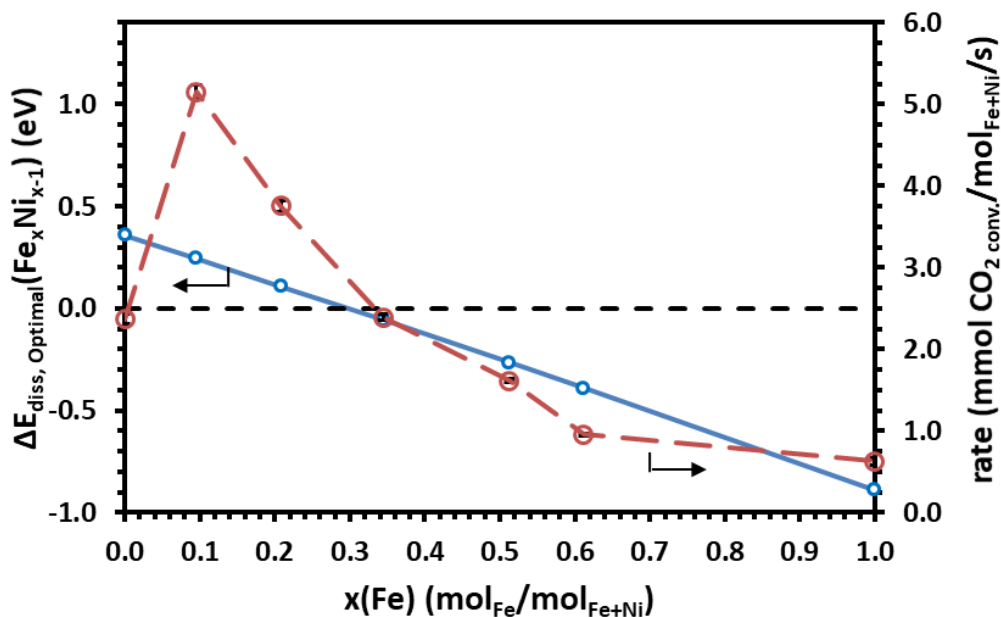
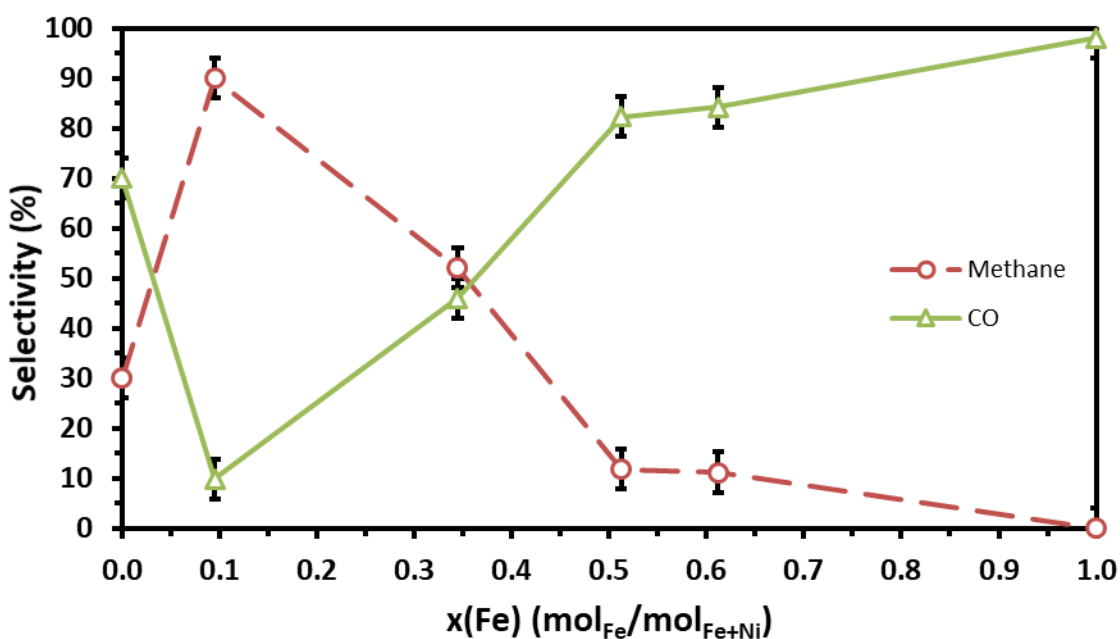


Figure 3.9 Synergistic effect of Fe-Ni alloys compared to sole metals on CO<sub>2</sub> methanation rate.

**Figure 3.10** summarizes selectivity of the prepared catalysts towards methane and carbon monoxide ( $\text{CO}$ ), the most active bimetallic catalyst, Ni-Fe/(Mg, Al) $\text{O}_x$  (Fe/Ni=0.1), enabled a superior  $\text{CH}_4$  selectivity of about 90%. A further increase of the Fe content reduced the  $\text{CH}_4$  selectivity and increased  $\text{CO}$  selectivity of the catalysts remarkably. The monometallic Fe/Mg/Al catalyst solely produces  $\text{CO}$  and no  $\text{CH}_4$  was detected as a product. Similar but less pronounced trends were observed in a study focused on the effect of the Fe content for  $\text{CO}$  and  $\text{CO}_2$  co-methanation using Ni-Fe/ $\text{Al}_2\text{O}_3$  catalysts [5]. Addressing the concept of the optimal  $\text{CO}$  dissociation energy the decrease of methane formation with higher iron content can be explained by assuming a strong adsorption due to the dissociation energies, which leads to a low rate of removal of carbon and oxygen species from the surface to form the reaction products. On the other hand for low iron content, the adsorption is weaker and the barrier for dissociation is high but at the same time, more hydrogen could be provided to form methane.



**Figure 3.10** Effect of Fe content on  $\text{CH}_4$  ( $\circ$ ) and  $\text{CO}$  ( $\Delta$ ) selectivity in comparison to sole metals. Reaction conditions: gas mixture with  $\text{CO}_2:\text{H}_2 = 1:4$ ,  $P = 1$  atm,  $T = 335^\circ\text{C}$ , and  $\text{GHSV} = 12020 \text{ h}^{-1}$ .

#### 3.4.2.1.2. Particle size effect

According to previous reports, the performance of CO<sub>2</sub> methanation catalyst is related to the number of active sites. Therefore, the increased activity can be a particle size/dispersion effect on the one hand and/or a structural/morphological effect on the other hand. Exposing more active sites necessarily causes a higher rate of CO<sub>x</sub> conversion. This concept was already shown for Ru based catalysts in CO hydrogenation, where enhanced activity was achieved by better dispersion of the active metal particles [40]. Wang et al. [36] also proved that CO<sub>2</sub> methanation catalysts are highly dependent on the size of the active metal particles obtained after in situ reductions. Correlating the particle size obtained from STEM analysis with the measured catalytic activity in CO<sub>2</sub> hydrogenation, the catalysts with comparatively smaller metal particles are more active and selective towards methane formation than catalysts composed of larger sized metal particles (**Figure 3.11 a**) due to more active centers of the former compared to the latter.

Even though the CO<sub>x</sub> hydrogenation mechanism itself is still up for discussion and no consensus has been reached so far [41- 44]. Several proposed mechanisms consider that dissociation of CO (as the dominant step) takes place at step-edge sites. DFT calculations supported this hypothesis for Ru [45 - 47], Rh [47, 48], and Ni [47, 49]. Thus, a change in concentration of step-edge sites with particle diameter should impact on selectivity towards the products. Although the particular particle shape could not be determined, the change in selectivity could be clearly observed (**Figure 3.11 b**).



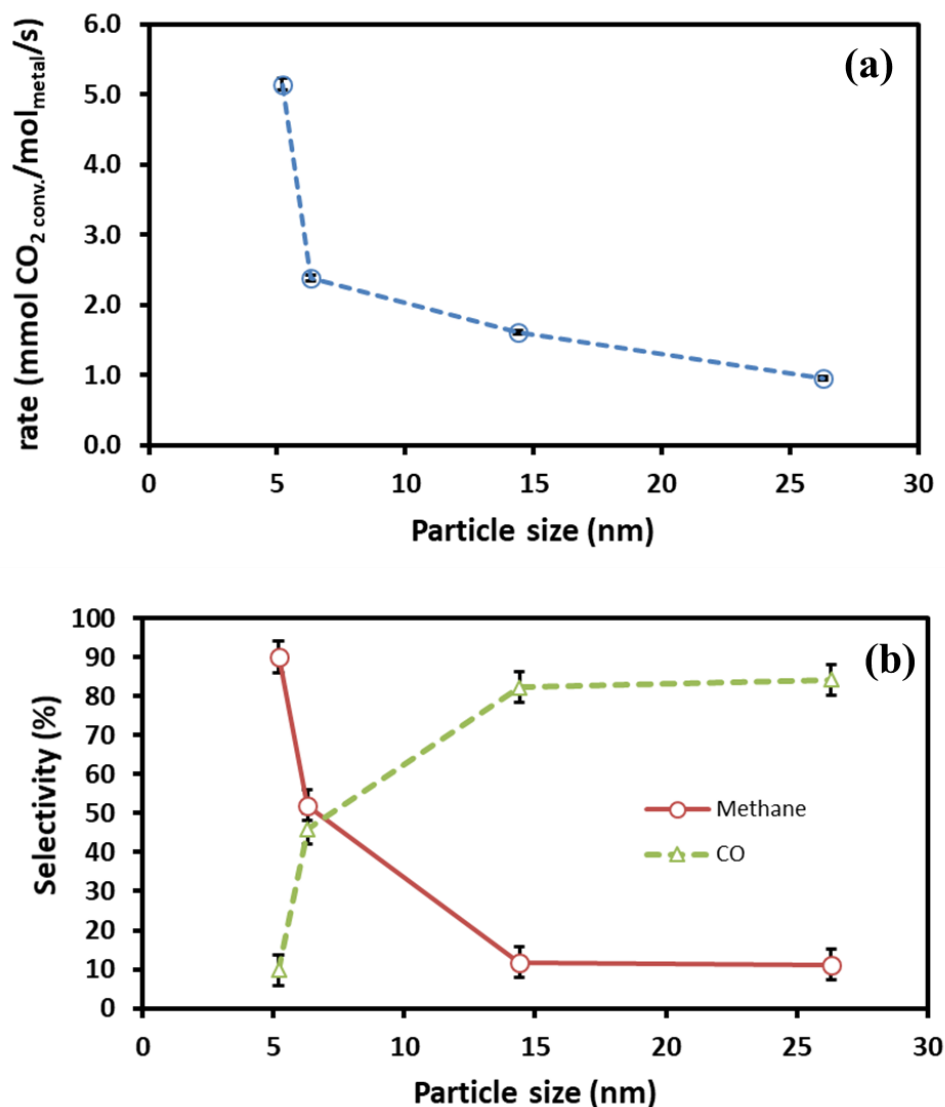


**Figure 3.11** Influence of metal particle size on activity (a) and product selectivity (b) in CO<sub>2</sub> methanation. Reaction conditions: gas mixture with CO<sub>2</sub>:H<sub>2</sub> = 1:4, P = 1 atm, T = 335°C, and GHSV = 12020 h<sup>-1</sup>.

#### 3.4.2.1.3. Effect of basic sites

Basicity of support plays an important role in CO<sub>2</sub> activation and dissociation. The basic sites with different strength strongly affect the adsorption and dissociation of CO<sub>2</sub> on the surface of hydrotalcite derived materials. Among the published works, Fehete et al. [40] demonstrated that a higher amount of basic sites on the surface of catalysts is advantageous for CO<sub>2</sub> adsorption and dissociation for reactions involving CO<sub>2</sub> as raw material. However, up to now, literature is

discordant which type of basic sites finally enhances the catalytic performance. Pan et al. [50] related the enhanced adsorption to medium basic sites while strong basic sites have no influence. On the contrary, He et al. [16] argued that strong basic sites are responsible, while Aldana et al. [51] assigned improvements to weak basic sites. Therefore, the effect of total basic site concentration on the performance of the catalysts in CO<sub>2</sub> conversion is illustrated in **Figure 3.12**. Better activity was obtained by Ni-Fe/(Mg, Al)O<sub>x</sub> (Fe/Ni=0.1). This might be due to the presence of an optimum amount of basic sites required for CO<sub>2</sub> adsorption and activation. It was also observed that higher concentrations of basic sites did not provide further benefit but a decrease of activity occurred. However, for the moment we could not identify a distinct correlation to a particular weak/strong basic site. This leads us to the conclusion that the system is much more complex and the observed behavior presents an interplay of several properties including active metal dispersion, surface area, CO<sub>x</sub> dissociation as well as support basicity.

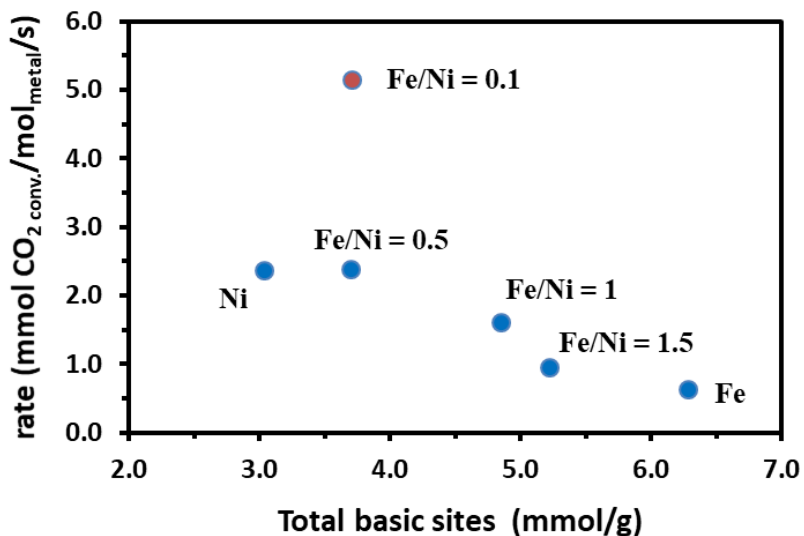


**Figure 3.12** CO<sub>2</sub> conversion rate vs. total basic sites of the HTs derived catalysts. Reaction conditions: gas mixture with CO<sub>2</sub>:H<sub>2</sub> = 1:4, P = 1 atm, T = 335°C, and GHSV = 12020 h<sup>-1</sup>.

#### 3.4.2.2. Effect of reduction temperature

It was observed that during the H<sub>2</sub>-TPR investigation, the hydrotalcite derived Ni-Fe bimetallic catalysts requires relatively higher reduction temperature. In order to investigate this aspect, two

catalysts were selected based on better activity, and tested by increasing the reduction temperature to 600°C for 2 h and results are shown in **Figure 3.13**. The CO<sub>2</sub> activity was found to increase by 3.5-fold for the Ni-Fe/(Mg, Al)O<sub>x</sub> (Fe/Ni=0.1) catalyst in comparison to the reduction pretreatment at 500°C for 1 h. However, the activity of the Ni-Fe/(Mg, Al)O<sub>x</sub> (Fe/Ni=0.5) catalyst only slightly increased for the reduction at a higher temperature. The enhanced activity of both catalysts after reduction at 600°C can be due to the reason that the first reduction pretreatment (500°C) was not enough to reduce the adequate amount of Ni-Fe alloy for the catalytic reaction.

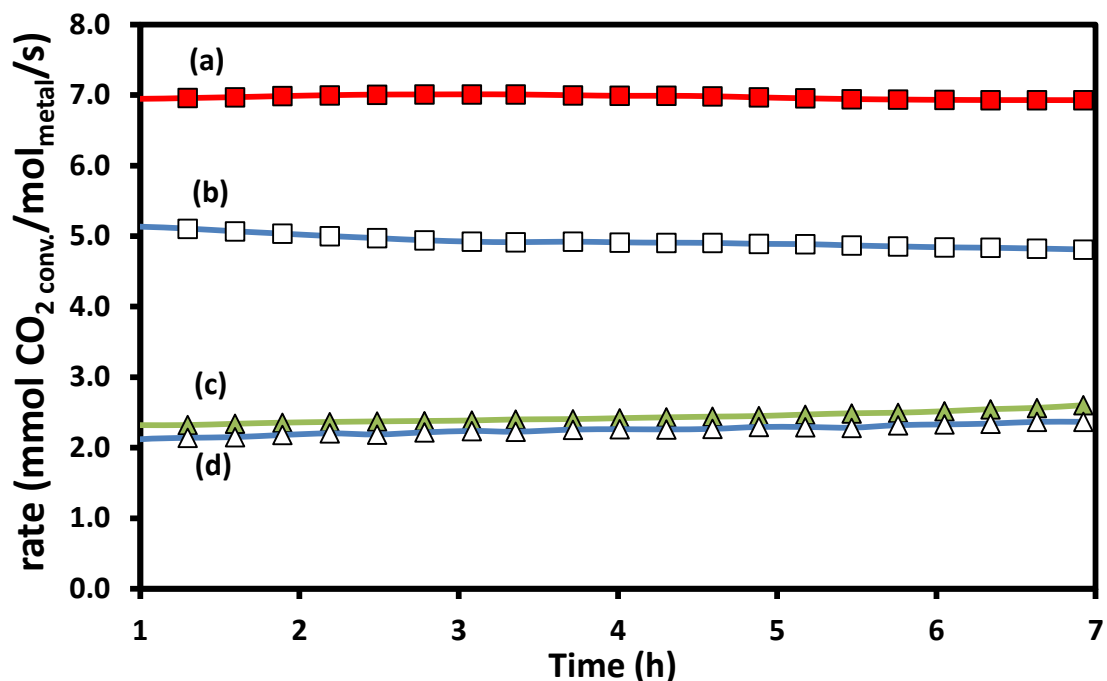


**Figure 3.13** Effect of reduction treatment on the CO<sub>2</sub> methanation reaction (Reaction conditions: gas mixture with CO<sub>2</sub>:H<sub>2</sub> = 1:4, P = 1atm, T = 335°C, and GHSV = 12020 h<sup>-1</sup>): (a) Ni-Fe/(Mg, Al)O<sub>x</sub> (Fe/Ni=0.1) at 600°C, (b) Ni-Fe/(Mg, Al)O<sub>x</sub> (Fe/Ni=0.1) at 500°C, (c) Ni-Fe/(Mg, Al)O<sub>x</sub> (Fe/Ni=0.5) at 600°C, (d) Ni-Fe/(Mg, Al)O<sub>x</sub> (Fe/Ni=0.5) at 500°C.

Methane selectivity of the most active catalyst Ni-Fe/(Mg, Al)O<sub>x</sub> (Fe/Ni=0.1) increased to 99.3% while CO selectivity was lowered to 0.7% when the catalyst was reduced at a higher temperature (600°C) for 2 h (**Figure 3.14**). Even though the change in both rates of CO<sub>2</sub> conversion and selectivity were small, the Ni-Fe/(Mg, Al)O<sub>x</sub> (Fe/Ni=0.5) catalyst also showed the same trend.

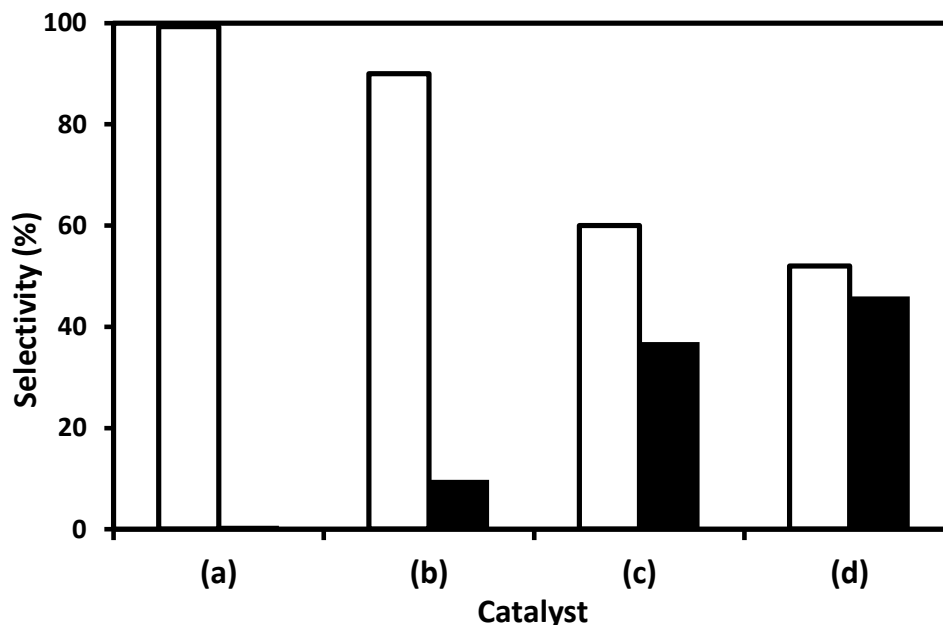


**Figure 3.14** Effect of reduction pretreatment on CH<sub>4</sub> (□) and CO (■) selectivity: (a) Ni-Fe/(Mg, Al)O<sub>x</sub> (Fe/Ni=0.1) at 600°C, (b) Ni-Fe/(Mg, Al)O<sub>x</sub> (Fe/Ni=0.1) at 500°C, (c) Ni-Fe/(Mg, Al)O<sub>x</sub> (Fe/Ni=0.5) at 600°C, (d) Ni-Fe/(Mg, Al)O<sub>x</sub> (Fe/Ni=0.5) at 500°C.

### 3.4.2.3. Stability test

Stability of Ni-Fe/(Mg, Al)O<sub>x</sub> (Fe/Ni=0.1) catalyst was tested during 24 h time on stream in the CO<sub>2</sub> methanation at 335°C (**Figure 3.15**). The CO<sub>2</sub> conversion remained constant at 80% and CH<sub>4</sub> selectivity was above 99.3% during the long-term test. The CO selectivity was less than 0.7% as seen previously.

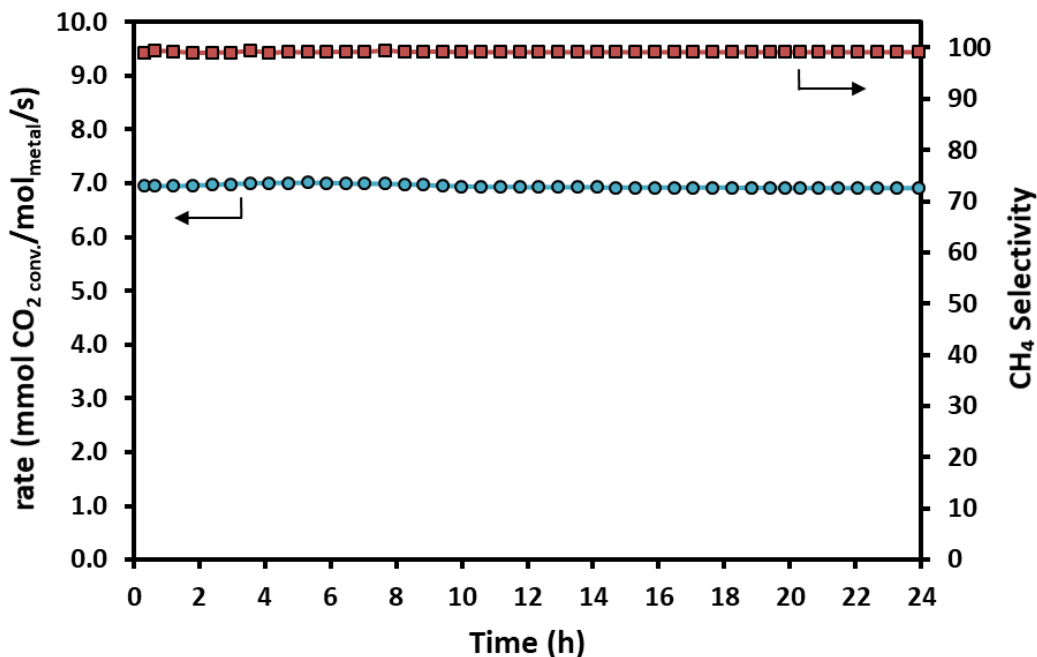


**Figure 3.15** Stability of catalyst activity and CH<sub>4</sub> selectivity with the reaction time over Ni-Fe/(Mg, Al)O<sub>x</sub> (Fe/Ni=0.1) catalyst. Reaction conditions: gas mixture with CO<sub>2</sub>:H<sub>2</sub> = 1:4, P = 1 atm, T = 335°C, and GHSV = 12020 h<sup>-1</sup>.

### 3.5. Characterization of the spent catalysts

XRD analysis of selected spent catalysts was performed in order to investigate the Ni-Fe alloy formation during reaction after the in-situ reduction (**Figure 3.16**). The diffraction patterns of catalysts after the CO<sub>2</sub> methanation have the periclase support in common.

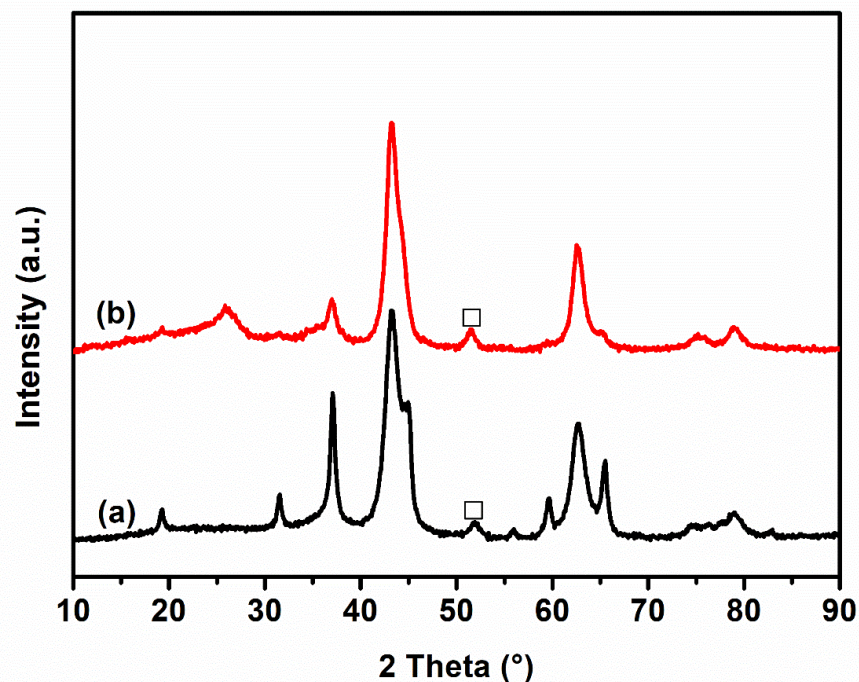


**Figure 3.16** XRD pattern of the catalysts after the CO<sub>2</sub> methanation (a) Ni-Fe/(Mg, Al)O<sub>x</sub> (Fe/Ni = 0.1) and (b) Ni-Fe/(Mg, Al)O<sub>x</sub> (Fe/Ni = 0.5): formation of Ni-Fe alloys (□).

Taking a closer look at the  $d(200)$  value for reflections at around  $2\theta \approx 51^\circ$  it is possible to study the formation of the alloy during the reaction by applying Vegard's law. Based on the calculated d-spacing values for catalysts with lower (Fe/Ni = 0.1) and higher (Fe/Ni = 0.5) iron content there is an evidence for an alloy formation because the values obtained are in between the theoretical values compared to pure elements and follow along Vegard's law (**Figure 3.17**). The data shows a good linear correlation, as Vegard's law is not exact; a perfect correlation is not expected. The formation of Ni-Fe alloys was also confirmed from TEM-EDS measurements. The values for fcc Ni metal = 0.1762 nm (JCPDS 01-070-1849) and fcc  $\gamma$ -Fe = 0.1823 nm (JCPDS 01-089-4185) were taken to plot the correlation curve.

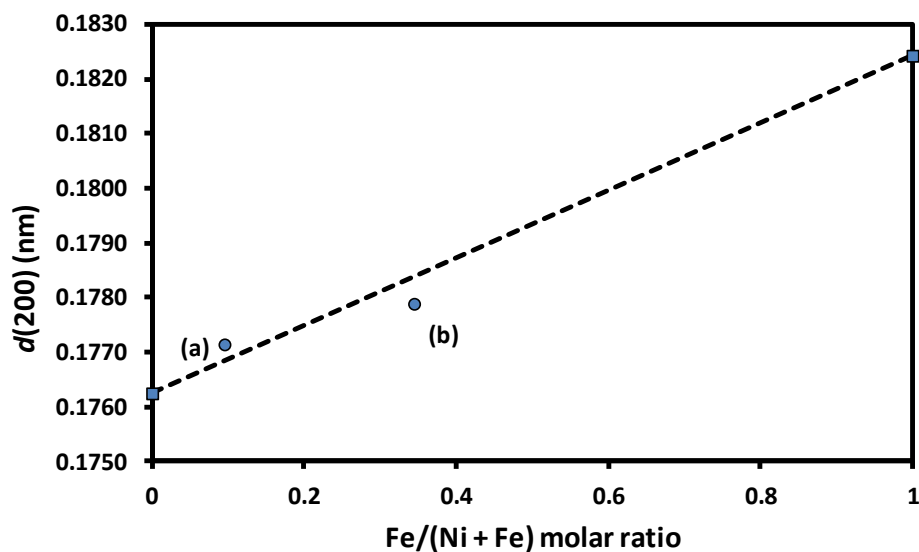


**Figure 3.17** Dependence of  $d(200)$  spacing for Fe-Ni alloys as a function of the Fe/(Ni + Fe) molar ratio for catalysts after CO<sub>2</sub> methanation: (a) Ni-Fe/(Mg, Al)O<sub>x</sub> (Fe/Ni = 0.1) and (b) Ni-Fe/(Mg, Al)O<sub>x</sub> (Fe/Ni = 0.5). The dashed line describes theoretical behavior using Vegard's law with fcc Ni metal (JCPDS 01-070-1849) and fcc  $\gamma$ -Fe (JCPDS 01-089-4185) as references (■).

Carbon deposition behavior of the HTs derived samples after the reaction was also evaluated by TG analysis under air atmosphere. According to previous reports, weight loss at a temperature between 400 to 500°C can be assigned to the removal of easily oxidizing amorphous carbon and the weight loss at above 500°C is attributed to the oxidation of graphitic carbon [52, 53]. As of **Figure 3.18**, the precipitated HTs derived catalyst, a weight loss due to oxidation of carbon at higher temperature ranges was not observed. This demonstrates that the hydrotalcite derived catalyst Ni-Fe (Mg, Al)O<sub>x</sub> (Fe/Ni = 0.1) has a profound effect on carbon tolerance during the CO<sub>2</sub> methanation. According to literature, incorporation of MgO on Ni-based catalysts for CO<sub>2</sub> reforming of methane was found as a promising approach to suppress the deposition of carbon and get improved catalyst stability [53]. Therefore, the presence of MgO on the structured hydrotalcite derived catalyst was found to be advantageous for its carbon tolerance nature through the improved CO<sub>2</sub> adsorption and dissociation properties.

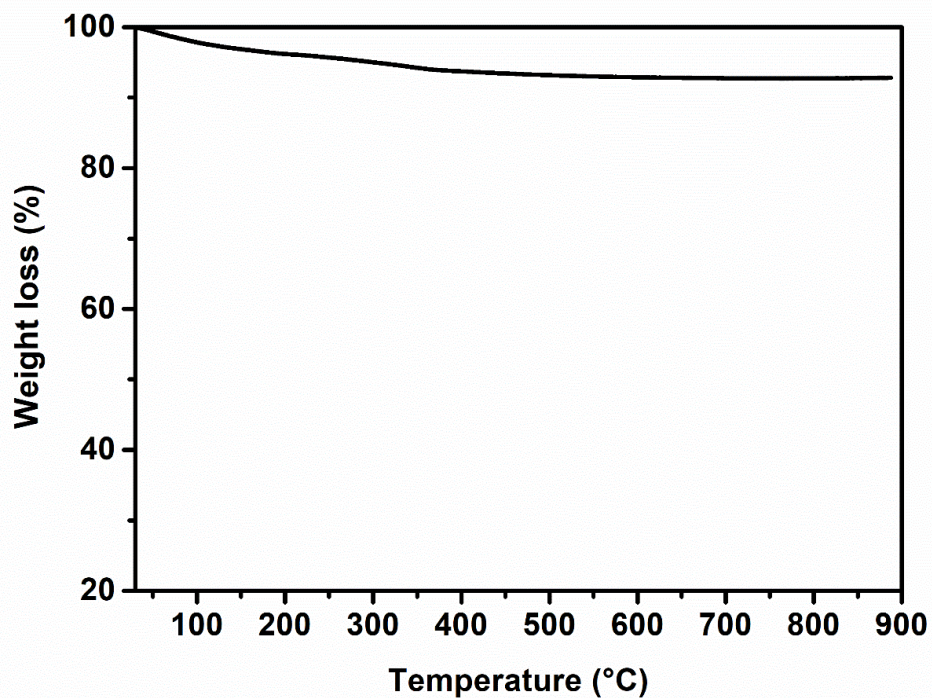


**Figure 3.18** TG analysis of spent catalyst Ni-Fe/(Mg, Al)O<sub>x</sub> (Fe/Ni=0.1) HTs.

Additionally, Raman spectroscopy was also used to check if carbon is deposited on the spent catalyst. Raman spectra were obtained using DXR Raman microscope with an exciting line of 532 nm and 2 mW power. According to Raman spectrum obtained (**Figure 3.19**), no peaks of carbon species were obtained for the spent Ni-Fe (Mg, Al)O<sub>x</sub> (Fe/Ni=0.1) catalyst which proves the carbon tolerance nature of the catalyst under the experimental conditions used.



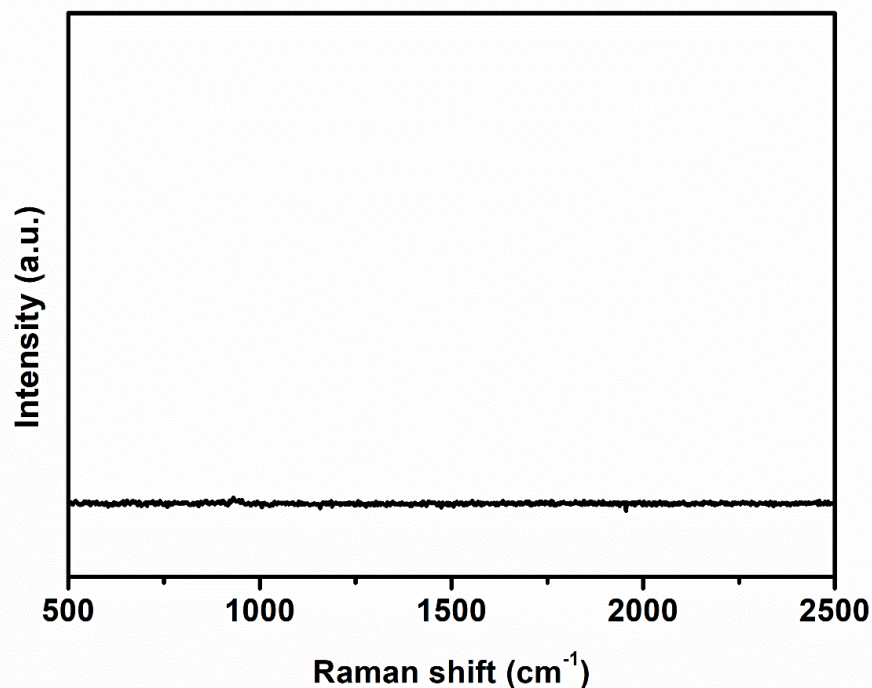


**Figure 3.19** Raman spectrum of Ni-Fe/(Mg, Al)O<sub>x</sub> (Fe/Ni=0.1) HTs spent catalyst.

### 3.6. Conclusion

In this chapter, hydrotalcite derived Ni-Fe/(Mg, Al)O<sub>x</sub> catalysts with different Fe/Ni ratio were successfully synthesized by co-precipitation method at constant pH. XRD analysis approved the precursor of the Ni-Fe-Mg-Al catalyst have HTs structure. BET results revealed both the specific surface area and total pore volume of the HTs derived catalysts decreased with increasing Fe content, might be due to the pore blockage during the incorporation of Fe. STEM-EDS analyses of the most active catalyst confirmed the formation of a small-sized Ni-Fe alloy which was favorable for the methanation of CO<sub>2</sub>.

The HTs derived bimetallic catalysts achieved better activities and excellent stabilities for CO<sub>2</sub> methanation than the monometallic catalysts. Among the prepared catalysts, the catalyst with relatively lower Fe content (Fe/Ni=0.1) was the most active and selective to methane. The incorporation of iron plays a critical role to improve the activity of the bimetallic catalysts. For Ni-Fe/(Mg, Al)O<sub>x</sub> (Fe/Ni=0.1) catalyst reduced at 600°C, the CO<sub>2</sub> conversion rate about 6.96 mmol

CO<sub>2</sub> conversion/mol<sub>metal</sub>/s at 335°C with a selectivity of 99.3% to CH<sub>4</sub> and remained unchanged for 24 h in the catalytic stability test. The catalysts with the relatively higher content of Fe exhibited the excess of CO in the products of the reaction, suggesting the formation of CO as intermediate under the reaction conditions used. Lowest activity was recorded by the Fe/(Mg, Al)O<sub>x</sub> catalyst. Main tendencies for better catalytic activity and stability of the catalysts are visible. However, the behavior of these bimetallic catalysts can't be explained solely based on dissociation energy of CO being the rate-determining step. Additional factors such as basicity of the support and metal particle size have to be optimized as well to assure a balanced supply of hydrogen from the metal and CO<sub>x</sub> species from the support to the active centers.

TGA and Raman analyses of the spent sample of the most active catalyst in our study also proved that no graphitic carbon deposition during the 24 h catalytic test. The bimetallic Ni-Fe catalysts derived from hydrotalcite precursor materials are a promising alternative to tailor basicity of the support and improve metal dispersion due to the incorporation of ions in the hydrotalcite structure. The used elements are abundantly available and therefore the material is a candidate for being economic feasible also in large-scale application towards CO<sub>2</sub> methanation. As a consequence, CO<sub>2</sub> can be recycled and greenhouse gas emissions diminished as well as an excess energy being transformed into a green and eco-friendly fuel with wide application.

### 3.7. References

- [1] R. Razzaq, C. Li, M. Usman, K. Suzuki, S. Zhang, *Chem Eng J.*, 262 (2015) 1090-1098.
- [2] M. Koike, D.L. Li, Y. Nakagawa, K. Tomishige, *Chemsuschem*, 5 (2012) 2312-2314.
- [3] L. Wang, D. L. Li, M. Koike, S. Koso, Y. Nakagawa, Y. Xu, K. Tomishige, *Appl Catal A-Gen*, 392 (2011) 248-255.
- [4] M.P. Andersson, T. Bligaard, A. Kustov, K.E. Larsen, J. Greeley, T. Johannessen, C.H. Christensen, J. K. Norskov, *J Catal.*, 239 (2006) 501-506.
- [5] J. Sehested, K.E. Larsen, A. L. Kustov, A. M. Frey, T. Johannessen, T. Bligaard, M.P. Andersson, J. K. Norskov, C.H. Christensen, *Top Catal.*, 45 (2007) 9-13.
- [6] S. Hwang, U.G. Hong, J. Lee, J. H. Baik, D. J. Koh, H. Lim, I.K. Song, *Catal Lett.*, 142 (2012) 860-868.
- [7] S. Hwang, J. Lee, U.G. Hong, J.H. Baik, D.J. Koh, H. Lim, I.K. Song, *J Ind Eng Chem.*, 19 (2013) 698-703.
- [8] S.H. Kang, J.H. Ryu, J.H. Kim, S.J. Seo, Y.D. Yoo, P.S.S. Prasad, H.J. Lim, C.D. Byun, *Korean J Chem Eng.*, 28 (2011) 2282-2286.
- [9] D. Pandey, G. Deo, *Journal of Molecular Catalysis A: Chemical*, 382 (2014) 23-30.
- [10] D. Pandey, G. Deo, *J Ind Eng Chem.*, 33 (2016) 99-107.
- [11] D. L. Li, M. Koike, L. Wang, Y. Nakagawa, Y. Xu, K. Tomishige, *Chemsuschem*, 7 (2014) 510-522.
- [12] J.-T. Feng, Y.-J. Lin, D. G. Evans, X. Duan, D.-Q. Li, *J Catal.*, 266 (2009) 351-358.
- [13] M.-Q. Zhao, Q. Zhang, W. Zhang, J.-Q. Huang, Y. Zhang, D. S. Su, F. Wei, *J. Am. Chem. Soc.*, 132 (2010) 14739-14741.
- [14] Q. Wang, D. O'Hare, *Chem Rev.*, 112 (2012) 4124-4155.
- [15] F. Cavani, F. Trifiro, A. Vaccari, *Catal Today*, 11 (1991) 173-301.
- [16] L. He, Q.Q. Lin, Y. Liu, Y.Q. Huang, *J Energy Chem.*, 23 (2014) 587-592.
- [17] S. Abello, C. Berruoco, D. Montane, *Fuel*, 113 (2013) 598-609.
- [18] G. Lee, Y. Jeong, A. Takagaki, J.C. Jung, *Journal of Molecular Catalysis A: Chemical*, 393 (2014) 289-295.

- [19] I. Delidovich, R. Palkovits, *J Catal.*, 327 (2015) 1-9.
- [20] R.D. Shannon, *Acta Crystallogr A.*, 32 (1976) 751-767.
- [21] L. Bian, W. Wang, R. Xia, Z. Li, *Rsc Adv.*, 6 (2016) 677-686.
- [22] C. E. Daza, J. Gallego, J. Andrés Moreno, F. Mondragón, S. Moreno, R. Molina, *Catalysis today* 133-135 (2008) 357-366.
- [23] C. Li, Y.-W. Chen, *Thermochimica Acta*, 256 (1995) 457-465.
- [24] B. Mile, D. Stirling, M.A. Zammit, A. Lovell, M. Webb, *J Catal*, 114 (1988) 217-229.
- [25] A. Kadkhodayan, A. Brenner, *J Catal*, 117 (1989) 211-321.
- [26] Z. Jiang, J. Su, M.O. Jones, H. Shi, T. Xiao, P.P. Edwards, *Energ Fuel*, 23 (2009) 1634-1639.
- [27] K. Mette, S. Kühn, H. Düdder, K. Kähler, A. Tarasov, M. Muhler, M. Behrens, *ChemCatChem*, 6 (2014) 100-104.
- [28] T.J. Vulic, A.F.K. Reitzmann, K. Lázár, *Chem Eng J.*, 207-208 (2012) 913-922.
- [29] Y. Ohishi, T. Kawabata, T. Shishido, K. Takaki, Q. Zhang, Y. Wang, K. Nomura, K. Takehira, *Applied Catalysis A: General*, 288 (2005) 220-231.
- [30] H. Muroyama, R. Nakase, T. Matsui, K. Eguchi, *Int J Hydrogen Energ.*, 35 (2010) 1575-1581.
- [31] W. Xie, H. Peng, L. Chen, *Journal of Molecular Catalysis A: Chemical*, 246 (2006) 24-32.
- [32] P.K. Sahu, S.K. Gupta, D.D. Agarwal, *Catal Sci Technol.*, 3 (2013) 1520-1530.
- [33] L. Chena, H. Dai, Y. Shen, J. Bai, *Journal of Alloys and Compounds*, 491 (2010) L33-L38.
- [34] G.C. Allen, S.J. Harries, J.A. Jutson, *Applied Surface Science*, 37 (1989) 111-134.
- [35] F. Meng, P. Zhong, Z. Li, X. Cui, H. Zheng, *Journal of Chemistry*, 2014 (2014) 7.
- [36] S. Hwang, U.G. Hong, J. Lee, J.G. Seo, J.H. Baik, , D.J. Koh, H. Lim, I.K. Song, *J Ind Eng Chem.*, 19 (2013) 2016-2021.
- [37] T. Bligaard, J.K. Norskov, S. Dahl, J. Matthiesen, C.H. Christensen, J. Sehested, *J Catal.*, 224 (2004) 206-217.
- [38] Frey, A. M., Technical University of Denmark 2008.

- [39] X. Wang, T. Zhen, C. Yu, *Applied Petrochemical Research*, 6(3) 2016, 217-223.
- [40] I. Fechete, J. Vadrine, *Molecules*, 20, (2015) 5638-5666.
- [41] F. Ocampo, B. Louis, A.C. Roger, *Appl Catal A-Gen.*, 369 (2009) 90-96.
- [42] A. Karelavic, P. Ruiz, *Appl Catal B-Environ.*, 113 (2012) 237-249.
- [43] T. Abe, M. Tanizawa, K. Watanabe, A. Taguchi, *Energ Environ Sci.*, 2 (2009) 315-321.
- [44] C.S. Kellner, A.T. Bell, *J Catal.*, 75 (1982) 251-261.
- [45] R.A. Van Santen, *Accounts of Chemical Research*, 42 (2009) 57-66.
- [46] I.M. Ciobica, A.W. Kleyn, R.A. Van Santen, *J Phys Chem B.*, 107 (2003) 164-172.
- [47] A.C. Lausche, A.J. Medford, T.S. Khan, Y. Xu, T. Bligaard, F. Abild-Pedersen, J.K. Norskov, F. Studt, *J Catal.*, 307 (2013) 275-282.
- [48] M. Mavrikakis, M. Baumer, H.J. Freund, J.K. Norskov, *Catal Lett.*, 81 (2002) 153-156.
- [49] M.P. Andersson, E. Abild-Pedersen, I.N. Remediakis, T. Bligaard, G. Jones, J. Engbæk, O. Lytken, S. Hørch, J.H. Nielsen, J. Sehested, J.R. Rostrup-Nielsen, J.K. Norskov, I. Chorkendorff, *J Catal.*, 255 (2008) 6-19.
- [50] Q.S. Pan, J.X. Peng, T.J. Sun, S. Wang, S.D. Wang, *Catal Commun*, 45 (2014) 74-78.
- [51] P.A.U. Aldana, F. Ocampo, K. Kolb, B. Louis, F. Thibault-Starzyk, M. Daturi, P. Bazin, S. Thomas, A.C. Roger, *Catal Today*, 215 (2013) 201-207.
- [52] K.Y. Koo, H.-S. Roh, Y.T. Seo, D. J. Seo, W.L. Yoon, S. B. Park, *Applied Catalysis A: General*, 340 (2008) 183-190.
- [53] S. Tada, R. Kikuchi, *Catal Sci Technol*, 5 (2015) 3061-3070.

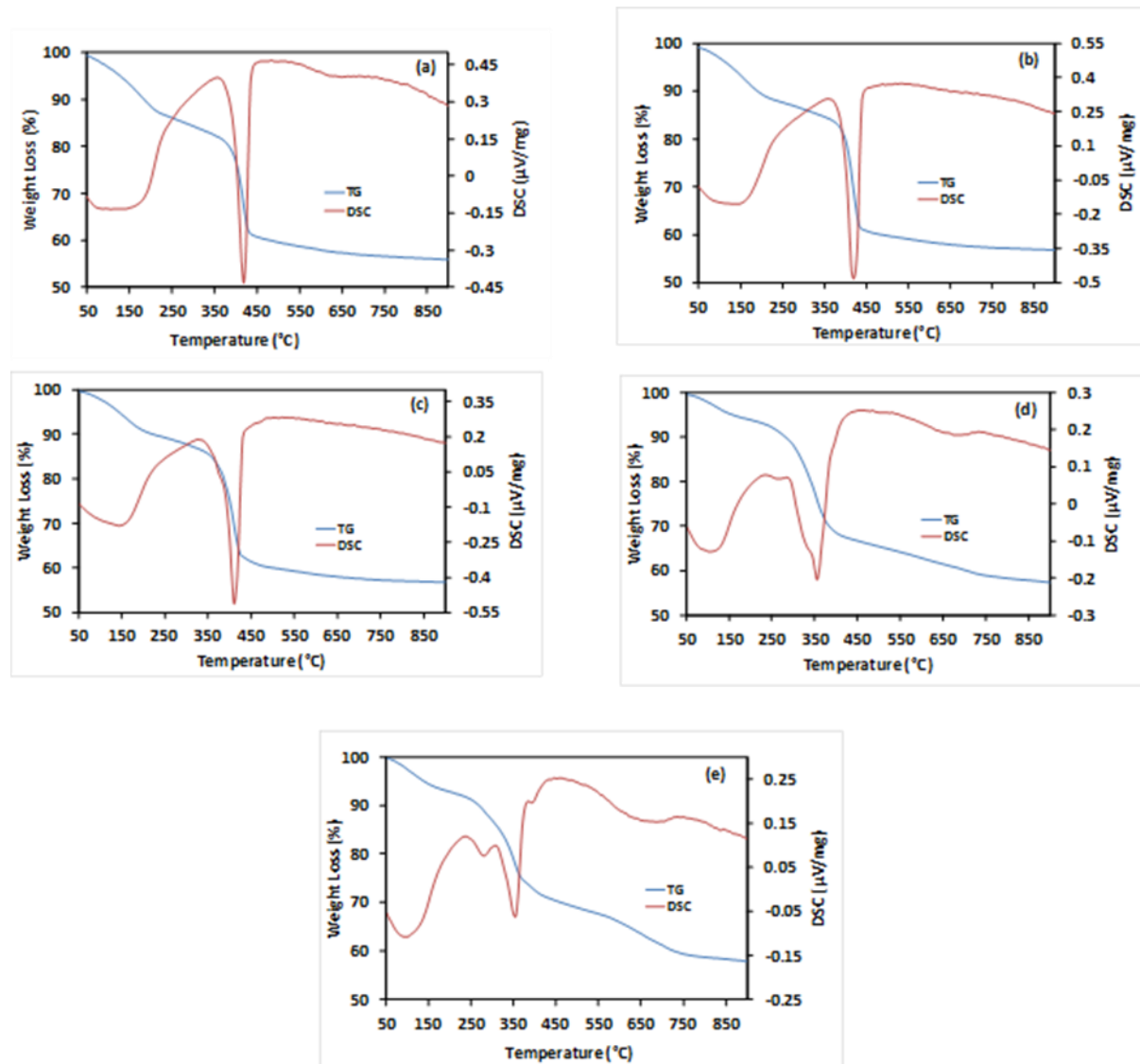


**Figure 1.** Representative TGA-DSC results of the dried precursors: a) Ni/(Mg, Al)O<sub>x</sub>, b) Ni-Fe/(Mg, Al)O<sub>x</sub> (Fe/Ni=0.1), c) Ni-Fe/(Mg, Al)O<sub>x</sub> (Fe/Ni=0.5), d) Ni-Fe/(Mg, Al)O<sub>x</sub> (Fe/Ni=1.5) and e) Fe/(Mg, Al)O<sub>x</sub>.

# CHAPTER 4

## 4. Effect of support basicity on hydrotalcite derived Ni-Fe catalysts towards low-temperature CO<sub>2</sub> methanation

### 4.1. Introduction

According to previous reports, it is observed that the CO<sub>2</sub> methanation reaction is affected by the type and amount of basic sites present on the catalysts used [1-3]. Pan et al. investigated the presence of medium basic sites responsible for the high activity of Ni/CZ with respect to Ni/SiO<sub>2</sub> [2]. The equilibrium CO<sub>2</sub> conversion is reached at 340°C. CO<sub>2</sub>-TPD profiles of Ni/CZ show weak and medium sites, different from Ni/Al<sub>2</sub>O<sub>3</sub>, which shows weak and strong basic sites; CO<sub>2</sub> adsorbed on strong basic sites cannot desorb from Ni/Al<sub>2</sub>O<sub>3</sub> surface until 700°C. Consequently, the strongly adsorbed CO<sub>2</sub> on the surface does not participate in the reaction carried out from 220°C to 400°C. Baker group also investigated trimetallic catalysts to the CO<sub>2</sub> methanation reaction [4-6], which highlights how the adsorption strength of CO<sub>2</sub> is controlled by the Lewis basicity of the catalyst, the d-band center of the metal surface, and the charge transfer from the metal surface to the chemisorbed CO<sub>2</sub>. In the contrary, another group He et al. [7] investigated the effect of strong basic sites, using KOH as a promoter to Ni-Al<sub>2</sub>O<sub>3</sub>-HT and form K-Ni/Al<sub>2</sub>O<sub>3</sub>-HT. Their experimental results showed that both the CO<sub>2</sub> conversion and CH<sub>4</sub> selectivity increased after introducing a small amount of potassium. They suggested that the addition of potassium to the catalyst provided extra strong basic sites, which comprehend for enhanced catalytic performance in the CO<sub>2</sub> methanation. Therefore, in the literature, there is no clear agreement on the strength and amount of basic sites for better activity and stability of catalysts used in CO<sub>2</sub> methanation.

Several authors also studied hydrotalcites as supports for Ni catalysts (Ni-Al/hydrotalcite), comparing their catalytic activity in CO<sub>2</sub> methanation with commercial Ni/γ-Al<sub>2</sub>O<sub>3</sub> catalysts. Recent works on hydrotalcite based catalysts report a high Ni dispersion on the hydrotalcite support with respect to the conventional Ni/γ-Al<sub>2</sub>O<sub>3</sub> catalyst, indicating that this new support is a promising material for preparing stable and well-dispersed Ni catalysts. Even if the amount of loaded nickel on the support ranges between 75 and 80 wt-%, the authors demonstrated that the catalysts possess a narrow nickel particle size distribution in the range of 3-9 nm [7, 8].



The hydrotalcite material seems to be a promising support for Ni catalysts due to the possibility of hosting a large amount of active metal without losing the important peculiarity of high dispersion and smaller particle size. The quantity of aluminum or other Lewis basic supports present in these materials must be taken into account because it affects the reducibility of species as well as amount and strength of the basic sites. It is, therefore, necessary to find a proper balance between Ni loading and basic sites concentration to achieve a high catalytic activity in the CO<sub>2</sub> methanation reaction. In this chapter, hydrotalcite derived Ni-Fe catalysts are investigated, focusing the attention on both the amount of basic sites and the active metal loading.

## 4.2. Scope of the chapter

The central idea behind the research work presented in this chapter is to study how the concentration of basic sites affect the activity of hydrotalcite derived Ni-Fe-Mg-Al catalysts. The work is based on catalysts prepared with the Fe-Ni ratio optimized in [Chapter 3](#) but different active metal to basic support ratio. The catalysts synthesized in this work are considered as (Mg, Al)O<sub>x</sub> supported Ni-Fe catalysts with active metal (% of Ni) loading ranges between 0% - 75% and Lewis base (i.e. MgO) loading of 0% - 75%. It is known, that the high Lewis basicity of MgO has a beneficial effect, as CO<sub>2</sub> adsorption and dissociation is enhanced on basic supports. The as-prepared catalysts were characterized by XRD, H<sub>2</sub>-TPR, XRF, CO<sub>2</sub>-TPD, SEM, and STEM.

## 4.3. Experimental

### 4.3.1. Catalysts preparation

The catalysts were prepared using the same method described in [Chapter 3](#) except the different Ni-Fe to (Mg, Al)O<sub>x</sub> ratio. Catalysts with both higher and lower basic concentration were prepared. For comparison, only the basic support (75%Mg-25%Al) was also synthesized using the same method. As-prepared catalysts (i.e. dried precursors), after calcination and reduction, were characterized by XRD, N<sub>2</sub>- physisorption, H<sub>2</sub>-TPR, XRF, SEM, and STEM techniques.

#### 4.3.2. Characterization of as-prepared catalysts

XRD analyses of samples in order to study the phase structure were made using a Bruker D2-Phaser diffractometer operating with Cu K $\alpha$  radiation at 30 kV and 10 mA with 0.5-2 mm scattering screen. The  $2\theta$  range of 10-90° was analyzed.

The X-ray fluorescence analysis of calcined catalysts was made using micro-X-ray fluorescence spectrometer (EAGLE  $\mu$ -Probe) from Eagle Applications Lab Mahwah N.J (EDAX Inc.) to estimate the surface composition.

Specific surface area (SSA) measurements were performed using Quadrasorb SI Automated Surface Area and Pore Size Analyzer from Quantachrome Instruments. The analyses were performed by physical adsorption of N<sub>2</sub> at the temperature of liquid nitrogen (-196°C). The total pore volume ( $V_{\text{total}}$ ) was calculated from the adsorbed volume of nitrogen for a relative pressure  $P/P_0$  of 0.97. The BET surface area was determined using the t-plot method.

Temperature programmed reduction (H<sub>2</sub>-TPR) experiments were carried out using a ChemBET Pulsar TPR/TPD/TPO (Quantachrome Instruments) equipped with a thermal conductivity detector. The gas mixture with composition H<sub>2</sub> (5 vol% in Ar) was used to reduce the sample with heating from room temperature to 1000°C at the rate of 10°C min<sup>-1</sup>. Prior to the reduction measurements, the samples were pre-treated at 200°C under He flow.

Carbon dioxide Temperature programmed desorption (CO<sub>2</sub>-TPD) was performed on a Micromeritics AutoChem-II device equipped with a TCD detector. The materials were degassed for 1 h at 300°C and cooled to 80°C. After outgassing, a pure CO<sub>2</sub> was fed for 1 h in order to adsorb CO<sub>2</sub>, and then the temperature was decreased to 50°C with a flow of He. It was maintained at 50°C for 1 h in order to desorb the physically adsorbed CO<sub>2</sub>. Subsequently, the material was heated up (5°C/min) under He flow from 50°C to 500°C in order to determine the desorption properties of CO<sub>2</sub>. The concentration of desorbed CO<sub>2</sub> was measured with the TCD detector.

Scanning electronic microscopy (SEM) images of both the dried and calcined samples were acquired using a DSM 982 Gemini (Zeiss) microscope with accelerating energy of 3 kV. The samples were coated with carbon prior to SEM investigation.

The STEM images of samples after reduction at 900°C were recorded using FEI Tecnai F20. It is a high-resolution TEM (up to 200 kV) and equipped with an energy filter (Gatan GIF 2000), EDX (EDAX) and HAADF-Detector.

#### 4.3.3. Catalytic performance

Carbon dioxide methanation was conducted in a fixed-bed quartz reactor with an interior diameter of 6 mm at atmospheric pressure and at a temperature of 300°C (using the same catalytic activity testing rig reported in [Chapter 3](#)). Catalytic tests were made under differential conditions in order to have a fair comparison between the prepared catalysts. The thermocouple was inserted into the catalyst bed to measure the actual pretreatment and reaction temperatures. The catalyst was sieved and selected in the 250-500  $\mu\text{m}$  mesh size. Initially, about 25 mg of catalyst diluted with 75 mg of SiC (used as inert) was treated in a pure  $\text{H}_2$  stream (50 mL/min) for 2 h at 900°C and cooled down to the desired reaction temperature in an  $\text{N}_2$  stream. When the temperature became stable, a mixture of  $\text{H}_2$ ,  $\text{CO}_2$ , and  $\text{N}_2$  (in the ratio of 76, 19, and 5 % respectively) was fed into the reactor at a gas hourly space velocity (GHSV) of 217430  $\text{h}^{-1}$ . All gases were controlled by calibrated mass flow controllers. The composition of the outlet gases was analyzed by an on-line Bruker (Scion 456) gas chromatograph equipped with a TCD and FID detectors. The rate of carbon dioxide conversion and selectivity were calculated using similar equations used in [Chapter 3](#).

## 4.4. Results and Discussion

### 4.4.1. Characterization results

**Figure 4.1** illustrates XRD pattern of the hydrotalcite precursors of all the prepared catalysts. The samples showed reflection at  $2\theta = 11.6^\circ$ ,  $23.0^\circ$ ,  $35.2^\circ$  which correspond to  $d(003)$ ,  $d(006)$  and  $d(009)$  basal planes in HTs. The nonbasal planes  $d(015)$ ,  $d(018)$ ,  $d(110)$  and  $d(113)$  cause reflexes at  $2\theta = 38.9^\circ$ ,  $45.9^\circ$ ,  $60.5^\circ$ ,  $61.8^\circ$ , respectively. The reflexes obtained by XRD analysis were sharp and confirmed a successful synthesis of hydrotalcite-like precursors.

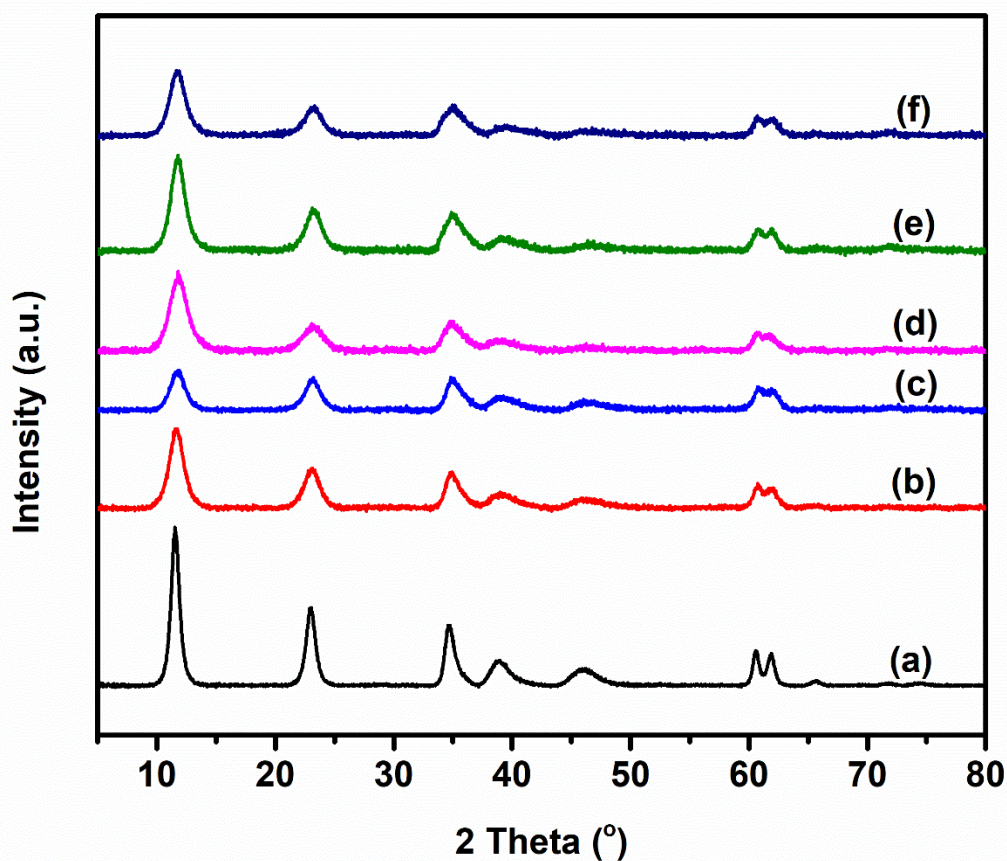


**Figure 4.1** XRD diffraction patterns of dried samples: (a)  $\text{Mg}_{0.75}\text{Al}_{0.25}$  (b)  $\text{Ni}_{0.12}\text{Fe}_{0.012}\text{Mg}_{0.63}\text{Al}_{0.238}$  (c)  $\text{Ni}_{0.2}\text{Fe}_{0.02}\text{Mg}_{0.55}\text{Al}_{0.23}$  (d)  $\text{Ni}_{0.4}\text{Fe}_{0.04}\text{Mg}_{0.35}\text{Al}_{0.21}$  (e)  $\text{Ni}_{0.6}\text{Fe}_{0.06}\text{Mg}_{0.15}\text{Al}_{0.19}$  and (f)  $\text{Ni}_{0.75}\text{Fe}_{0.075}\text{Al}_{0.175}$ .

The XRD patterns of the as-calcined samples along with NiO and MgO-Al<sub>2</sub>O<sub>3</sub> as references were shown in **Figure 4.2**. On the basis of literature data [9, 10], it is assumed that a solid solution of Ni<sub>x</sub>Mg<sub>1-x</sub>O has formed. The Al<sup>3+</sup> and Fe<sup>3+</sup> ions are expected to be incorporated partly into the MgO lattice leading to a periclase-type phase (Ni, Al)<sub>x</sub>Mg<sub>1-x</sub>O in which Mg<sup>2+</sup> is substituted both by Ni<sup>2+</sup> and Al<sup>3+</sup> [10-12]. Furthermore, the characteristic reflections at 37.3°, 43.4°, 62.9°, 75.5° and 79.4° for NiO and the reflections at 37.2°, 43.2°, 62.4° and 78.9° for MgO (periclase) were observed, corresponding to (111), (200), (220), (311) and (222) of the face-centered cubic (fcc) NiO and MgO phase, respectively.

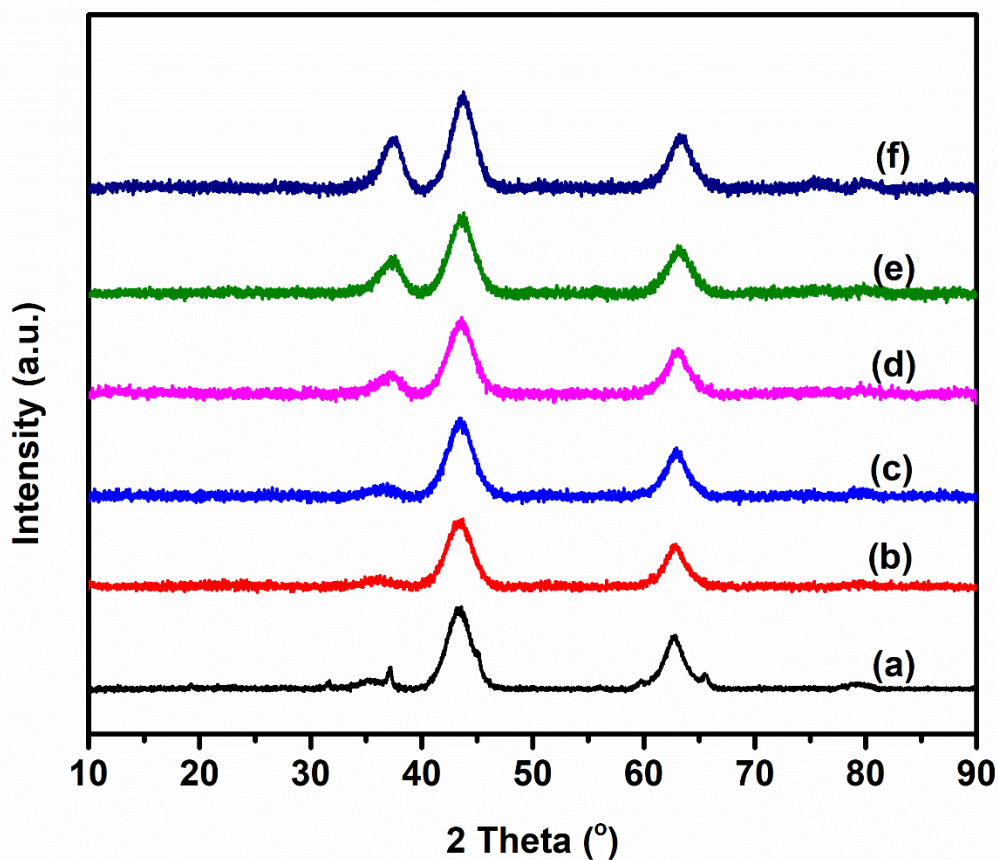


**Figure 4.2** XRD diffraction patterns of calcined samples: (a) Mg<sub>0.75</sub>Al<sub>0.25</sub> (b) Ni<sub>0.12</sub>Fe<sub>0.012</sub>Mg<sub>0.63</sub>Al<sub>0.238</sub> (c) Ni<sub>0.2</sub>Fe<sub>0.02</sub>Mg<sub>0.55</sub>Al<sub>0.23</sub> (d) Ni<sub>0.4</sub>Fe<sub>0.04</sub>Mg<sub>0.35</sub>Al<sub>0.21</sub> (e) Ni<sub>0.6</sub>Fe<sub>0.06</sub>Mg<sub>0.15</sub>Al<sub>0.19</sub> and (f) Ni<sub>0.75</sub>Fe<sub>0.075</sub>Al<sub>0.175</sub>.

After reduction in a flow of H<sub>2</sub> for 2 h at 900°C (Figure 4.3), sharp peaks ascribed to metallic Ni at 44.4° (111), 51.8° (200) and 76.4° (220) appeared and the peaks assigned to MgO were still discerned for the catalysts with higher loading of MgO [10, 13]. The intensity of reflections characteristic for the periclase-like structure of mixed oxides decreasing with the increasing nickel content and they were absent for sample Ni<sub>0.75</sub>Fe<sub>0.075</sub>Al<sub>0.175</sub>. Upon reduction treatment, nickel species are extracted from the framework of periclase-like mixed oxides. No peaks assigned to Fe species were observed in the XRD patterns of Ni-Fe (Mg, Al)O<sub>x</sub>, neither on the calcined sample nor on the reduced one, suggesting that Fe species were highly dispersed in Ni (Mg, Al)O<sub>x</sub> matrix in a stabilized state.

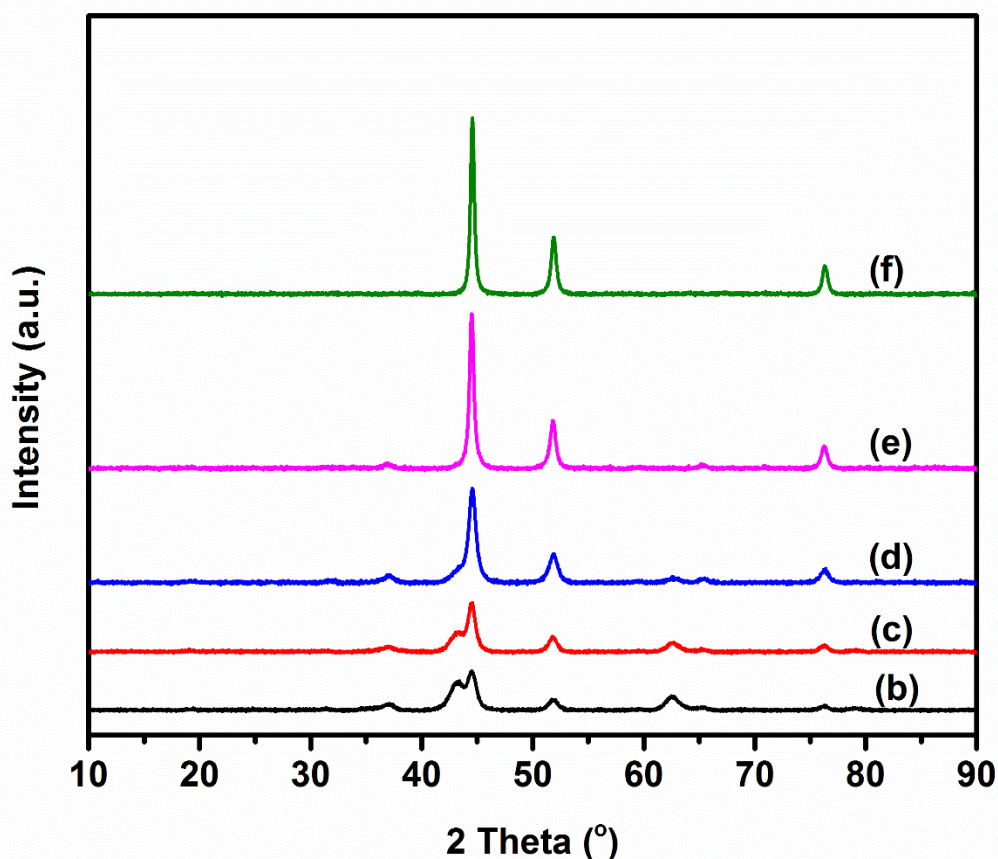


**Figure 4.3** XRD diffraction patterns of reduced samples: (b) Ni<sub>0.12</sub>Fe<sub>0.012</sub>Mg<sub>0.63</sub>Al<sub>0.238</sub> (c) Ni<sub>0.2</sub>Fe<sub>0.02</sub>Mg<sub>0.55</sub>Al<sub>0.23</sub> (d) Ni<sub>0.4</sub>Fe<sub>0.04</sub>Mg<sub>0.35</sub>Al<sub>0.21</sub> (e) Ni<sub>0.6</sub>Fe<sub>0.06</sub>Mg<sub>0.15</sub>Al<sub>0.19</sub> and (f) Ni<sub>0.75</sub>Fe<sub>0.075</sub>Al<sub>0.175</sub>.

As shown in **Table 4.1**, BET surface areas range between 174-234 m<sup>2</sup>/g) were obtained from as-calcined Ni-Fe (Mg, Al)O<sub>x</sub> samples, a slight decrease (about 60 m<sup>2</sup>/g) in the surface area was observed on the Ni-Fe (Al)O<sub>x</sub> catalyst which might be due the higher metal loading which results in pore blockage during the substitution of Mg by Ni. A similar trend was also observed for the total pore volume values. The metal loading was also measured by using XRF and summarized in **Table 4.1**. The compositions were found to be close to the nominal values used during the synthesis.

**Table 4.1** Physicochemical properties of calcined samples.

Catalyst	BET SSA <sup>a</sup> (m <sup>2</sup> /g)	Total PV <sup>b</sup> (mL/g)	Mole % (metal basis) <sup>c</sup>			
			Measured by XRF/Nominal value			
			Ni	Fe	Mg	Al
Mg <sub>0.75</sub> Al <sub>25</sub>	210	0.73	-	-	69.7/ <b>75</b>	30.3/ <b>25</b>
Ni <sub>0.12</sub> Fe <sub>0.012</sub> Mg <sub>0.63</sub> Al <sub>0.238</sub>	205	0.55	12.4/ <b>12</b>	1.6/ <b>1.2</b>	62.9/ <b>63</b>	23.1/ <b>23.8</b>
Ni <sub>0.2</sub> Fe <sub>0.02</sub> Mg <sub>0.55</sub> Al <sub>0.23</sub>	234	0.48	19.4/ <b>20</b>	1.8/ <b>2</b>	59.8/ <b>55</b>	19.0/ <b>23</b>
Ni <sub>0.4</sub> Fe <sub>0.04</sub> Mg <sub>0.35</sub> Al <sub>0.21</sub>	219	0.48	44.4/ <b>40</b>	4.2/ <b>4</b>	37.2/ <b>35</b>	14.2/ <b>21</b>
Ni <sub>0.6</sub> Fe <sub>0.06</sub> Mg <sub>0.15</sub> Al <sub>0.19</sub>	190	0.42	62.5/ <b>60</b>	5.9/ <b>6</b>	19.4/ <b>15</b>	12.2/ <b>19</b>
Ni <sub>0.75</sub> Fe <sub>0.075</sub> Al <sub>0.175</sub>	174	0.53	79.2/ <b>75</b>	7.4/ <b>7.5</b>	-	13.4/ <b>17.5</b>

<sup>a, b</sup> Calculated by the Multipoint-BET equation from N<sub>2</sub> adsorption branch.

<sup>c</sup> Measured by XRF analysis

**Fig. 4.4** displayed the H<sub>2</sub>-TPR profiles of the calcined samples. For the samples with a lower content of Ni, a weak H<sub>2</sub> consumption peak at 450°C was identified, which was attributed to the reduction of Ni located at the outermost layer of the support [14, 15]. The broad and intense peak at around 913°C could be assigned to the reduction of Ni<sup>2+</sup> located deep in the lattice of the Ni-Mg solid solution [16]. The higher temperature peak was shifted to a lower value (from 913°C to 604°C) while increasing the amount of active metal loaded. This shift in reduction temperature resulted from the weak interaction between the (Mg, Al)O<sub>x</sub> support and the active metals. Moreover, no reduction peak was observed for the Mg<sub>0.75</sub>Al<sub>0.25</sub> sample which indicates all the reduction peaks are contributed by the Ni-Fe active metals presented in the samples.

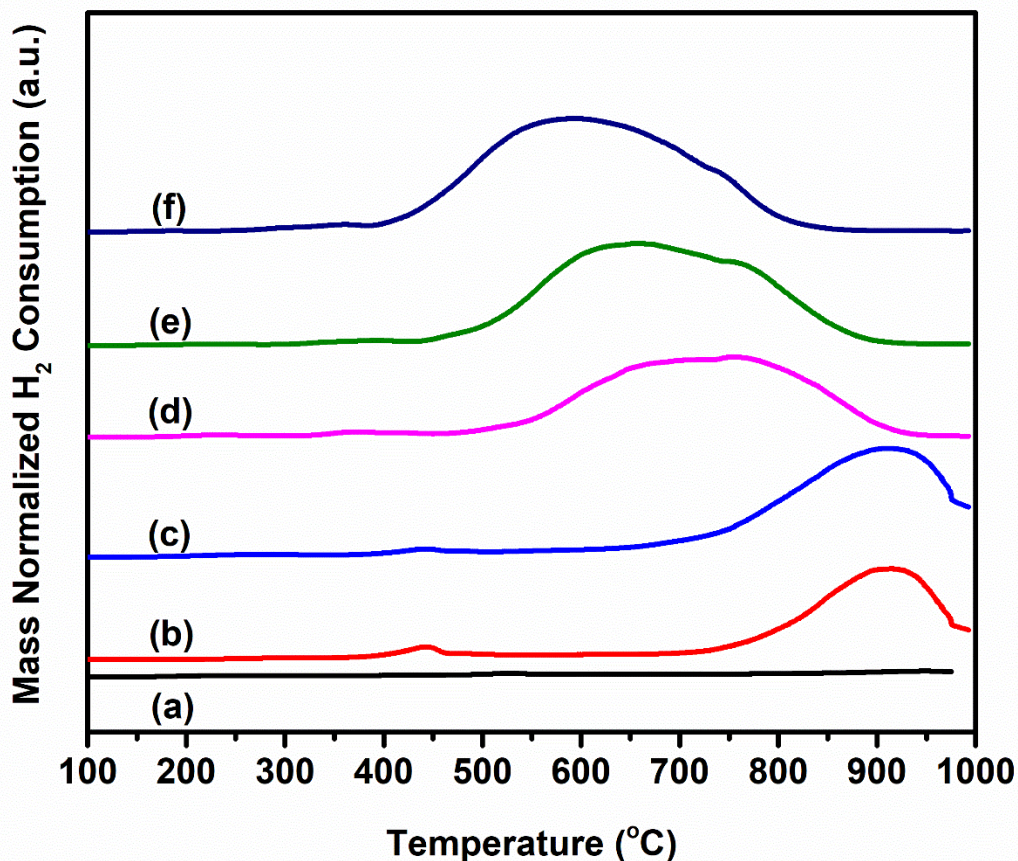


**Figure 4.4** H<sub>2</sub>-TPR profiles of calcined samples: (a) Mg<sub>0.75</sub>Al<sub>0.25</sub> (b) Ni<sub>0.12</sub>Fe<sub>0.012</sub>Mg<sub>0.63</sub>Al<sub>0.238</sub> (c) Ni<sub>0.2</sub>Fe<sub>0.02</sub>Mg<sub>0.55</sub>Al<sub>0.23</sub> (d) Ni<sub>0.4</sub>Fe<sub>0.04</sub>Mg<sub>0.35</sub>Al<sub>0.21</sub> (e) Ni<sub>0.6</sub>Fe<sub>0.06</sub>Mg<sub>0.15</sub>Al<sub>0.19</sub> and (f) Ni<sub>0.75</sub>Fe<sub>0.075</sub>Al<sub>0.175</sub>.

CO<sub>2</sub>-TPD is typically applied to determine the strength and density of the basic sites in mixed oxides derived from the calcination of hydrotalcites. **Figure 4.5** shows the CO<sub>2</sub>-TPD profiles obtained for the hydrotalcite derived samples. The CO<sub>2</sub>-TPD profiles were mathematically treated and deconvoluted into three Gaussian peaks corresponding to weak basic sites (110 - 130°C), medium basic sites (200 - 220°C) and strong basic sites (295 - 305°C). The contribution to each type of basic sites was estimated and presented in **Table 4.2**. The calcined catalysts showed a total concentration of basic sites in the range of 1.7-7.6 mmol/g. The amount of basic sites decreases with decreasing Lewis base concentration (i.e MgO) in the sample.



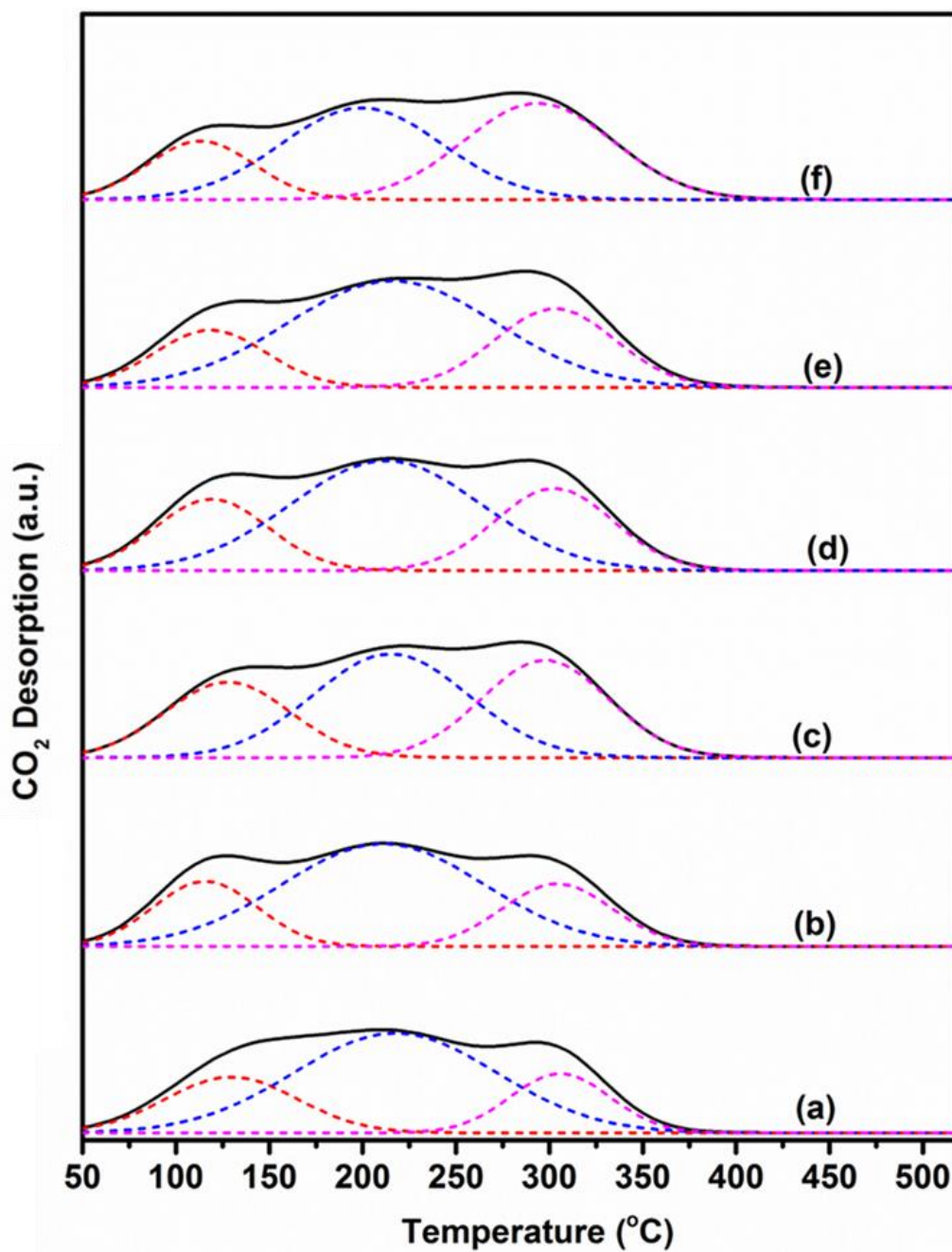


**Figure 4.5** CO<sub>2</sub>-TPD profiles of calcined catalysts: (a) Mg<sub>0.75</sub>Al<sub>0.25</sub> (b) Ni<sub>0.12</sub>Fe<sub>0.012</sub>Mg<sub>0.63</sub>Al<sub>0.238</sub> (c) Ni<sub>0.2</sub>Fe<sub>0.02</sub>Mg<sub>0.55</sub>Al<sub>0.23</sub> (d) Ni<sub>0.4</sub>Fe<sub>0.04</sub>Mg<sub>0.35</sub>Al<sub>0.21</sub> (e) Ni<sub>0.6</sub>Fe<sub>0.06</sub>Mg<sub>0.15</sub>Al<sub>0.19</sub> and (f) Ni<sub>0.75</sub>Fe<sub>0.075</sub>Al<sub>0.175</sub>.

**Table 4.2** Distribution of the basic sites at different desorption temperatures.

Catalyst	Total basic sites <sup>a</sup> (mmol/g <sub>cat</sub> )	Basic sites (%)		
		Weak Basic Sites <sup>b</sup>	Medium Basic Sites <sup>c</sup>	Strong Basic Sites <sup>d</sup>
Mg <sub>0.75</sub> Al <sub>25</sub>	7.6	22	60	18
Ni <sub>0.12</sub> Fe <sub>0.012</sub> Mg <sub>0.63</sub> Al <sub>0.238</sub>	6.8	20	60	20
Ni <sub>0.2</sub> Fe <sub>0.02</sub> Mg <sub>0.55</sub> Al <sub>0.23</sub>	5.4	25	43	32
Ni <sub>0.4</sub> Fe <sub>0.04</sub> Mg <sub>0.35</sub> Al <sub>0.21</sub>	3.3	21	54	25
Ni <sub>0.6</sub> Fe <sub>0.06</sub> Mg <sub>0.15</sub> Al <sub>0.19</sub>	2.1	17	58	25
Ni <sub>0.75</sub> Fe <sub>0.075</sub> Al <sub>0.175</sub>	1.4	17	42	41

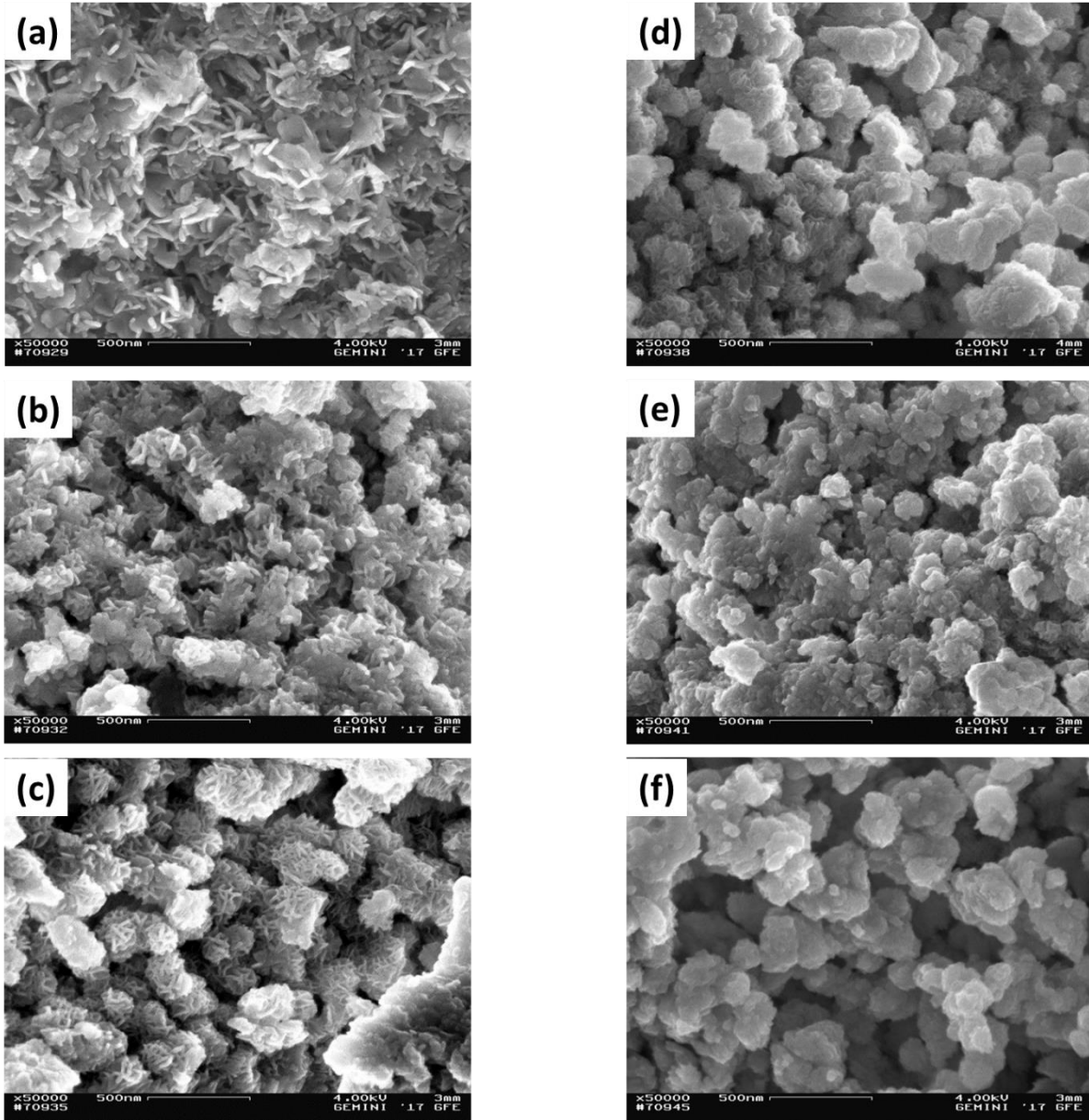
<sup>a</sup> Estimated over the whole temperature

<sup>b</sup> Percentage of weak basic sites: Temperature = 110 - 130°C

<sup>c</sup> Percentage of medium basic sites: Temperature = 200 - 220°C

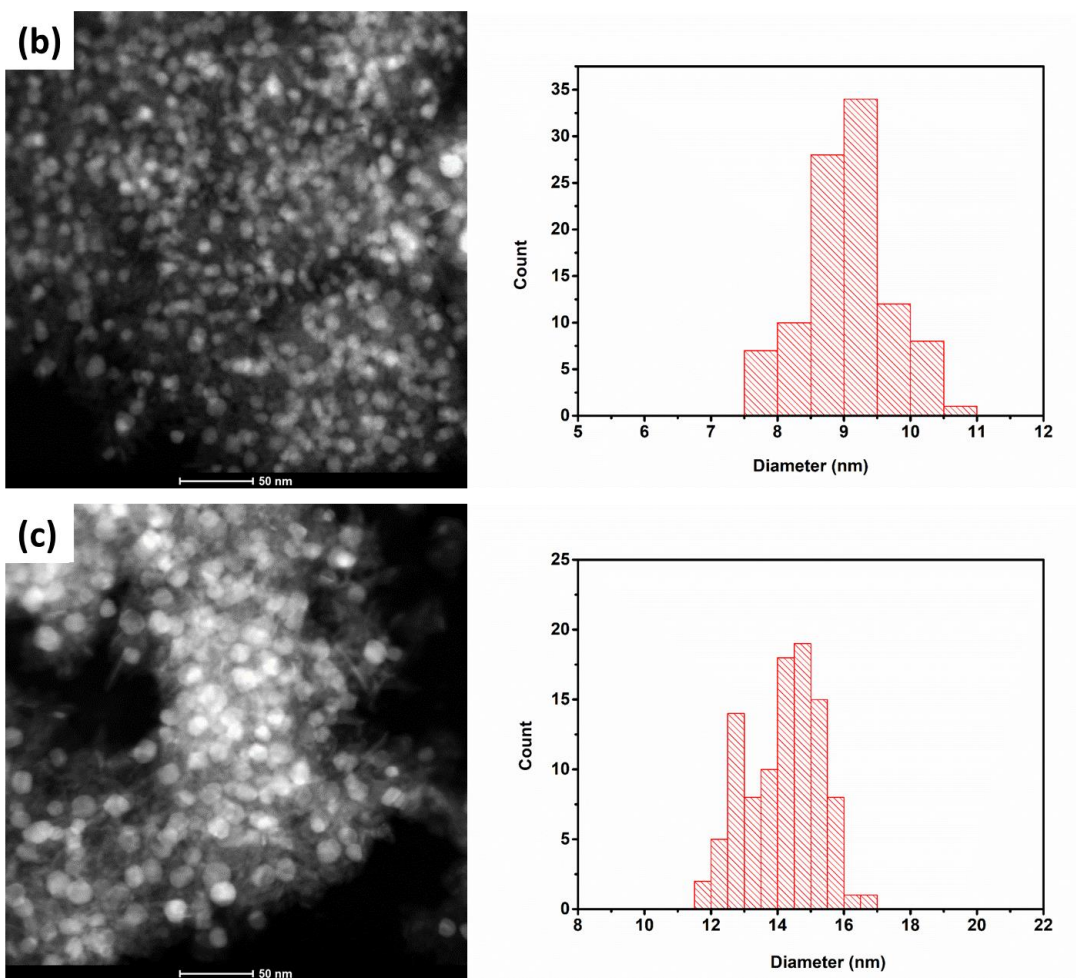
<sup>d</sup> Percentage of strong basic sites: Temperature = 295 - 305°C

SEM images (**Figure 4.6**) exhibit platelet-like crystals for Mg<sub>0.75</sub>Al<sub>25</sub> and Ni<sub>0.12</sub>Fe<sub>0.012</sub>Mg<sub>0.63</sub>Al<sub>0.238</sub> samples. For the samples with a medium amount of active metal loadings, platelet-like crystals aggregated as rosettes were observed, which are typical for HTs compounds [17-19]. The samples with higher active metal loadings showed stacked particles. Moreover, the platelet-like morphology of samples with lower active metals remains intact during the calcination step (**ANNEX<sup>4</sup> Figure 1**), which is in good agreement with the findings of Mette et al. [20].



**Figure 4.6** SEM images of dried samples: (a)  $Mg_{0.75}Al_{0.25}$  (b)  $Ni_{0.12}Fe_{0.012}Mg_{0.63}Al_{0.238}$  (c)  $Ni_{0.2}Fe_{0.02}Mg_{0.55}Al_{0.23}$  (d)  $Ni_{0.4}Fe_{0.04}Mg_{0.35}Al_{0.21}$  (e)  $Ni_{0.6}Fe_{0.06}Mg_{0.15}Al_{0.19}$  and (f)  $Ni_{0.75}Fe_{0.075}Al_{0.175}$ .

Darkfield STEM micrographs obtained for the reduced catalysts and the distribution of nickel particles are shown in [Fig. 4.7](#). In all micrographs, bright spots were observed, which were ascribed to the  $\text{Ni}^0$  particles, dispersed on the support, as confirmed by the diffraction analysis. All catalysts exhibited a homogeneous distribution of nickel particles. The size of nickel particles was dependent on the nickel loading, and as expected, decreased with the decreasing nickel content ([Table 4.3](#)). For the whole set of the hydrotalcite derived catalysts, Ni particle size decreased from 44 nm (sample  $\text{Ni}_{0.75}\text{Fe}_{0.075}\text{Al}_{0.175}$ ) to 9 nm (sample  $\text{Ni}_{0.12}\text{Fe}_{0.012}\text{Mg}_{0.63}\text{Al}_{0.238}$ ).



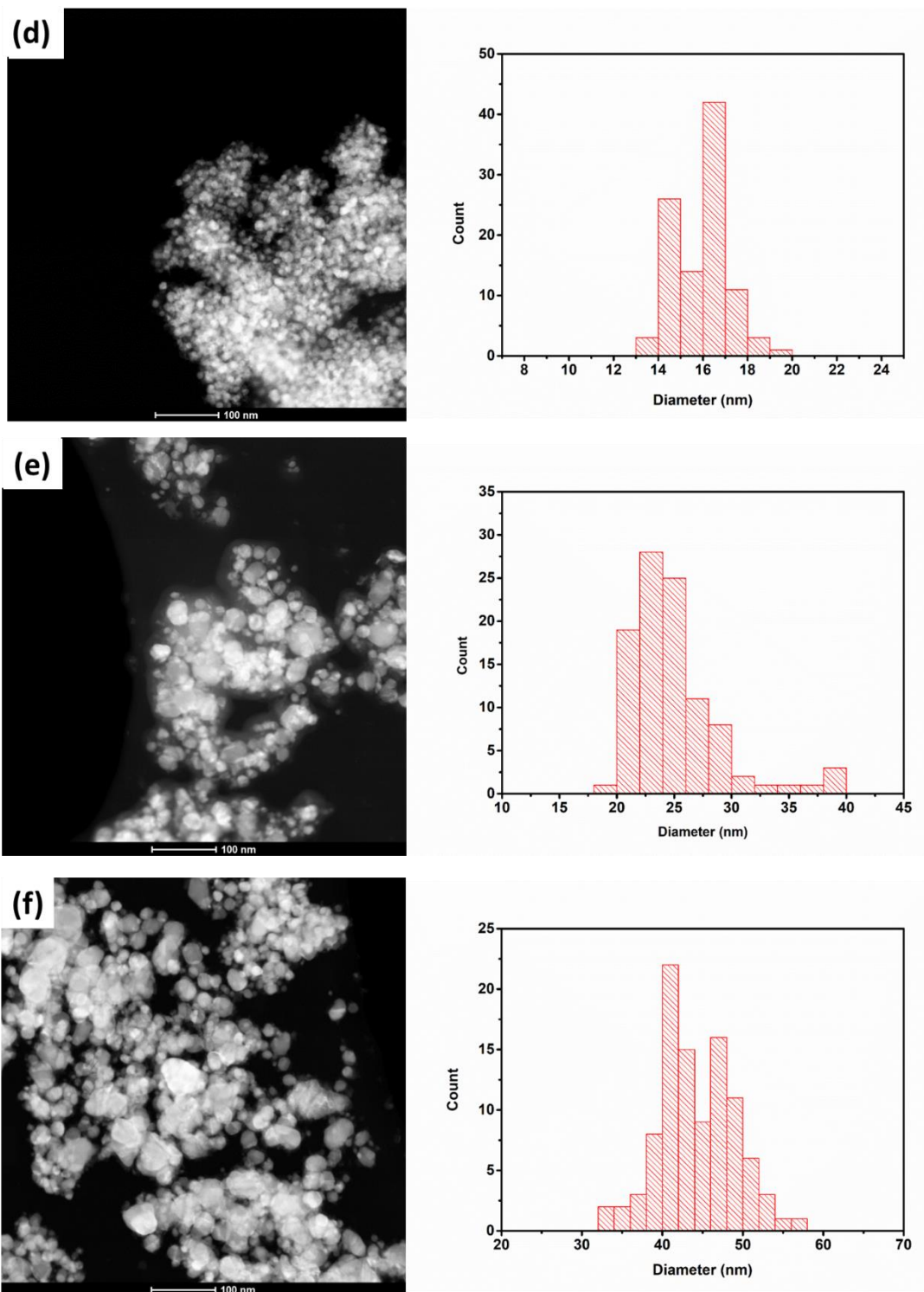


**Figure 4.7** Dark field STEM images and the corresponding histograms of nickel particle size distribution for the reduced catalysts: (b)  $\text{Ni}_{0.12}\text{Fe}_{0.012}\text{Mg}_{0.63}\text{Al}_{0.238}$  (c)

Ni<sub>0.2</sub>Fe<sub>0.02</sub>Mg<sub>0.55</sub>Al<sub>0.23</sub> (d) Ni<sub>0.4</sub>Fe<sub>0.04</sub>Mg<sub>0.35</sub>Al<sub>0.21</sub> (e) Ni<sub>0.6</sub>Fe<sub>0.06</sub>Mg<sub>0.15</sub>Al<sub>0.19</sub> and (f) Ni<sub>0.75</sub>Fe<sub>0.075</sub>Al<sub>0.175</sub>.

**Table 4.3** shows the metal dispersion which is estimated from the average particle size and is found to be decreased as the particle diameter is increased.

**Table 4.3** The average Ni particle size estimated based on STEM images of the reduced samples.

Catalyst	Average Ni particle size <sup>a</sup> (nm)	Metal dispersion <sup>b</sup> (%)
Ni <sub>0.12</sub> Fe <sub>0.012</sub> Mg <sub>0.63</sub> Al <sub>0.238</sub>	9	11.1
Ni <sub>0.2</sub> Fe <sub>0.02</sub> Mg <sub>0.55</sub> Al <sub>0.23</sub>	14	7.14
Ni <sub>0.4</sub> Fe <sub>0.04</sub> Mg <sub>0.35</sub> Al <sub>0.21</sub>	16	6.25
Ni <sub>0.6</sub> Fe <sub>0.06</sub> Mg <sub>0.15</sub> Al <sub>0.19</sub>	25	4.00
Ni <sub>0.75</sub> Fe <sub>0.075</sub> Al <sub>0.175</sub>	44	2.27

<sup>a</sup> Values calculated by analysis of STEM images using *Image J*.

<sup>b</sup> Determined using the equation % Dispersion =  $A_{\text{Ni-Fe}} / \text{Average particle size (nm)} \times 100$ .

$A_{\text{Ni-Fe}} = A_{\text{Ni}}[\text{Ni}/(\text{Ni}+\text{Fe})] + A_{\text{Fe}}[\text{Fe}/(\text{Ni}+\text{Fe})]$ ,  $A_{\text{Ni}} = 0.971$  nm and  $A_{\text{Fe}} = 1.225$  nm.

#### 4.4.2. Activity, selectivity, and stability of the hydrotalcite derived catalysts towards CO<sub>2</sub> methanation

**Figure 4.8** depicts the rate of CO<sub>2</sub> conversions measured during the CO<sub>2</sub> methanation performed at 300°C over different hydrotalcite-derived catalysts. The activity of tested catalysts in CO<sub>2</sub> methanation reaction may be divided into two groups. The samples with the high and low content of Ni (active metal), obtained by substitution of 12 or 75% of Mg by Ni, showed a lower rate of CO<sub>2</sub> conversion, and except for the 0% Ni (Mg<sub>0.75</sub>Al<sub>0.25</sub> catalyst), excess CO was registered in the products. The catalytic activity was strongly affected by the active metal content to basic site ratio. On the other hand, the second group, the catalysts with the medium loading of Ni (20, 40, and 60% of Ni) exhibited a higher rate of CO<sub>2</sub> conversion than the other catalysts. Sample Mg<sub>0.75</sub>Al<sub>0.25</sub> (i.e. only the basic support) turned out to be the least active of all the tested catalysts. No CH<sub>4</sub> or CO products were detected from the reaction performed by using this catalyst. The rate of CO<sub>2</sub>

conversion value ranges from 0 mol CO<sub>2</sub> conv./mol<sub>Ni+Fe</sub>/S by the Mg<sub>0.75</sub>Al<sub>0.25</sub> catalyst to 0.251 mol CO<sub>2</sub> conv./mol<sub>Ni+Fe</sub>/S obtained by the Ni<sub>0.2</sub>Fe<sub>0.02</sub>Mg<sub>0.55</sub>Al<sub>0.23</sub> catalyst.

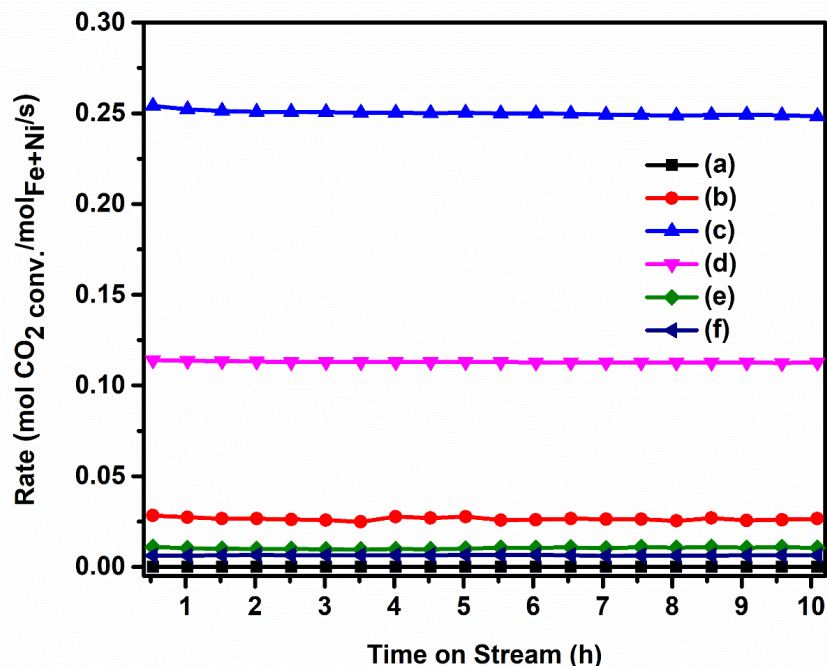


**Figure 4.8** Rate of CO<sub>2</sub> conversion of all prepared catalysts under differential reaction conditions: gas mixture with CO<sub>2</sub>:H<sub>2</sub> = 1:4, P = 1 atm, T = 300°C, and GHSV = 217430 h<sup>-1</sup>): (a) Mg<sub>0.75</sub>Al<sub>0.25</sub> (b) Ni<sub>0.12</sub>Fe<sub>0.012</sub>Mg<sub>0.63</sub>Al<sub>0.238</sub> (c) Ni<sub>0.2</sub>Fe<sub>0.02</sub>Mg<sub>0.55</sub>Al<sub>0.23</sub> (d) Ni<sub>0.4</sub>Fe<sub>0.04</sub>Mg<sub>0.35</sub>Al<sub>0.21</sub> (e) Ni<sub>0.6</sub>Fe<sub>0.06</sub>Mg<sub>0.15</sub>Al<sub>0.19</sub> and (f) Ni<sub>0.75</sub>Fe<sub>0.075</sub>Al<sub>0.175</sub>.

Ni-based catalysts supported on alumina, or magnesia [21], as these oxides are also present in the catalysts studied in this work, as well as hydrotalcite-like systems [22-25] are reported in the literature. But, reaction conditions are largely different from the current experimental conditions used which makes a direct comparison impossible. However, some general activity and structure relationships of such catalysts can be derived. When the activity of hydrotalcite derived catalysts are compared with single oxide supported Ni-based catalysts, the hydrotalcite derived materials found to be more active and stable towards CO<sub>2</sub> methanation. Additionally, the Ni-Al hydrotalcites with higher active metal loading (about 75-80% of Ni) [8, 19, 25] seem to be more active than those catalysts with a lower Ni content when considered the CO<sub>2</sub> conversion rate per gram of catalyst used during the reaction. On the other hand, when the catalytic activity, instead, is

normalized per gram of the active metal, the hydrotalcite catalysts with higher Ni loading, are less active than the catalysts prepared (i.e. Ni loading of the most active catalyst was 20%). Hence, the activity is not directly related to the Ni loading (wt.-% of Ni) but also to the amount of basic sites. Therefore, the activity of hydrotalcite derived catalysts can be enhanced by optimizing the basic sites to active metal ratio.

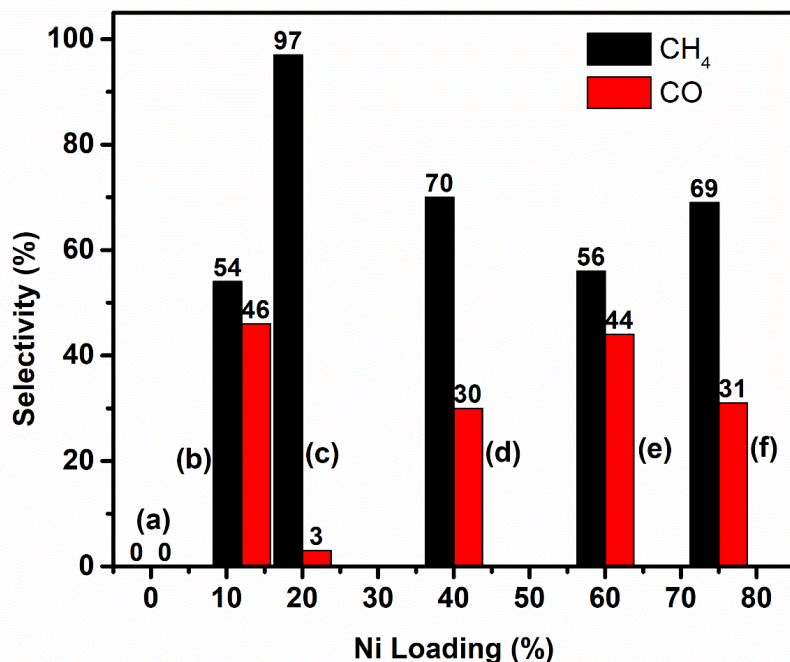


**Figure 4.9** Selectivity towards CH<sub>4</sub> and CO of all prepared catalysts under differential reaction conditions: gas mixture with CO<sub>2</sub>:H<sub>2</sub> = 1:4, P = 1 atm, T = 300°C, and GHSV = 217430 h<sup>-1</sup>): (a) Mg<sub>0.75</sub>Al<sub>0.25</sub> (b) Ni<sub>0.12</sub>Fe<sub>0.012</sub>Mg<sub>0.63</sub>Al<sub>0.238</sub> (c) Ni<sub>0.2</sub>Fe<sub>0.02</sub>Mg<sub>0.55</sub>Al<sub>0.23</sub> (d) Ni<sub>0.4</sub>Fe<sub>0.04</sub>Mg<sub>0.35</sub>Al<sub>0.21</sub> (e) Ni<sub>0.6</sub>Fe<sub>0.06</sub>Mg<sub>0.15</sub>Al<sub>0.19</sub> and (f) Ni<sub>0.75</sub>Fe<sub>0.075</sub>Al<sub>0.175</sub>.

The selectivity towards methane and carbon monoxide during catalytic tests for all catalysts is shown in **Figure 4.9**. The Mg<sub>0.75</sub>Al<sub>0.25</sub> catalyst was not selective to both products. For the other catalysts tested, a general trend of decreasing in selectivity towards CH<sub>4</sub> was obtained as the activity of the catalysts decreased. About 97% selectivity to CH<sub>4</sub> was recorded for the Ni<sub>0.2</sub>Fe<sub>0.02</sub>Mg<sub>0.55</sub>Al<sub>0.23</sub> catalyst. The selectivity towards side product CO was increased with the catalyst which was less active towards the CO<sub>2</sub> methanation. No other products except CH<sub>4</sub> and CO were detected for most of the catalysts tested.



In order to assess the stability, 20 h test was performed on the  $\text{Ni}_{0.2}\text{Fe}_{0.02}\text{Mg}_{0.55}\text{Al}_{0.23}$  catalyst and reported in **Figure 4.10**. No change in activity was registered under the current experimental conditions. This may be explained by the absence of sintering, due to the better metal dispersion and the absence of graphite-like deposits (proved in *Chapter 3* for the same types of catalysts).

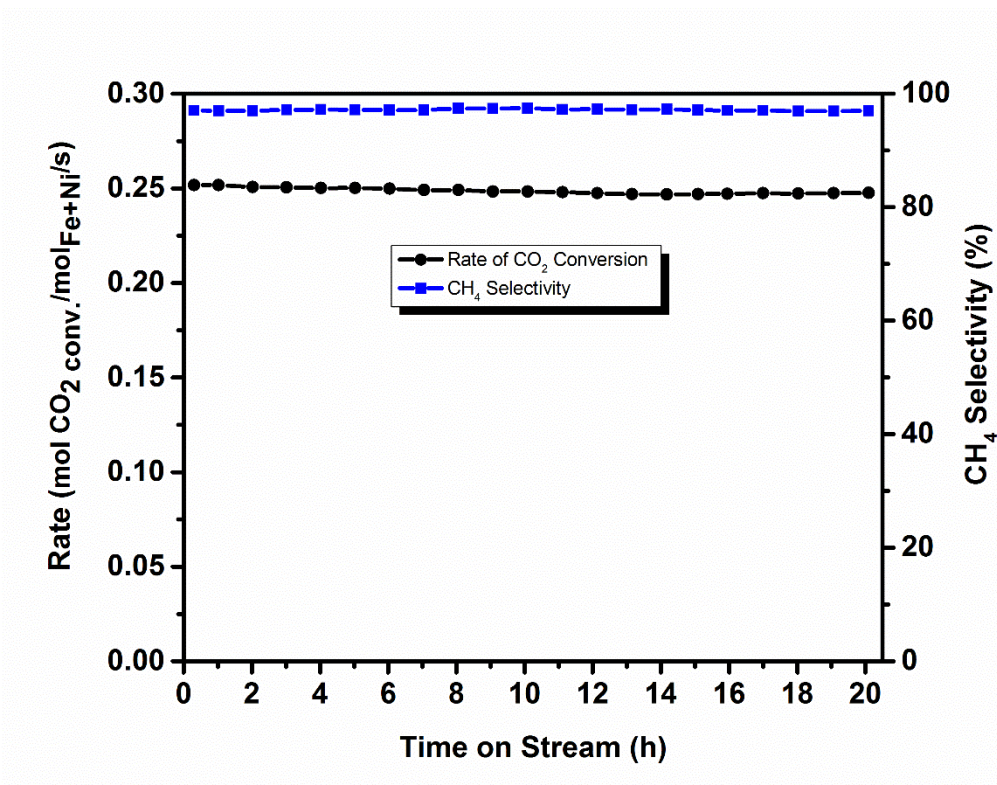


**Figure 4.10** Stability of  $\text{Ni}_{0.2}\text{Fe}_{0.02}\text{Mg}_{0.55}\text{Al}_{0.23}$  catalyst under differential reaction conditions: gas mixture with  $\text{CO}_2:\text{H}_2 = 1:4$ ,  $P = 1$  atm,  $T = 300^\circ\text{C}$ , and  $\text{GHSV} = 217430 \text{ h}^{-1}$ .

The catalysts performance vs. the amount of Mg on the sample was compared and summarized in **Figure 4.11 (A)**. The trend indicates a catalyst with a substitution of 20% of Mg by Ni and 2% of Al by Fe was found as the optimum value for better activity and selectivity of the hydrotalcites-like catalysts.

Except for the catalysts without or lower content of Ni, the higher catalytic activity of catalysts with medium and higher %Ni can be further correlated to the amount of total basic sites present in the sample. The  $\text{Mg}_{0.75}\text{Al}_{0.25}$  and  $\text{Ni}_{0.12}\text{Fe}_{0.012}\text{Mg}_{0.63}\text{Al}_{0.238}$  catalysts were therefore excluded from

the correlation plot in order to have a fair comparison between the catalysts with medium and higher active metal loadings. **Figure 4.11 (B)** therefore, shows a linear correlation between rate of CO<sub>2</sub> conversion and the amount of total basic sites which is in good agreement with Pan et al. [26] who claimed that the presence of higher amount of basic sites resulted in improved catalytic activity due to the promoted formation of monodentate formate species, which was an active intermediate in the formation of methane from CO<sub>2</sub>.

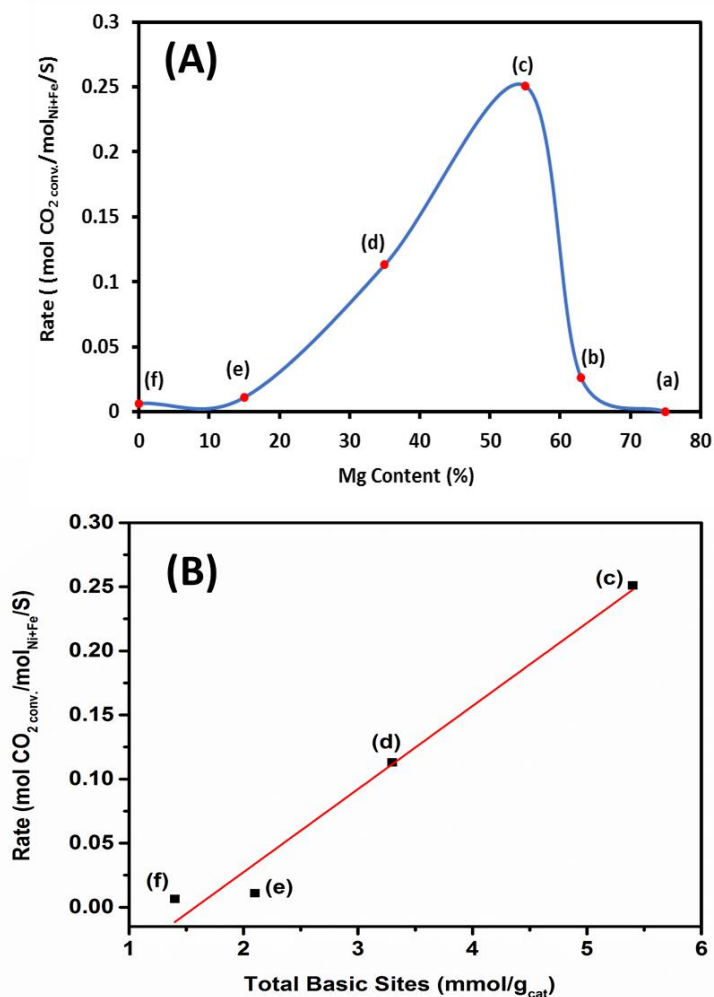


**Figure 4.11 (A)** Comparison of % Mg vs catalytic activity (differential reaction conditions: gas mixture with CO<sub>2</sub>:H<sub>2</sub> = 1:4, P = 1 atm, T = 300°C, and GHSV = 217430 h<sup>-1</sup>): (a) Mg<sub>0.75</sub>Al<sub>0.25</sub> (b) Ni<sub>0.12</sub>Fe<sub>0.012</sub>Mg<sub>0.63</sub>Al<sub>0.238</sub> (c) Ni<sub>0.2</sub>Fe<sub>0.02</sub>Mg<sub>0.55</sub>Al<sub>0.23</sub> (d) Ni<sub>0.4</sub>Fe<sub>0.04</sub>Mg<sub>0.35</sub>Al<sub>0.21</sub> (e) Ni<sub>0.6</sub>Fe<sub>0.06</sub>Mg<sub>0.15</sub>Al<sub>0.19</sub> and (f) Ni<sub>0.75</sub>Fe<sub>0.075</sub>Al<sub>0.175</sub>. **(B)** Rate of

CO<sub>2</sub> conversion vs total amount of basic sites: (c) Ni<sub>0.2</sub>Fe<sub>0.02</sub>Mg<sub>0.55</sub>Al<sub>0.23</sub> (d) Ni<sub>0.4</sub>Fe<sub>0.04</sub>Mg<sub>0.35</sub>Al<sub>0.21</sub> (e) Ni<sub>0.6</sub>Fe<sub>0.06</sub>Mg<sub>0.15</sub>Al<sub>0.19</sub> and (f) Ni<sub>0.75</sub>Fe<sub>0.075</sub>Al<sub>0.175</sub>.

Furthermore, no direct correlation was obtained between the catalytic activity and amount of strong /weak basic sites obtained from the CO<sub>2</sub>-TPD analysis.

#### 4.5. Conclusion

Hydrotalcite derived catalysts based on Ni-Fe as active metals were prepared by co-precipitation method. The amount of basic sites was tailored by changing the ratio between Mg-Al and Ni-Fe. Characterization techniques confirmed the preparation of catalysts with higher basic sites and low active metal loadings (12%Ni-1.2%Fe) as well as catalysts with higher active metal loadings (up to 75%Ni-7-5%Fe). The as-prepared catalysts were investigated towards low-temperature CO<sub>2</sub> methanation under differential conditions.

The CO<sub>2</sub>-TPD measurements evidence that introduction of Ni and Fe to the Mg-Al hydrotalcites affected the CO<sub>2</sub> adsorption capacity of as-prepared catalysts by decreasing the amount of total basic sites. As verified by H<sub>2</sub>-TPR analyses, the presence of higher amount of active metal influenced also the interaction between Ni and the hydrotalcite-derived matrix, where Ni-species are commonly present in the form of solid oxide solutions NiO-MgO. A shift to lower reduction temperature (from 900°C to 600°C) was observed for the catalysts with relatively higher active metal loading.

The catalytic activity tests revealed that the highest activity was obtained by the Ni<sub>0.2</sub>Fe<sub>0.02</sub>Mg<sub>0.55</sub>Al<sub>0.23</sub> catalyst, which was most probably due to the higher metal dispersion and optimum amount total basic sites. This catalyst attains 0.251 mol CO<sub>2</sub> conv./mol<sub>Ni+Fe</sub>/S the rate of CO<sub>2</sub> conversion at 300°C with a CH<sub>4</sub> selectivity of 97%. The catalyst also showed a stable performance during the 20 h test. Furthermore, for the catalysts with medium and higher %Ni, a linear correlation was obtained between the amount total basic sites and catalytic activity. Therefore, the study under this chapter showed that optimal activity of hydrotalcite derived catalysts can be achieved by tailoring the ratio between Lewis base support content and active

metal loadings. It was also demonstrated that the activity of the as-prepared catalysts is not affected only by the amount of basic sites, can be also influenced by other parameters such as average particle size and dispersion of the active metal.

#### 4.6. References

- [1] P.A. Ussa Aldana, F. Ocampo, K. Kolb, B. Louis, F. Thibault-Starzyk, M. Daturi, P. Bazina, S. Thomas, A.C. Roger, *Catal. Today*, 215 (2013) 201-207.
- [2] Q. Pan, J. Peng, T. Sun, S. Wang, S. Wang, *Catal. Commun.*, 45 (2014) 74-78.
- [3] S.T. Korhonen, M. Calatayud, A.O.I. Krause, *J. Phys. Chem. C*, 112 (2008) 16096-16102.
- [4] A.H. Zamani, R. Ali, W.A.W.A. Bakar, *J. Ind. Eng. Chem.*, 29 (2015) 238-248.
- [5] A.H. Zamani, R. Ali, W.A.W.A. Bakar, *J. Tawain Inst. Chem. Eng.*, 45 (2014) 143-152.
- [6] S. Toemen, W.A.W.A. Bakar, R. Ali, *J. Tawain Inst. Chem. Eng.*, 45 (2014) 2370-2378.
- [7] L. He, Q. Lin, Y. Liu, Y. Huang, *J. Energy Chem.*, 23 (2014) 587-592.
- [8] S. Abate, K. Barbera, E. Giglio, F. Deorsola, S. Bensaid, S. Perathoner, R. Pirone, G. Centi, *Ind. Eng. Chem. Res.*, 55 (2016) 8299-8308.
- [9] F. Arena, F. Frusteri, A. Parmaliana, L. Plyasova, A. N. Shmakov, *J. Chem. Soc. Faraday Trans.* 92 (1996) 469-471.
- [10] D. Matteuzzi, F. Trifirk, A. Vaccari, M. Gazzano, O. Clause, *Mater. Sci. Forum*, 152-153 (1994) 391-394.
- [11] A. F. Lucrédio, G. Jerkiewickz, E. M. Assaf, *Appl. Catal. A*, 333 (2007) 90-95.
- [12] B. Rebours, J.-B. O'Espinoze de laCaillerie, O. Clause, *J. Am. Chem. Soc.*, 116 (1994) 1707-1717.
- [13] M. Gazzano, W. Kagunya, D. Matteuzzi, A. Vaccari, *J. Phys. Chem. B*, 101 (1997) 4514-4519.
- [14] A. Parmaliana, F. Arena, F. Frusteri, N. Giordano, *J. Chem. Soc. Faraday Trans.*, 86 (1990) 2663-2669.
- [15] Q. Liu, J. Gao, M. Zhang, H. Li, F. Gu, G. Xu, Z. Zhong, F. Su, *RSC Adv.*, 4 (2014)16094-16103.

- [16] J. Liu, J. Yu, F. Su, G. Xu, *Catal. Sci. Technol.*, 4 (2014) 472-481.
- [17] A. Vaccari, *Catal. Today*, 41(1998) 53-71.
- [18] Q. Wang, H.H. Tay, D.J.W. Ng, L. Chen, Y. Liu, J. Chang, Z. Zhong, J. Luo, A. Borgna, *ChemSusChem*, 3 (2010) 965-973.
- [19] S. Abelló, F. Medina, D. Tichit, J. Pérez-Ramírez, J.C. Groen, J.E. Sueiras, P. Salagre, Y. Cesteros, *Chem. Eur. J.*, 11 (2005) 728-739.
- [20] K. Mette, S. Kühn, H. Düdder, K. Kähler, A. Tarasov, M. Muhler, M. Behrens, *ChemCatChem*, 6 (2014) 100-104.
- [21] J. Gao, L.-S. Jia, W.-P. Fang, Q.-B. Li, H. Song, *J. Fuel Chem. Technol.* 37 (2009) 573-577.
- [22] S. Tada, T. Shimizu, H. Kameyama, T. Haneda, R. Kikuchi, *Int. J. Hydrogen Energy* 37 (2012) 5527-5531.
- [23] R. Dębek, M.E. Galvez, F. Launay, M. Motak, T. Grzybek, P. Da Costa, *Int. J. Hydrogen Energy* 41 (2016) 11616-11623.
- [24] A. Serrano-Lotina, L. Rodríguez, G. Muñoz, L. Daza, *J. Power Sources* 196 (2011) 4404 - 4410.
- [25] N. Bette, J. Thielemann, M. Schreiner, F. Mertens, *ChemCatChem*, 8 (2016) 2903 - 2906
- [26] Q. Pan, J. Peng, T. Sun, D. Gao, S. Wang, S. Wang, *Fuel Processing Technology*, 123 (2014) 166-171

ANNEX 4

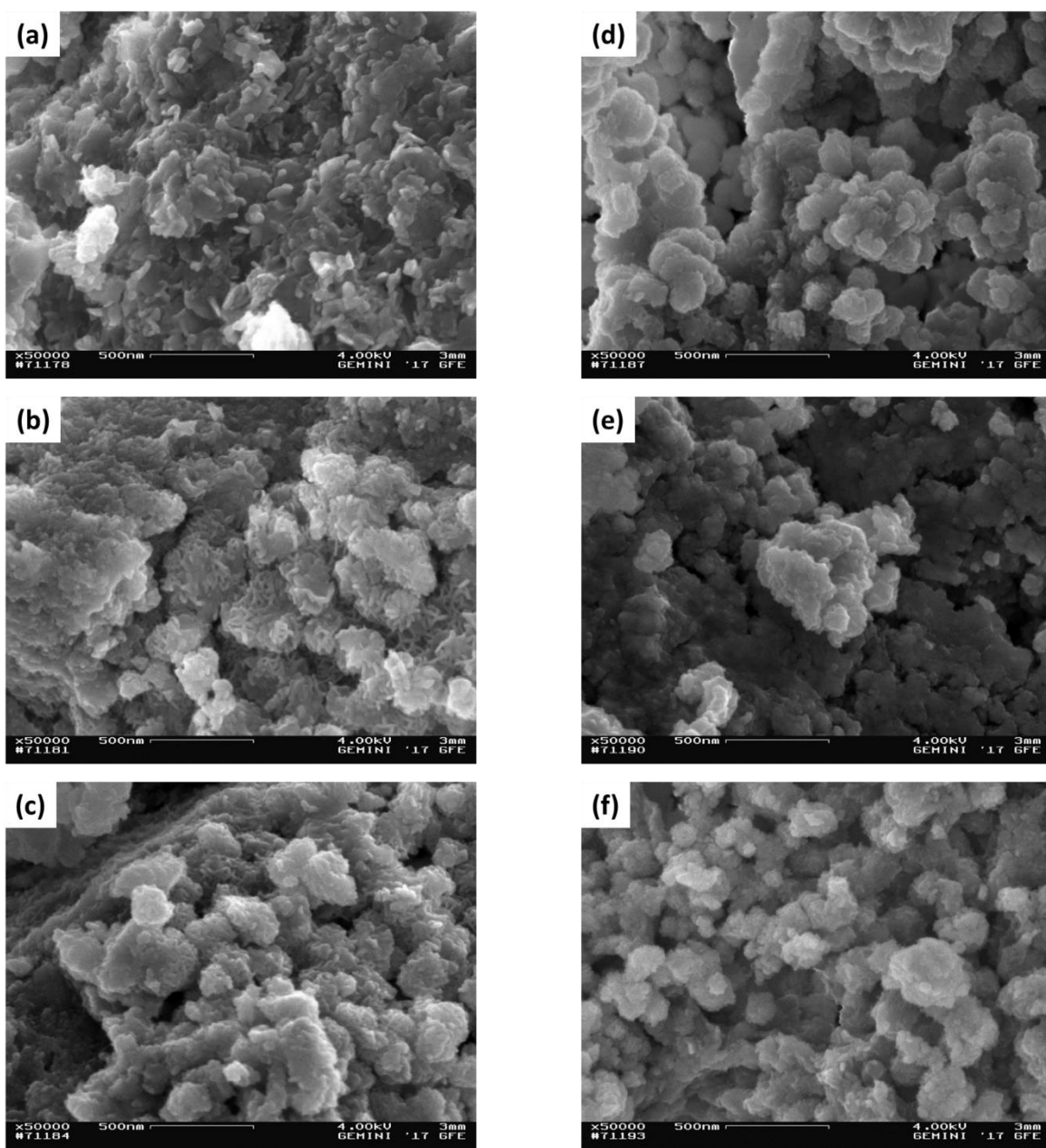


**Figure 1** SEM micrographs of calcined hydrotalcite derived mixed oxides: (a)  $\text{Mg}_{0.75}\text{Al}_{0.25}$  (b)  $\text{Ni}_{0.12}\text{Fe}_{0.012}\text{Mg}_{0.63}\text{Al}_{0.238}$  (c)  $\text{Ni}_{0.2}\text{Fe}_{0.02}\text{Mg}_{0.55}\text{Al}_{0.23}$  (d)  $\text{Ni}_{0.4}\text{Fe}_{0.04}\text{Mg}_{0.35}\text{Al}_{0.21}$  (e)  $\text{Ni}_{0.6}\text{Fe}_{0.06}\text{Mg}_{0.15}\text{Al}_{0.19}$  and (f)  $\text{Ni}_{0.75}\text{Fe}_{0.075}\text{Al}_{0.175}$ .

# CHAPTER 5

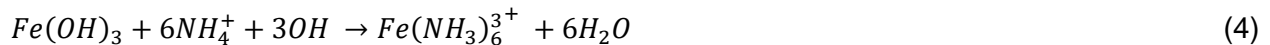
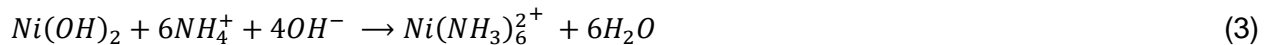
## 5. Fe - promoted Ni/ $\gamma$ -Al<sub>2</sub>O<sub>3</sub> nanosheets as highly active and stable catalyst for CO<sub>2</sub> methanation

### 5.1. Introduction

Given the strong dependence of the catalytic activity on active sites exposure, it is believed that different morphologies of the catalysts will differently contribute to the geometrical exposure of active sites [1-3]. Despite its crucial role on catalytic CO<sub>2</sub> methanation, the effect of catalyst morphology has so far remained unexplored.

In this chapter novel materials with improved properties in CO<sub>2</sub> methanation were prepared via a two-step hydrothermal synthesis in the presence of Fe as a promoter. This preparation leads to the formation of nanosheets, due to a partial dissolution of the metal hydroxides formed during the first-step of hydrothermal reaction [1, 4].

Zhang et al. [1] reported a two-step hydrothermal synthesis method to improve the reducibility of nanosheet like Ni/Al<sub>2</sub>O<sub>3</sub> catalyst by altering the dispersion properties of Ni metal on the support. Briefly, the partial dissolution of Ni(OH)<sub>2</sub> and Fe(OH)<sub>3</sub> particles obtained from the first step hydrothermal reaction into the solution of second hydrothermal reaction plays a significant role in the formation of a nanosheet like structured catalyst and leading to a modified interaction between the active metal and support. According to previous reports [1, 4], possible chemical reactions taking place during the second step hydrothermal synthesis can be summarized as follows (Equations 1-5).





During the second step of the hydrothermal reaction, the  $\text{Ni(OH)}_2$  and  $\text{Fe(OH)}_3$  nanoparticles gradually dissolve to generate  $\text{Ni(NH}_3)_6^{2+}$  and  $\text{Fe(NH}_3)_6^{3+}$  species which react with either  $\text{Al(OH)}_3$  or  $\text{AlOOH}$ . Meanwhile, the re-dissolved  $\text{Ni(OH)}_2$  and  $\text{Fe(OH)}_3$  enter the lattice  $\text{Al(OH)}_3$  or co-precipitate with the  $\text{Al(OH)}_3$ .

The formation of the nanosheets occurs by growth of the crystals through an oriented attachment mechanism from small primary nanoparticles, e.g. the aggregate and orient of the primal units along a certain direction to form secondary single crystalline structures. Different reports showed that nano leaves, nano-architectures, and nanoflowers can be obtained based on oriented attachment growth of crystals [5-7]. Therefore, this method leads to a nanostructure which potentially allows obtaining enhanced properties in Ni-based catalysts, and different from those obtained by other synthesis methods reported for this type of catalysts to obtain well-defined morphologies, such as solvothermal/hydrothermal reduction [8], thermal decomposition [9, 10] and microwave-assisted reduction [10-12].

The synthesis by the hydrothermal method is a versatile, low-cost and environmentally friendly method for the preparation of materials with different size and morphology [1, 13]. However, the method leads often to the formation of a catalyst with strong metal-support interaction, which may negatively influence the reducibility of the active Ni particles. This negative effect could be reduced by introducing a two-step hydrothermal method. The  $\text{Ni(OH)}_2$  particles obtained in the first step of hydrothermal reaction are partially dissolved during the second hydrothermal reaction (due to the formation of amino-complexes), leading to the formation of nanosheets with reduced interaction between the active metal (Ni) and the alumina support [1, 4].

## 5.2. Scope of the chapter

This chapter focuses on studying the effect of catalyst morphology towards  $\text{CO}_2$  methanation. Using the procedure developed by Zhang et al. [1] as starting point, Fe was used to further improve the reducibility of  $\text{Ni/Al}_2\text{O}_3$  nanostructured catalyst. From the previous chapters, it was found that a small amount of Fe addition (i.e. in the ratio of  $\text{Fe/Ni}=0.1$ ) significantly improves the reducibility and activity of hydrotalcite derived catalysts towards  $\text{CO}_2$  methanation. Therefore, the addition of

Fe could further promote the reducibility of Ni particles. The aim of this work is thus to study in CO<sub>2</sub> methanation the properties of Fe promoted Ni/ $\gamma$ -Al<sub>2</sub>O<sub>3</sub> nanosheets catalysts, prepared by a two-step hydrothermal method. The as-prepared catalysts were characterized by XRD, N<sub>2</sub>-adsorption, H<sub>2</sub>-TPR, CO<sub>2</sub>-TPD, SEM, and TEM.

### 5.3. Experimental

#### 5.3.1. Synthesis of materials

The catalysts were synthesized using a two-step hydrothermal method, adapted to that reported by Zhang and Zhang for Ni/Al<sub>2</sub>O<sub>3</sub> catalysts for methane dry reforming [1], in order to introduce iron. Nickel (II) 2, 4-pentanedione (Sigma Aldrich, 95% purity), Iron (III) 2, 4-pentanedione (Sigma Aldrich, 99.9% purity) and Al (NO<sub>3</sub>)<sub>3</sub>·9H<sub>2</sub>O (Sigma Aldrich, 99.9% purity) were used as precursors. (NH<sub>2</sub>)<sub>2</sub>CO (Sigma Aldrich, 98% purity) and TX-100 (Sigma Aldrich, 90-100% purity) were used as alkali source and surfactant, respectively. The active metal loadings were 25% and 2.5% (w/w) for Nickel and Iron, respectively. The atomic ratio was Fe/Ni=0.1, which we observed to be optimal in hydrotalcite-derived catalysts. A Teflon-lined autoclave (150 mL) was used to disperse the reactant mixtures at 150°C for 2 h (for the synthesis of Ni(OH)<sub>2</sub> and/or Fe(OH)<sub>3</sub>). After cooling to room temperature, the Ni(OH)<sub>2</sub> and/or Fe(OH)<sub>3</sub> nanoparticles were re-dispersed by ultrasonic treatment and then Al(NO<sub>3</sub>)<sub>3</sub>·9H<sub>2</sub>O and (NH<sub>2</sub>)<sub>2</sub>CO were added to this solution. The mixture was then transferred to a 150 mL Teflon-lined autoclave and heated at 150°C for 5 h again. After cooling, the solid was recovered by centrifugation, dried overnight and calcined then at 500°C for 3 h in the air with a ramp of 2°C/min. The codes 25%Ni-2.5%Fe-Al<sub>2</sub>O<sub>3</sub>-NS and 25%Ni-Al<sub>2</sub>O<sub>3</sub>-NS indicate the fresh samples containing, or not, iron, respectively.

For comparison, a 25%Ni-2.5%Fe/ $\gamma$ -Al<sub>2</sub>O<sub>3</sub> catalyst was prepared by incipient wetness impregnation method using  $\gamma$ -Al<sub>2</sub>O<sub>3</sub> (Sasol-Puralox SCCa-20/200) and aqueous Ni(NO<sub>3</sub>)<sub>2</sub>·6H<sub>2</sub>O (Sigma Aldrich, 99.9% purity) and Fe(NO<sub>3</sub>)<sub>3</sub>·9H<sub>2</sub>O (Sigma Aldrich, 99.9% purity) solutions as precursors. This sample is indicated hereinafter as 25%Ni-2.5%Fe-Al<sub>2</sub>O<sub>3</sub>-B, where B indicates that it is based on the bulk-type catalyst to differentiate from the nanosheet type obtained in the preparation above.

As a reference, a commercial methanation catalyst (ca. 76 wt% Ni on Al<sub>2</sub>O<sub>3</sub>) was also used. The metal loadings in the catalysts were confirmed by AAS.

### 5.3.2. Catalyst characterizations

Reducibility of the catalysts was studied by H<sub>2</sub> temperature-programmed reduction (H<sub>2</sub>-TPR) using a Micromeritics AutoChem-II apparatus equipped with a TCD detector. 100 mg of catalyst were first pre-treated with He (50 mL/min) at 120°C for 2 h and TPR analysis was made underflow of 5% H<sub>2</sub> in Ar. The H<sub>2</sub>-TPR measurement of the reduced sample was made after reduction of the calcined sample using similar condition applied for catalysts activation prior to the CO<sub>2</sub> methanation reaction (at 600°C for 2 h under a flow of 60 mL/min pure H<sub>2</sub>). The temperature range was from 50 to 950°C with a ramp of 10°C/min. Reduction degree of the catalysts was quantified using the [equation \(5.1\)](#):

$$\text{Reduction Degree (\%)} = \frac{\text{TPR peak area of calcined sample} - \text{TPR peak area of Reduced sample}}{\text{TPR peak area of calcined sample}} \times 100\% \quad (5.1)$$

N<sub>2</sub> adsorption-desorption isotherms of the catalysts were measured using an Autosorb iQ3 automated gas sorption analyzer at liquid nitrogen temperature. Before the measurements, the samples were subjected to vacuum at 150°C for 1 h and then at 300°C for 3 h. The specific surface areas and pore volumes were obtained using the Brunauer-Emmett-Teller (BET) method using the N<sub>2</sub> adsorption branch.

Atomic absorption spectroscopy (AAS) (Perkin-Elmer Analyst 200) was used to analyze the chemical composition of the as-prepared materials.

XRD analyses of samples to study the phase structure were made using a Bruker D2-Phaser diffractometer operating with Cu K $\alpha$  radiation at 30 kV and 10 mA with 0.5 - 2 mm scattering screen. The 2 $\theta$  range of 10-80° was analyzed.

The metallic surface area was determined via CO chemisorption method using a Micromeritics AutoChem-II apparatus equipped with a TCD detector. Prior to the chemisorption experiment, 50

mg of each catalyst was pre-reduced at 600°C for 2 h using 60 mL/min of pure H<sub>2</sub>. Then the CO chemisorption analysis was made at 35°C using 10%CO in He.

The X-ray photoelectron spectroscopy (XPS) analyses were carried out using a PHI VersaProbe II (Physical Electronics). The survey (Su), C1s, O1s, Ni2p<sub>3/2</sub> and Fe2p<sub>3/2</sub> binding energies (BE) were recorded using Al K $\alpha$  (1486.6 eV) as the excitation source and a pass energy of 23.5 eV. For the survey acquisition, the pass energy was 117 eV. The X-ray settings were 100  $\mu$ m beam size at 100 W and 20 kV HP. A Shirley background was applied and all the XPS peaks were fitted with asymmetric function by using Multipack (Matlab) and Origin software. The position of XPS peaks of the corresponding elements was referred to graphite carbon, whose energy was taken equal to 284.8 eV.

Scanning electron microscopy (SEM) images of the calcined samples were acquired using a DSM 982 Gemini (Zeiss) microscope with accelerating energy of 4 kV. The samples were coated with carbon prior to SEM investigation.

Transmission electron microscopy (TEM) measurements were made using a 2200FS-200 kV TEM (Jeol). The samples were ground in a mortar and a few milligrams were suspended in 3 mL of absolute ethanol (Sigma Aldrich,  $\geq 99.8\%$ ), followed by sonication for 3 min at room temperature. Then, a drop was deposited on a Formvar/carbon-coated 300-mesh Cu TEM grid and dried under ambient air.

Thermogravimetric analysis of the catalysts after the reaction was made using a Simultaneous Thermal Analyzer (STA 600, PerkinElmer) apparatus. Samples were heated from 30° to 900°C with a heating rate of 5°C /min in air. Products evolved from the catalyst were analyzed by the on-line mass spectrometer.

CO<sub>2</sub> temperature programmed desorption (CO<sub>2</sub> TPD) experiments were made with a Micromeritics AutoChem-II apparatus with TCD detector. The calcined catalysts (150 mg) were pretreated under He flow (50 mL/min) at 300°C for 1h. Then, cooled down to 80°C for CO<sub>2</sub> adsorption (50 mL/min, 60 min) and finally flushed with He (50 mL/min, 60 min) at 50°C to

eliminate physically adsorbed CO<sub>2</sub>. The TPD profiles were finally recorded under He flow (30 mL/min) with a heating rate of 5°C/min up to 500°C.

### 5.3.3. Catalytic activity tests

Catalytic activity tests were made at 5 bars pressure, the temperature of 300°C or 350°C and a space velocity of 10,000 h<sup>-1</sup> on pre-reduced catalysts. In situ reduction was carried out at 600°C and 60 mL/min of pure H<sub>2</sub> for 2 h. The tests were made using a Microactivity Efficient equipment (Micromeritics) with two fixed bed continuous reactors (**Figure 5.1**), loading about 150 mg of catalyst premixed with SiC (4.5 g) in order to reach the desired catalytic bed volume (3 mL). The CO<sub>2</sub>/H<sub>2</sub> in the feed (without diluents) is 1:4. The reaction products were analyzed by using a double channel Agilent MicroGC equipped with 10mMS5A and 8m5C columns. Further details on the procedure for catalysts testing were earlier reported [14].



**Figure 5.1** Microactivity Efficient equipment (Micromeritics) used for the catalytic CO<sub>2</sub> methanation tests.

The relationship between catalytic properties and Ni active sites over the three most active catalysts for CO<sub>2</sub> methanation is further analyzed by determining the turnover frequencies (TOFs), which reflect the intrinsic activity of the active sites in the catalyst, and it is calculated by using the **equation (5.2)**:

$$TOF = \frac{\dot{n}_{CH_4}}{MSA * g_{CAT} * Ni_{planar\ Density}} \quad (5.2)$$

Where  $\dot{n}_{CH_4}$  is the outlet methane flow [mol<sub>CH<sub>4</sub></sub>/h] calculated at CO<sub>2</sub> conversion lower than 15%, MSA is the metallic surface area [m<sup>2</sup>/g Ni], Ni planar density [mol Ni<sub>surface</sub>/m<sup>2</sup>] and g CAT is the amount of catalyst used in the reaction.

## 5.4. Results and Discussion

### 5.4.1. Characterization results

Physicochemical characteristics of the nanosheet like samples with or without iron are reported in **Table 5.1**. Although BET surface area and total pore volume of the sample containing iron are slightly lower, there are no relevant differences between the two samples. The N<sub>2</sub> adsorption-desorption isotherms of these two samples are also quite similar, and there are no relevant changes after long-term catalytic tests.

**Table 5.1** Physicochemical properties and metal content of samples.

Catalyst	Metal content		BET surface area (m <sup>2</sup> /g) <sup>b</sup>	Total PV (mL/g) <sup>c</sup>
	(%) <sup>a</sup>			
	Ni	Fe		
25%Ni-Al <sub>2</sub> O <sub>3</sub> -NS	25.50	-	185	0.40
25%Ni-2.5%Fe-Al <sub>2</sub> O <sub>3</sub> -NS	24.91	2.25	172	0.33

<sup>a</sup> Measured by AAS.

<sup>b,c</sup> Calculated by the Multipoint-BET equation from N<sub>2</sub> adsorption branch.

The precursor of 25%Ni-2.5%Fe-Al<sub>2</sub>O<sub>3</sub>-NS catalyst obtained from the first step hydrothermal reaction was characterized using XRD and XPS methods to prove the formation of Ni(OH)<sub>2</sub> nanoparticles after the first step hydrothermal reaction. **Figure 5.2** is the XRD pattern of 25%Ni-2.5%Fe-Al<sub>2</sub>O<sub>3</sub>-NS precursor, in which all the peaks can be indexed to Ni(OH)<sub>2</sub> (in agreement with previous reports) [15].

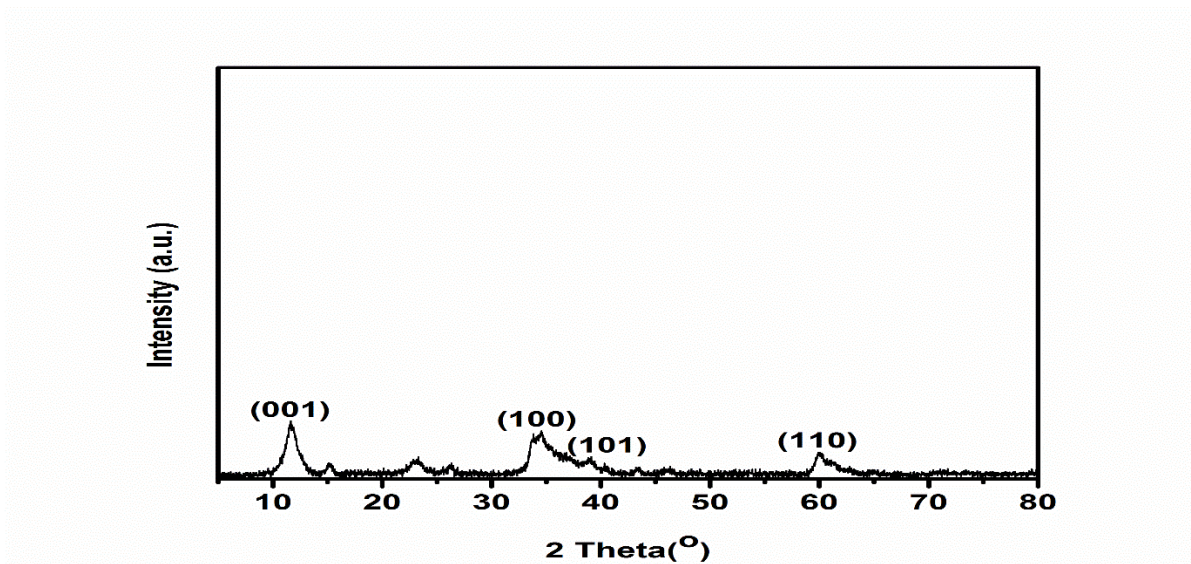


**Figure 5.2** XRD pattern of Ni(OH)<sub>2</sub> nanoparticles obtained from the first-step hydrothermal reaction.

Ni2p<sub>3/2</sub> and O1s XPS spectra of the sample obtained from the first step hydrothermal reaction are presented in **Figure 5.3**. The spectra were compared with results from literature and found to be in good agreement [16, 17].

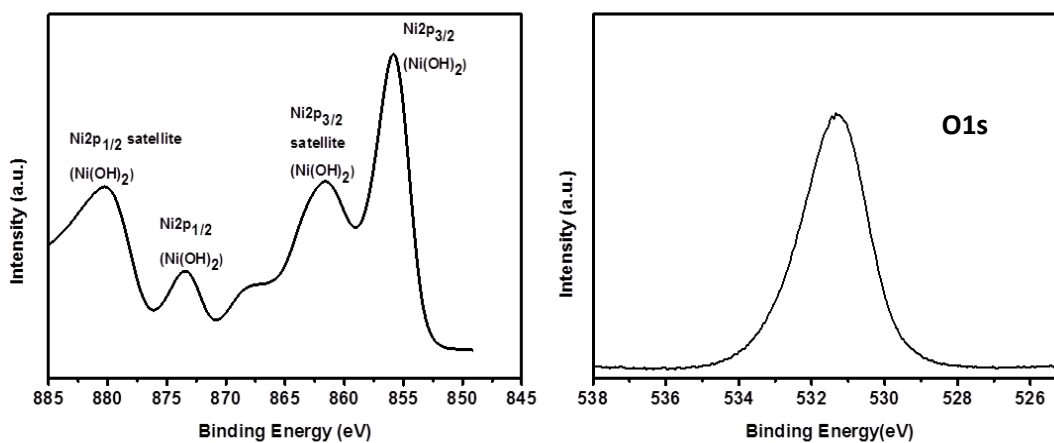


**Figure 5.3** Ni2p<sub>3/2</sub> and O1s XPS spectra of Ni(OH)<sub>2</sub> nanoparticles obtained from the first-step hydrothermal reaction.

XRD patterns of the fresh catalysts (**Figure 5.4**) show a low intensity of NiO diffraction peaks, in agreement with the presence of highly dispersed and small NiO particles. The presence of alumina

and Ni-aluminate is observed in both samples. Upon reduction at 600°C (2 h in pure H<sub>2</sub>), the characteristic diffraction peak for Ni metal at 2θ=51.8° and 2θ=76.1° are observed (Figure 5.5) after reduction of the catalysts a shift in 2 theta value was observed due to the formation of fcc Ni-Fe alloy (Figure 5.5 b). Figure 5.6 evidence that the value for d-spacing for Ni particles in 25%Ni-Al<sub>2</sub>O<sub>3</sub>-NS and 25%Ni-2.5%Fe-Al<sub>2</sub>O<sub>3</sub>-NS catalysts after reduction at 600°C and catalysts after long-term test fit very well the expected linear correlation between the d-spacing values of fcc Ni metal (JCPDS 01-070-1849) and fcc γ-Fe (JCPDS 01-089-4185) [18].

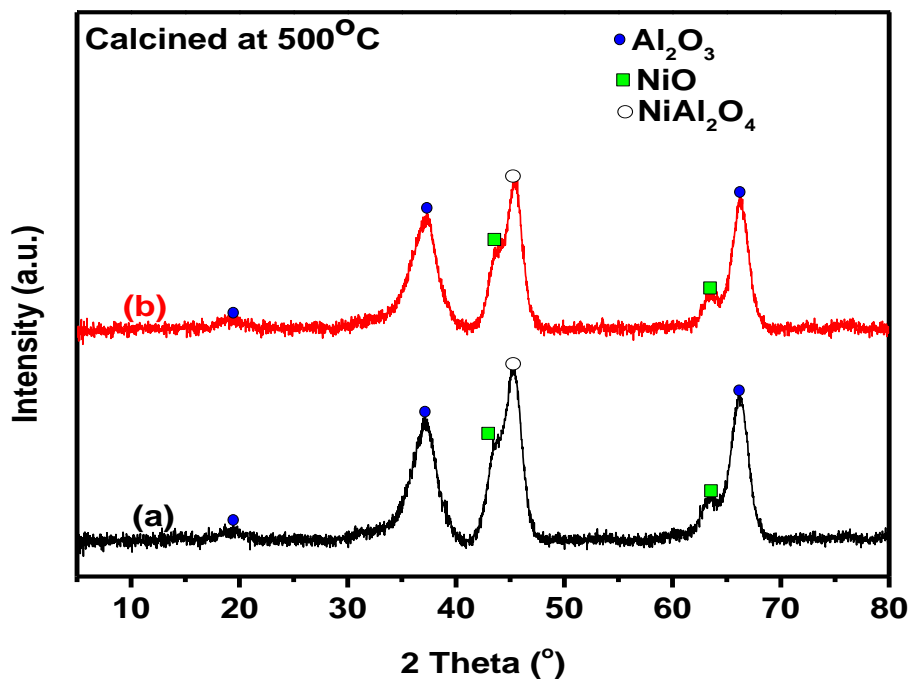


**Figure 5.4** XRD patterns of samples calcined at 500°C: (a) 25%Ni-Al<sub>2</sub>O<sub>3</sub>-NS and (b) 25%Ni-2.5%Fe-Al<sub>2</sub>O<sub>3</sub>-NS.



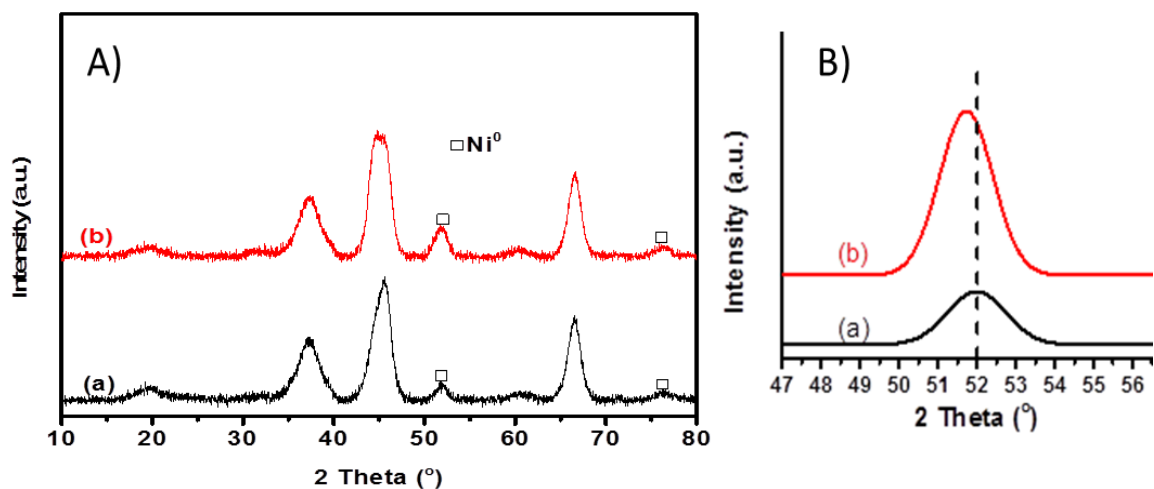


**Figure 5.5** A) XRD patterns of samples reduced at 600°C: (a) 25%Ni-Al<sub>2</sub>O<sub>3</sub>-NS and (b) 25%Ni-2.5%Fe-Al<sub>2</sub>O<sub>3</sub>-NS. B) 47-56° region in the XRD patterns: (a) 25%Ni-Al<sub>2</sub>O<sub>3</sub>-NS and (b) 25%Ni-2.5%Fe-Al<sub>2</sub>O<sub>3</sub>-NS.

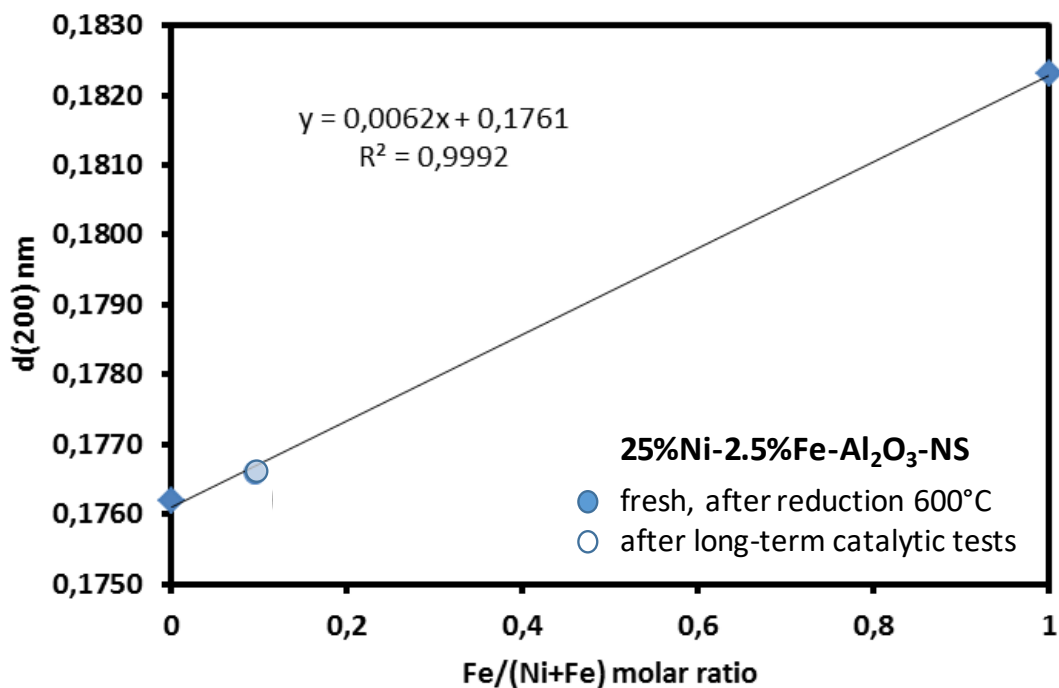


**Figure 5.6** d-spacing value for Fe-Ni alloy formation as a function of the Fe/(Ni + Fe) molar ratio of 25%Ni-2.5%Fe-Al<sub>2</sub>O<sub>3</sub>-NS catalyst reduced at 600°C or after long-term (>50 h) catalytic tests, with respect to the linear relation described using Vegard's law between *fcc* Ni metal (JCPDS 01-070-1849) and *fcc*  $\gamma$ -Fe (JCPDS 01-089-4185).

H<sub>2</sub>-TPR profiles of the calcined and reduced catalysts are presented in **Figure 5.7**. For the calcined samples, the catalyst without Fe (top figure) showed two reduction peaks arising from the reduction of NiO differently interacted with the support. In the latter (the sample with 2.5% Fe, bottom figure), an additional reduction peak centered at 384°C is evident, besides to two broad reduction peaks at higher temperatures (about 660°C and 800°C). The lower temperature peak in the H<sub>2</sub>-TPR profile is in good agreement with our previous results for very-small unsupported NiO particles (ca. 383°C) [14]. This suggests that Fe promotes dispersion of NiO particles, rather than their reducibility, in agreement with other observations [19, 20].

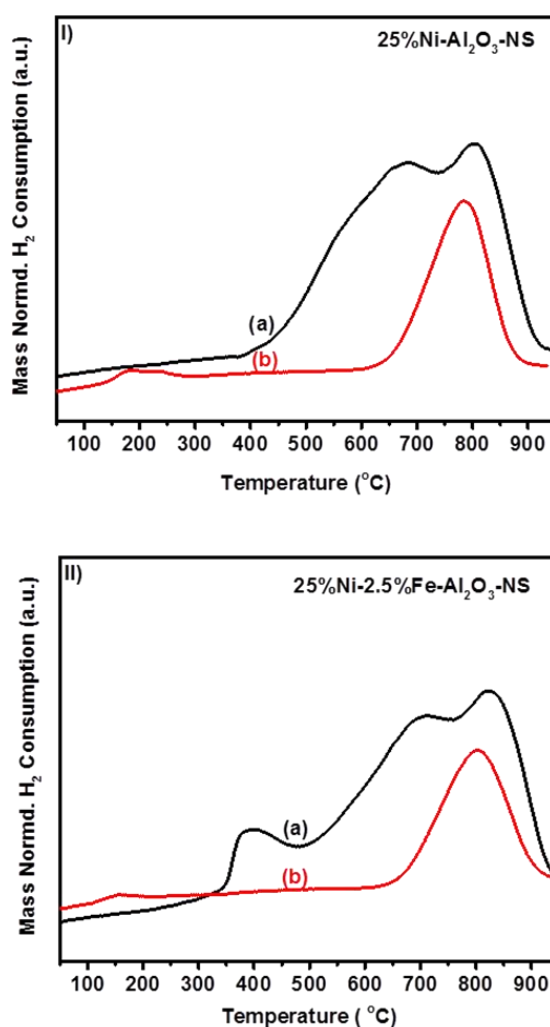


**Figure 5.7** H<sub>2</sub>-TPR profiles. I - top Figure: 25%Ni-Al<sub>2</sub>O<sub>3</sub>-NS (a) calcined, (b) reduced. II - bottom Figure: 25%Ni-2.5%Fe-Al<sub>2</sub>O<sub>3</sub>-NS (a) calcined, (b) reduced.

Quantitative analysis of hydrogen consumption normalized by the amount of catalyst used was estimated from the H<sub>2</sub>-TPR test and reported in **Table 5.2** for calcined catalysts together with the catalyst reduction degree, estimated using **Eq. (5.1)**. The total amount of H<sub>2</sub> consumed by the Fe promoted Ni/Al<sub>2</sub>O<sub>3</sub> catalyst over the whole temperature range in the H<sub>2</sub>-TPR profile is higher than that of the catalyst without iron, leading thus to a higher reduction degree. Sehested et al. [21] for Ni-Fe catalysts for CO methanation suggested that the improved reducibility derives from the formation of nickel-iron alloys. However, the H<sub>2</sub>-TPR profiles (**Figure 5.7**) of the two samples, containing or not iron, which was pre-reduced at 600°C for 2 h with pure H<sub>2</sub>, do not show relevant differences.

**Table 5.2** Quantitative H<sub>2</sub>-TPR analysis and CO-chemisorption measurements for the calcined catalysts.

Catalyst	H <sub>2</sub> consumed (mmol/g <sub>cat</sub> ) <sup>a</sup>	Reduction degree (%) <sup>b</sup>	MSA (m <sup>2</sup> /g of metal) <sup>d</sup>
25%Ni-Al <sub>2</sub> O <sub>3</sub> -NS	0.90	70	9.78
25%Ni-2.5%Fe-Al <sub>2</sub> O <sub>3</sub> -NS	1.10	75	10.92

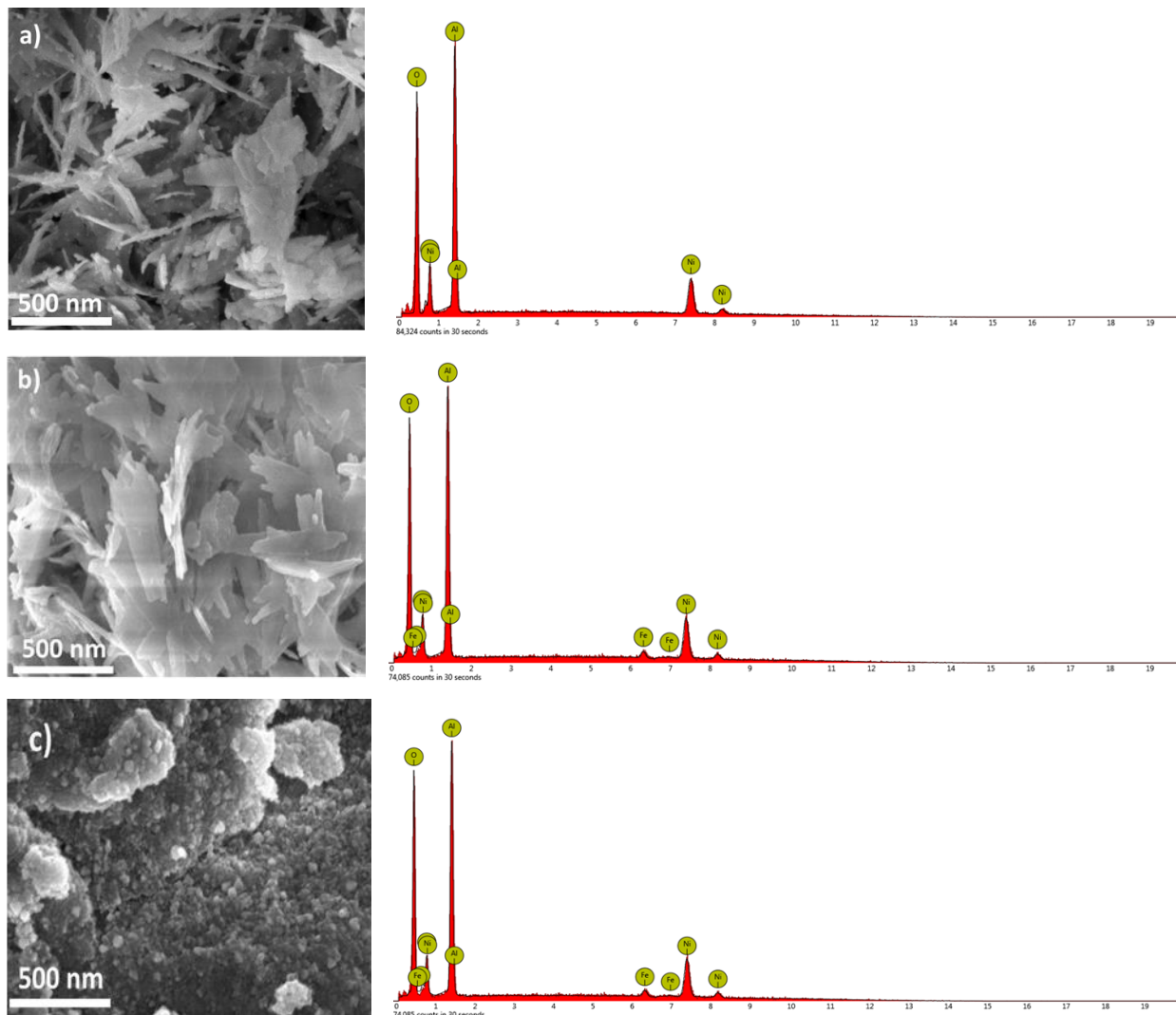
<sup>a</sup> Estimated from the whole temperature range of the H<sub>2</sub>-TPR profiles.

<sup>b</sup> Calculated using **Equation 5.1** (see experimental part)

<sup>c</sup> Calculated from CO chemisorption analysis at ~35°C.

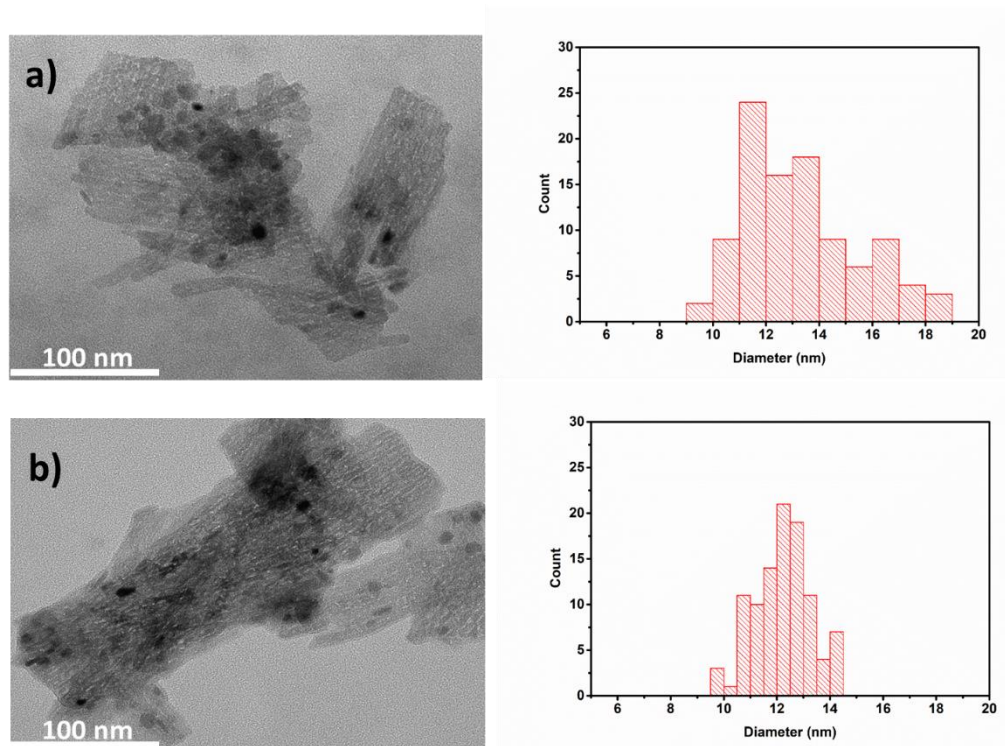
In order to analyze the metallic surface area of Nickel, pulse CO-chemisorption experiments were made. **Table 5.2** also summarizes the results in terms of metal dispersion and the metallic surface area obtained from the pulse CO chemisorption experiments. Smaller NiO particles (better dispersion) were observed to have better reducibility and higher activity in CH<sub>4</sub>-CO<sub>2</sub> reforming [22] and syngas methanation [23]. The metal surface was calculated from the CO uptake by assuming a chemisorption stoichiometric factor of 1.0 meaning that one CO molecule was chemisorbed per Ni and/or Fe surface atom. The results, therefore, well evidence that the metallic surface area for the 25%Ni-2.5%Fe-Al<sub>2</sub>O<sub>3</sub>-NS catalyst is higher than that of 25%Ni-Al<sub>2</sub>O<sub>3</sub>-NS.

SEM-EDX images of calcined materials synthesized via the two-step hydrothermal route and the bulk type catalyst are shown in **Figure 5.8**. Both samples synthesized using the hydrothermal reaction exhibited a definite structure composed of nanosheet-like structures while the catalyst prepared by wet impregnation did not show any definite nanostructure. The presence of Fe was also confirmed by means of energy dispersive X-ray analysis (EDX) as shown in **Fig. 5.8** (b and c).



**Figure 5.8** SEM-EDX images of calcined (a) 25%Ni-Al<sub>2</sub>O<sub>3</sub>-NS, (b) 25%Ni-2.5%Fe-Al<sub>2</sub>O<sub>3</sub>-NS and (c) 25%Ni-2.5%Fe-Al<sub>2</sub>O<sub>3</sub>-B samples.

The morphology of reduced catalysts was also investigated using TEM and an average particle diameter was estimated using Image-J (USA National Institutes of Health) software. As shown in **Figure 5.9**, homogeneously distributed Ni particles were obtained after reduction at 600°C consisting of nanoparticles with a diameter of  $13.0 \pm 2.3$  nm and  $11.0 \pm 1.6$  nm for 25%Ni-Al<sub>2</sub>O<sub>3</sub>-NS and 25%Ni-2.5%Fe-Al<sub>2</sub>O<sub>3</sub>-NS, respectively. No significant difference in particle diameter is observed between the reduced catalyst at 600°C and the sample after long-term (>50 h) catalytic reaction (**Table 5.3**). The metal dispersion was also estimated from the average particle size obtained and results are summarized in **Table 5.3**. It is worth to note that the average particle diameter, as well as dispersion of the particles, remains quite constant after the long-term tests.



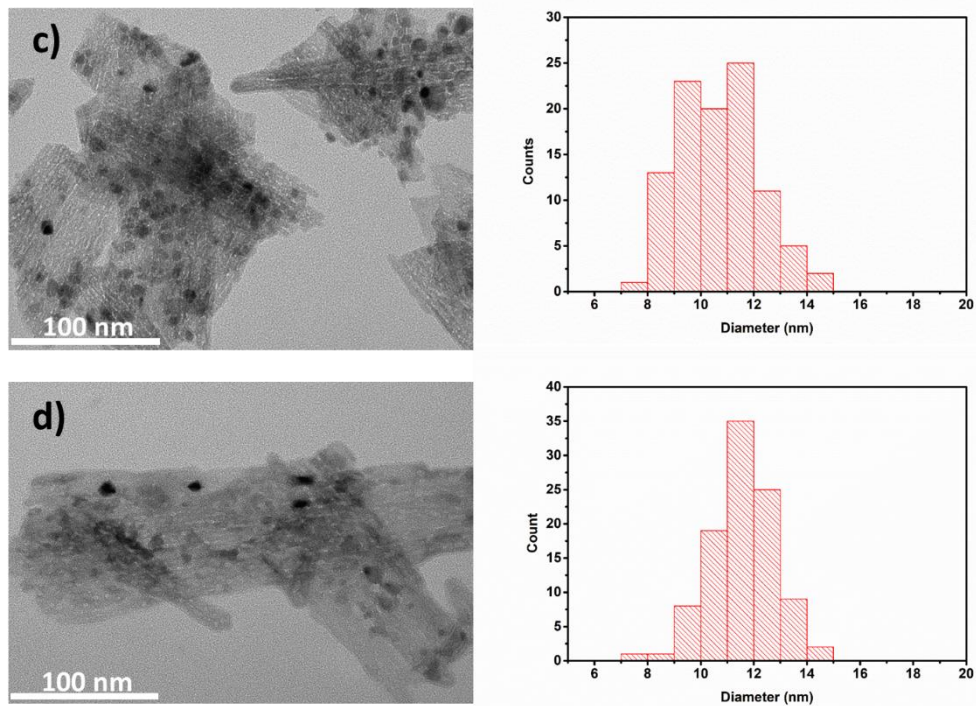


**Figure 5.9** TEM images of reduced and spent catalysts: 25%Ni-Al<sub>2</sub>O<sub>3</sub>-NS (a) reduced at 600°C (b) spent and 25%Ni-2.5%Fe-Al<sub>2</sub>O<sub>3</sub>-NS (c) reduced at 600°C (d) spent.

No significant difference in particle diameter is observed between the reduced catalyst at 600°C and the sample after long-term (>50 h) catalytic reaction (**Table 5.3**). It is remarkable how the average particle diameter, as well as dispersion in the particle diameters, remains quite constant.

**Table 5.3** Summary of average particle diameter (nm) and metal dispersion from TEM analyses.

Catalyst	Reduced at 600°C <sup>a</sup>	After reaction 24 h or 50 h <sup>b</sup>	Metal dispersion (%) <sup>c</sup>
25%Ni-Al <sub>2</sub> O <sub>3</sub> -NS	13.0 ± 2.3	12.8 ± 1.8	7.6
25%Ni-2.5%Fe-Al <sub>2</sub> O <sub>3</sub> -NS	11.3 ± 1.6	11.1 ± 1.3	9.1

<sup>a,b</sup> Estimated using *Image-J*.

<sup>c</sup> calculated using the equation  $\% D = (1/PD) * 100$ ,  $PD$  = Average Particle diameter estimated by *Image J*.

The chemical state of Ni species found on the surface of the catalyst can be identified from the binding energy values of respective XPS spectra (**Figure 5.10**). The Ni<sub>2p</sub><sub>3/2</sub> signals of both reduced and spent catalysts appear at 855.9 eV and 855.7 eV with satellite peaks at 862.15 eV and 861.90 eV, respectively. The main peaks obtained were deconvoluted and mathematically treated to identify the chemical species of nickel present on the surface. Accordingly, the peak at around 852 eV is ascribed to the presence of Ni in its metallic state. The peaks in the range 854.95-856 eV can be assigned to NiO and/or NiFe<sub>2</sub>O<sub>3</sub> spinel species on the surface [24-26]. The XPS signal for Fe<sub>2p</sub> was very weak due to the low amount of Fe on the surface of the Fe promoted Ni/Al<sub>2</sub>O<sub>3</sub> catalyst. The presence of a characteristic peak for Ni metal in XPS spectra for both the reduced and catalysts after long-term catalytic tests evidence catalysts stability, since no oxidation occurred during CO<sub>2</sub> methanation.

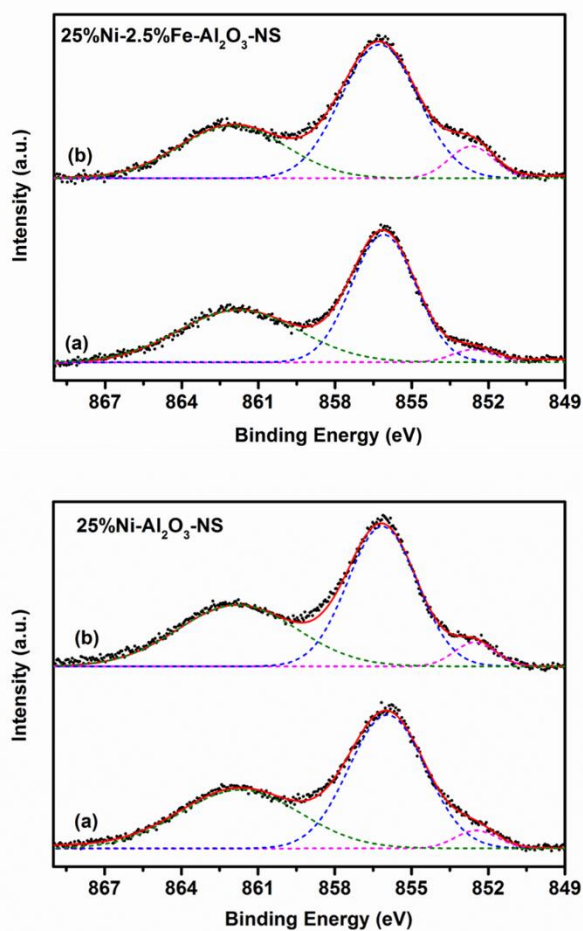


**Figure 5.10** XPS spectra of 25%Ni-Al<sub>2</sub>O<sub>3</sub>-NS and 25%Ni-2.5%Fe-Al<sub>2</sub>O<sub>3</sub>-NS catalysts: (a) reduced at 600°C, (b) after long-term catalytic tests.

The basicity of catalysts is an important factor in CO<sub>2</sub> methanation reaction, as CO<sub>2</sub> adsorption facilitated on basic sites. Thus, a high basicity of the catalysts can influence its activity. CO<sub>2</sub> TPD experiments were applied to establish the effect of Fe as well as a unique structure on basic properties of the prepared catalysts. The obtained CO<sub>2</sub>-TPD profiles are depicted in **Figure 5.11**. All calcined catalysts evidence a wide and asymmetric CO<sub>2</sub> desorption peak centered at temperatures around 140-170°C, 200-260 °C, 300-350°C. These desorption peaks correspond to weak, medium-strong, and strong base site, respectively [27].

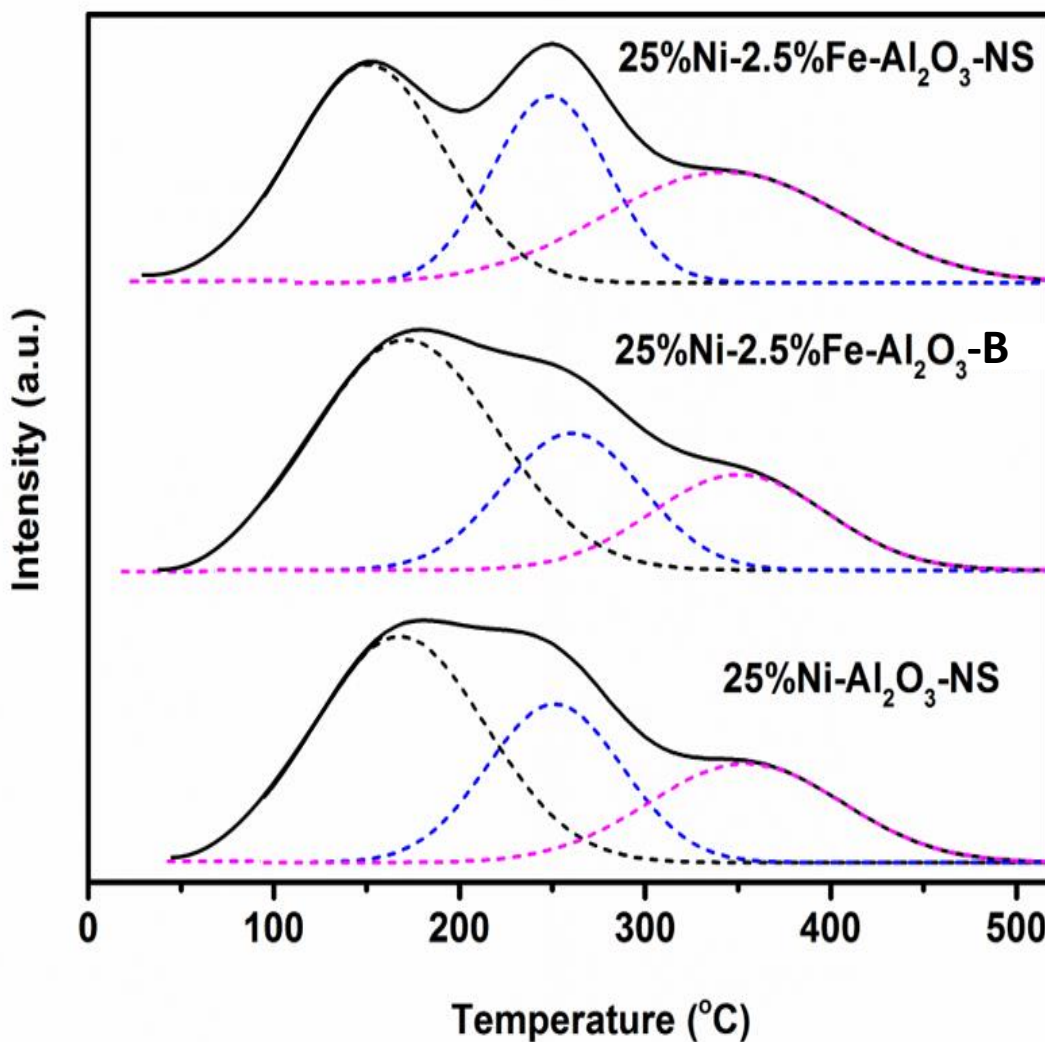


**Figure 5.11** CO<sub>2</sub> TPD profiles of selected calcined catalysts.



The total basicity was calculated by means of integration of the overall desorption profile, which was deconvoluted into three Gaussian contributions corresponding to each type of basic sites **Table 5.4**. The shape and broadness of the CO<sub>2</sub> desorption curves indicate a considerable heterogeneity in the basic site strength distributions and densities.

**Table 5.4** Integrated peak areas and temperature maximum of basic sites (BS).

Catalyst	Temperature (°C)/Amount of BS (cm <sup>3</sup> /g <sub>cat</sub> )		
	Weak BS	Medium BS	Strong BS
25%Ni-Al <sub>2</sub> O <sub>3</sub> -NS	143/2.68	246/1.48	349/1.32
25%Ni-2.5%Fe-Al <sub>2</sub> O <sub>3</sub> -B	166/3.54	255/1.18	346/0.93
25%Ni-2.5%Fe-Al <sub>2</sub> O <sub>3</sub> -NS	145/1.84	243/1.20	338/1.48

Calculated from the whole temperature peak of the CO<sub>2</sub>-TPD.

25%Ni-2.5%Fe-Al<sub>2</sub>O<sub>3</sub>-B: stands for the bulk-type catalyst prepared by impregnation method.

For the calcined catalysts, considering the amount of CO<sub>2</sub> desorbed per gram of sample, the higher density of basic sites follows the order: 25%Ni-2.5%Fe-Al<sub>2</sub>O<sub>3</sub>-B > 25%Ni-Al<sub>2</sub>O<sub>3</sub>-NS ≥ 25%Ni-2.5%Fe-Al<sub>2</sub>O<sub>3</sub>-NS which is the same order seen for basic sites strength. In fact, the maximum temperature of the desorption peaks is shifted to lower values in passing from the bulk-type to the nanosheet-like catalyst. The presence of iron slightly enhances this effect.

#### 5.4.2. Catalytic activity tests

**Figure 5.12** depicts the integral rate of CO<sub>2</sub> conversion (per mol of Ni and time in seconds) and the CO<sub>2</sub> conversion (%) vs. time on stream during the CO<sub>2</sub> methanation reactions. Among the catalysts tested, the Fe promoted Ni-alumina nanosheet-like catalyst (sample c) shows a relevant CO<sub>2</sub> conversion of ca. 90%, with an integral rate of CO<sub>2</sub> conversion of about 0.24 mol CO<sub>2</sub> conv./mol Ni/s (about 860 mol<sub>CH<sub>4</sub></sub> mol<sub>Ni</sub><sup>-1</sup> h<sup>-1</sup>; see **Table 5.5**) and a selectivity to CH<sub>4</sub> of 99% at 300°C and 5 bar. The relevant enhancement of the rate of reaction both with respect to the nanosheet sample not containing Fe (sample a) or the sample containing iron, but prepared using bulk-type alumina (sample b) could be noted. Sample c shows an integral rate around 5 times higher than sample a (NS, without Fe) and about 2.5 times higher than sample b (the same composition, but prepared

on bulk-type alumina). At 350°C, the difference is apparently lower, but because the behavior of the more active catalysts is conditioned from the equilibrium. All samples show instead of a high selectivity in methane formation (above 98-99%), with very low CO formation. These catalysts show good stability during the time on stream investigated (10 h).

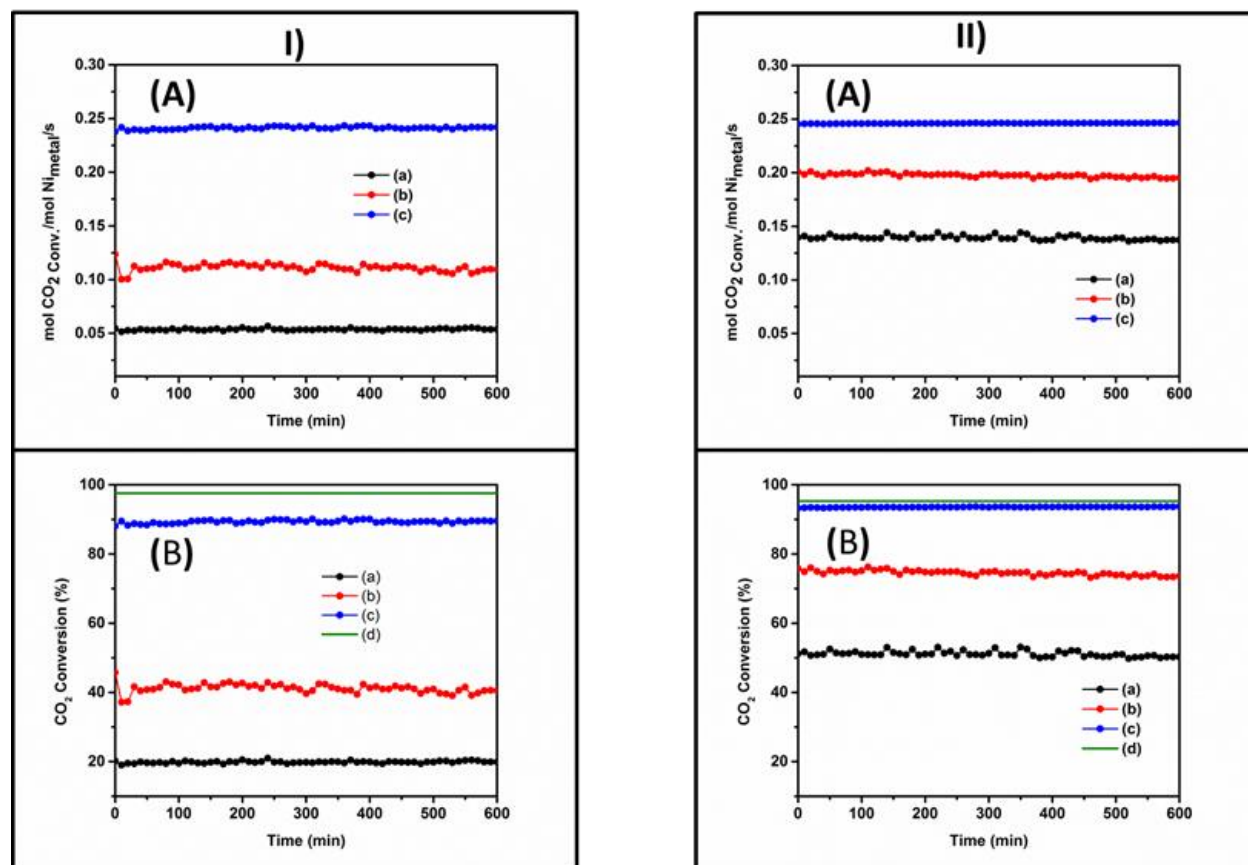


**Figure 5.12** Catalytic CO<sub>2</sub> methanation at (I) 300°C and (II) 350°C (gas mixture with CO<sub>2</sub>:H<sub>2</sub> = 1:4, P = 5 bar, and GHSV = 10000 h<sup>-1</sup>): (A) integral rate in CO<sub>2</sub> depletion (mol CO<sub>2</sub> per mol Ni and time in s) and (B) CO<sub>2</sub> conversion (%): (a) 25%Ni-Al<sub>2</sub>O<sub>3</sub>-NS, (b) 25%Ni-2.5%Fe-Al<sub>2</sub>O<sub>3</sub>-B, (c) 25%Ni-2.5%Fe-Al<sub>2</sub>O<sub>3</sub>-NS and (d) equilibrium.

The 25%Ni-2.5%Fe-Al<sub>2</sub>O<sub>3</sub>-NS sample showed good stability during the 50 h on-stream, and no decay of activity was found in the sample compared to the results of a commercial methanation catalyst (ca. 76 wt-% Ni on Al<sub>2</sub>O<sub>3</sub>). Note that this commercial methanation catalyst has about three times higher Ni loading. It is the most active among various tested methanation catalysts. The

results are presented in **Figure 5.13**. The 25%Ni-2.5%Fe-Al<sub>2</sub>O<sub>3</sub>-NS catalyst, after a slight initial increase in the activity in the first 3h of time on stream, shows a rather stable behavior (around 90% CO<sub>2</sub> conversion), without any deactivation within 50 h of time on stream. On the contrary, the commercial methanation catalyst (ca. 76 wt-% Ni on Al<sub>2</sub>O<sub>3</sub>) shows an initial decrease of the CO<sub>2</sub> conversion from about 95% to 90% in the first 10 h of time on stream, and then a slight continuous deactivation for longer times on stream, reaching a CO<sub>2</sub> conversion of less than 88% after 50 h of time on stream.

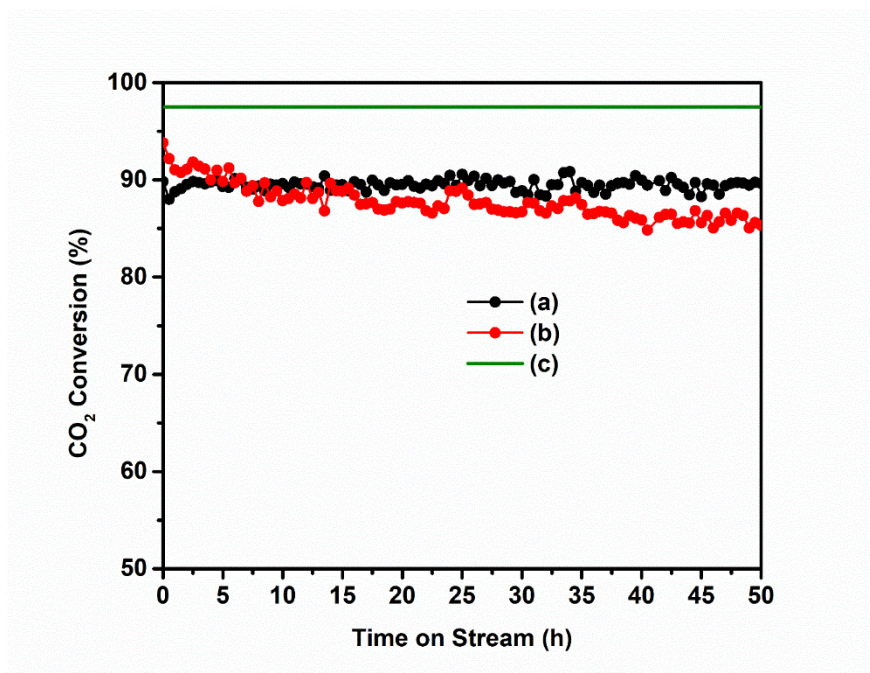


**Figure 5.13** Stability test in CO<sub>2</sub> methanation for 50 h of time on stream (Reaction conditions: gas mixture with CO<sub>2</sub>:H<sub>2</sub> = 1:4, T = 300°C, P = 5 bar, and GHSV = 10000 h<sup>-1</sup>): (a) 25%Ni-2.5%Fe-Al<sub>2</sub>O<sub>3</sub>-NS and (b) commercial catalyst (ca. 76 wt% Ni on Al<sub>2</sub>O<sub>3</sub>) and (c) equilibrium.

**Table 5.5** reports the comparison of 25%Ni-2.5%Fe-Al<sub>2</sub>O<sub>3</sub>-NS catalyst with the commercial one, in terms of integral rate of CO<sub>2</sub> conversion to methane and rate of deactivation (loss in CO<sub>2</sub> conversion percentage in 50 h of time on stream, after the initial 3h of stabilization). The data in **Table 5.5** well evidence that the sample having the nanosheet structure and containing Fe as promoter shows a specific activity (per mol Ni) at 300°C more than three times higher than the commercial methanation reference sample, and a rate of deactivation at least 40 times lower.

**Table 5.5** Integral rate of reaction and rate of deactivation at 300°C of 25%Ni-2.5%Fe-Al<sub>2</sub>O<sub>3</sub>-NS with respect to a commercial catalyst (ca. 76 wt-% Ni on Al<sub>2</sub>O<sub>3</sub>).

Catalyst	Integral rate of CO <sub>2</sub> conversion to methane, mol <sub>CH<sub>4</sub></sub> mol <sub>Ni</sub> <sup>-1</sup> h <sup>-1</sup>	Deactivation: decrease in CO <sub>2</sub> conversion (%) in 50 h (*)
25%Ni-2.5%Fe-Al <sub>2</sub> O <sub>3</sub> -NS	860	< 0.1 %
Commercial methanation catalyst (#)	281	3.9 %

\* after the initial 3 h of catalyst stabilization  
 # about 76 wt% Ni on Al<sub>2</sub>O<sub>3</sub>

The obtained TOF values for all the investigated catalysts in a temperature range of 300°C-350°C are reported in **Table 5.6**. The TOF values reported in **Table 5.6** were determined using a feed based only on CO<sub>2</sub> and H<sub>2</sub> as requested for industrial exploitation, while often literature data refer to diluted streams rather than a pure stoichiometric CO<sub>2</sub>/H<sub>2</sub> feed. It is reasonable that the behavior in the two cases may be different, in particular, that the chemisorption of CO<sub>2</sub> may be rate determining step with diluted CO<sub>2</sub> feeds. On the other hand, for practical applications, it is necessary to evaluate conditions as those used here, rather than diluted conditions. The 25%Ni-2.5%Fe-Al<sub>2</sub>O<sub>3</sub>-NS catalyst show higher TOF value than both the 25%Ni-2.5%Fe-Al<sub>2</sub>O<sub>3</sub>-B and the commercial catalysts.

**Table 5.6** TOF values of most active catalysts at temperatures ranging from 300°C-350°C.

Catalyst	TOF (s <sup>-1</sup> ) <sup>a</sup>			
	300°C	315°C	330°C	350°C
25%Ni-2.5%Fe-Al <sub>2</sub> O <sub>3</sub> -NS	0.92	1.48	2.04	3.40
25%Ni-2.5%Fe-Al <sub>2</sub> O <sub>3</sub> -B	0.41	0.66	1.07	1.67
Commercial methanation catalyst	0.44	0.70	1.20	2.34

<sup>a</sup> Calculated using **equation 5.2** (see experimental part).

The CO<sub>2</sub> methanation activity experiments for the determination of activation energy were made at temperatures ranging from 300°C-350°C. The Arrhenius plots used for this calculation are

provided in the supporting information. The activation energies ( $E_a$ ) were determined from the slope of the Arrhenius plot (Figure 5.14) and reported in Table 5.7. These values are consistent, even slightly lower, with respect to those presented in the existing literature on Ni-based catalysts [28-30].

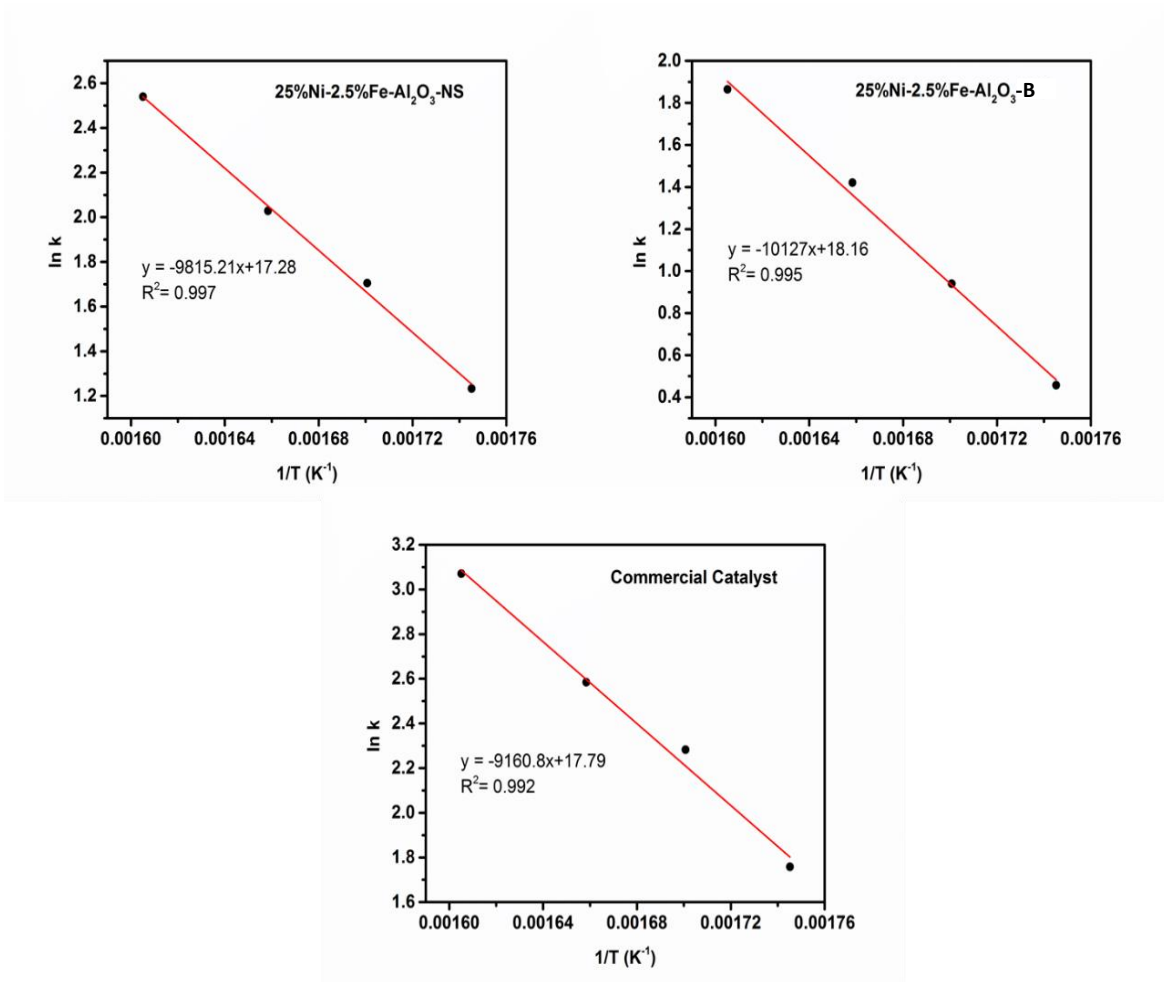


**Figure 5.14** Arrhenius plots for CO<sub>2</sub> hydrogenation on different catalysts. Reaction conditions: gas mixture with CO<sub>2</sub>:H<sub>2</sub> = 1:4, T = 300°C-350°C, P = 5 bar, and GHSV = 10000 h<sup>-1</sup>.

**Table 5.7** Activation energy ( $E_a$ ) for the most active catalysts at temperatures ranging from 300°C-350°C.

Catalyst	$E_a$ (kJ/mol)
25%Ni-2.5%Fe-Al <sub>2</sub> O <sub>3</sub> -NS	76.36
25%Ni-2.5%Fe-Al <sub>2</sub> O <sub>3</sub> -B	84.19
Commercial methanation catalyst	76.16

#### 5.4.2.1. Factors affecting the catalytic activity

The CO<sub>2</sub> methanation activity of as-prepared catalysts in this chapter mainly influenced both by the unique structure with the Fe promotional effect and the CO<sub>2</sub> adsorption properties (particularly the strength of basic sites). Those issues are explained in the following part.

##### 5.4.2.1.1. Effect of catalyst structure and Fe promotion

The catalytic data obtained (**Figures 5.12 and 5.13, Table 5.6**) showed a strong dependency on both the structure and Fe addition. The most active sample (Fe promoted with nanosheet structure) shows a specific activity at 300°C more than three times higher than the commercial methanation reference sample, and a rate of deactivation at least 40 times lower. Therefore a synergic effect between nanosheet structure and Fe promotion is present. At 300°C, the integral rate of CO<sub>2</sub> depletion for this catalyst is around 5 times higher with respect to the nanosheet catalysts without Fe as a promoter, and about 2.5 times higher with respect to a catalyst with the same composition, but prepared by on bulk-type alumina. Therefore, the presence of a nanosheet-like structure, confirmed by SEM and TEM data (**Figures 5.8 and 5.9**), in combination with Fe modification leads to enhanced performance and better stability in comparison to a commercial methanation catalyst.

Metal dispersion (**Table 5.3**), metallic surface area (**Table 5.2**) and particle diameter in the fresh (reduced) sample as well as after long-term catalytic tests (**Table 5.4**) confirm that both samples have a very similar particle diameter (about 11-12 nm), which do not change after long-term (50 h) catalytic tests. Textural properties of the two samples are also very close (**Table 5.1**). Therefore, the formation of a Ni-Fe alloy in the Ni particles for Fe-promoted NS sample, clearly demonstrated by XRD data (**Figure 5.4**), is slightly improving the reducibility, stability and the metallic surface area. This is confirmed by XPS data (**Figure 5.10**). Note, how the spectra are quite similar, although the ratio of intensities of multiplet-split Ni2p<sub>3/2</sub> (NiO) with respect to Ni2p<sub>3/2</sub> (indicative of the surface oxidation of Ni particles) is slightly higher after catalytic tests in 25%Ni-Al<sub>2</sub>O<sub>3</sub>-NS with respect to 25%Ni-2.5%Fe-Al<sub>2</sub>O<sub>3</sub>-NS. These slight differences do not explain the about five times higher reactivity in the sample containing Fe. On the other hand, selectivity to methane is quite comparable in the two samples (>98-99%), with rather minimal CO formation. This is also

consistent with the indication that the formation of the Ni-Fe alloy does not significantly change the surface reactivity, in terms of CO hydrogenation, which is considered the rate-limiting step as indicated in the introduction.

This synergy between NS structure and Fe promotion discussed above has also a positive effect in terms of stability of the catalyst in long-term catalytic experiments (**Figure 5.13**). To remark that the most active sample (nanosheet like structure, Fe promotion) shows a rate of deactivation at least 40 times lower than the reference commercial sample, which is one of the best catalysts among the various commercial one we tested. Moreover, the integral rate of CO<sub>2</sub> conversion to methane ( $\text{molCH}_4 \text{ molNi}^{-1} \text{ h}^{-1}$ ) for the 25%Ni-2.5%Fe-Al<sub>2</sub>O<sub>3</sub>-NS catalyst is about 3 times higher with respect to the commercial catalyst, although the amount of Ni in the commercial catalysts is about 76 wt.-% (see **Table 5.5**).

#### 5.4.2.1.2. Effect of CO<sub>2</sub> adsorption sites

The amount and type of basic sites were correlated with TOF obtained in order to study the effect on adsorption and dissociation of CO<sub>2</sub>. In terms of the relationship with the specific activity (TOF), there is not a straight relationship between catalytic behavior and the number of basic sites able to chemisorb CO<sub>2</sub>. For example, the CO<sub>2</sub> adsorbed by 25%Ni-2.5%Fe-Al<sub>2</sub>O<sub>3</sub>-B sample is 25% higher with respect to the 25%Ni-2.5%Fe-Al<sub>2</sub>O<sub>3</sub>-NS catalyst, while the TOF at 300°C (**Table 5.6**) of the latter catalyst is over two times higher. In literature, it was often remarked this correlation. If we consider the amount of BS of a given strength (weak, medium, strong), also no apparent relationship is observed (**Figure 5.15**).

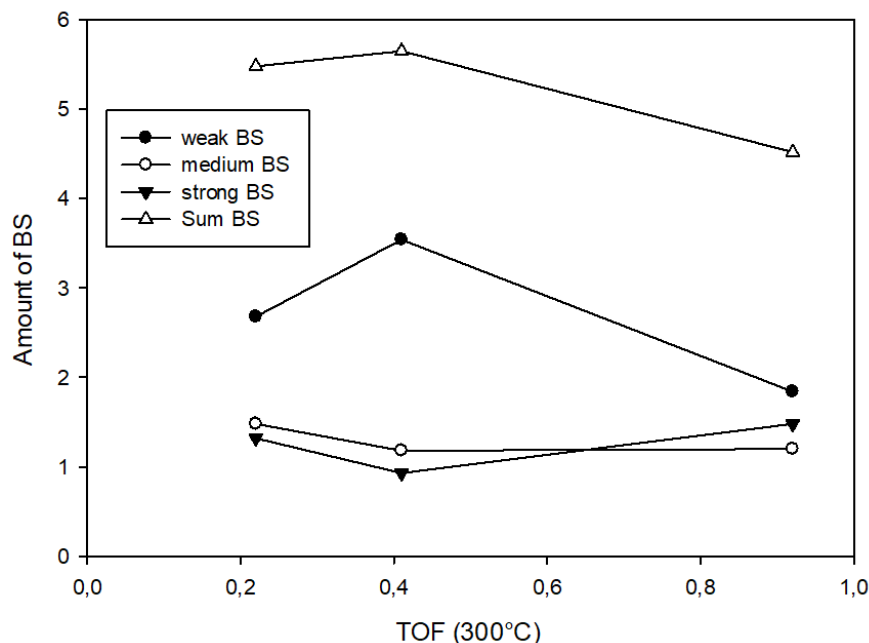


**Figure 5.15** Relationship between TOF and amount of basic sites (BS) (Reaction conditions: gas mixture with  $\text{CO}_2:\text{H}_2 = 1:4$ ,  $T = 300^\circ\text{C}$ ,  $P = 5$  bar, and  $\text{GHSV} = 10,000 \text{ h}^{-1}$ ).

The 25%Ni-2.5%Fe- $\text{Al}_2\text{O}_3$ -NS catalyst shows a higher TOF value (specific activity per amount of Ni surface sites) than both the 25%Ni-2.5%Fe- $\text{Al}_2\text{O}_3$ -B sample and the commercial catalyst (**Table 5.6**). In particular, the TOF of the Fe-promoted sample based on nanosheet (25%Ni-2.5%Fe- $\text{Al}_2\text{O}_3$ -NS) is twice that of the sample with the same composition, but based on bulk alumina (25%Ni-2.5%Fe- $\text{Al}_2\text{O}_3$ -B). This higher specific activity (TOF) is present in all the range of temperatures investigated (**Table 5.6**). There is thus a specific influence of the alumina morphology (NS vs. bulk-type) as support for Ni (Fe-promoted) nanoparticles. As commented before, there is an influence on the characteristics of Ni nanoparticles itself, but it is worthwhile to consider whether there is an influence to also the  $\text{CO}_2$  chemisorption properties.

While no relation is observed between TOF and amount of BS, we could note, on the contrary, a rough relation between the weakening of the strong BS (**Table 5.4**) and TOF.  $\text{CO}_2$  TPD analysis (**Fig. 5.13** and **Table 5.4**) shows that nanosheet-based samples (NS), with respect to 25%Ni-2.5%Fe- $\text{Al}_2\text{O}_3$ -B, possess i) a lower total amount of basic sites, although less weak BS and more medium-strong BS, and ii) basic sites of lower strength, as shown by the peak shift to lower temperatures. The presence of Fe (compared 25%Ni- $\text{Al}_2\text{O}_3$ -NS with 25%Ni-2.5%Fe- $\text{Al}_2\text{O}_3$ -NS)



has a minor influence on the strength of weak and medium BS but decreases their amount. On the contrary, the presence of Fe slightly increases the amount of strong BS, but which have a lower strength. Note that the most active catalyst in terms of TOF (25%Ni-2.5%Fe-Al<sub>2</sub>O<sub>3</sub>-NS) has the lower amount of BS sites, but the highest amount of strong BS, although with the weakest strength.

### 5.5. Characterization of spent catalysts

XRD patterns of catalysts after long-term tests are given in **Figure 5.16**. The XRD patterns of reduced and spent catalysts are quite similar which indicates there was no phase or structural change happened during the long-term tests. Additionally, no diffraction peak for graphitic carbon was observed after the long-term tests.

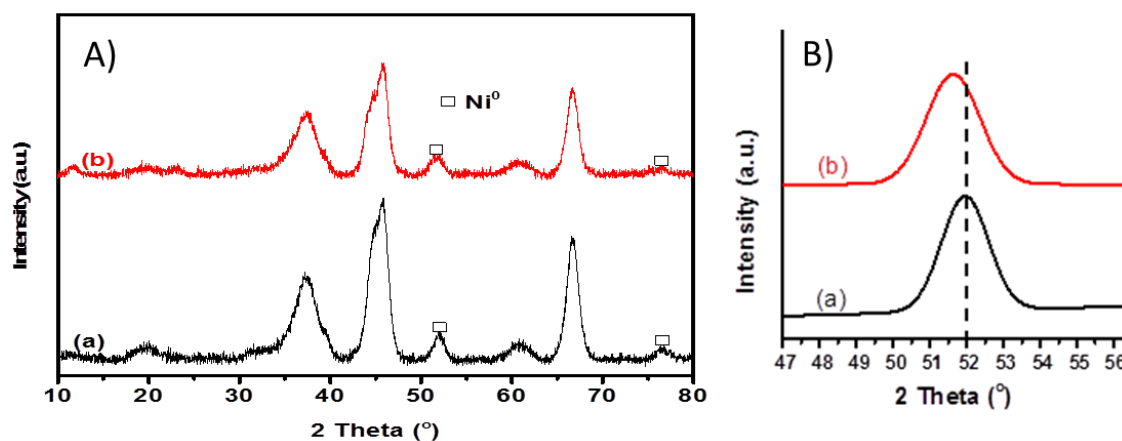


**Figure 5.16** A) XRD patterns of spent catalysts: (a) 25%Ni-Al<sub>2</sub>O<sub>3</sub>-NS and (b) 25%Ni-2.5%Fe-Al<sub>2</sub>O<sub>3</sub>-NS. B) 47-56° regional XRD patterns: (a) 25%Ni-Al<sub>2</sub>O<sub>3</sub>-NS and (b) 25%Ni-2.5%Fe-Al<sub>2</sub>O<sub>3</sub>-NS.

TGA data (**Figure 5.17**) of the spent catalysts show how the Ni nanoparticles in the Fe-containing NS sample (sample a) are rather resistant to re-oxidation, differently from the sample with the same composition, but prepared using bulk-type alumina (sample c). Note how the NS sample not containing Fe (sample b) shows only some weak indication of a possible oxidation. This is in agreement with the quantitative H<sub>2</sub>-TPR data (**Table 5.2**) indicating only a slight improvement in the reduction degree of the Fe-containing NS sample, in comparison with the NS sample without Fe.

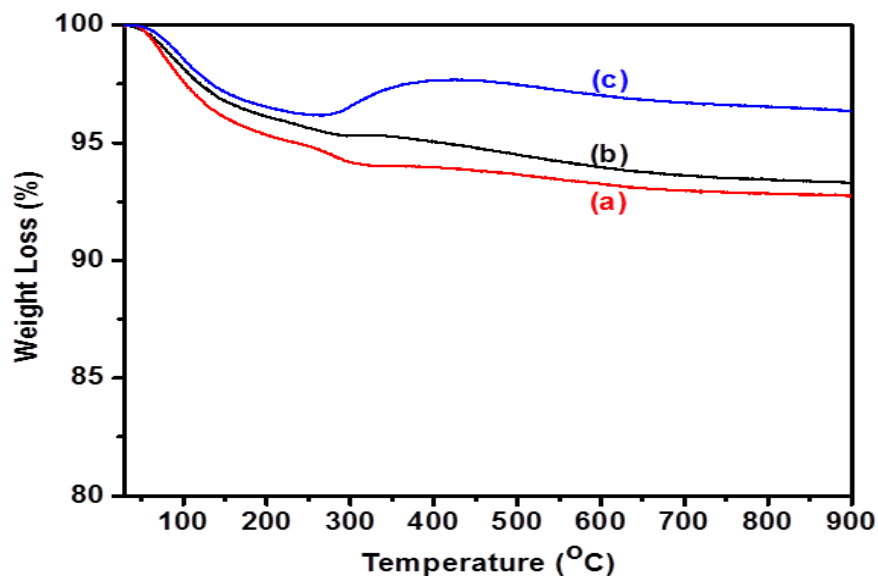


**Figure 5.17** TGA profiles (in air) of catalysts after reaction: (a) 25%Ni-2.5%Fe-Al<sub>2</sub>O<sub>3</sub>-NS, (b) 25%Ni-Al<sub>2</sub>O<sub>3</sub>-NS and (c) 25%Ni-2.5%Fe-Al<sub>2</sub>O<sub>3</sub>-B (B stands for bulk-type).

Characterization data reported for the spent catalysts, well confirm the stability of the Ni particles during the long-term catalytic tests. The average particle diameter, as well as the Ni dispersion, remains quite constant (see [Table 5.4](#)), and the TGA did not show any weight loss typically in the temperature range 450-700°C (see [Figure 5.17](#)) indicating the absence of coke formation after long-term tests. It is important to note that for catalysts used in CO<sub>2</sub> methanation, Ni particles sintering and coke formation are the two main reasons for catalysts deactivation for CO<sub>2</sub> methanation reaction. Therefore, the synergy between NS structure and Fe promotion is a promising route for improving the catalyst stability.

## 5.6. Conclusion

In this study, we have prepared two different types of catalytic materials and compared with a commercial methanation catalyst. The combination of a two-step hydrothermal synthesis and Fe promotions allows preparing nanosheet-type Ni/Al<sub>2</sub>O<sub>3</sub> catalyst with high catalytic activity and stability in the CO<sub>2</sub> methanation. With respect to a commercial methanation catalyst, the sample having the nanosheet structure and containing Fe as promoter shows a lower rate of deactivation. With respect to nanosheet catalysts without Fe as a promoter, the integral rate of CO<sub>2</sub> depletion is around 5 times higher, while with respect to a catalyst with the same composition prepared by wetness impregnation, the activity is about 2.5 times higher. There is thus a synergic role of the nanostructure and of Fe promotion.

The characterization data on the catalysts, before and after long-term catalytic tests, show that Fe forms an alloy with Ni, but likely this effect is only responsible for a slight increase in dispersion and metallic surface area. There is thus an additional effect of iron, likely related to a promotion of the activation of CO<sub>2</sub>, which is determined from the close vicinity of iron and Ni nanoparticles, and in thus depending on the catalyst nanostructure. This is the reason for the observed synergy between NS structure and Fe promotion, and the positive effect in terms of stability of the catalyst in long-term catalytic experiments. The characterization data confirm the stability of the Ni particles during these extended catalytic tests. No relation is observed between the quantitative amount of basic sites and TOF values, but data suggest that the mobility of adsorbed CO<sub>2</sub> towards the Ni particles, favored by the weakening of medium-strong basic sites related to Fe promotion and NS structure, determines the reaction rate and TOF.

Based on the results presented in this chapter, the synergy between NS structure and Fe promotion leads to highly active and stable catalysts for CO<sub>2</sub> methanation at low temperature (300°C), with significantly better performance than a reference commercial methanation catalyst.

## 5.7. References

- [1] L. Zhang, Y. Zhang, *RSC Adv.*, 5 (2015) 62173-62178.
- [2] M. A. Lucchini, A. Testino, C. Ludwig, A. Kambolis, M. El-Kazzi, A. Cervellino, P. Riani, F. Canepa, *Appl. Catal. B: Env.*, 156 (2014) 404-415.
- [3] E. Kiss, G. Bošković, M. Lazić, G. Lomić, R. Marinković-Nedučin, *Scanning*, 28 (2006) 236-241.
- [4] M. Msharrafieh, M. Al-Ghoul, H. Batlouni, R. Sultan, *J. Phys. Chem. A*, 111 (2007) 6967-6976.
- [5] H. Xu, W. Wang, W. Zhu, L. Zhou, M. Ruan, *Crystal Growth & Design*, 7 (2007) 2720-2724.
- [6] J. Liu, X. Huang, Y. Li, K. Sulieman, X. He, F. Sun, *Crystal Growth & Design*, 6 (2006) 1690-1696.
- [7] L. Wang, T. Fei, Z. Lou, T. Zhang, *ACS Appl. Mat. Interfaces*, 3 (2011) 4689-4694.
- [8] Y.-L. Hou, S. Gao, *J. Alloys and Comp.*, 365 (2004) 112-116.
- [9] K. P. Donegan, J. F. Godsell, D. J. Otway, M. A. Morris, S. Roy, J. D. Holmes, *J. Nanopart. Res.*, 14 (2012) 670-1/10.
- [10] M.A. Dominguez-Crespo, E. Ramirez-Meneses, V. Montiel-Palmab, A.M. Torres Huertaa, H. Dorantes Rosales, *Int. J. Hydrogen Energy*, 34 (2009) 1664-1676.
- [11] R. Eluri, B. Paul, *Mat. Lett.*, 76 (2012) 36-39.
- [12] D. Li, S. Komarneni, *J. Am. Ceram. Soc.*, 89 (2006) 1510-1517.
- [13] X. Wu, D. Wang, Z. Hu, G. Gu, *Mat. Chem. and Phys.*, 109 (2008) 560-564.
- [14] S. Abate, K. Barbera, E. Giglio, F. Deorsola, S. Bensaid, S. Perathoner, R. Pirone, G. Centi, *Ind. & Eng. Chem. Res.*, 55 (2016) 8299-8308.
- [15] K. Wang, L. Li1, T. Zhang. *Int. J. Electrochem. Sci.* 8 (2013) 6252-6257.
- [16] M.C. Biesinger, B.P. Payne, L.W.M. Lau, A. Gerson, R. St. C. Smart, *Surf. Interface Anal.*, 41(2009) 324-332.
- [17] <https://srdata.nist.gov/xps/>
- [18] D. Li, M. Koike, L. Wang, Y. Nakagawa, Y. Xu, K. Tomishige, *ChemSusChem*, 7 (2014) 510-522.

- [19] D. Pandey, G. Deo, *J. Ind. Eng. Chem.*, 33 (2016) 99-107.
- [20] H. Lu, X. Yang, G. Gao, J. Wang, C. Han, X. Liang, C. Li, Y. Li, W. Zhang, X. Chen, *Fuel*, 183 (2016) 335-344.
- [21] J. Sehested, K. E. Larsen, A. L. Kustov, A. M. Frey, T. Johannessen, T. Bligaard, M. P. Andersson, J. K. Nørskov, C. H. Christensen, *Top. Catal.*, 45 (2007) 9-13.
- [22] Z. Hao, Q. Zhu, Z. Jiang, B. Hou, H. Li, *Fuel Proc. Techn.*, 90 (2009) 113-121.
- [23] A. Zhao, W. Ying, H. Zhang, M. Hongfang, D. Fang, *J. Natural Gas Chem.*, 21 (2012) 170-177.
- [24] G. C. Allen, S. J. Harris, J. A. Jutson, J. M. Dyke, *Appl. Surface Science*, 37 (1989) 111-134.
- [25] L. Chen, H. Dai, Y. Shen, J. Bai, *J. Alloys and Compounds*, 491 (2010) L33-L38.
- [26] M. C. Biesinger, B. P. Payne, L. W. M. Lau, A. Gerson, R. St. C. Smart, *Surf. Interface Anal.*, 41 (2009) 324-332.
- [27] R. Dębek, M. Radlik, M. Motak, M. E. Galvez, W. Turek, P. D. Costa, T. Grzybek, *Catal. Today*, 257 (2015) 59-65.
- [28] R. A. Hubble, J. Y. Lim, J. S. Dennis, *Faraday Discuss.*, 192 (2016) 529-544.
- [29] Jin YangLim, J. McGregor, A.J. Sederman, J.S. Dennis, *Chem. Eng. Science*, 141 (2016) 28-45.
- [30] T. K. Campbell, J. Falconer, *Appl. Catal.*, 50 (1989) 189-197.

The H<sub>2</sub>-TPR profile (**Fig. 1**) of 25%Ni-2.5%Fe-Al<sub>2</sub>O<sub>3</sub>-B catalyst. The maximum temperature to reduce fully the catalyst is 550°C, which indicates the catalyst is easy to reduce and oxidize at lower temperatures.

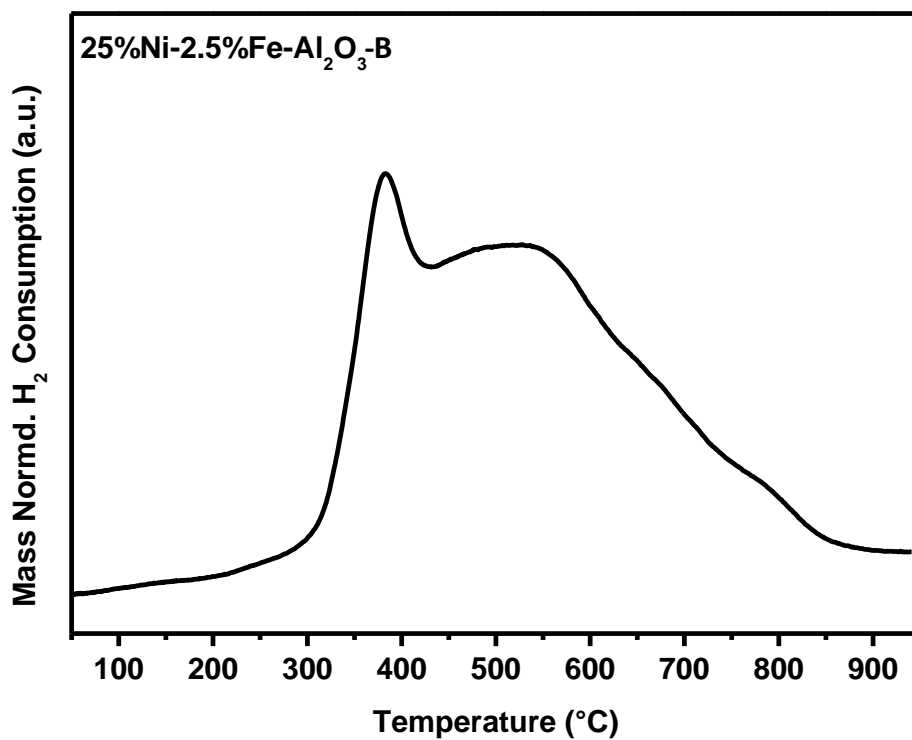


**Figure 1.** H<sub>2</sub>-TPR profile of 25%Ni-2.5%Fe-Al<sub>2</sub>O<sub>3</sub>-B sample.

# CHAPTER 6

## 6. General conclusion and outlooks

The presented Ph.D. thesis was focused on the development of advanced catalysts with higher activity and long-term stability for low-temperature CO<sub>2</sub> methanation. The literature study revealed that the most efficient catalytic systems applied for CO<sub>2</sub> methanation process should be based on nickel as an active phase and alumina as support. The beneficial application of Ni comes from the fact that it is the most active metal in the CO<sub>2</sub> hydrogenation reaction, which may be applied on the industrial scale. Although the noble-metal based catalysts showed higher activity in CO<sub>2</sub> methanation, their application in large-scale methanation plants is limited due to high price and low availability. However, Ni-based catalytic systems suffer deactivation upon methanation due to the carbon deposition and sintering of active phase. Different strategies were proposed in the literature in order to increase the stability of Ni-based catalytic systems. The most common ones include the application of mixed oxide supports and/or promoters with high basicity in order to improve CO<sub>2</sub> adsorption and dissociation properties on the catalyst surface. Another approach is to increase interactions between nickel active phase and support and thus inhibit sintering.

Therefore, the main goal of this Ph.D. thesis was to evaluate catalytic performance of different systems containing nickel as active metal for CO<sub>2</sub> methanation. Literature reviews showed that there are several areas of research concerning applications of different methods to improve Ni-based catalysts. The research presented in this Ph.D. thesis was thus aimed at filling these gaps and was divided into four parts: (i) the application of multicomponent mixed oxides as support for Ni-based catalyst, (ii) the evaluation and influence of Fe content as second active metal in hydrotalcite-like layered materials and their catalytic properties, (iii) the study of wide range of nickel and Mg content to study the effect of support basicity as well as metal loading on hydrotalcite derived Ni-Fe catalysts and (iv) investigating the effect of catalyst morphology on the activity of Ni-based catalysts. In order to address these issues, different catalysts were synthesized using different methods such as impregnation-precipitation, co-precipitation, and two-step hydrothermal. The physicochemical properties of the prepared catalysts were evaluated by means of elemental analysis (AAS, ICP-OES or XRF), XRD, N<sub>2</sub>-sorption, H<sub>2</sub>-TPR, TG experiments, amount of basic sites (irreversible acid adsorption method or CO<sub>2</sub>-TPD), SEM, STEM and XPS techniques. The prepared catalysts were subsequently tested in low-temperature CO<sub>2</sub> methanation.



It should be stated that the application of low reaction temperatures is advantageous both from catalyst stability and economic perspective. Three types of reactors: high-throughput reactor (Amtech SPIDER 16) with sixteen fixed bed reactors, a Microactivity Efficient equipment (Micromeritics) with two fixed bed reactors and a laboratory built fixed bed reactor were used to perform the CO<sub>2</sub> methanation tests.

The application of mixed oxide supported Ni-based catalysts in CO<sub>2</sub> methanation has been proven to give materials with improved properties. Nickel-based catalysts supported on ternary ( $\gamma$ -Al<sub>2</sub>O<sub>3</sub>-ZrO<sub>2</sub>-TiO<sub>2</sub>) and quaternary ( $\gamma$ -Al<sub>2</sub>O<sub>3</sub>-ZrO<sub>2</sub>-TiO<sub>2</sub>-CeO<sub>2</sub>) mixed oxides showed a higher surface area and better metal dispersion than the reference Ni/ $\gamma$ -Al<sub>2</sub>O<sub>3</sub> catalyst. The H<sub>2</sub>-TPR profile deconvolution led to the identification of three elementary peaks related to three NiO types: ‘ $\alpha$ ’ (bulk NiO), ‘ $\beta$ ’ (NiO weakly interacted with Al<sub>2</sub>O<sub>3</sub>), and ‘ $\gamma$ ’ (NiO strongly interacted with Al<sub>2</sub>O<sub>3</sub>). The mixed oxides supported Ni-based catalysts have a major fraction of  $\beta$ -type NiO, which is considered to be the active component for CO<sub>2</sub> methanation. The results of CO<sub>2</sub> methanation showed that enhanced catalytic activity depends on both textural improvements (for the ternary mixed oxide supported Ni) and reducibility and metal dispersion (for the quaternary mixed oxide supported Ni). Even though, mixed oxide supported Ni-based catalysts performed better compared to the Ni/ $\gamma$ -Al<sub>2</sub>O<sub>3</sub> catalyst, a Ni-based based catalyst with higher active metal loading equal to the existing commercial methanation catalysts (75-80% of Ni) is difficult to prepare using impregnation method. Therefore, due to the limitations of the preparation method, we draw our attention on using hydrotalcite-type Ni-based catalysts with an introduction of Fe as second metal. Because several studies showed that active metal content on HTs type of catalysts can be easily tuned without affecting the dispersion and particle size.

As it is noted, hydrotalcite-like Ni-Fe catalysts were selected because it is reported that Ni-Fe bimetallic catalysts show the lowest peak temperature in temperature-programmed surface reactions compared to monometallic catalysts or other bimetallic systems, which experimentally supports the optimal CO dissociation energy in the CO<sub>2</sub> methanation. Therefore, for the optimization of the Fe content in hydrotalcite derived Ni (Mg, Al)O<sub>x</sub> materials a series of catalysts with different Fe: Ni ratio (0-1.5) were prepared. The effect of different factors such as the amount of basic sites, particle size and amount of Fe were studied. Among the investigated catalysts in the

CO<sub>2</sub> methanation reaction, Ni-Fe catalyst with the relatively lower Fe content (Fe/Ni=0.1) showed better activity with the rate of 6.96 mmol CO<sub>2</sub> conversion/mol<sub>metal</sub>/s, 99.3% of CH<sub>4</sub> selectivity and excellent stability for 24 h at 335°C. Main factors for enhanced performance and stability of hydrotalcite derived Fe/Ni=0.1 catalyst comprehend to the higher specific surface area, smaller particle size, and better metal dispersion. It is worth mentioning that, for the group of catalysts studied in this *Chapter 3* there was no clear evidence for the relationship between the rate of CO<sub>2</sub> conversion and amount of basic sites present in the sample.

Therefore, in order to address the issue of how the amount of basic sites can influence the activity of hydrotalcite derived Ni-Fe catalysts, catalysts with tailored basicity were investigated towards CO<sub>2</sub> methanation. Hydrotalcite derived catalysts in which 0, 12, 20, 40, 60 or 75% of Mg<sup>2+</sup> of the brucite-like layers substituted by Ni<sup>2+</sup> cations using the M<sup>2+</sup>/M<sup>3+</sup> ratio of 3 were prepared. A constant Fe/Ni ratio which equals to 0.1 was used (based on results from *Chapter 3*). All prepared catalysts were characterized using different techniques and tested towards CO<sub>2</sub> methanation at 300°C under differential conditions. CO<sub>2</sub>-TPD analysis evidences the preparation of catalysts with a significant difference in the amount of basic sites. STEM measurements of the reduced samples were also demonstrated how the particle size and dispersion can be changed with increasing active metal loading. Among the as-prepared catalysts, the Ni<sub>0.2</sub>Fe<sub>0.02</sub>Mg<sub>0.55</sub>Al<sub>0.23</sub> catalyst was found to be the most active catalyst. The rate of CO<sub>2</sub> conversion was about 0.251 mol CO<sub>2</sub> conv./mol<sub>Ni+Fe</sub>/S with a CH<sub>4</sub> selectivity of 97% was recorded at 300°C. It was also stable during the 20 h reaction. Its improved performance might be due to the optimum basic sites, better dispersion and smaller particle size formed after reduction at 900°C. Though the catalytic activity of as-prepared catalysts was largely affected by the basicity of the support, other factors such as average particle size and metal dispersion were also showed considerable effect. Therefore, for hydrotalcite derived catalysts, it is not only the basic site governs the activity rather a combined effect of different factors results in an enhanced performance.

Finally, aiming at further improving the Ni-Fe catalysts, the effect of catalyst morphology (shape and geometry of both the active metal and support) towards CO<sub>2</sub> methanation, nanosheet like catalysts were prepared using a two-step hydrothermal synthesis method. Physicochemical properties of the new materials were studied using different characterization techniques and

catalytic activity was tested. The catalytic activity of nanosheet like catalysts was compared with the Fe promoted bulk type catalyst in order to study the effect of the microstructure. SEM and TEM analyses confirmed the synthesis of materials with nanosheet like structure. The Fe promotion and unique microstructure are considered to be the most affecting parameters the CO<sub>2</sub> methanation activity of the Fe promoted nanosheet-like a catalyst. With respect to nanosheet catalysts without Fe as a promoter, the integral rate of CO<sub>2</sub> conversion is around 5 times higher, while with respect to a catalyst with the same composition, but prepared using a bulk-type alumina, the activity is about 2.5 times higher. There is thus a synergic role of the nanostructure and Fe promotion. But, no clear relationship is observed between the amount of basic sites and TOF values, but data suggest that the mobility of adsorbed CO<sub>2</sub> towards the Ni particles, favored by the weakening of medium-strong basic sites related to Fe promotion and NS structure, determines the reaction rate and TOF. The Ni-Fe based nanosheet like catalyst was also compared with a commercial CO<sub>2</sub> methanation catalyst (76%Ni/Al<sub>2</sub>O<sub>3</sub>), and a slightly enhanced stability was obtained with the nanosheet like a catalyst in 50 h reaction.

In conclusion, the results of this Ph.D. study confirmed that the catalytic properties of nickel-based catalysts towards CO<sub>2</sub> methanation can be tailored and improved by:

- (i) Preparation of mixed oxide supported nickel-based catalysts.
- (ii) Optimization of Fe: Ni ratio, Ni loading and amount of basic sites on hydrotalcite derived Ni-Fe catalysts for better activity and stability.
- (iii) Application of synthesis methods which enables to prepare catalysts with unique morphology and properties.

Generally, the catalysts prepared during this Ph.D. study showed very good catalytic performance in CO<sub>2</sub> methanation reaction at temperatures between 300-350°C. Compared to commercial catalysts, the as-prepared catalyst with unique morphology showed better activity and stability under the same experimental conditions used. Further research in this area will allow developing even more active, selective and stable catalyst for CO<sub>2</sub> methanation, allowing in this way a future commercialization of the catalysts with improved properties.

## Curriculum vitae

### PERSONAL INFORMATION CHALACHEW MEBRAHTU ASMELASH



Address: ERSU, Residence Papardo  
Contrada di dio  
98166, Messina, Italy

Phone: +393245463879

E-mail: [casmelash@unime.it](mailto:casmelash@unime.it) or [challm2008@gmail.com](mailto:challm2008@gmail.com)

### WORK EXPERIENCE

---

September 2008 - October 2014 Assistant Lecturer and Researcher.  
Haramaya University, Ethiopia

### EDUCATION AND TRAINING

---

November 2014 - Present Ph.D. (SINCHEM-Erasmus Mundus Joint Doctorate Program) at:  
Dep't of Engineering University of Messina: Home University  
ITMC RWTH Aachen University: Host University

September 2011- July 2013 M.Sc. in Physical Chemistry  
Haramaya University, Ethiopia  
Thesis: Development of novel semiconductors for PECs.  
Supervisor: Prof. Teketel Yohannes (AASTU, Addis Ababa, Ethiopia)

September 2006- July 2008 B.Sc. in Applied Chemistry  
Arba Minch University, Ethiopia

### PERSONAL SKILLS

---

**Languages** English, Amharic and Tigrinya

- Others professional skills**
- Design of semiconductors, PECs constructions and evaluation.
  - Development of advanced catalysts for CO<sub>2</sub> methanation for effective power to gas (P2G) process.
  - Working on different characterization instruments to study properties of heterogeneous catalysts such as XRD, TGA, TPR-TPD-TPO instruments, S/TEM, AAS, and GC-MS etc.

## PUBLICATIONS

---

### Publications based on the Ph.D. thesis:

1. Salvatore Abate, **Chalachew Mebrahtu**, Emanuele Giglio, Fabio Deorsola, Samir Bensaid, Siglinda Perathoner, Raffaele Pirone, Gabriele Centi, *Ind. Eng. Chem. Res.*, **2016**, *55 (16)*, **4451-4460**.
2. **C. Mebrahtu**, F. Krebs, K. Simeonov, S. Abate, S. Perathoner, G. Centi, R. Palkovits. *Chemie Ingenieur Technik* **88(9):1261-1261. September 2016**.
3. **Chalachew Mebrahtu**, Salvatore Abate, Siglinda Perathoner, Shiming Chen, Gabriele Centi, *Catalysis Today*, **2018**, *304*, **181-189**.
4. **Chalachew Mebrahtu**, Salvatore Abate, Shiming Chen, Andres Felipe Sierra salazar, Siglinda Perathoner, Florian Krebs, Regina Palkovits, Gabriele Centi, *Energy Technology Accepted Manuscript*, DOI: **10.1002/ente.201700835**.
5. **Chalachew Mebrahtu**, Florian Krebs, Siglinda Perathoner, Salvatore Abate, Gabriele Centi, Regina Palkovits, *Catal. Sci. & Technol.*, **2018**, *8*, **1016-1027**.

### Other publications:

1. Shiming Chen, Siglinda Perathoner, Claudio Ampelli, **Chalachew Mebrahtu**, Dangsheng Su, Gabriele Centi, *Angew. Chem. Int. Ed.* **2017**, *56*, **2699-2703**.

2. Shiming Chen, Siglinda Perathoner, Claudio Ampelli, **Chalachew Mebrahtu**, Dangsheng Su, Gabriele Centi, *ACS Sustainable Chem. Eng.*, 2017, 5 (8), 7393-7400.
3. **C. Mebrahtu**, A. M. Taddesse, G. Goro, T. Yohannes, *Bull. Chem. Soc. Ethiop.* 2017, 31(2), 263-279.

## CONFERENCE PRESENTATIONS

---

1. X National Meeting on Materials Sciences and Technology. June 28<sup>th</sup>- July 1<sup>st</sup>, 2015. Favignana, Italy. **(Short oral presentation)**
2. ISGC 2017, the 4<sup>th</sup> International Symposium on Green Chemistry from May 16<sup>th</sup> - 19<sup>th</sup>, 2017. La Rochelle, France. **(Short oral presentation)**
3. 25<sup>th</sup> North American Catalysis Society Meeting, June 4<sup>th</sup> - 9<sup>th</sup>, 2017. Denver, CO, the USA. **(Oral presentation)**
4. 13<sup>th</sup> European Catalysis Congress, August 27<sup>th</sup> -31<sup>st</sup>, 2017. Florence, Italy. **(Short oral presentation)**